

DOCTORAL THESIS

Deposition of Sb_2S_3 Thin Films by Ultrasonic Spray Pyrolysis for Photovoltaic Applications

Jako Siim Eensalu

TALLINN UNIVERSITY OF TECHNOLOGY
DOCTORAL THESIS
1/2022

**Deposition of Sb₂S₃ Thin Films by
Ultrasonic Spray Pyrolysis for
Photovoltaic Applications**

JAKO SIIM EENSALU



TALLINN UNIVERSITY OF TECHNOLOGY

School of Engineering

Department of Materials and Environmental Technology

This dissertation was accepted for the defence of the degree 22/12/2021

Supervisor:

Prof. Malle Krunk
School of Engineering
Tallinn University of Technology
Tallinn, Estonia

Co-supervisor:

Prof. Ilona Oja Acik
School of Engineering
Tallinn University of Technology
Tallinn, Estonia

Opponents:

Prof Julien Bachmann
Friedrich-Alexander Universität Erlangen-Nürnberg
Erlangen, Germany

Prof Marco Kirm
Institute of Physics
University of Tartu
Tartu, Estonia

Defence of the thesis: 26/01/2022, Tallinn

Declaration:

Hereby I declare that this doctoral thesis, my original investigation and achievement, submitted for the doctoral degree at Tallinn University of Technology has not been submitted for doctoral or equivalent academic degree.

Jako Siim Eensalu

signature



European Union
European Regional
Development Fund



Investing
in your future

Copyright: Jako Siim Eensalu, 2021

ISSN 2585-6898 (publication)

ISBN 978-9949-83-781-6 (publication)

ISSN 2585-6901 (PDF)

ISBN 978-9949-83-782-3 (PDF)

Printed by Koopia Niini & Rauam

TALLINNA TEHNIKAÜLIKOOL
DOKTORITÖÖ
1/2022

**Päikesepatareides rakendatavate Sb_2S_3
õhukeste kilede sadestamine
ultrahelipihustuspürolüüsi meetodil**

JAKO SIIM EENSALU



Contents

Contents.....	5
List of Publications	7
Author's Contribution to the Publications	8
Introduction	9
Abbreviations, Terms and Symbols.....	11
1 Literature review.....	13
1.1 Fundamentals of photovoltaics	13
1.2 Established photovoltaic technologies	13
1.2.1 Silicon PV	13
1.2.2 Thin film PV	14
1.3 Emerging photovoltaic technologies	15
1.4 Antimony based photovoltaic absorbers.....	18
1.4.1 Sb_2S_3 , Sb_2Se_3 , and $Sb_2(S,Se)_3$	18
1.4.2 Ternary and quaternary Sb based absorbers	20
1.5 Solar cells based on Sb_2S_3 absorber	21
1.5.1 Structure of Sb_2S_3 solar cells	21
1.5.2 Development of Sb_2S_3 solar cells.....	22
1.5.3 Further development of Sb_2S_3 solar cells	24
1.6 Deposition methods for Sb_2S_3 thin films	30
1.6.1 Physical methods	30
1.6.2 Chemical methods.....	30
1.7 Deposition of Sb_2S_3 thin films by spray pyrolysis.....	34
1.7.1 Pneumatic spray pyrolysis.....	34
1.7.2 Ultrasonic spray pyrolysis	35
1.7.3 Selection of precursors to deposit Sb_2S_3 thin films by USP.....	35
1.8 Summary of the literature review and aim of the thesis.....	37
2 Experimental	39
2.1 Preparation of Sb_2S_3 thin films and solar cells.....	39
2.2 Applied characterization methods	42
3 Results and discussion.....	43
3.1 Deposition of Sb_2S_3 thin films from $SbCl_3$ /TU solutions by ultrasonic spray pyrolysis.....	43
3.1.1 Phase composition and structure	43
3.1.2 Elemental composition	46
3.1.3 Optical properties	47
3.1.4 Morphology.....	47
3.1.5 Growth mechanism of Sb_2S_3 thin films on a planar substrate	48
3.1.6 Summary	49
3.2 Application of Sb_2S_3 thin films grown by ultrasonic spray pyrolysis in planar thin film solar cells.....	50
3.2.1 Influence of Sb_2S_3 film thickness on PV performance of solar cells	50
3.2.2 Influence of cell area, storage time and light intensity on PV performance of Sb_2S_3 solar cells	52
3.2.3 Summary	54

3.3 Thermal analysis of SbEX as an alternative precursor for depositing Sb ₂ S ₃ thin films	55
3.3.1 Synthesis and identification of SbEX	55
3.3.2 Thermal analysis of SbEX.....	55
3.3.3 Summary	56
3.4 Deposition of Sb ₂ S ₃ thin films from SbEX solutions by ultrasonic spray pyrolysis	58
3.4.1 Deposition of Sb ₂ S ₃ films from SbEX solution	58
3.4.2 Deposition of Sb ₂ S ₃ films from SbEX/thioamide solutions.....	59
3.4.3 Summary	61
Conclusions	62
Future outlook	64
References	65
Acknowledgements.....	82
Abstract.....	83
Lühikokkuvõte.....	85
Appendix	87
Curriculum vitae.....	147
Elulookirjeldus.....	150

List of Publications

The list of the author's publications based on which the thesis has been written:

- I **J. S. Eensalu**, A. Katerski, E. Kärber, I. Oja Acik, A. Mere, M. Krunks. "Uniform Sb₂S₃ optical coatings by chemical spray method," *Beilstein Journal of Nanotechnology*, vol. 10, pp. 198–210, Jan. 2019, doi: 10.3762/bjnano.10.18.
- II **J. S. Eensalu**, A. Katerski, E. Kärber, L. Weinhardt, M. Blum, C. Heske, W. Yang, I. Oja Acik, M. Krunks. "Semitransparent Sb₂S₃ thin film solar cells by ultrasonic spray pyrolysis for use in solar windows," *Beilstein Journal of Nanotechnology*, vol. 10, pp. 2396–2409, Dec. 2019, doi: 10.3762/bjnano.10.230.
- III **J. S. Eensalu**, K. Tõnsuaadu, J. Adamson, I. Oja Acik, M. Krunks. "Thermal decomposition of *tris*(O-ethylthiocarbonato)-antimony(III)—a single-source precursor for antimony sulfide thin films," *Journal of Thermal Analysis and Calorimetry*, Jun. 2021, doi: 10.1007/s10973-021-10885-1.
- IV **J. S. Eensalu**, K. Tõnsuaadu, I. Oja Acik, M. Krunks. "Sb₂S₃ thin films by ultrasonic spray pyrolysis of antimony ethyl xanthate," *Materials Science in Semiconductor Processing*, vol. 137, p. 106209, Jan. 2022, doi: 10.1016/j.mssp.2021.106209.

Author's Contribution to the Publications

The author's contribution to the papers in this thesis is as follows:

- I Deposition of TiO_2 , and Sb_2S_3 thin films by ultrasonic spray pyrolysis; post-deposition heat treatment of thin films; characterization of structure, optical and vibrational properties of glass/ITO/ TiO_2 / Sb_2S_3 stacks by X-ray diffraction (XRD), Raman spectroscopy, and ultraviolet-visible spectroscopy (UV-VIS); data analysis; visuals; major role in writing.
- II Deposition of TiO_2 , and Sb_2S_3 thin films by ultrasonic spray pyrolysis; major role in preparation of glass/ITO/ TiO_2 / Sb_2S_3 /P3HT/Au solar cells; post-deposition heat treatment of samples; characterization of structure, optical, electrical and vibrational properties of glass/ITO/ TiO_2 / Sb_2S_3 stacks by XRD, Raman, van der Pauw, and UV-VIS; major role in characterization of solar cells by current-voltage and external quantum efficiency; data analysis; visuals; major role in writing.
- III Synthesis, identification and thermal analysis of antimony ethyl xanthate, preparation and *ex-situ* analysis of its intermediate and final solid decomposition products; characterization of structure, and vibrational properties of the aforementioned samples by XRD, Fourier transform infrared spectroscopy (FTIR), and Raman; data analysis; visuals; major role in writing.
- IV Synthesis of antimony ethyl xanthate; deposition of thin films from antimony ethyl xanthate solution with or without thiourea, or thioacetamide; post-deposition heat treatment of thin films; characterization of structure, optical, and vibrational properties of as-grown and heat treated thin films on glass/ITO/ TiO_2 substrate by XRD, UV-VIS, FTIR, and Raman; data analysis; visuals; major role in writing.

Introduction

Several countries have ambitiously promised to achieve net-zero carbon emissions (NZE) by 2050 to combat global warming and environmental pollution [1], [2]. The worldwide adaptation of NZE requires a swift transition from non-renewable energy sources, i.e. oil, coal, and nuclear (71 % of global electricity generation in 2019), to 70 % renewables, i.e. wind, water, and solar power by 2050 [3]. The optimistic NZE scenario requires increasing the annual installed capacity of photovoltaics (PV) fivefold by 2050 [3]. Accordingly, PV could contribute substantially to achieving NZE by 2050.

At present, crystalline silicon (c-Si), and thin film PV contribute 95 %, and 5 %, respectively, to the worldwide PV installation capacity [4]. Additionally, emerging PV, e.g. kesterites, dye sensitized solar cells, organic PV, perovskites, quantum dot PV, and binary chalcogenide PV, could support the effort toward achieving NZE. Currently, standalone, tandem and bifacial solar cells based on emerging PV and c-Si are considered promising for contributing to NZE. In addition, building integrated PV, e.g. solar windows, and product integrated PV, e.g. consumer products, are also perceived as viable applications for emerging PV. As these applications rely on long-term stability, solar cells based on inorganic absorber materials would be advantageous.

Among inorganic emerging PV technologies, Sb_2S_3 solar cells are increasingly more popular for semitransparent PV applications due to the stability of the material toward temperature, moisture, ultraviolet light, and oxidation, and an absorption coefficient of 10^5 cm^{-1} in visible light, and a direct band gap = 1.7 eV [5]. Furthermore, as Sb, and S are abundantly available resources, there is definitely potential to prepare transparent Sb_2S_3 solar cells in a substantial installation capacity.

In order to produce solar cells in a capacity that contributes to achieving NZE by 2050, the fabrication process must be appropriate. Sb_2S_3 thin films have been commonly grown by chemical bath deposition, spin coating, atomic layer deposition, and ultrasonic spray pyrolysis (USP), yielding solar cells with $\eta = 7.5 \%$ [6], 4.3 % [7], 5.8 % [8], and 1.9 % [9] by 2017, respectively. The η achieved by USP- Sb_2S_3 solar cells was lower because the preparation of Sb_2S_3 films by USP was relatively unexplored. Thus far, Sb_2S_3 had been grown in a single step by USP on a planar substrate [9], and by a two-step process onto a nonplanar substrate [10].

USP is a robust and rapid solution based technique applicable for continuous deposition onto large substrates, e.g. window glass panes in air. Furthermore, spent feedstock can be recycled with commonly available processes to reduce waste. However, the processing conditions to deposit continuous planar Sb_2S_3 films must be developed.

The aim of this research is to deposit phase pure continuous Sb_2S_3 thin films with a uniform thickness by ultrasonic spray pyrolysis, and to apply the films in planar solar cells. The procedure to achieve the aim, and to understand the growth mechanism of Sb_2S_3 thin films by ultrasonic spray pyrolysis was developed by tuning the deposition conditions for a halogenide-based, and a halogenide-free precursor solution. The suitability of the halogenide-free precursor for the purposes of the thesis was investigated by thermal analysis. Planar Sb_2S_3 thin film solar cells were prepared from the halogenide-based precursor solution using ultrasonic spray pyrolysis. The effect of absorber thickness, cell area, storage time, and light intensity was investigated for these solar cells to provide a more thorough understanding of the photovoltaic performance of Sb_2S_3 solar cells, and to identify possible challenges.

The novelty of this study is that the technological route was developed for preparing continuous phase pure Sb_2S_3 thin films on a planar substrate from a solution of $\text{Sb}(\text{TU})_3\text{Cl}_3$ by a two-step process. The methodology was developed by varying the solution composition and USP deposition temperature, and the post-deposition heat treatment temperature. Furthermore, it was proven that these Sb_2S_3 thin films grown by USP are applicable for use in planar thin film solar cells, yielding up to 5.5 % power conversion efficiency after optimizing the thickness of the absorber. Moreover, the applicability of antimony ethyl xanthate (SbEX) as a precursor for depositing Sb_2S_3 thin films by USP was assessed via thermal analysis and solid SbEX decomposition product analysis. Finally, the technological route to deposit continuous phase pure Sb_2S_3 thin films was developed based on the results of varying the solution of SbEX/thiourea or SbEX/thioacetamide, deposition temperature and precursor solution composition.

This thesis is based on four published papers, and contains three chapters. The first chapter is a literature overview of established and emerging photovoltaics with a focus on Sb_2S_3 as a photovoltaic material. Development of Sb_2S_3 solar cells before 2017, and in parallel to this thesis is discussed. Deposition methods used to grow Sb_2S_3 thin films for photovoltaic applications are described. USP as a prospective deposition method is discussed at length. The hypothesis and the aim of this thesis conclude the literature survey. The applied experimental procedures and characterization methods are summarized in the second chapter. The third chapter containing the results and discussion of the thesis is divided into four sections.

The first section in the results and discussion chapter summarizes the results of paper **I** and **II** on depositing uniform phase pure Sb_2S_3 thin films by USP at different deposition temperatures, and at different molar ratios of SbCl_3 and thiourea (TU) in the solution. The second section summarizes the results of paper **II** on the photovoltaic performance of solar cells based on a Sb_2S_3 thin film grown by USP from a solution of $\text{SbCl}_3/\text{TU} = 1/3$. The third section summarizes the results of paper **III** on the thermal analysis of SbEX as a possible halogenide-free precursor to deposit Sb_2S_3 thin films by USP. The fourth section summarizes the results of paper **IV** on the deposition of Sb_2S_3 thin films by USP from a solution of SbEX with TU or TA at different deposition temperatures.

This thesis is directly related to the ongoing research projects in the Laboratory of Thin Film Chemical Technologies, which focus on the development of antimony chalcogenide thin films by chemical and physical processes for application in transparent, bifacial, and conventional thin film solar cells. The research in this thesis was funded by the Estonian Ministry of Education and Research project IUT19-4, the Estonian Research Council grant PRG627, the European Regional Development Fund project TK141 “Advanced materials and high-technology devices for energy recuperation systems”, the project “Development of Semi-Transparent Bifacial Thin Film Solar Cells for Innovative Applications” contract with the Research Council of Lithuania (LMTLT), No S-BMT-21-1(LT08-2-LMT-K-01-003) financed by Iceland, Liechtenstein and Norway through the EEA Grants, and the European Council grant H2020 ERA Chair Emerging next generation photovoltaics, 5GSOLAR (2020–2026) Grant agreement ID: 952509. The research in this thesis was also partially supported by ASTRA “TUT Institutional Development Programme for 2016–2022” Graduate School of Functional Materials and Technologies. DoRa+ 1.1 travel scholarships to international conferences were financed by the Archimedes Foundation.

Abbreviations, Terms and Symbols

ALD	Atomic layer deposition
AM1.5G	Air mass 1.5 global
a-Si	Amorphous silicon
AVT	Average visible transmittance
BIPV	Building integrated photovoltaics
CBD	Chemical bath deposition
CIGS	Cu(In,Ga)(S,Se) ₂
c-Si	Crystalline silicon
CSS	Close spaced sublimation
CSP	Chemical spray pyrolysis
CZTS	Cu ₂ ZnSn(S,Se) ₄
<i>D</i>	Droplet diameter
DSSC	Dye sensitized solar cells
EDX	Energy dispersive X-ray spectroscopy
E_g	Band gap
EQE	External quantum efficiency
ETL	Electron transport layer
<i>f</i>	Frequency
FF	Fill factor
FTIR	Fourier transform infrared spectroscopy
HTL	Hole transport layer
<i>J-V</i>	Current density–voltage
J_{sc}	Short circuit current density
MAFAPBI	(CH ₃ NH ₃) _{1-x} (NH ₂ CHNH ₂) _x Pb(Br,I) ₃
NZE	Net zero carbon emissions
NMR	Nuclear magnetic resonance spectroscopy
OPV	Organic photovoltaics
P3HT	Poly(3-hexylthiophene-2,5-diyl)
PCPDTBT	poly(2,6-(4,4-bis-(2-ethylhexyl)-4Hcyclopenta[2,1-b;3,4-b']dithiophene)-alt-4,7(2,1,3-benzothiadiazole)
PEDOT:PSS	poly(3,4-ethylenedioxythiophene) polystyrene sulfonate
PV	Photovoltaic
QD	Quantum dot
R_s	Series resistance
R_{SH}	Shunt resistance
SEM	Scanning electron microscopy
SbEX	Antimony ethyl xanthate
Spiro-OMeTAD	2,2',7,7'- <i>tetrakis</i> -(N,N-di- <i>p</i> -methoxyphenylamine)-9,9'-spirobifluorene
TA	Thioacetamide
TG/DTA-EGA-MS	Thermogravimetry/differential thermal analysis-evolved gas analysis-mass spectrometry
TCO	Transparent conductive oxide
TU	Thiourea
USP	Ultrasonic chemical spray pyrolysis
UV-VIS	Ultraviolet-visible light

V_{oc}	Open-circuit voltage
VTD	Vapor transport deposition
W_p	Watt-peak
XES	Soft X-ray emission spectroscopy
XPS	X-ray photoelectron spectroscopy
XRD	X-ray diffraction
α	Light absorption coefficient
γ	Surface tension
η	Power conversion efficiency
θ	X-ray diffraction incidence angle
ρ	Volumetric mass density

1 Literature review

This chapter presents an overview of the fundamentals of photovoltaics, established and emerging photovoltaic technologies. The materials properties, common thin film deposition methods and development of solar cells pertaining to antimony sulfide (Sb_2S_3) is presented. A more thorough discussion is presented on ultrasonic chemical spray pyrolysis (USP) as a deposition method, and the selection criteria of precursors for the preparation of Sb_2S_3 thin films by the USP method. Power conversion efficiency (η) of all solar cells is reported at air-mass 1.5 global (AM1.5G) conditions throughout the thesis, unless explicitly mentioned otherwise.

1.1 Fundamentals of photovoltaics

A photovoltaic cell, or solar cell, is the smallest independent building block of photovoltaic modules. The built-in electric field at the *p-n-junction* formed at the interface of a p-type and an n-type semiconductor separates photogenerated electrons and holes, generating photocurrent under illumination [11].

In heterojunction thin film solar cells, the p-type semiconductor is usually the *absorber* layer and the n-type semiconductor is the *buffer* layer [11], [12]. Commonly, absorber materials with a direct band gap of $\approx 1.0\text{--}2.0$ eV, and an absorption coefficient (α) of $10^4\text{--}10^5$ cm^{-1} in visible light, are applied [11], [12]. The buffer is a generally a wide band gap n-type semiconductor that bridges the energy levels of the absorber and the n-type transparent conductive oxide (TCO) front contact [12], [13]. The buffer is also used to prevent shunting between the absorber and cathode, and to compensate for any potential mismatch in the crystal structure of the cathode and the absorber [12], [13].

Emerging heterojunction thin film solar cells often contain a p-i-n junction, where an intrinsic (i-type) absorber is sandwiched between the n-type buffer or *electron transport layer* (ETL) and the p-type *hole transport layer* (HTL). The benefit of a p-i-n vs p-n junction is that the depletion region is wider, which potentially increases the photon absorption yield, and that i-type absorbers can be used.

1.2 Established photovoltaic technologies

In this section, an overview is provided on established photovoltaic technologies.

Photovoltaic installations are estimated to consist globally of 95 % crystalline silicon (c-Si) PV and 5 % thin film PV, i.e. a-Si (0.1 %), CIGS (1.1 %), and CdTe (3.8 %) modules [4]. Evidently, c-Si PV is expected to contribute the most to fulfilling NZE PV targets. Gallium arsenide (GaAs) is the most efficient PV technology in single junction or multi junction configuration [14], however, it is too expensive for terrestrial use at present.

1.2.1 Silicon PV

The current record power conversion efficiency (η) of silicon modules is 26.7 % at AM1.5G, held by n-type c-Si [4]. This η is ≈ 80 % of the Shockley-Queisser limit for single junction cells with $E_g = 1.1$ eV [15], [16]. Hence, η of c-Si PV will likely be remarkably increased only by constructing a two-cell tandem with a ≈ 1.7 eV top cell and c-Si bottom cell to overcome the single junction limit [17]. The concept has been proven by $\eta = 29.2$ % achieved with a perovskite/c-Si two terminal laboratory solar cell [14]. The main issue with the two-cell tandem is ensuring a competitive module price and that the top cell performs on par with the bottom cell for an expected lifetime of 20–30 years.

Power generation can also be boosted by constructing bifacial solar cells, wherein light is absorbed from the front and back of the solar cell to boost energy production by some 20–30 % [18]–[20]. The record η of bifacial c-Si is 24.0 % [14]. Furthermore, reducing greenhouse gas emissions in the energy intensive c-Si processing life cycle is of critical importance for NZE [4], [21], as is consuming less silver (Ag) for contacts and less tin (Sn) for solder per module [22]. The aim to reduce the energy intensity of c-Si PV fabrication triggered the development of thin film PV [23].

1.2.2 Thin film PV

The earliest thin film PV to be developed was amorphous silicon (a-Si), which has an $E_g = 1.7$ eV and a single junction cell record $\eta = 10.2$ % [14]. The prompt degradation of η of a-Si to less than 8 % in sunlight has motivated the development of double and triple junction a-Si devices and a-Si/c-Si devices [23].

CdTe has an $E_g = 1.45$ eV and a high absorption coefficient in visible light, which makes it a top contender for thin film PV applications, considering that $\eta = 22.1$ % (cell) and 19.0 % (module) has been attained [4], [23]. Despite the accelerated growth of the installation capacity and recycling of CdTe PV in the United States [4], [24], Cd containing electrical goods are banned in Europe [25], as cadmium (Cd) and its compounds are listed as carcinogens [26]. The aversion to CdTe is potentially unfounded, as CdTe is reportedly 100 times less toxic than elemental Cd [27], and is claimed to pose a negligible hazard throughout its life cycle [13].

Aside from the controversy on toxicity of CdTe, the availability of tellurium (Te) is limited. Te is a byproduct of copper mining at a primary supply of 490 t yr⁻¹ of Te (\$55 kg⁻¹) [22], [28]. As 40 % of Te is already used to produce CdTe PV [28], the maximum installation capacity of CdTe PV is estimated at ≈ 14 gigawatt-peak per year (GW_p yr⁻¹), based on the current 5.7 GW_p yr⁻¹ [4], by assuming a constant capacity of Te refining.

CuIn_xGa_{1-x}S_ySe_{2-y} (CIGS) is popular for thin film PV due to a high absorption coefficient = 10⁵ cm⁻¹ in visible light and a tunable bandgap = 1.0–1.7 eV [29]. Although trailing in annual installation after CdTe PV, CIGS PV leads in efficiency, with $\eta = 23.4$ % for Cd-free cell and $\eta = 19.2$ % for module [4].

The main concern with upscaling production of CIGS PV modules is the availability and price of high purity In (900 t yr⁻¹; \$400 kg⁻¹), Ga (300 t yr⁻¹; \$570 kg⁻¹), and, to a degree, Se (2900 t yr⁻¹; \$44 kg⁻¹) [22], [28]. Thus, by replacing In and Ga in other applications, e.g. In₂O₃:Sn (ITO) coatings and GaN light emitting diodes [28], and by recycling nearly all of In and Ga, the maximum installation capacity of CIGS PV is estimated to be ≈ 31 GW_p yr⁻¹.

Nowadays, the most efficient CdTe modules are fabricated in the front to back superstrate configuration (glass/TCO/MgZnO/CdSe_xTe_{1-x}/2–8 μ m CdTe/back reflector/metal) [12], [13]. State of the art CIGS modules are mostly fabricated in the opposite substrate configuration (glass/Mo/1–2.5 μ m CIGS/Cd-free buffer/intrinsic ZnO/n-type ZnO/antireflect) [12], [30]. In either case, the layers are deposited from the most to the least heat tolerant by reducing the deposition and post-growth treatment temperature for every consecutive step. This allows to avoid uncontrolled diffusion of elements in bulk phase and provides control over intermixing at interfaces that can otherwise influence η [12], [13].

Regarding applications, c-Si, a-Si, CdTe, and CIGS modules are intentionally opaque to maximize photogenerated current and to minimize loss of η related to the bulk of the absorber [12], [13]. Accordingly, conventional PV is mostly installed onto opaque surfaces, e.g. solar fields [4], [31], and onto floors, walls and roofs as building attached PV [32].

1.3 Emerging photovoltaic technologies

Emerging PV encompasses prospective photovoltaic technologies that have yet to reach the market [14]. In case an emerging PV technology reaches maturity in terms of reasonable price per watt and module lifetime, solar fields similar to conventional PV could be built. The increasing demand for renewable PV energy to achieve NZE could also be partially met by combining conventional and emerging PV into bifacial and tandem solar cell PV arrays, as outlined in section 1.2.1. Emerging PV could thereby add value to industrial scale conventional PV installations as the semitransparent top cell in tandem solar cells in both single sided and bifacial configuration.

However, ground PV installations compete for flat land with agriculture, forests, real estate development, and wildlife habitats [33]. Thus, the installation capacity of PV could be accelerated by utilizing the surface area on the outside of buildings, infrastructure, and vehicles. Conventional PV is opaque, and is therefore appropriate for nontransparent surfaces. Semitransparent emerging PV, however, could be applied on e.g. windows, skylights, transparent walls, and product integrated PV.

Therefore, in search of novel ways to increase PV production capacity by inexpensive and environmentally sustainable means, this section reviews the *status quo* and potential applications of representative emerging photovoltaic technologies. Namely, kesterites, dye-sensitized solar cells, organic PV, quantum dot cells, perovskites, and select binary inorganic absorber thin film PV are discussed. In addition, the timeline of record laboratory scale emerging PV cells is presented in Figure 1.1.

Emerging PV is often grouped according to historical trends, the choice of active layers (inorganic, organic, or hybrid; liquid or solid), and the morphology of layers in the solar cell. *Structured* solar cells incorporate meso- or nanoporous materials, or elongated nanostructures in one or more layers in the stack, mostly as a scaffold for the absorber [35]–[37]. *Planar*, or flat solar cells are composed of horizontally stacked thin films [5], [38], [39], mirroring the conventional CdTe and CIGS thin film PV structure.

Kesterite, i.e. $\text{Cu}_2\text{ZnSn}(\text{S}_y\text{Se}_{1-y})_4$ (CZTS) PV development was started due to the limited availability of Ga, In, and Te for production of CIGS and CdTe, *vide ante* section 1.2.2, as Cu, Zn, Sn, and S are abundantly available at low cost as primary mining products [22], [28]. The record $\eta = 12.6\%$ of kesterite PV was achieved in 2014 [40], whereas η obtained with cation-substituted CZTS derivatives has been lower thus far [41]. The lag in progression of η beyond the current level in kesterite solar cells has been attributed to band tailing and the open circuit voltage deficit that originates from uncontrollable detrimental deep-level defects in the absorber [41]. Currently, efforts are ongoing in dedicated worldwide research networks to overcome these issues.

Dye-sensitized solar cells (DSSCs) pioneered the “third generation” of PV after c-Si and thin film PV [42], [43]. In a typical DSSC, a thin layer of an organic, mostly Ru-based, light absorbing dye is pasted onto a mesoporous TiO_2 underlayer, and a redox electrolyte or an organic hole transport layer (HTL) between the dye and the back contact effectuates charge transport [43]. Since the advent of DSSC in 1991, the record η of DSSCs reached a plateau of $\approx 11\%$ in the late 1990s, and was improved to $\eta = 13.1\%$ in 2018 (Figure 1.1) with the use of Cu-complex redox electrolytes [44]. The reliance on organic materials means that the dye, redox electrolyte, and organic HTL in DSSCs require protection via encapsulation against ultraviolet light, humidity, and overheating to preserve η over a reasonable module lifetime [45]–[47].

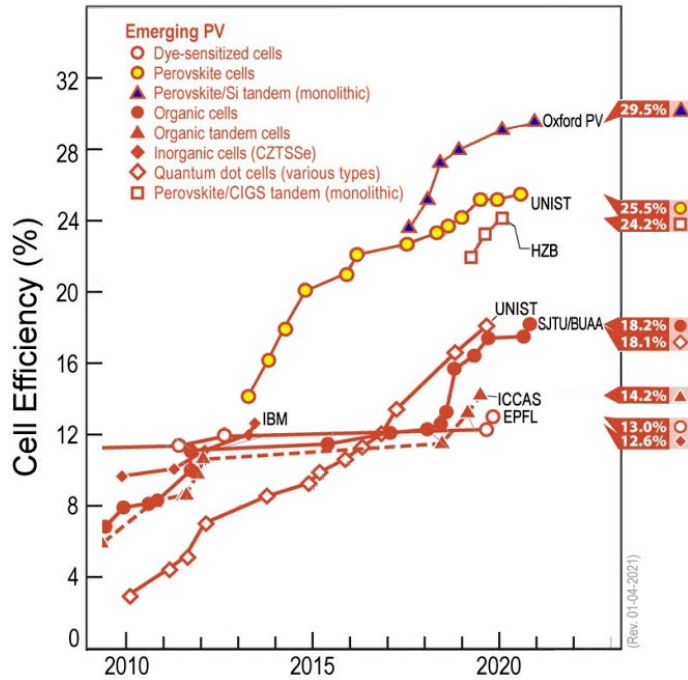


Figure 1.1. Timeline of record emerging solar cell efficiencies. Modified from [34].

Organic photovoltaics (OPV) were created by replacing the absorber dye with a solid polymer. The record η of OPV has evolved from under 4 % in 2001 to 18.2 % in 2020 (Figure 1.1). Flexible and ultralight OPV modules can be rapidly produced by inexpensive solution processing at mild temperatures [48], [49]. Similarly to DSSC, however, the organic components in OPV are also sensitive to moisture, UV, and elevated temperature [50]–[52]. The issues related to instability of OPV has resulted in area scaling lag of η [49].

The extreme dependence of η of OPV on light intensity has garnered interest in the field of light scavenging in low-light [53]. Further yet, the light absorption spectrum and visual transparency of OPV modules is modifiable at the cost of reduced η , as illustrated by transparent OPV with $\eta = 10.8\%$ at an adjusted average visible transparency (AVT) of $\approx 50\%$ [54], and infrared-active OPV with up to $\eta = 9.8\%$ [55].

Perovskite solar cells were initially also based on DSSC, yet are closer to thin film PV. Perovskite PV is highly efficient and inexpensive to fabricate, being the most actively developed emerging PV technology on the verge of commercialization [35], [56]. The record η of perovskite PV, at first with a liquid electrolyte, leaped from 3.8 % in 2009 [57], to 25.6 % in 2021 [58], having undergone several transformations in the solar cell stack in the process [35]. Perovskites are grouped into mixed organic-inorganic, e.g. $(\text{CH}_3\text{NH}_3)_{1-x}(\text{NH}_2\text{CHNH}_2)_x\text{Pb}(\text{Br},\text{I})_3$ (MAFAPBI), inorganic metal chalcogenides-halides, and metal oxides [35], [56]. The facile tuning of the cation and anion in perovskites allows to tailor the structure and optoelectronic properties of the absorber, e.g. composition dependent band gap engineering [35], [56].

Metal halide perovskites tower over other perovskites in terms of the record η achieved, although the organic cations and halide anions in the perovskite lattice create

a considerable stability problem due to phase segregation induced by temperature, ultraviolet light and hygroscopicity [35]. Evidently, the deterioration of η over time must be addressed to commercialize perovskite PV.

Although the highest η in perovskite PV has been consistently achieved with the use of lead (Pb) compounds [35], Pb compounds are banned in the European Union and other countries [25] due to neurotoxicity and bioaccumulation [59], [60]. Unlike CdTe, MAFAPBI compounds are unstable and water soluble, necessitating extremely strict measures and module encapsulation techniques [61], which dampens the positive aspects of perovskite PV. Replacing Pb with Sn, Bi, Sb or other metals in perovskite has resulted in increased stability, yet decreased η [35], [62]. According to life cycle analysis, the environmental impact of Pb-perovskite PV will depend on the scale of production and the thoroughness of the safety measures applied in the module's life cycle [63].

Extremely thin inorganic absorber (ETA) solar cells are a combination of a mesoporous or nanowire core-shell scaffold with an ETA shell instead of a dye [10], [37], [64]–[66]. The motivation behind ETA solar cell research is that a 15–20 nm thick layer of a material with a high absorption coefficient can be applied to theoretically achieve $\eta = 15\%$ at negligible materials usage due to a geometrically enhanced interface area [67]. The standing record η of ETA solar cells is 9.0 % in combination with a PbS quantum dot absorber [68].

Quantum dot (QD) PV is based on growing the absorber layer as an array of solution-deposited colloidal quantum dots onto flat or structured substrates [69], [70]. The main feature of QD cells is that by synthesizing absorber nanoparticles in the size range of the Bohr exciton radius, the absorption spectrum of the absorber can be freely tuned [69]. The record η of QD cells has increased from under 4 % in 2010 to 18.1 % in 2020 (Figure 1.1), exemplifying the future perspective of this technology.

Transitioning further toward conventional thin film PV, solar cells based on several metal chalcogenide absorbers other than CIGS and CdTe are being explored. A non-comprehensive list of representative elementary, and binary oxide, sulfide, and selenide absorbers with the corresponding solid state solar cell record η achieved before 2017 is as follows: Se (6.5 %) [71], Cu₂O (8.1 %) [72], SnS (4.4 %) [73], Ag₂S (3.2 %) [74], Sb₂S₃ (7.5 %) [6], Sb₂Se₃ (5.9 %) [75], and Bi₂S₃ (3.3 %) [76]. Judging by the absolute value and the relative increase in record η in the last decade, Sb₂S₃ and Sb₂Se₃ are considered among the most promising emerging chalcogenide absorber materials for further study.

In addition, emerging ternary and quaternary inorganic PV absorbers are often combinations of the aforementioned elements or binary compounds, e.g. A_xSb_y(S,Se)_z, (A = Cu, Ag, Sn, Bi) [41]. Among ternary materials, a most prospective solar cell $\eta = 10.5\%$ was achieved in 2020 by applying a hydrothermally grown planar Sb₂(S,Se)₃ thin film absorber [77]. Considering the appreciable η achieved in solar cells based on Sb₂S₃, and Sb₂Se₃ before 2017, (and later Sb₂(S,Se)₃), this class of metal chalcogenides will be scrutinized further in section 1.4.

Currently, research in materials science and photovoltaics is application oriented. Thus, the development of materials generally culminates in the preparation of a device. The progressive scale-up and cost reduction of c-Si PV solar cells indicates that the perhaps the most rapid way to implement emerging PV is in combination with conventional PV as tandem solar cells. For example, two-cell tandem solar cells based on a combination of e.g. perovskite/c-Si and perovskite/CIGS, have yielded $\eta = 29.2\%$, and 24.2 %, respectively [14]. Thus, the synergy between emerging and conventional PV in tandem devices could accelerate achieving NZE targets.

Semitransparent PV is one of the prospective applications for emerging PV that faces the least competition. In addition to η , semitransparent PV is assessed by the average visible transmittance (AVT), corresponding color temperature, and color rendering index [78]. The AVT is the average transmittance of the solar cell in the visible wavelength range, which has not yet been standardized, and it must be at least 20–30 % for solar cells to qualify as semitransparent [78]–[80].

Thus far, most studies on transparent PV have focused on improving η and AVT [80], [81], with fewer studies on color tuning [54]. Based on estimations made for transparent OPV, the module cost could be $\$0.47 \text{ W}_p^{-1}$ at an energy payback time of 2–6 years [81]. OPV solar cells can be made color neutral, yielding $\eta = 10.8 \%$ with human eye adjusted AVT = 50 % in visible light [54]. Semitransparent halide perovskite PV has yielded $\eta = 13 \%$ with AVT = 26 % at 350–900 nm wavelength [82] Regarding module stability, semitransparent PV can be protected from humidity and atmospheric pollutants at little to no extra cost by filling the space between glass panes with inert gas and airtight sealing. As the described sequence is already a standard procedure in the window glass manufacturing industry, encapsulating semitransparent PV is likely not a major concern.

1.4 Antimony based photovoltaic absorbers

This section provides a more thorough overview of Sb_2S_3 , Sb_2Se_3 , and $\text{Sb}_2(\text{S,Se})_3$ as some of the most prospective emerging absorber materials. Related ternary and quaternary compounds are also briefly discussed.

1.4.1 Sb_2S_3 , Sb_2Se_3 , and $\text{Sb}_2(\text{S,Se})_3$

The absorber class encompassing Sb_2S_3 , Sb_2Se_3 , and $\text{Sb}_2(\text{S,Se})_3$, has been investigated for PV applications during more a decade due to the isostructural single phase composition, and a high optical absorption coefficient of 10^5 cm^{-1} at 2.8 eV [83]. Moreover, the band gap can be tuned to 1.1–1.7 eV in bulk or as a gradient of film thickness by varying the proportion of S/Se in the material [5], [83]. The tailored band gap is useful for both $\text{Sb}_2\text{S}_3/\text{Sb}_2\text{Se}_3$ two-cell tandem [84], and Sb_2S_3 , Sb_2Se_3 , and $\text{Sb}_2(\text{S,Se})_3$ based solar cells, [5], [83]. Furthermore, the high absorption coefficient allows to thin the absorber to α^{-1} ($\approx 100 \text{ nm}$) for transparent applications at a loss of $\approx 40 \%$ of the theoretical maximum η [85].

The orthorhombic *Pnma* structure (Figure 1.2), composed of infinite quasi-1D $[\text{Sb}_4(\text{S,Se})_6]_n$ ribbons, leads to anisotropic properties [86]–[88]. As Sb_2S_3 , Sb_2Se_3 , and the solid solution of $\text{Sb}_2(\text{S,Se})_3$ are isostructural [89], their structural and optoelectronic properties are predictably similar.

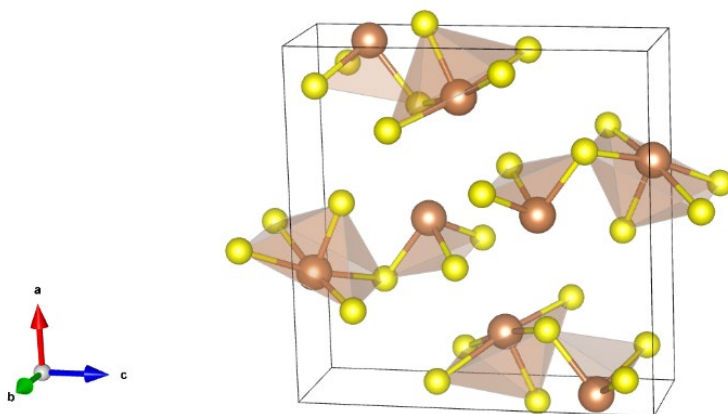


Figure 1.2. Unit cell of Sb_2S_3 . Drawn using VESTA [90] and data from [91].

The anisotropic structure of Sb_2S_3 is reportedly beneficial for PV applications as it influences the band position and formation of defects [5]. Moreover, the resistivity along ribbons was found to be 100 times smaller than across ribbons [92]. Furthermore, grain boundaries in Sb_2Se_3 were confirmed to be electrically benign based on first principles simulations, as the predominant surfaces were calculated to have low surface energy, no dangling bonds, and deep-level defect free band gaps [5], [93]. Aligning the crystallites and grains to minimize recombination in the bulk and the distance travelled by charge carriers, however, entails engineering of the crystal structure [93]. Ideally, preferred orientation is sought in the (211), (212), or (010) direction of the $Pnma$ structure in relation to a flat horizontal substrate surface [93].

The development of solar cells based on Sb_2S_3 thin films was pioneered by Savadogo and Mandal in the early 1990s [94]–[96], wherein $\eta = 5.5\%$ was achieved with a glass/ITO/ Sb_2S_3 / WO_3 /Pt thin film solar cell with a W-halogenide light source [96]. Over a decade later, research on Sb_2S_3 for PV applications was reinvigorated, mostly as a sensitizer for mesoporous and nanostructured TiO_2 scaffolding similarly to DSSC, OPV and ETA cells, culminating in the standing record $\eta = 7.5\%$ [6], [66], [97]–[100].

In addition, in 2021, it was confirmed by studying Sb_2S_3 films with S-rich and Sb-rich composition, grown by thermal co-evaporation, that this crystal structure can accommodate impurity atoms to a certain degree, and that preparing a S-rich atomic ratio of S/Sb increases η of solar cells (6.2%) compared to an Sb-rich an atomic ratio of S/Sb ($\eta = 5.0\%$) due to beneficial defect engineering [101].

Furthermore, during aging, fresh surfaces of Sb_2S_3 (and Sb_2Se_3 [102]) are passivated by a few nm of natural oxide, which is claimed to be beneficial for PV, as it reportedly reduces surface recombination or the back contact barrier height at the absorber/HTL interface, thereby boosting FF, and η [66], [103]. Aside from oxidation, Sb_2S_3 is chemically stable toward moisture and UV-VIS irradiation, alkali and acids, except concentrated hot HCl [104], [105], which is a major advantage compared to organic materials and labile halide perovskites. The stability of Sb_2S_3 is accompanied by a prohibitively high resistivity of 10^4 – $10^8 \Omega \text{ cm}$ [106]–[109], and ultrafast intrinsic self-trapping of photogenerated charge carriers by lattice deformations, which was reported to set the open-circuit voltage (V_{oc}) limit for Sb_2S_3 solar cells to $\approx 0.8 \text{ V}$, and maximum attainable $\eta = 16\%$ [110].

The aforementioned issues have been identified as some of the main bottlenecks that need to be addressed to increase η of Sb_2S_3 solar cells closer to the Shockley-Queisser limit.

As the absorber material itself is suitable for PV, some practical considerations have to be accounted for before committing to applying it for PV. For instance, the melting point of $\text{Sb}_2\text{S}_3 = 546^\circ\text{C}$ [104], and that of $\text{Sb}_2\text{Se}_3 = 612^\circ\text{C}$ [104], allows to recrystallize the Sb_2S_3 absorber at $\approx 300^\circ\text{C}$ [5], [83], and Sb_2Se_3 at $\approx 400^\circ\text{C}$ [83]. These temperatures are well below the softening point of float glass of $500\text{--}550^\circ\text{C}$ [12], [13], which is a base requirement for developing inexpensive transparent PV or bifacial PV. Interestingly, crystallization is achievable at even lower temperatures, as in 2021, $\text{Sb}_2(\text{S,Se})_3$ was crystallized at as low as 200°C [111], opening up possibilities for these materials in combination with a wide selection of flexible organic substrates.

Furthermore, according to supply data from 2021, the annual supply of Sb ($\$8.8 \text{ kg}^{-1}$, $1.5 \cdot 10^5 \text{ t yr}^{-1}$) and S ($\0.09 kg^{-1}, $7.8 \cdot 10^8 \text{ t yr}^{-1}$) [28] as two affordable primary mining products is sufficient for producing PV modules in the $\text{GW}_p\text{--TW}_p$ scale ($66 \text{ t Sb}_2\text{S}_3 \text{ yr}^{-1}$ up to $6.6 \cdot 10^4 \text{ t Sb}_2\text{S}_3 \text{ yr}^{-1}$, respectively), assuming an absorber thickness of $1 \mu\text{m}$ and a conservative module $\eta = 5 \%$.

Sb_2S_3 and Sb_2Se_3 become Sb-rich in elemental composition at a temperature above the respective crystallization point due to incongruent sublimation of S and Se [112], [113]. This results in the generation of point defects detrimental to solar cell η [6], [114]. Hence, S and Se content is often supplemented during deposition [9], [115], [116], or remediated in post-growth heat treatment with e.g. S, H_2S , Se or H_2Se [6], [117], [118]. In fact, the high partial pressure of S and Se presents an opportunity to *in situ* engineer the elemental composition of Sb_2S_3 and Sb_2Se_3 films during preparation.

In terms of PV applications, Sb_2Se_3 and $\text{Sb}_2(\text{S,Se})_3$ solar cells with $\eta > 1 \%$ first appeared in 2014 [119], [120]. Since then, η of solar cells has rapidly grown to 9.2% for Sb_2Se_3 [121], and to 10.5% for $\text{Sb}_2(\text{S,Se})_3$ [77], following numerous conceptual improvements, e.g. grain control and use of HTL [122], or favorable preferred orientation [123]. Theoretically, without considering defect-related losses, a 200 nm thick layer of Sb_2S_3 or Sb_2Se_3 would be sufficient to construct solar cells with $\eta = 22 \%$ or 28% , respectively [124]. Therefore, once the challenge of defect engineering of the antimony chalcogenide series has been surmounted, η of Sb_2S_3 , Sb_2Se_3 , and $\text{Sb}_2(\text{S,Se})_3$ solar cells comparable to that of conventional PV could likely be prepared.

1.4.2 Ternary and quaternary Sb based absorbers

In addition to $\text{Sb}_2(\text{S,Se})_3$, other ternaries and some quaternaries based on Sb_2S_3 or Sb_2Se_3 have been explored for PV applications partially based on the concepts developed in CIGS and CZTS studies. Currently, the record η of these thin film solar cells is as follows: CuSbSe_2 (4.7%), CuSbS_2 (3.2%), SbSI (3.1%), $\text{Sb}_{0.67}\text{Bi}_{0.33}\text{SI}$ (4.1%) [41]. The future perspective of these ternary and quaternary materials is difficult to gauge, as understanding of even the binary compounds and $\text{Sb}_2(\text{S,Se})_3$ is quite limited at present. Regarding Cu-Sb-compounds, the tendency for Cu to form several phases of Cu-Sb-S [125] could prove to be problematic, especially after heat treatment. In addition, Cu is known to diffuse in bulk phases at moderate temperatures, as observed in CIGS, CdTe [12], [13], and Sb_2S_3 [126]. Thus, at present, the Sb-chalcogenide-halides appear to be more advantageous for PV than the Cu-Sb-based compounds.

1.5 Solar cells based on Sb_2S_3 absorber

Regarding Sb_2S_3 , Sb_2Se_3 , and $\text{Sb}_2(\text{S,Se})_3$, in terms of fabrication of thin films and coatings, Sb_2S_3 is mostly grown by chemical methods, whereas Sb_2Se_3 is mostly grown by physical methods, and $\text{Sb}_2(\text{S,Se})_3$ is prepared by both types of methods [5], [83], [114]. The research group hosting this study had previous experience with the deposition of Sb_2S_3 by ultrasonic spray pyrolysis, which is a chemical method. Also, the record η of Sb_2S_3 solar cells was higher than for Sb_2Se_3 and $\text{Sb}_2(\text{S,Se})_3$ solar cells at the start of research relevant to this thesis in Sept, 2017. Thus, a brief overview of representative solar cells based on Sb_2S_3 thin films grown onto planar and structured substrates is provided in this section.

1.5.1 Structure of Sb_2S_3 solar cells

The structure of the Sb_2S_3 solar cell stack has developed similarly to the trends in DSSC, CdTe and perovskite research. Therein, the solar cell stack is composed of a TCO front contact, an ETL, an absorber, a HTL, and a metal back contact. The stack is grown onto a transparent substrate starting from the front contact (superstrate type) or onto an optionally transparent substrate starting from the back contact (substrate type).

Float glass is a standard substrate for PV because it is inexpensive, transparent and durable. Commonly, TCOs with a band gap of 3–4 eV, e.g. $\text{In}_2\text{O}_3:\text{Sn}$ (ITO), $\text{SnO}:\text{F}$ (FTO), or $\text{ZnO}:\text{Al}$ (AZO), serve as the front electrode, or cathode (Figure 1.3) [127]. An n-type TiO_2 , CdS, ZnO, or SnO_2 coating is used as the ETL due to passable alignment of the conduction band minima, a sufficient offset in the valence band maxima, and a tolerable lattice mismatch with Sb_2S_3 [127]. In some studies, the ETL is constructed as a bilayer [127], e.g. $\text{TiO}_2/\text{In}(\text{OH,S})$ in FTO/mesoporous- $\text{TiO}_2/\text{In}(\text{OH,S})/\text{Sb}_2\text{S}_3/\text{CuSCN}:\text{KSCN}/\text{Au}$ [66], TiO_2/CdS in FTO/ $\text{TiO}_2/\text{CdS}/\text{Sb}_2\text{S}_3/\text{spiro-OMeTAD}/\text{Au}$ [128], or ZnO nanowire/ TiO_2 in FTO/ZnO nanowire/ $\text{TiO}_2/\text{Sb}_2\text{S}_3/\text{P3HT}/\text{Au}$ [10], to reduce charge recombination at the ETL/ Sb_2S_3 interface.

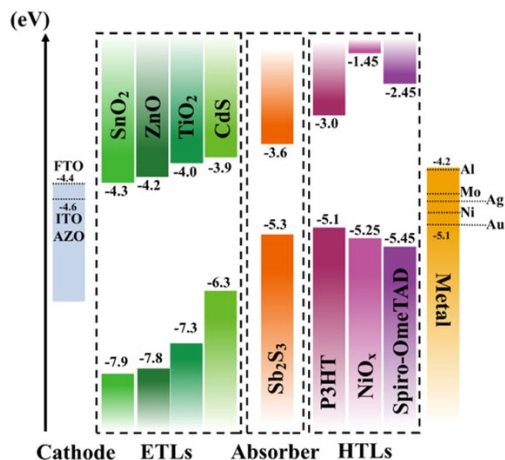


Figure 1.3. Energy level alignment of Sb_2S_3 with common cathodes, ETLs, HTLs, and anode metals. Modified from ref. [127] according to CC-BY 4.0 license permissions.

Poly(3-hexylthiophene-2,5-diyl) (P3HT) and spiro-OMeTAD (2,2',7,7'-tetrakis-(N,N-di-p-methoxyphenylamine)-9,9'-spirobifluorene) represent the most common p-type organic semiconductors applied as the HTL. Both have a favorable band alignment with the

valence band maximum of Sb_2S_3 , a large enough offset with the conduction band minimum of Sb_2S_3 , and the capability to prevent short-circuiting at pinholes in the absorber by preventing the formation of shunts [5], [83], [127]. Inorganic metal oxides, e.g. NiO_x in FTO/ TiO_2 / Sb_2S_3 / NiO_x /Au [129], V_2O_5 in FTO/ TiO_2 / Sb_2S_3 / V_2O_5 /Au [130], Sb_2O_3 /CuSCN in FTO/mesoporous- TiO_2 /In(OH,S)/ Sb_2S_3 /CuSCN:KSCN/Au [66], and hybrid combinations, e.g. Sb_2O_3 /spiro-OMeTAD in FTO/mesoporous- TiO_2 /In(OH,S)/ Sb_2S_3 / Sb_2O_3 /spiro-OMeTAD/Au [97], P3HT: NiO_x in FTO/ TiO_2 /mesoporous- TiO_2 / Sb_2S_3 /P3HT: NiO_x /Ag [131], have also been applied to a comparable effect.

The anode, or back contact metal is selected to align with the valence band maximum of the HTL. Direct contacting of the metal to the absorber is rarely applied because short-circuiting through pinholes in the absorber film between ETL and metal is likely to occur. Furthermore, inhomogeneous electrical contacting at the absorber/metal interface can cause interface recombination due to a reduced effective contact area. An offset of over ≈ 0.3 eV in the valence band maximum of the HTL and the work function of the metal, i.e. the back contact barrier height, has been calculated to considerably decrease the η of any chalcogenide solar cell [12]. Thus, metals with a high work function, e.g. Au, Ni, Pt, Ag, are used the most in Sb_2S_3 solar cells [5], [83], [127] to create a quasi-ohmic contact [132].

1.5.2 Development of Sb_2S_3 solar cells

Sb_2S_3 thin film solar cells were first prepared in the early 1990s [94]–[96]. Afterwards, structured Sb_2S_3 solar cells were actively developed from late 2000s to mid-2010s. Reports on planar Sb_2S_3 solar cells started appearing in early 2010s, as focus gradually shifted from structured to planar Sb_2S_3 solar cell development. The main achievements for both types of solar cells are summarized in this section. An overview of thickness, grain size, S/Sb atomic ratio, and band gap for Sb_2S_3 coatings on planar and structured substrates, and the PV output parameters of corresponding solar cells that had been reported before the start of this study in Sept. 2017 is presented in Table 1.1.

Structured solar cells

In 2009, an ETA solar cell of FTO/mesoporous- TiO_2 /In(OH,S)/ Sb_2S_3 /CuSCN:KSCN/Au with $\eta = 3.4\%$ was prepared with Sb_2S_3 grown by chemical bath deposition (CBD) [66]. In 2010, an organic HTL, spiro-OMeTAD, was used for the first time in a Sb_2S_3 solar cell of FTO/mesoporous- TiO_2 /In(OH,S)/CBD- Sb_2S_3 /spiro-OMeTAD/Au, yielding $\eta = 3.1\%$ under W-halogen lamp illumination [97]. Applying P3HT as the HTL yielded $\eta = 5.1\%$ in solar cells of FTO/mesoporous- TiO_2 /CBD- Sb_2S_3 /P3HT/Au [133]. The increase in η was attributed to reduced interface recombination due to the smaller offset in valence band alignment of Sb_2S_3 with P3HT [133] compared to spiro-OMeTAD (Figure 1.3).

In 2013, the first study on doping Sb_2S_3 , with 5 mol% Ti, Zn, and Bi in an FTO/mesoporous- TiO_2 /MgO/Ba TiO_3 /CBD- Sb_2S_3 /CuSCN:KSCN/Au was reported [100]. Thereby, η was improved from 4.1% without doping to 4.5% with Zn doping, and 5.7% with Ti doping, whereas Bi doping decreased η to 2.1% [100].

In 2014, a CBD-grown Sb_2S_3 film grown on a mesoporous TiO_2 scaffold was heat treated with H_2S vapors by decomposing thioacetamide (TA), setting the standing record $\eta = 7.5\%$ with a FTO/ TiO_2 /mesoporous- TiO_2 / Sb_2S_3 /PCPDTBT/PEDOT:PSS/Au solar cell (poly(2,6-(4,4-bis-(2-ethylhexyl)-4Hcyclopenta[2,1-b;3,4-b']dithiophene)-alt-4,7(2,1,3-benzothiadiazole) – PCPDTBT; poly(3,4-ethylenedioxythiophene) polystyrene sulfonate – PEDOT:PSS) [6].

In 2015, the effect of varying the ratio of thiourea (TU) to SbCl_3 (SbCl_3/TU) in solution was investigated in the first major spin coating study on Sb_2S_3 thin film solar cells of FTO/ TiO_2 /mesoporous- TiO_2 / Sb_2S_3 /PCPDTBT/PEDOT:PSS/Au, attaining $\eta = 6.4\%$ [115].

In 2017, the group hosting this thesis applied a two-step procedure involving USP to grow a continuous coating of crystalline Sb_2S_3 onto TiO_2 -covered ZnO nanowires [10]. First, an amorphous Sb_2S_3 coating was deposited by USP. Second, the coating was crystallized at 300°C in N_2 , yielding $\eta = 2.3\%$ in a FTO/ZnO nanowire/ TiO_2 / Sb_2S_3 /P3HT/Au ETA solar cell.

In summary, studies on structured Sb_2S_3 solar cells have demonstrated that introducing inorganic and organic HTLs to the stack, doping or sulfurizing the absorber, and varying the molar ratio within the precursor solution resulted in increased η . Applying multi-step processing for preparing the absorber was standard procedure for CBD and spin coating due to the specifics of those methods, and proved viable for USP as well.

Planar solar cells

In 1994, a planar thin film solar cell of ITO/ Sb_2S_3 / WO_3 /Pt was prepared based on a 3800 nm thick Sb_2S_3 film grown by CBD, yielding $\eta = 5.5\%$ under illumination by a W-halogen light source from the semitransparent metal side [96]. In 2011, P3HT was applied for the first time in a planar Sb_2S_3 thin film solar cell of ITO/ZnO/ Sb_2S_3 /P3HT/Ag, yielding $\eta = 2.4\%$ [134]. In 2013, P3HT and CuSCN were applied for the first time as HTL in planar TiO_2 / Sb_2S_3 /HTL thin film solar cells of ITO/ TiO_2 / Sb_2S_3 /P3HT/Au [135], and FTO/ TiO_2 / Sb_2S_3 /CuSCN/Au [136], yielding $\eta = 1.4\%$ and 3.3% , respectively.

The era of planar Sb_2S_3 thin film solar cell research began in earnest in 2014, when a planar FTO/ TiO_2 / Sb_2S_3 /P3HT/PEDOT:PSS/Au solar cell with $\eta = 5.8\%$ was reported, and the superiority of ALD over aqueous CBD for growing Sb_2S_3 films was demonstrated [8].

In 2015, the effect of varying P3HT thickness and back contact transparency on the PV performance of planar ITO/ TiO_2 / Sb_2S_3 /P3HT/Ag solar cells was studied [137]. Therein, $\eta = 4.1\%$ was achieved in a non-transparent cell with 26 nm thick P3HT and 85 nm thick Sb_2S_3 [137]. Based on EQE, short circuit current density (J_{sc}) was slightly reduced in a transparent cell with a 15 nm thick Ag contact [137]. Incidentally, it was the first study reporting transparent Sb_2S_3 solar cells, although AVT of solar cells was not provided. Also in 2015, Sb_2S_3 films prepared by spin-coating were used for the first time in planar Sb_2S_3 solar cells, yielding $\eta = 2.3\%$ in a solar cell of FTO/ TiO_2 / Sb_2S_3 /P3HT/Au [138].

In 2016, phase pure separate crystalline Sb_2S_3 flakes ($E_g = 1.65\text{ eV}$) were prepared using single-step USP by the group hosting this thesis, yielding $\eta = 1.9\%$ in a solar cell of ITO/ TiO_2 / Sb_2S_3 /P3HT/Au [9].

In 2017, a chemical approach was reported, wherein antimony butyldithiocarbamate ($\text{Sb}(\text{S}_2\text{CN}(\text{C}_3\text{H}_7)_2)_3$) was used as a single source precursor for spin coating, followed by heat treatment at 300°C for only 2 min in N_2 to form Sb_2S_3 films with mean lateral grain size of 12 μm and $E_g = 1.65\text{ eV}$ [7]. The process yielded solar cells with $\eta = 4.3\%$ vs $\eta = 2.0\%$ for CBD-based counterparts [7]. Also in 2017, Sb_2S_3 films were prepared by rapid thermal evaporation, and were treated in Se atmosphere, yielding planar FTO/ TiO_2 / Sb_2S_3 /Au solar cells with $\eta = 3.2\%$ (selenized) vs 2.5% (pristine), respectively [139].

To summarize, studies on planar Sb_2S_3 thin film solar cells proved that inorganic and organic HTLs are viable; that the deposition process and choice of precursor affects the structure, morphology, and optoelectronic properties of Sb_2S_3 films and η of solar cells;

that semitransparent solar cells can be made; and that preparation of Sb_2S_3 films in a single step is plausible by USP, whereas ALD, CBD, and spin coating were demonstrated to require at least two processing steps.

1.5.3 Further development of Sb_2S_3 solar cells

Parallel to the progression of research in the thesis, several new concepts and approaches to enhance the photovoltaic performance of planar Sb_2S_3 solar cells have been published in 2017–2021. Studies published after Sept. 2017 were not taken into account when planning this study because the general outline was based on existing studies. As these studies were published in parallel to, or after papers I, II, III, and IV, a measure of overlap with recent publications was anticipated.

In literature, doping of Sb_2S_3 films with ZnCl_2 [140], alkali hydroxides [141], [142], Bi–I co-doping [143], and Se alloying [111] has been applied to enhance the majority charge carrier concentration and to increase mean lateral grain size of the absorber. Surface treatment of the ETL (TiO_2 by CsCO_3 [144], ZnCl_2 , ZnBr_2 , ZnI_2 [145]; CdS by KOH [146]) and the absorber (Sb_2S_3 by SbCl_3 [147]), has been applied to passivate interface defects, to increase continuity and lateral grain size of the absorber, and to improve the electronic properties of the ETL/absorber and the absorber HTL/interface.

In addition, interfacial layers (ZnS between $\text{TiO}_2/\text{Sb}_2\text{S}_3$ [148], [149]) or seed layers of Sb_2S_3 [150], [151] have been applied to modify the morphology, structure, and optoelectronic properties of Sb_2S_3 films. Furthermore, inorganic HTLs NiO_x [129] and V_2O_5 [130] have been applied in planar Sb_2S_3 solar cells, yielding η on par with organic HTL based Sb_2S_3 solar cells. NiO_x , Cu_2O and CuI have been proposed as prospective inorganic HTLs in a theoretical calculation study, with up to $\eta = 22.8\%$ claimed achievable in an optimized $\text{ZnS}/800\text{ nm } \text{Sb}_2\text{S}_3/\text{Cu}_2\text{O}$ stack [151].

The aggregated data on the thickness, E_g , atomic ratio of S/Sb and lateral grain size of planar Sb_2S_3 thin films, and the relevant PV output parameters of representative Sb_2S_3 solar cells is presented in section 1.5, Table 1.1. Concepts introduced in literature during this research are revisited in the future outlook on page 64.

In summary, in 2017–2021, doping of the absorber, passivation of ETL/absorber and absorber/HTL interfaces, seed layers, and inorganic HTLs have been applied to increase η , and stability of η over time of mainly planar Sb_2S_3 solar cells. Although η has increased from 5.8 % in 2014 [8] to 7.1 % in 2020 [145], [147] for planar Sb_2S_3 solar cells, V_{oc} has not improved significantly. Thus, strategies to overcome the V_{oc} deficit of $\approx 600\text{ mV}$ [110], the main factor limiting η of Sb_2S_3 solar cells, have yet to be discovered.

Table 1.1. An overview of thickness, grain size, Sb–S elemental composition, and band gap of representative Sb₂S₃ coatings on a planar or structured ETL, and PV output parameters of corresponding solar cells, reported before Sept. 2017. The thickness of the Sb₂S₃ coating is presented for thin films on a planar substrate.

Sb ₂ S ₃ growth method	Solar cell structure ^a	Sb ₂ S ₃				V _{oc} , mV	J _{sc} , mA cm ⁻²	FF, %	η, %	Area, cm ²	Year	Ref.
		Thick-ness, nm	Grain size, μm	S/Sb, at%/at%	E _g , eV							
CBD	ITO/Sb ₂ S ₃ /WO ₃ /Pt	3800	–	–	1.74	770	11.3	63	5.5	0.09	1994	[96]
CBD	FTO/mp-TiO ₂ /In(OH,S)/Sb ₂ S ₃ /Sb ₂ O ₃ /CuSCN:KSCN/Au	–	–	–	1.75	490	14.1	49	3.4	0.15	2009	[66]
CBD	FTO/mp-TiO ₂ /Sb ₂ S ₃ /CuSCN:LiSCN/Au	–	–	–	–	560	11.6	58	3.7	0.54	2010	[99]
CBD	FTO/mp-TiO ₂ /In(OH,S)/Sb ₂ S ₃ /spiro-OMeTAD/Au	–	–	–	1.75	610	10.6	48	3.1	0.49	2010	[97]
CBD	FTO/mp-TiO ₂ /Sb ₂ S ₃ /P3HT/Au	–	–	–	–	556	12.3	70	5.1	0.16	2010	[133]
CBD	FTO/mp-TiO ₂ /Sb ₂ S ₃ /PCPDTBT/Au	–	–	–	–	616	15	66	6.2	0.096	2011	[152]
Thermal evapor.	ITO/ZnO/Sb ₂ S ₃ /P3HT/Ag	210	–	–	1.76	450	12.6	42	2.4	–	2011	[134]
CBD	FTO/mp-TiO ₂ /MgO/BaTiO ₃ /Sb ₂ S ₃ /CuSCN:KSCN/Au	–	–	–	1.7	584	13.4	53	4.1	0.25	2012	[153]

Sb ₂ S ₃ growth method	Solar cell structure ^a	Sb ₂ S ₃				V _{oc} , mV	J _{sc} , mA cm ⁻²	FF, %	η, %	Area, cm ²	Year	Ref.
		Thick- ness, nm	Grain size, μm	S/Sb, at%/at%	E _g , eV							
CBD	FTO/mp-TiO ₂ /Sb ₂ S ₃ / P3HT:Au/Au	–	–	–	–	626	12.8	61	4.9	0.16	2012	[154]
CBD	FTO/mp-TiO ₂ /Sb ₂ S ₃ / PCPDTBT–PCBM/Au	–	–	–	–	595	16.0	66	6.3	0.16	2012	[155]
CBD	FTO/nw-TiO ₂ /Sb ₂ S ₃ / P3HT/PEDOT:PSS/Au	–	–	–	–	500	17.0	53	4.5	0.31	2012	[156]
CBD	ITO/nf-TiO ₂ /Sb ₂ S ₃ /Sb ₂ O ₃ / P3HT/PEDOT:PSS/Ag	–	–	–	–	603	9.9	39	2.3	0.04	2013	[157]
CBD	FTO/mp-TiO ₂ /Sb ₂ S ₃ / Polyaniline nanobelts/Pt	–	–	–	–	1100	6.9	50	3.8	0.12	2013	[158]
CBD	FTO/mp-TiO ₂ /MgO/BaTiO ₃ /Sb ₂ S ₃ :Ti/CuSCN:KSCN/Au	–	–	–	1.7	607	16.5	57	5.7	0.25	2013	[100]
CBD	ITO/TiO ₂ /Sb ₂ S ₃ /P3HT/Au	200–250	–	–	1.8	630	6.1	35	1.4	0.09	2013	[135]
CBD	FTO/TiO ₂ /Sb ₂ S ₃ /CuSCN/Au	–	–	–	1.71	455	12.4	59	3.3	0.1	2013	[136]
CBD	FTO/mp-TiO ₂ /Sb ₂ S ₃ /P3HT/ PEDOT:PSS/Au	–	–	–	–	550	13.2	62	4.4	0.085	2014	[159]
CBD	FTO/mp-TiO ₂ /Sb ₂ S ₃ / PCPDTBT/PEDOT:PSS/Au	–	–	–	–	711	16.1	65	7.5	0.16	2014	[6]

Sb ₂ S ₃ growth method	Solar cell structure ^a	Sb ₂ S ₃				V _{oc} , mV	J _{sc} , mA cm ⁻²	FF, %	η, %	Area, cm ²	Year	Ref.
		Thick- ness, nm	Grain size, μm	S/Sb, at%/at%	E _g , eV							
Spin coating	ITO/mp-TiO ₂ /Sb ₂ S ₃ / P3HT/Ag	–	–	–	–	680	9.5	52	3.4	–	2014	[160]
ALD	FTO/TiO ₂ /Sb ₂ S ₃ /	90	–	–	1.76	667	14.9	58	5.8	0.096	2014	[8]
CBD	P3HT/PEDOT:PSS/Au	90	–	–	1.76	489	9.6	46	2.2	0.096	2014	[8]
CBD	ITO/TiO ₂ /Sb ₂ S ₃ /P3HT/Ag	155	–	–	1.65	732	9.3	62	4.3	0.13	2015	[137]
CBD	FTO/mp-TiO ₂ /Sb ₂ S ₃ / PCPDTBT/PEDOT:PSS/Au	–	–	–	–	548	13.9	68	5.1	0.096	2015	[161]
Spin coating	FTO/mp-TiO ₂ /Sb ₂ S ₃ / PCPDTBT/PEDOT:PSS/Au	–	–	1.50	1.70	596	16.1	67	6.4	0.123	2015	[115]
Spin coating	FTO/TiO ₂ /Sb ₂ S ₃ /P3HT/Au	–	–	–	–	616	8.1	46	2.3	0.096	2015	[138]
USP	ITO/TiO ₂ /Sb ₂ S ₃ /P3HT/Au	150	0.85	1.53	1.6	618 635	6.0 5.0	51 42	1.9 1.3	0.017 1.0	2016	[9]
Thermal evapor.	FTO/TiO ₂ /Sb ₂ S ₃ /Au	650	0.5	–	1.69	570	10.2	55	3.2	0.09	2017	[139]
Spin coating	FTO/TiO ₂ /Sb ₂ S ₃ / Spiro-OMeTAD/Au	137	6	–	1.65	632	12.9	52	4.3	0.12	2017	[7]

Sb ₂ S ₃ growth method	Solar cell structure ^a	Sb ₂ S ₃				V _{oc} , mV	J _{sc} , mA cm ⁻²	FF, %	η, %	Area, cm ²	Year	Ref.
		Thick- ness, nm	Grain size, μm	S/Sb, at%/at%	E _g , eV							
USP	FTO/nw-ZnO/TiO ₂ /Sb ₂ S ₃ / P3HT/Au	–	–	–	1.79	656	7.5	47	2.3	0.017	2017	[10]
Beginning of work related to the thesis in September, 2017												
Thermal evapor.	FTO/TiO ₂ /Sb ₂ S ₃ / Spiro-OMeTAD/Ag	300	–	1.43	1.69	620	10.7	56	3.8	0.1	2018	[163]
Spin coating	FTO/TiO ₂ /Sb ₂ S ₃ /NiO _x /Au	100	–	–	1.78	590	14.5	41	3.5	0.12	2018	[129]
Spin coating	FTO/TiO ₂ /Sb ₂ S ₃ /V ₂ O ₅ /Au	87	–	–	1.65	590	15.3	53	4.8	0.12	2018	[130]
Spin coating	FTO/TiO ₂ /Sb ₂ S ₃ :Zn/ Spiro-OMeTAD/Au	130	–	1.30	1.69	647	17.2	57	6.4	0.12	2018	[141]
Spin coating	FTO/TiO ₂ /Sb ₂ S ₃ :Cs/ Spiro-OMeTAD/Au	120	–	1.36	1.68	690	17.3	55	6.6	0.12	2018	[140]
CBD	FTO/TiO ₂ /Sb ₂ S ₃ / Spiro-OMeTAD/Au	84	–	–	1.65	690	13.4	50	4.6	0.12	2018	[194]
Spin coating	FTO/TiO ₂ /Sb ₂ S ₃ / Spiro-OMeTAD/Au	400	0.65	–	1.65	660	13.1	59	5.2	0.04	2019	[150]
CSS	FTO/CdS/Sb ₂ S ₃ /C	600	0.3-1	1.53	1.71	660	13.0	45	3.8	0.08	2019	[170]

Sb ₂ S ₃ growth method	Solar cell structure ^a	Sb ₂ S ₃				V _{oc} , mV	J _{sc} , mA cm ⁻²	FF, %	η, %	Area, cm ²	Year	Ref.
		Thick- ness, nm	Grain size, μm	S/Sb, at%/at%	E _g , eV							
USP	ITO/TiO ₂ /Sb ₂ S ₃ /P3HT/Au	100	10	1.5	1.65	693	13.8	58	5.5	0.017	2019	[II]
						726	12.3	52	4.7	0.071		
						682	14.5	33	3.2	0.88		
VTD	ITO/CdS/Sb ₂ S ₃ /Au	≈1800	1–2	–	1.62	710	15.7	43	4.7	0.78	2020	[167]
Spin coating	FTO/TiO ₂ /ZnCl ₂ /Sb ₂ S ₃ / Spiro-OMeTAD/Au	162	13	–	-	650	17.7	62	7.1	0.1	2020	[145]
Spin coating	FTO/TiO ₂ /Sb ₂ S ₃ /SbCl ₃ / Spiro-OMeTAD/Au	146	–	–	1.71	720	17.2	57	7.1	0.1	2020	[147]
Hydro- thermal	FTO/CdS/Sb ₂ S ₃ / Spiro-OMeTAD/Au	300	1.5	–	1.71	707	15.2	56	6.0	0.089	2020	[207]
Thermal evapor.	FTO/CdS/Sb ₂ S ₃ / Spiro-OMeTAD/Au	200	–	1.55	1.70	720	15.9	54	6.2	0.12	2021	[101]
				1.28	1.70	680	15.4	48	5.0			
Hydro- thermal	FTO/TiO ₂ /CdS:KOH/ Sb ₂ S ₃ /Spiro-OMeTAD/Au	≈1000	0.09	1.24	1.76	748	15.3	57	6.5	–	2021	[146]
ALD	FTO/TiO ₂ /ZnS/Sb ₂ S ₃ /P3HT/PEDOT:PSS/Au	75	–	–	–	626	15.7	52	5.1	0.12	2021	[149]

^amp – mesoporous; nw – nanowire; nf – nanofiber; PCBM – [6,6]-phenyl-C61-butyric acid methyl ester.

1.6 Deposition methods for Sb₂S₃ thin films

In this section, the physical and chemical deposition methods used to prepare Sb₂S₃ thin films are briefly reviewed with a focus on chemical methods. Power conversion efficiency of respective Sb₂S₃ thin film solar cells is mentioned where available. Detailed information on the phase composition, film thickness, lateral grain size, and band gap of representative Sb₂S₃ thin films, grown by chemical and physical deposition methods, and the photovoltaic performance parameters of corresponding solar cells is presented in section 1.5, Table 1.1.

1.6.1 Physical methods

Sb₂S₃ thin films with a thickness of 200–1800 nm, grain size = 0.3–1 μm, S/Sb = 1.3–1.6, and $E_g = 1.7$ eV (see section 1.5, Table 1.1) have been prepared by physical methods such as thermal evaporation [134], [162], [139], [163], magnetron sputtering [164], [165], vapor transport deposition (VTD) [166]–[168], and close spaced sublimation (CSS) [169], [170].

The high vapor pressure and incongruent volatilization of Sb₂S₃ [105], [112], [112], [171], [172], complicate processing of Sb₂S₃ by physical methods. Consequently, taking into account the S partial pressure during thermal co-evaporation of Sb₂S₃ films from Sb₂S₃ and S as precursors allowed to engineer S/Sb and deep-level defects, yielding $\eta = 6.2\%$ in a planar solar cell [101].

1.6.2 Chemical methods

Before the start of this study in September 2017, Sb₂S₃ coatings had been fabricated mainly by the following chemical methods: chemical bath deposition [8], [98], [100], [115], [156], [173]–[176], atomic layer deposition [8], [177]–[179], spin coating [115], [180], [181], [138], [7], hydro- and solvothermal deposition [106], [182]–[184], and chemical spray pyrolysis (CSP) [185]–[190].

Chemical bath deposition (CBD) is the most widely used method for preparing Sb₂S₃ coatings. According to queries conducted on the Web of Knowledge, Scopus and IEEE search engines, there are over 100 published papers on the topic. In CBD, a chemical precipitation reaction is used at a controlled temperature in a stirred solution to deposit metal chalcogenide films. Sb₂S₃ films are grown in CBD via precipitation of Sb³⁺ and S²⁻ from dissolved chemicals as Sb₂S₃. The deposition of Sb₂S₃ films by CBD is possible due to the extremely small solubility constant of Sb₂S₃ in most solvents [104], [105], [191].

In terms of features, CBD provides facile process control via temperature, precursor concentration and solution pH, as well as inexpensive low maintenance equipment [8], [115]. Thus, studying CBD-grown Sb₂S₃ films has been historically popular (see section 1.5, Table 1.1).

In CBD, SbCl₃ is the most common source of Sb³⁺ for growing Sb₂S₃ films. Na₂S₂O₃ [100], [156], [173]–[175], and complexes of SbCl₃ with thiourea (TU) [115], e.g. Sb(TU)₂Cl₃ [115], [192] or Sb(TU)₃Cl₃ [193] have been used in acidic conditions. Complexes of SbCl₃ with thioacetamide (TA) [98], [174], e.g. Sb(TA)₃Cl₃ have been mainly used in basic conditions. In some instances, complexation via potassium antimony tartrate K₂Sb₂(C₄H₂O₆)₂ [175], [176] has been applied.

In CBD, Sb-based coordination complexes are prone to hydrolyze into Sb₂O₃, SbOCl, Sb(OH)₃, and Sb₂(SO₄)₃ during deposition in aqueous solutions, which contaminates the bulk of the deposited Sb₂S₃ film and has been proven to be detrimental to η of solar cells

[8], [116], [194]. Thus, post-growth sulfurization via e.g. H₂S [6], or adding phosphotungstic acid (H₃PW₁₂O₄₀·nH₂O) [194] to the CBD solution has been applied to counteract oxidation within the bulk of CBD-grown Sb₂S₃ films. Oxidation of a few nm of the surface of Sb₂S₃ after crystallization has, however, been reported to passivate surface defects, which in turn increased η of solar cells [66], [103].

Sb₂S₃ films have been prepared by CBD on planar SnO₂ at room temperature from an aqueous solution of K₂Sb₂(C₄H₂O₆)₂, NH₄OH, TA, and triethanolamine (N(C₂H₅OH)₃) [94]. After heat treatment at 300°C in N₂ for 1 h, crystalline n-type Sb₂S₃ films with $E_g = 1.74$, lateral grain size = 0.8 μm , and $\rho = 5 \cdot 10^6 \Omega \text{ cm}$ were obtained [94]. In another study, a complex of SbCl₃ with Na₂S₂O₃ dissolved in acetic acid and water yielded Sb₂S₃ films on planar SnO₂ [195]. After heat treatment at 170°C in air for 6h, crystalline n-type Sb₂S₃ films with $E_g = 1.70 \text{ eV}$ were obtained [195].

Notably, most later studies on CBD-grown Sb₂S₃ films applied these two deposition routes, whereas heat treatment for crystallization has been mainly done at 250–300°C in N₂ or Ar for 30 min [107], [116], [137], [174]. Furthermore, Sb₂S₃ films grown via CBD from SbCl₃ and Na₂S₂O₃ have been reported to crystallize via the formation of metallic Sb and Sb₂O₃ as intermediate phases, as recorded by *in situ* XRD and Raman measurements [116]. As for solar cell achievements, the record η is 7.5 % for structured [6], and 4.6 % for planar solar cells based on CBD-grown Sb₂S₃ thin films [194].

A concern for large scale production of Sb₂S₃ films by CBD is that the processing time is generally in hours or days. Furthermore, as deposition temperature during CBD is generally below 100°C, amorphous Sb₂S₃ is produced. Thus, heat treatment as a second step is required to crystallize the Sb₂S₃ films. Moreover, applying CBD to grow Sb₂S₃ thin films on a large scale would require batch processing, and implementation of recycling for the spent feedstock.

Atomic layer deposition (ALD) is the method of choice to produce the most pristine chemical composition of Sb₂S₃ thin films or other morphologies, independent of the substrate morphology [8], [148], [177]–[179], [196]. Conventional temporal ALD of metal sulfide films entails repeated pulsing, decomposition, and purging of gases at low pressure in an inert gas until a film with the desired thickness has grown. Usually, ALD-grown crystalline Sb₂S₃ films are prepared by first depositing an amorphous film of Sb₂S₃ by ALD, followed by purification and crystallization in an inert gas at $\approx 300^\circ\text{C}$ [8], [148], [177].

Precursors used in ALD must be volatile, reactive, and decompose at a suitable temperature, which limits the range of Sb-based precursors available for use. Furthermore, ensuring a sufficient purge time results in a modest deposition rate of $\approx 6 \text{ nm h}^{-1}$ for Sb₂S₃ films [8]. However, ALD is superior compared to other chemical deposition methods because the consumption of precursor chemicals is minimal and no solvent is required.

Until now, only *tris*-dimethylamido antimony Sb(N(CH₃)₂)₃ and H₂S, which are sufficiently volatile, thermally stable, and reactive, have been used for depositing Sb₂S₃ thin films and coatings by ALD [8], [148], [177]–[179], [196].

In a study comparing the growth of Sb₂S₃ films on a planar FTO/TiO₂ substrate by ALD and CBD, it was found that ALD prevents oxidation and provides precise control over the thickness of the deposited film [8]. CBD, on the other end, resulted in heterogeneous nucleation, less consistent film thickness, and inclusion of oxidized byproducts in the deposited film [8]. After heat treatment in an unspecified concentration of H₂S gas

at 330°C for 30 min, the amorphous as-grown Sb₂S₃ films had crystallized, yielding $E_g = 1.76$ eV in either case, according to EQE [8].

The highest η for ALD-Sb₂S₃ based planar thin film solar cells is 5.8 %, obtained at an Sb₂S₃ thickness of 90 nm [8]. In 2020, the first report was published on complete semitransparent planar solar cells based on Sb₂S₃ films grown by ALD [197]. Therein, $\eta = 3.4$ % and AVT = 13 % was achieved [197], proving that ALD-grown Sb₂S₃ films are suitable for semitransparent PV.

In terms of limitations, temporal ALD is by design a batch process. The limiting factors of temporal ALD, i.e. slow deposition rate, batch processing, and the need for vacuum, have been addressed by the development of the atmospheric pressure spatial ALD and its variants [198]–[201]. Thus, spatial ALD can be considered one of the most prospective deposition methods for rapid preparation of uniform phase pure Sb₂S₃ thin films on large area substrates at reasonable cost.

Spin coating is a rapid wet chemical deposition method for preparation of inorganic and organic films. Spin coating is performed, often at room temperature, by spreading a colloidal suspension or a solution over a substrate, which is spun during or after dispensing the solution while the solvent evaporates [202]. The centrifugal acceleration generated by spinning expels the leftover solution from the substrate, yielding a solid layer [202]. Film uniformity and thickness is controlled via precursor concentration, solvent evaporation rate, angular velocity, and solvent–substrate wettability [202].

Depositing Sb₂S₃ thin films by spin coating requires a two-stage process, wherein the precursor solution is spin coated onto the substrate, and then heat treated in one or more steps in air [138] or primarily in an inert atmosphere to decompose the precursor film into Sb₂S₃ and to crystallize the Sb₂S₃ film [140], [141]. In some studies, the preparation sequence has been repeated a number of times to obtain a thicker film [138]. As one sequence can be completed in a few minutes per sample, spin coating is advantageous for rapid preparation of films on cm² size substrates.

Some precursor solutions used for spin coating of Sb₂S₃ films are similar to those used in CBD, i.e. SbCl₃ with TU [115], [180], [181], [140], [203], or TA [138], dissolved in organic solvents. A recently popularized group of single-source precursors for spin coating Sb₂S₃ films is the halogenide-free series of Sb-alkyldithiolates: Sb-diethyldithiocarbamate Sb(S₂CN(C₂H₅)₂)₃ [129], [130], [141], Sb-dibutyldithiocarbamate Sb(S₂CN(C₄H₉)₂)₃ [7], [203], [204], and Sb-ethyldithiocarbonate Sb(S₂COC₂H₅)₃ (SbEX) [205], which are dissolved in organic solvents, e.g. dimethylformamide ((CH₃)₂NC(O)H), 2-methoxyethanol (CH₃OC₂H₄OH), dimethylsulfoxide ((CH₃)₂SO), or ethanol (C₂H₅OH).

Crystalline Sb₂S₃ thin films, oxide-free according to X-ray photoelectron spectroscopy (XPS), although E_g and S/Sb were not reported, have been grown by repeating the cycle of spin coating Sb(TA)₂Cl₃ dissolved in dimethylformamide, followed by heat treatment at 120°C in air, and 300°C in N₂ for 20 min [138]. In addition, 137 nm thick crystalline Sb₂S₃ films with mean lateral grain size = 6 μ m, and $E_g = 1.65$ eV, have been deposited by spin coating a solution of Sb-dibutyldithiocarbamate dissolved in ethanol, followed by heat treatment at 300°C in N₂ for 2 min [7]. However, phase purity of these Sb₂S₃ films was verified only by XRD. Solar cells based on these Sb₂S₃ films yielded $\eta = 4.3$ % [7]. This was the record for planar solar cells based on Sb₂S₃ films grown by spin coating before the start of this thesis.

The highest η of thin film solar cells based on a spin coated Sb₂S₃ absorber layer is 7.1 % for planar [147], and 6.8 % for structured [142] configurations, respectively. More information on the absorber and solar cell can be found in section 1.5, Table 1.1.

The main challenge of spin coating is that films are often thinner at the edges than in the center due to centrifugal acceleration, and that up to 95–98 % of the solution is discarded from the substrate during processing [206]. Furthermore, spin coating is by design a batch process that requires post-growth heat treatment to prepare metal oxide and metal sulfide thin films.

Hydro- and solvothermal synthesis has also been used to fabricate Sb_2S_3 coatings. The process is largely similar to CBD in most aspects. The deposition procedure differs from CBD by the fact that overpressure of several atmospheres, higher temperature, and inert atmosphere is used in an autoclave filled with an aqueous or organic solution to increase the growth rate and chemical purity of the grown material. In addition, crystalline films can be grown in one step if the deposition temperature is higher than the crystallization temperature in the relevant medium. Also, overpressure allows to shift gases to liquid or solid state during deposition, and to form metastable phases.

The reagents used in hydrothermal synthesis of Sb_2S_3 thin films, structures and layers are SbCl_3 or potassium antimony tartrate with $\text{Na}_2\text{S}_2\text{O}_3$ [106], [207]. In solvothermal synthesis, antimony dithiocarbamates, dithiocarbonates, and dithiophosphates [182], [183], including SbEX [184], have been used.

Sb_2S_3 thin films had been prepared in few papers by hydro- or solvothermal synthesis before the start of this thesis. Sb_2S_3 thin films with $E_g = 1.7$ eV have been hydrothermally grown onto TiO_2 -covered Ti nanotube arrays from a solution of SbCl_3 and Na_2S dissolved in ethanol–water after 8 h at 180°C [208]. In another paper, amorphous 680 nm thick Sb_2S_3 films were grown hydrothermally from a solution of $\text{KSbC}_4\text{H}_4\text{O}_7$ and $\text{Na}_2\text{S}_2\text{O}_3$ onto planar ITO-covered glass substrates after 8h at 150°C [106]. After heat treatment at 450°C in Ar for 1 h, crystalline p-type Sb_2S_3 films with $E_g = 1.63$ eV, oxide-free surface per XPS, $\text{S}/\text{Sb} = 1.44$, and $\rho = 1.3 \cdot 10^4 \Omega\text{cm}$ were obtained [106].

The highest η of thin film solar cells based on a hydrothermally grown Sb_2S_3 absorber layer is 6.5 % for planar [146], and 4.7 % for structured configurations [209], respectively, as of 2021. Moreover, in another study, η was increased from 6.0 % to 10.0 % by hydrothermally depositing a thin film of $\text{Sb}_2\text{S}_{2.13}\text{Se}_{0.87}$ with $E_g = 1.49$ eV, and by optimizing its heat treatment temperature [207]. The appreciable increase of η indicates that introducing Se into Sb_2S_3 is a prospective procedure for PV applications.

Applying an overpressure of several atmospheres requires thick walled high pressure autoclaves and corresponding safety features, which is bound to be more expensive compared to the simple setup of CBD. Furthermore, hydro- and solvothermal synthesis is limited to batch processing by design. Although, the extendable reactor length could partially compensate for it. However, similarly to CBD, recycling or disposal of the spent feedstock is required.

Chemical spray pyrolysis (CSP) is a simple and robust wet chemical method that is used to deposit thin films and other morphologies of metal oxides and sulfides [210]. In CSP, the precursor solution is nebulized into an aerosol and is conveyed by a carrier gas stream onto the substrate on a heated plate where the droplets dry and thermally decompose into a film [210].

CSP can be used to prepare single or multi-layered metal chalcogenide thin films with a graded composition on large areas in air in a continuous process [210]. CSP allows to control the structure, morphology and optoelectronic properties of the deposited thin films by deposition temperature, choice of solvent, composition and concentration of the precursors, gas flow rate, nozzle distance, and droplet size [210], [211]. CSP can be

divided into three subclasses based on the nebulization technique: pneumatic, electrostatic, and ultrasonic [211].

Ultrasonic nebulization is performed by oscillating an electromechanical device at high frequency that shears the tips of capillary surface waves into droplets [212]. The drawback is that only Newtonian liquids with low viscosity can be nebulized into droplets when passing over the vibrating surface [211]. Therefore, solutions based on fluid organic solvents are the most suitable for producing the smallest droplet size by ultrasonic spray pyrolysis (USP).

In case of USP, droplets are produced only if enough power is produced at the ultrasonic frequency to overcome the viscosity and surface tension of the spray solution [213]. Furthermore, the mean droplet size depends on the frequency of the oscillator and the surface tension of the solution by the following empirical equation [212]:

$$D = 0.34 \cdot \left(\frac{8\pi\gamma}{\rho f^2} \right)^{1/3} \quad (1),$$

where D is the mean droplet diameter, γ is the liquid's surface tension vs air, ρ is the density of the solution, and f is the ultrasonic frequency. Evidently, at isothermal conditions, D is a function of the frequency at a power = -2/3. For instance, in order to nebulize droplets of methanol ($\gamma = 0.02217 \text{ N m}^{-1}$ at 25°C ; $\rho = 791.4 \text{ kg m}^{-3}$ at 20°C [191]) with a mean diameter = $10 \text{ }\mu\text{m}$, $f = 5 \text{ MHz}$ is required.

The preparation of Sb_2S_3 coatings and corresponding solar cells by pneumatic CSP, and USP, and the selection of precursors are presented in sections 1.7.1, 1.7.2, and 1.7.3, respectively.

In terms of challenges, application of CSP and USP depends significantly on the preparation of the spray solution, whereby a stable metal organic coordination complex is prepared as the precursor. Thus, process chemistry is an important aspect for preparing metal oxide and metal sulfide thin films by CSP and USP. Moreover, an additive that forms a liquid protective coating, e.g. TU, is required during deposition to prevent oxidation of the deposited metal sulfide thin film [9], [214]–[216].

Thus, tuning the composition of the spray solution is critically important for growing Sb_2S_3 thin films by CSP. To add, clogging of the nozzle by the precursor or solid byproducts during the CSP process has to be avoided. Thus, CSP as a method to grow Sb_2S_3 films from solutions of Sb and S containing metal organic coordination complexes is definitely viable for industrial production on the condition that these practical issues are addressed.

1.7 Deposition of Sb_2S_3 thin films by spray pyrolysis

In this section, the deposition of Sb_2S_3 thin films by pneumatic and ultrasonic spray pyrolysis is discussed. Furthermore, a guide for screening appropriate precursors to grow Sb_2S_3 thin films by USP is presented.

1.7.1 Pneumatic spray pyrolysis

Several reports appeared in the 1990s and early 2000s using primarily solutions of SbCl_3/TU [185]–[187], or seldom SbCl_3/TA [188], dissolved in acetic acid, or aqueous HCl to grow Sb_2S_3 films. However, the phase purity of these Sb_2S_3 films was not firmly established, and the morphology was either not investigated or the films were not homogeneous.

In 2002, Sb_2S_3 thin films were grown by pneumatic CSP from an aqueous solution ($\text{SbCl}_3/\text{TU}/\text{tartaric acid} = 1/1.5/2.5$) and a non-aqueous solution ($\text{SbCl}_3/\text{TU} = 1/1.5$ dissolved in acetic acid) at 300°C or 250°C , respectively, onto glass substrates [188].

Therein, the films grown from the aqueous solution remained amorphous after heat treatment, whereas the films grown from the non-aqueous solution were crystalline ($E_g = 1.8$ eV) after deposition. In either case, the films were n-type, with $\rho = 10^6$ – 10^7 Ω cm, yielding up to $\eta = 0.06$ % at 80 mW cm⁻² illumination with an unspecified light source in a photoelectrochemical cell of Sb₂S₃/0.5 M KI – 0.01 M I₂/C.

The surface topography of 634 nm thick possibly continuous Sb₂S₃ films with $E_g = 1.78$ eV and grain size = 620 nm was reported in 2014 by atomic force microscopy, yielding root mean square roughness > 50 nm [189]. Therein, the crystalline films were prepared, presumably in one step, at 197°C in air by pulsed pneumatic CSP from an aqueous solution of SbCl₃/TU 1/1.5 acidified with HCl, and the phase purity was confirmed by XRD and Raman.

In 2015, the group hosting this thesis proved by spraying an aqueous solution of SbCl₃/TU/tartaric acid in molar ratios of 1/3/1 and 1/3/10 at 205–230°C and 205–355°C, respectively, that stabilization with tartaric acid, and the use of aqueous solutions is detrimental to phase purity and morphology of Sb₂S₃ films grown by pneumatic spray pyrolysis [216]. In the same study, the use of alcohols as solvent without tartaric acid yielded Sb₂S₃ thin films with vastly increased phase purity [216].

1.7.2 Ultrasonic spray pyrolysis

There were no reports on USP-grown Sb₂S₃ coatings before 2016. In 2016 [9], the group hosting this study opted for ultrasonic nebulization of a solution of Sb(TU)₃Cl₃, (synthesis and phase according to ref. [193]) with optionally extra TU to suppress oxidation. This single step preparation yielded separate crystalline Sb₂S₃ grains ($E_g = 1.6$, S/Sb = 1.53) by spraying a solution of SbCl₃/TU in a molar ratio of 1/6 at 250°C in air [9]. Thereby, the first (planar) solar cell of ITO/TiO₂/Sb₂S₃/P3HT/Au based on a USP-grown Sb₂S₃ coating with $\eta = 1.9$ % was achieved [9]. Notably, no explanation was provided to relate these deposition conditions to the formation of separate grains instead of continuous films.

In 2017, an ETA solar cell of ITO/ZnO-nanowire/TiO₂/Sb₂S₃/P3HT/Au, with $\eta = 2.3$ %, was also prepared by the group hosting this thesis [10]. The absorber was deposited by a two-step process. Accordingly, a uniform conformal amorphous Sb₂S₃ coating was deposited onto TiO₂-coated ZnO nanowires at 220°C by USP in air from a SbCl₃/TU = 1/3 solution, followed by heat treatment in N₂ at 300°C to crystallize the absorber layer [10]. Notably, the ≈ 10 nm thick absorber coating was not entirely phase pure, as it contained Sb₂O₃ according to Raman analysis [10].

1.7.3 Selection of precursors to deposit Sb₂S₃ thin films by USP

In order to be useful for USP, the precursors must dissolve in the chosen organic solvent and yield a low-viscosity Newtonian solution. Furthermore, the precursor should be nonvolatile, stable in the spray solution, and decompose into a metal chalcogenide and volatile byproducts at a temperature below the deposition temperature [213]. In turn, the deposition temperature has to be low enough to prevent oxidation of the Sb₂S₃ film. It is known that Sb₂S₃ oxidizes readily above ≈ 200 °C [171]. Increasing the deposition temperature any further in air requires an increasing concentration of the reducing agent [9], which becomes a source of contamination. Thus, the deposition of metal sulfide thin films by CSP requires a temporary protective coating on top of the growing film to suppress oxidation of the deposited film [9], [216]. Therefore, the precursors that had been used by chemical methods to produce Sb₂S₃ thin film solar cells with appreciable η were filtered according to these requirements of USP.

As aqueous solutions require buffers such as tartaric acid, which contaminate Sb_2S_3 films, only Sb-based coordination complexes soluble in non-aqueous low-viscosity solvents are relevant. Hence, as Sb_2S_3 coatings with the most pure phase and elemental composition, and conformal morphology were prepared by spraying $\text{SbCl}_3/\text{TU} = 1/3-1/6$ dissolved in methanol [9], [10], this precursor–solvent combination is considered the most promising for further study. However, it is evident that only polar solvents and SbCl_3 based metal organic coordination complexes have been explored for use in CSP. Consequently, there is no frame of reference to claim that spraying SbCl_3/TU dissolved in methanol is the only viable option. Furthermore, it is not known whether halogenide-free precursors dissolved in non-aqueous solvents could be used to deposit continuous phase pure Sb_2S_3 thin films in air. This study aims to address these questions.

Among halogenide-free precursors, antimony dithiolates, especially dithiocarbonates (xanthates), and dithiocarbamates potentially fit the requirements of USP, *vide ante*. However, none of them have been used in spray pyrolysis before. To date, ultrasonic aerosol assisted chemical vapor deposition of Sb_2S_3 coatings from asymmetric dithiocarbamates in N_2 [217], and a selection of xanthates, dithiocarbamates, and dithiophosphates, dissolved in toluene has been reported [183]. Although, only discontinuous layers of amorphous or crystalline Sb_2S_3 have been obtained.

Accordingly, as SbEX is reported to have the lowest melting point of 68–70°C, the lowest decomposition end point of 200°C [183], and the second lowest carbon content ($\text{C}/\text{Sb} = 9$) among these antimony dithiolate precursors, it is the most likely to yield phase pure Sb_2S_3 thin films by USP at $\approx 200^\circ\text{C}$. Prior to this study, the thermal decomposition of SbEX had been determined by TG in air [218], N_2 [183], [219], or Ar atmosphere [205], or by TG/DTA analysis combined with *ex-situ* evolved gas analysis [220], whereas intermediate solid decomposition product analysis had not been reported. It is important to consider that thermal analysis via TG/DTA, and even more so by TG alone, does not provide all the required information needed to validate a precursor for use by chemical methods, e.g. CSP. Thus, analysis of the phase composition of intermediate solid decomposition products, and evolved gases by *in situ* measurements is necessary to describe the thermal behavior of SbEX, and to provide proof of the chemical purity of the resultant solid phase. This study aims to provide such vital information for SbEX.

To conclude, based on the requirements of ultrasonic spray pyrolysis, SbCl_3 and TU dissolved in methanol, and SbEX dissolved in a compatible fluid organic solvent are the two most promising options to deposit uniform phase pure Sb_2S_3 thin films by USP. In addition, TG/DTA-EGA-MS and intermediate solid decomposition product analysis is a prerequisite to use SbEX as a precursor for USP.

1.8 Summary of the literature review and aim of the thesis

Sb₂S₃ is attractive for PV because of its anisotropic quasi-1D structure, chemical stability, suitable optoelectronic properties ($E_g = 1.7$ eV, $\alpha = 10^5$ cm⁻¹ in visible range, anisotropic conductivity), and the availability of Sb and S as primary mining products for GW_p-TW_p scale annual production of solar cells.

Before the start of this study, Sb₂S₃ thin films had been deposited by chemical methods such as CBD, spin coating, ALD, hydrothermal synthesis, and CSP. In terms of area-scalability and processing rate, USP is perhaps the most advantageous wet chemical method. However, a continuous uniform phase pure Sb₂S₃ thin film, which had had a critical role in achieving the record $\eta = 5.8\%$ in planar solar cells based on a Sb₂S₃ film grown by ALD [8], had not been prepared by pneumatic CSP or USP.

Furthermore, deposition of Sb₂S₃ thin films, especially by CSP and USP, was relatively unexplored in terms of solvent and precursor composition, Sb/S source concentration, and heat treatment conditions. Thus, the effect of these parameters on the phase composition, structure, morphology, and optical properties of USP-grown Sb₂S₃ thin films has to be investigated as a basic requirement.

Essentially, the approach to achieve continuous uniform phase pure Sb₂S₃ thin films by USP was designed according to the following existing knowledge:

- A *stable* metal organic coordination complex *precursor* soluble in a fluid low surface tension solvent is required to generate a liquid aerosol by USP [211].
- Furthermore, the precursor must *decompose* into Sb₂S₃ below the deposition temperature [213].
- In addition, an additive that forms a *liquid protective coating*, which repels oxidation of the Sb₂S₃ film during deposition, is likely required [9].
- Using aqueous solutions, and applying tartaric acid to stabilize the Sb(TU)₃Cl₃ complex is detrimental, whereas using *non-aqueous* solvents is favorable to the phase purity of the deposited Sb₂S₃ thin films [216].
- Continuous phase pure Sb₂S₃ thin films could not be prepared in a *single step* on planar TiO₂ from a methanolic solution of SbCl₃/TU = 1/6 by USP at 250°C in air, as *separate crystalline grains* of phase pure Sb₂S₃ were formed [9].
- A structured substrate of ZnO/TiO₂ nanowires was covered with a *continuous* shell of crystalline Sb₂S₃ by a *two-step process*. Therein, an amorphous Sb₂S₃ coating was deposited from a methanolic solution of SbCl₃/TU = 1/3 at 220°C in air, and thereafter crystallized in an inert atmosphere. However, the Sb₂S₃ shell was not phase pure, as Sb₂O₃ had been detected [10].
- Employing a *Sb-alkyldithiolate* precursor had yielded continuous phase pure Sb₂S₃ thin films by spin-coating, resulting in solar cells with $\eta = 4.3\%$ [7].

Based on the literature review and the aforementioned gaps in knowledge, the hypothesis of this thesis is formulated as follows:

- 1) The process to prepare phase pure polycrystalline Sb_2S_3 thin films, uniform in thickness and morphology, conforming to the planar polycrystalline ITO/ TiO_2 substrate, by spraying SbCl_3/TU solutions via USP is developed, thereby forming the basis to evaluate their applicability in planar thin film solar cells.
- 2) The uniformity, conformal coverage of the planar polycrystalline ITO/ TiO_2 substrate, and phase purity of the Sb_2S_3 thin films grown by USP from the SbCl_3/TU solution enable application of these films as the absorber in planar solar cells that yield increased η compared to previous results on the condition that the thickness of the absorber film is optimized.
- 3) The synthesis and analysis of the phase composition, structure, and thermal decomposition of the halogenide-free precursor (SbEX) determine its applicability for use as a precursor for depositing Sb_2S_3 thin films by USP.
- 4) The process to prepare continuous, uniform in thickness, phase pure polycrystalline Sb_2S_3 thin films, which conform to the planar ITO/ TiO_2 substrate, by USP from a solution of SbEX is developed.

Accordingly, the aim of this thesis is to prepare uniform phase pure thin films of polycrystalline Sb_2S_3 by USP from a halogenide-containing, and a halogenide-free precursor solution, and to test a selection of these Sb_2S_3 thin films in planar solar cells.

Thus, the following tasks are outlined to reach the aim of the thesis:

- 1) To determine the preparation conditions that allow to deposit uniform continuous phase pure polycrystalline Sb_2S_3 thin films by USP from a SbCl_3/TU solution on a planar ITO/ TiO_2 substrate. To characterize the phase composition, elemental composition, optical properties, and morphology of the deposited films.
- 2) To prepare planar $\text{TiO}_2/\text{Sb}_2\text{S}_3/\text{P3HT}$ thin film solar cells based on a Sb_2S_3 thin film grown by USP from a SbCl_3/TU solution. To characterize the PV output parameters of these solar cells as a function of the thickness of the absorber.
- 3) To evaluate the applicability of SbEX as a prospective halogenide-free precursor for the deposition of Sb_2S_3 thin films by USP via thermal analysis in an inert and air atmosphere, and intermediate solid decomposition product analysis.
- 4) To determine the preparation conditions to deposit uniform continuous phase pure thin films of polycrystalline Sb_2S_3 by USP from a solution of SbEX or SbEX/thioamide on a planar ITO/ TiO_2 substrate, and to characterize the phase composition, elemental composition, optical properties, and morphology of the deposited films.

2 Experimental

In this chapter, the experimental methods applied in papers I, II, III, and IV for the preparation, characterization, and analysis of Sb₂S₃ thin films, the respective solar cells, and powders for thermal analysis, are summarized.

2.1 Preparation of Sb₂S₃ thin films and solar cells

All chemicals were used as-bought. Chemicals applied in papers I, II, III, and IV are listed with their purity and origin in Table 2.1.

Table 2.1. List of chemicals used in this thesis.

Name	Linear formula	Purity	Supplier	Paper
Deionized water	H ₂ O	18.2 MΩcm ⁻¹	Made on site	I, II, III, IV
Sulfuric acid	H ₂ SO ₄	98 wt%	Merck	I, II
Antimony trichloride	SbCl ₃	99 wt%	Sigma-Aldrich	I, II, III
		99.999 wt%	Sigma-Aldrich	IV
Methanol	CH ₃ OH	99.9 vol%	Sigma-Aldrich	I
		99.8 vol%	Honeywell	II
Thiourea	SC(NH ₂) ₂	99 wt%	Sigma Aldrich	I
		98 wt%	Fluka	II
		99 wt%	Alfa Aesar	IV
Thioacetamide	SC(NH ₂)(CH ₃)	99 wt%	Merck	IV
Acetonitrile	CH ₃ CN	99.9 wt%	Honeywell	IV
Ethanol	C ₂ H ₅ OH	96.6 vol%	Estonian Spirit	I, II, IV
Potassium ethyl xanthate	KS ₂ COC ₂ H ₅	97 wt%	Acros	III, IV
Acetone	CH ₃ COCH ₃	99.8 vol%	Merck	III, IV
Titanium(IV) isopropoxide	Ti(OC ₃ H ₇) ₄	97 wt%	Sigma-Aldrich	I, II
		98 wt%	Acros	IV
Diethyl ether	(CH ₃ CH ₂) ₂ O	99.5 vol%	Sigma-Aldrich	III, IV
Acetylacetone	(CH ₃ CO) ₂ CH ₂	98 %	Sigma-Aldrich	I
		99 %	Acros	II, IV
Chlorobenzene	C ₆ H ₅ Cl	99.5 vol%	Sigma-Aldrich	II
Poly(3-hexylthiophene-2,5-diyl)	(C ₁₀ H ₁₄ S) _n	85–100kDa, >90 % regioregular	Sigma-Aldrich	II

The $\text{In}_2\text{O}_3:\text{Sn}$ (ITO) covered 1 mm thick soda lime glass substrates ($25 \Omega \text{ sq}^{-1}$, 150 nm ITO, papers **I**, **II**), ($10 \Omega \text{ sq}^{-1}$, 230 nm ITO, paper **IV**) were cut to 25 mm by 15 mm rectangles and cleaned before use [**I**, **II**, **IV**]. The substrates were then coated with a thin film of anatase- TiO_2 by USP from a solution of titanium (IV) isopropoxide and acetylacetonone [**I**, **II**, **IV**]. The glass/ITO/ TiO_2 stack was used for further experiments.

The USP setup is illustrated in Figure 2.1. Deionized cooling water was continuously pumped through the ultrasonic oscillator chamber. Waste heat generated by the oscillators was removed via an open loop shell and tube heat exchanger. The carrier gas flow rate was regulated via a motorized proportional-integral-derivative needle valve coupled with a pressure sensor. A proportional-integral-derivative temperature regulator was used to maintain a constant substrate temperature.

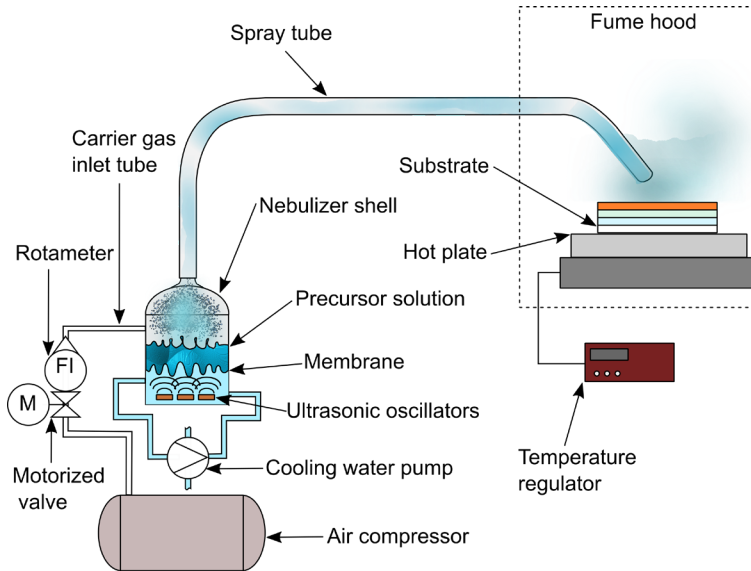


Figure 2.1. Schematic of the ultrasonic spray pyrolysis setup.

To start the deposition process, the precursor solution was poured into the nebulizer shell. Then, the clean dry substrates were placed on the preheated hot plate. After preparations had been finished, the ultrasonic oscillators were switched on. The ultrasonic waves traveled through the cooling water and the fluoropolymer membrane, nebulizing the precursor solution into a liquid aerosol. The fine mist was transported by the compressed air stream through the spray tube onto the heated substrates. The dispersed precursor decomposed on the surface of the heated substrate, thereby forming a thin film. Any gaseous products were ventilated via a fume hood.

Sb_2S_3 thin films were deposited by USP onto the glass/ITO/ TiO_2 stack from a solution of 30 mM SbCl_3 , and $\text{SC}(\text{NH}_2)_2$ (TU) dissolved in methanol. Thereby, the $\text{Sb}(\text{TU})_3\text{Cl}_3$ complex was formed in solution (verified by comparing the XRD pattern of the powder obtained after vacuum drying the precursor solution to ref. [193]), at SbCl_3/TU molar ratio = 1/3 [**I**]. In addition, drying the solution of SbCl_3/TU in a molar ratio = 1/6 yielded $\text{Sb}(\text{TU})_3\text{Cl}_3$ and free TU by XRD analysis. Based on preliminary experiments, the deposition time in paper **I** was set to 20 min for the $\text{SbCl}_3/\text{TU} = 1/3$ solution, and to 40 min for the $\text{SbCl}_3/\text{TU} = 1/6$ solution to obtain a similar film thickness. The thickness of

Sb_2S_3 films was varied in paper II by changing the concentration of the precursor solution (30–90 mM) at a fixed molar ratio of $\text{SbCl}_3/\text{TU} = 1/3$ and a constant deposition time. The flow rate of compressed air was 5 L min^{-1} . The deposition temperature was 200°C , 210°C , or 220°C . Afterwards, samples were heat treated in dynamic vacuum ($\approx 5 \cdot 10^{-4} \text{ Pa}$) at 170°C [I, II], 200°C [I], or 250°C [I] for 5 min at an average heating and cooling rate of 8°C min^{-1} . The stock solution of SbCl_3 in methanol was prepared in a glove box pumped with 99.999 vol% N_2 , at $\text{O}_2 < 20 \text{ ppm}$, humidity $< 14 \text{ ppm}$.

The metal organic coordination complex precursor SbEX was synthesized according to the procedure described in paper III. Layers of Sb_2S_3 were deposited onto the glass/ITO/ TiO_2 stack from a solution of 60 mM SbEX dissolved in acetonitrile at a deposition temperature of 105°C , 135°C , or 165°C [IV]. Solutions of 60 mM SbEX/TU in a molar ratio of 1/1, and 1/3, and 60 mM SbEX/TA in a molar ratio of 1/3, and 1/10 were sprayed at a deposition temperature of 135°C , 165°C , or 215°C onto the glass/ITO/ TiO_2 stack. The flow rate of compressed air was 5 L min^{-1} . Thereafter, the samples were heat treated in dynamic vacuum ($2 \cdot 10^{-1} \text{ Pa}$) in a quartz tube at 225°C for 30 min at an average heating and cooling rate of 5°C min^{-1} .

For the preparation of solar cells, Sb_2S_3 thin films with a thickness of approximately 30, 70, 100, and 150 nm were deposited by USP onto the glass/ITO/ TiO_2 stack in 20 min at a deposition temperature of 200°C by varying the concentration of the solution of SbCl_3/TU at a constant molar ratio of 1/3 [III]. The flow rate of compressed air was 5 L min^{-1} . After deposition, samples were heat treated in dynamic vacuum ($\approx 5 \cdot 10^{-4} \text{ Pa}$) at 170°C for 5 min. Then, a layer of P3HT was deposited onto the stack from a 2 wt% solution of P3HT in chlorobenzene, and the vacuum heat treatment was repeated. The solar cells were completed by thermally evaporating Au as back contact through a metal mask. The steps of the experimental procedure are illustrated in Figure 2.2.

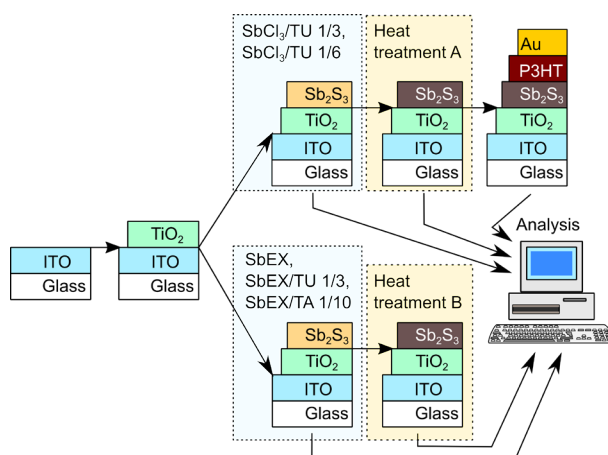


Figure 2.2. Schematic of the sequence of operations in the experimental procedure for depositing Sb_2S_3 films by ultrasonic spray pyrolysis from solutions based on SbCl_3 or SbEX. Heat treatment: (A) 170°C , $5 \cdot 10^{-4} \text{ Pa}$, 5 min; (B) 225°C , $2 \cdot 10^{-1} \text{ Pa}$, 30 min.

2.2 Applied characterization methods

Unless specified otherwise, any measurements were made at the Department of Materials and Environmental Technology, Tallinn University of Technology. The list of characterization methods used in this thesis is provided in Table 2.2.

Table 2.2. List of characterized properties, applied methods and equipment.

Object	Characterized properties	Method	Equipment	Paper
Glass/ITO/TiO ₂ /Sb ₂ S ₃ , various powders	Phase composition, crystallite size	XRD	Rigaku Ultima IV	I, II, III, IV
Glass/ITO/TiO ₂ /Sb ₂ S ₃ , various powders	Phase composition	FTIR	Perkin Elmer GX 2000, Bruker Alpha	III, IV
Glass/ITO/TiO ₂ /Sb ₂ S ₃ , various powders	Phase composition	Raman	Horiba LabRam HR800	I, II, III, IV
Glass/ITO/TiO ₂ /Sb ₂ S ₃	Electronic structure, chemical bonding	XES	SALSA endstation ^a	II
SbEX powder	Molecular structure, phase composition	NMR	800 MHz Bruker Avance III ^b	III
SbEX powder, TA powder	Thermal analysis of precursor	TG/DTA-EGA-MS	Setaram LabSys EVO, ThermoStar GSD320	III, IV
Glass/ITO/TiO ₂ /Sb ₂ S ₃	Transmittance, reflectance, band gap, absorption coefficient	UV-VIS	Jasco V-670 with integrating sphere vs air	I, II, IV
Glass/ITO/TiO ₂ /Sb ₂ S ₃	Elemental composition	EDX	Bruker ESPRIT 1.8	I, II, III, IV
Glass/ITO/TiO ₂ /Sb ₂ S ₃	Morphology, film thickness	SEM	Zeiss Ultra 55 FEG HR-SEM, Helios NanoLab 600 ^c , Merlin Gemini II	I, II, III, IV
Glass/ITO/TiO ₂ /Sb ₂ S ₃ /P3HT/Au	Solar cell parameters	<i>J-V</i>	Newport Oriel Sol3A	II
Glass/ITO/TiO ₂ /Sb ₂ S ₃ /P3HT/Au	Spectral quantum yield response, band gap, integrated <i>J</i> _{sc}	EQE	Newport 69911, Newport Cornerstone 260, Merlin lock-in detector	II

^aAdvanced Light Source, Lawrence Berkeley National Laboratory, Berkeley, CA, USA

^bNational Institute of Chemical Physics and Biophysics, Tallinn, Estonia

^cInstitute of Physics, Tartu University, Tartu, Estonia

3 Results and discussion

In this chapter, the results of this thesis are presented and discussed. This chapter is divided into four sections according to the topics published in papers I, II, III, and IV.

3.1 Deposition of Sb_2S_3 thin films from SbCl_3/TU solutions by ultrasonic spray pyrolysis

Herein, the effect of deposition temperature, SbCl_3/TU molar ratio, and heat treatment on the phase composition, structure, elemental composition, optical properties, and morphology of Sb_2S_3 thin films grown by USP from SbCl_3/TU solutions was investigated. The results of this study are published in papers I and II.

Sb_2S_3 thin films were deposited at 200°C, 210°C, and 220°C at SbCl_3/TU molar ratios of 1/3 and 1/6 onto planar glass/ITO/ TiO_2 substrates by USP. In addition, heat treatment in vacuum was applied after deposition to crystallize the Sb_2S_3 thin films. Heat treatment at 200°C and 250°C in vacuum resulted in sublimation of Sb_2S_3 thin films [I]. Hence, heat treatment of Sb_2S_3 films was optimized to 170°C, $\approx 5 \cdot 10^{-4}$ Pa, 5 min. The deposition conditions and sample names are presented in Table 3.1.

Table 3.1. Labeling of Sb_2S_3 films grown by USP from SbCl_3/TU solutions. Substrate: glass/ITO/ TiO_2 . Heat treatment: 170°C, $\approx 5 \cdot 10^{-4}$ Pa, 5 min.

SbCl_3/TU in solution	Deposition temperature, °C	Sample name	
		As-grown	Heat treated
1/3	200	3-200	3-200-170
	210	3-210	3-210-170
	220	3-220	3-220-170
1/6	200	6-200	6-200-170
	210	6-210	6-210-170
	220	6-220	6-220-170

3.1.1 Phase composition and structure

The phase composition of as-grown and post-growth heat treated films was studied by Raman spectroscopy and XRD. The relative intensity of the Raman bands of Sb_2S_3 measured using a non-polarized laser source is not scrutinized in this thesis, as polarized Raman is required to obtain meaningful information [221].

Raman spectra of the films grown at 200°C (3-200; see paper I, Figure 1a) and 210°C (3-210; Figure 3.1a) contained a broad band centered at 290 cm^{-1} with a shoulder at 340 cm^{-1} , which is attributed to amorphous Sb_2S_3 [9], [116]. The band centered at 145 cm^{-1} is attributed to TiO_2 [9], [116]. Bands centered at 126, 155, 188, 237, 281, 301, and 310 cm^{-1} in the Raman spectrum of the sample (3-220) grown at 220°C matched orthorhombic Sb_2S_3 , according to literature [9], [116], [189]. After post deposition heat treatment, the Raman spectra of samples 3-200-170 (see paper I, Figure 1a), 3-210-170 and 3-220-170 (Figure 3.1a) also matched crystalline Sb_2S_3 .

The Raman spectrum of the as-grown film (6-200) deposited from $\text{SbCl}_3/\text{TU} = 1/6$ solution at 200°C matched amorphous Sb_2S_3 (Figure 3.1b), and bands attributed to crystalline Sb_2S_3 were detected in Raman spectra of the films grown at 210°C (6-210) and

220°C (6-220; see paper I, Figure 1b). The major difference compared to films grown from $\text{SbCl}_3/\text{TU} = 1/3$ solution was that crystallization occurred at 210°C during deposition and the intensity of the TiO_2 band was magnified in relation to the intensity of the Sb_2S_3 bands (Figure 3.1b). After heat treatment, only bands attributed to crystalline Sb_2S_3 were detected (6-200-170, 6-210-170). Notably, bands attributable to secondary phases were not detected by Raman in any of the studied samples, irrespective of the deposition conditions.

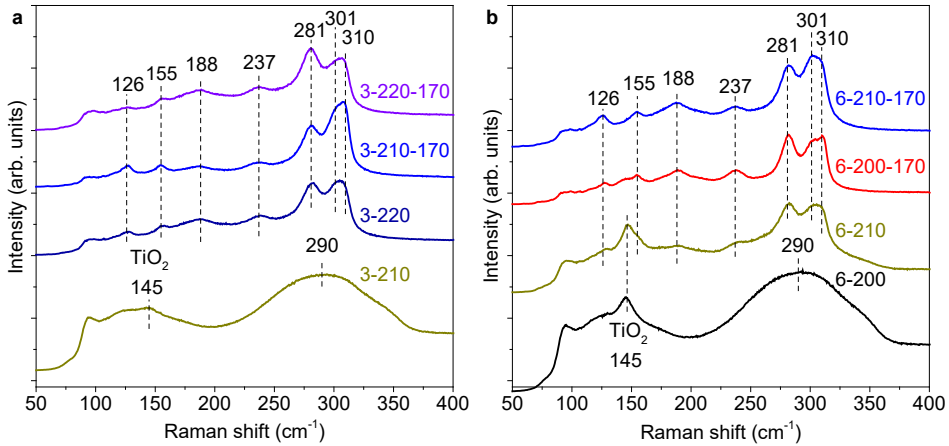


Figure 3.1. (a) Raman spectra of Sb_2S_3 thin films, (a) grown from $\text{SbCl}_3/\text{TU} = 1/3$ solution at a deposition temperature of 210°C and 220°C, or (b) from $\text{SbCl}_3/\text{TU} = 1/6$ solution at a deposition temperature of 200°C and 210°C, as-grown and after heat treatment. Substrate: glass/ITO/ TiO_2 . Post deposition heat treatment: 170°C, $\approx 5 \cdot 10^{-4}$ Pa, 5 min.

According to XRD, there were no crystalline Sb-phases in the as-grown films deposited at 200°C (3-200; see paper I, Figure 2a) and 210°C (3-210; Figure 3.2a) from $\text{SbCl}_3/\text{TU} = 1/3$ solution. After heat treatment of these samples in vacuum at 170°C, reflections attributed to crystalline Sb_2S_3 (ICDD 01-075-4012) were detected (3-200-170, paper I, Figure 2; 3-210-170, Figure 3.2a). Crystalline Sb_2S_3 was also detected in the thin film grown at 220°C (Figure 3.2a), both before (3-220) and after heat treatment (3-220-170), indicating that Sb_2S_3 crystallized during deposition.

Secondary phases were not detected by XRD in any of the analyzed samples. The relative intensity of reflections attributed to Sb_2S_3 in these samples was similar to the ratio in the ICDD 01-075-4012 powder reference file. As the deposition temperature was increased from 200°C to 220°C, mean crystallite size calculated from the full width at half maximum of the reflection of the (2 0 2) crystallographic plane increased in the heat treated films from 19 nm to 100 nm (see paper I, Table 2).

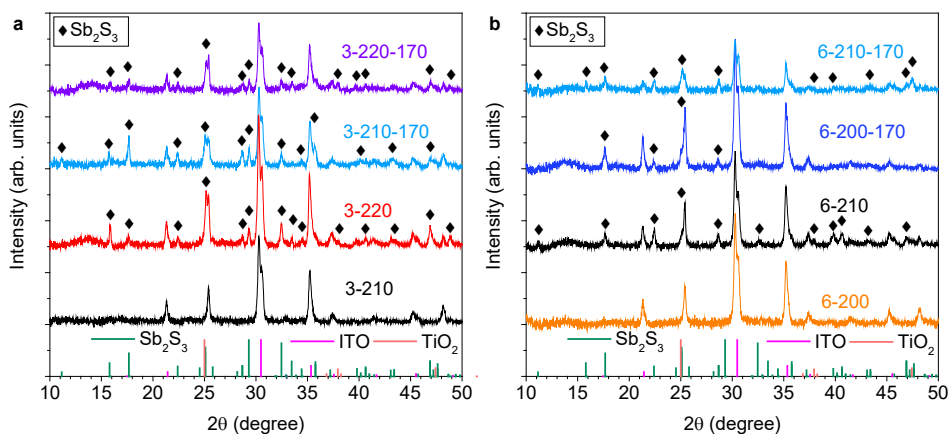


Figure 3.2. XRD patterns of as-grown and heat treated Sb_2S_3 thin films grown from (a) $SbCl_3/TU = 1/3$ solution at a deposition temperature of 210°C and 220°C, or from (b) $SbCl_3/TU = 1/6$ solution at a deposition temperature of 200°C and 210°C. Substrate: glass/ITO/ TiO_2 . Post deposition heat treatment: 170°C, $\approx 5 \cdot 10^{-4}$ Pa, 5 min.

The as-grown film deposited at 200°C (6-200; Figure 3.2b) from $SbCl_3/TU = 1/6$ solution did not contain any crystalline Sb-containing phases, whereas the heat treated film (6-200-170; Figure 3.2b) was composed of crystalline Sb_2S_3 , according to XRD. As-grown and heat treated films deposited at 210°C (6-210 & 6-210-170 in Figure 3.2b) and 220°C (6-220 & 6-220-170 in paper I, Figure 2b), contained crystalline Sb_2S_3 , based on XRD, indicating crystallization during deposition. Secondary phases were not detected by XRD in any of these samples. Mean crystallite size in heat treated Sb_2S_3 films, calculated from the reflection of the (2 0 2) crystallographic plane, increased from 37 nm to 49 nm (see paper I, Table 2) as the deposition temperature was increased from 200°C to 220°C.

Table 3.2. Phase composition by XRD and Raman, S/Sb calculated from EDX, and E_g calculated from UV-VIS of Sb_2S_3 thin films deposited by USP from $SbCl_3/TU$ 1/3 and 1/6 solutions.

SbCl ₃ /TU in soln.	Dep. temp., °C	Phase composition of as-deposited films ^a		S/Sb, at%/at%		E_g , eV	
		XRD	Raman	As-dep.	Heat treated	As-dep.	Heat treated
1/3	200	Amorph.	a-Sb ₂ S ₃	1.3	1.3	2.6	1.8
	210	Amorph.	a-Sb ₂ S ₃	1.3	1.3	2.7	1.8
	220	c-Sb ₂ S ₃	c-Sb ₂ S ₃	1.5	1.5	1.8	1.8
1/6	200	Amorph.	a-Sb ₂ S ₃	1.6	1.6	2.7	1.8
	210	c-Sb ₂ S ₃	c-Sb ₂ S ₃	1.5	1.6	1.8	1.8
	220	c-Sb ₂ S ₃	c-Sb ₂ S ₃	1.5	1.5	1.8	1.8

^aa-Sb₂S₃ – amorphous Sb₂S₃; c-Sb₂S₃ – crystalline Sb₂S₃.

According to Raman and XRD, as SbCl_3/TU in solution was increased from 1/3 to 1/6, crystalline Sb_2S_3 thin films were obtained at 220°C and 210°C, respectively. In a previous paper [9], Sb_2S_3 thin films grown at 250°C from a 15 mM $\text{SbCl}_3/\text{TU} = 1/3$ solution were amorphous–crystalline, whereas using $\text{SbCl}_3/\text{TU} = 1/6$ yielded separate grains of crystalline Sb_2S_3 . Hence, increasing the concentration of TU vs SbCl_3 in solution likely decreases the energy requirement for the amorphous-crystalline phase transition of Sb_2S_3 films during USP deposition. The phase composition of USP-grown Sb_2S_3 thin films, as measured by Raman and XRD, is summarized in Table 3.2.

3.1.2 Elemental composition

According to energy dispersive X-ray spectroscopy (EDX), the Sb_2S_3 thin films grown at 200°C and 210°C from $\text{SbCl}_3/\text{TU} = 1/3$ solution yielded an atomic ratio of $\text{S}/\text{Sb} = 1.3$ in as-grown state (Table 3.2), and after heat treatment. The Sb_2S_3 thin films grown at 220°C, however, yielded $\text{S}/\text{Sb} = 1.5$ before and after heat treatment. The increase of S/Sb from 1.3 to 1.5 as deposition temperature was increased from 210°C to 220°C could possibly be caused by the observed crystallization of Sb_2S_3 at 220°C during deposition.

The Sb_2S_3 thin films grown at 200°C from $\text{SbCl}_3/\text{TU} = 1/6$ solution yielded a composition of $\text{S}/\text{Sb} = 1.6$ before and after heat treatment. The Sb_2S_3 thin films grown at 210°C, and 220°C from the same solution yielded an atomic ratio of $\text{S}/\text{Sb} = 1.5$ –1.6, and 1.5, respectively. Increasing deposition temperature to 220°C caused S/Sb to approach stoichiometry in Sb_2S_3 thin films grown from either solution. Notably, heat treatment had no significant effect on S/Sb in any of the studied samples.

In comparison, an atomic ratio of $\text{S}/\text{Sb} = 1.28$ and 1.55 has been reported for Sb_2S_3 films grown by thermal co-evaporation [101]. Furthermore, an atomic ratio of $\text{S}/\text{Sb} = 1.38$, and 1.42 has been reported for amorphous, and crystalline Sb_2S_3 thin films, respectively, grown by thermal evaporation from a single Sb_2S_3 target [164].

Based on EDX measurements, the concentration of Cl and C in all of the USP-grown Sb_2S_3 thin films was below the detection limit. Notably, the fact that the atomic ratio of S/Sb in USP-grown Sb_2S_3 thin films is affected by SbCl_3/TU in solution and deposition temperature, but not by heat treatment, provides a robust input to regulate the atomic ratio of S/Sb in the composition of Sb_2S_3 thin films grown by USP.

In addition, soft X-ray emission spectroscopy (XES) was applied at the Advanced Light Source synchrotron center in California, USA, to probe the chemical bonding of Sb and S atoms in USP-grown Sb_2S_3 thin films (see paper II, Figure 2). The XES spectra of 50 nm thick Sb_2S_3 films grown from $\text{SbCl}_3/\text{TU} = 1/3$ and 1/6 solutions, in as-grown, and heat treated state (vacuum, 170°C or flowing N_2 , 300°C), with and without the ITO layer, were measured. The penetrating depth of the XES beam exceeded the thickness of the USP-grown Sb_2S_3 thin films. Therefore, the entire thickness of the Sb_2S_3 thin films was probed.

According to $\text{S } L_{2,3}$ XES data, the center positions of the main transitions, designated as “ $\text{S } 3s$ ” (147.5 eV), “ $\text{Sb } 5s$ ” (151 eV), and “upper valence band” (156 eV), were constant for all measured samples, independent of the atomic ratio of S/Sb calculated from EDX. Moreover, XES data proved that the chemical bonding of Sb and S was similar in the studied Sb_2S_3 thin films. Hence, only the spectrum corresponding to a post deposition heat treated sample grown from $\text{SbCl}_3/\text{TU} = 1/3$ solution at 220°C is shown in paper II, Figure 2. In addition, the presence of S-O bonds was not detected by XES in any of the measured samples.

3.1.3 Optical properties

According to UV-VIS absorption coefficient calculations, the as-grown amorphous Sb_2S_3 thin films yielded a direct band gap (E_g) = 2.6–2.7 eV (see paper I, Table 5) and $\alpha = 10^5 \text{ cm}^{-1}$ at 400 nm wavelength (see paper I, Figure 7a,b), independent of deposition conditions. Samples containing crystalline Sb_2S_3 yielded a direct $E_g = 1.8$ eV and $\alpha = 10^5 \text{ cm}^{-1}$ at 650 nm wavelength (see paper I, Table 5), which is suitable for a thin film PV absorber layer. In literature, a direct $E_g = 1.91$ –2.48 eV has been reported for amorphous Sb_2S_3 thin films [164], [195], [222], and a direct $E_g = 1.6$ –1.78 eV for crystalline Sb_2S_3 thin films (see section 1.5, Table 1.1). Accordingly, the results reported herein are consistent with literature.

3.1.4 Morphology

The morphology of the entire series of Sb_2S_3 thin films is discussed in papers I and II. Here, the ultimate goal was to obtain uniform continuous Sb_2S_3 thin films. The amorphous Sb_2S_3 thin films grown at 200°C (3-200) and 210°C (3-210; Figure 3.3a, c) from $\text{SbCl}_3/\text{TU} = 1/3$ solution had almost entirely coalesced into a continuous film at a film thickness of ≈ 70 –90 nm.

Heat treatment of the amorphous as-grown Sb_2S_3 thin film (3-210) caused the Sb_2S_3 to distribute into a continuous coating (3-210-170; Figure 3.3b, d), yielding an average lateral grain size $\approx 10 \mu\text{m}$ (see paper II, Figure 1b). By 220°C, the growth mechanism had changed, as domains of separate Sb_2S_3 grains oriented at various angles were seen protruding from the substrate in SEM images (see paper I, Figure 3i, j).

The amorphous Sb_2S_3 thin film grown at 200°C from $\text{SbCl}_3/\text{TU} = 1/6$ solution (6-200; see Figure 3.3e, g) was thinner (50–70 nm) than the 1/3 counterpart (3-200), leaving the underlying TiO_2 film more exposed due to a shortage of material. The Sb_2S_3 thin film grown at 210°C (6-210) was also discontinuous, and consisted partially of ≈ 400 nm thick pyramidal agglomerated grains (see paper I, Figure S5c, d). Increasing the deposition temperature to 220°C (6-220) resulted in slanted or vertically aligned crystalline Sb_2S_3 grains without horizontal grain boundaries (see paper I, Figure 3e, f), which were separated by voids in the top-down view.

Heat treatment of the amorphous Sb_2S_3 thin film (6-200; Figure 3.3f, h) flattened the surface of the film, but uncovered areas remained because there was not enough Sb_2S_3 to form a continuous film. Thus, uniform Sb_2S_3 thin films could likely be grown by USP at 200°C from $\text{SbCl}_3/\text{TU} = 1/6$ solution if the deposition time is prolonged or the precursor concentration is increased sufficiently to fill in voids. That would be attainable at a film thickness of ≈ 80 –90 nm, while ensuring that the amorphous state of Sb_2S_3 thin films is sustained during deposition.

In conclusion, the aim to deposit uniform phase pure Sb_2S_3 thin films was fulfilled by a two-step process. First, an amorphous film of Sb_2S_3 , free of Cl, C, and secondary phases to detectable limits, was grown by USP in air at 200°C or 210°C from $\text{SbCl}_3/\text{TU} = 1/3$ solution. Second, the film was crystallized by heat treatment in vacuum at 170°C.

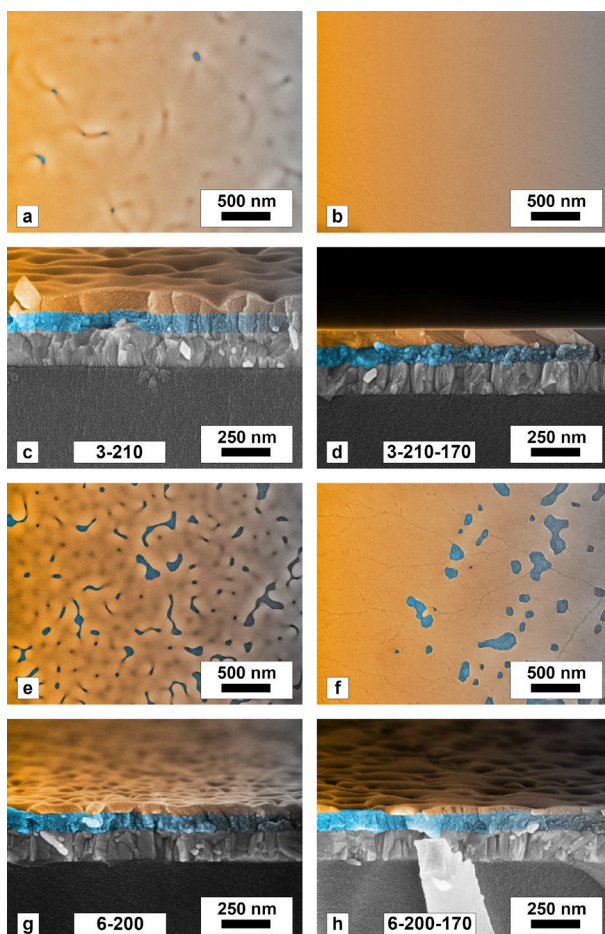


Figure 3.3. Top-down and cross-section SEM views of as-grown and heat treated Sb_2S_3 thin films. (a, c) As-grown, and (b, d) heat treated Sb_2S_3 thin film deposited at 210°C from $\text{SbCl}_3/\text{TU} = 1/3$ solution. (e, g) As-grown, and (f, h) heat treated Sb_2S_3 thin film deposited at 200°C from $\text{SbCl}_3/\text{TU} = 1/6$ solution. Post deposition heat treatment: 170°C , $\approx 5 \cdot 10^{-4}$ Pa, 5 min. Substrate: glass/ITO/ TiO_2 .

3.1.5 Growth mechanism of Sb_2S_3 thin films on a planar substrate

Sb_2S_3 thin films deposited by USP from SbCl_3/TU solutions were determined to grow via the Volmer-Weber island growth mechanism (see paper I). Moreover, this is the only growth mechanism wherein the substrate is not entirely covered by a seed layer of the deposited material after the height of the growing clusters exceeds a few nm. In addition, films of materials that wet the substrate poorly, for various reasons, generally grow by the island growth mechanism. Therefore, in order to prepare uniform coatings of Sb_2S_3 , the deposited film must have a thickness exceeding a threshold value (70–90 nm in case of USP of SbCl_3/TU solution; Figure 3.3c, d, g, h) to allow the growing nuclei to coalesce.

The surface and cross-sectional views, by SEM, presented in Figure 3.3a–h, show that as thickness increases (see route A in Figure 3.4), the round amorphous Sb_2S_3 islands spread (step A1) until the entire substrate is covered (step A2), effectively eliminating pinholes and voids in the film. Afterwards, leaner sections are filled in until the film thickness equalizes (step A-3). The synthesis route of depositing an amorphous Sb_2S_3

layer until full coverage of the substrate is attained, followed by crystallization after deposition, led to the required continuous morphology. Alternatively, if the Sb_2S_3 thin film crystallizes during deposition, separate slanted grains are formed (route B in Figure 3.4).

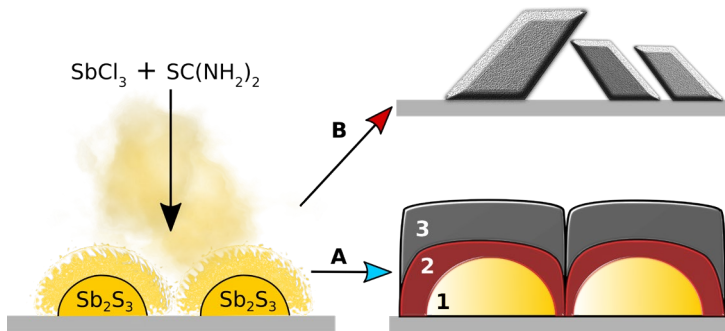


Figure 3.4. Proposed growth mechanism of Sb_2S_3 films by USP from SbCl_3/TU solution. After the liquid SbCl_3/TU mixture decomposes into Sb_2S_3 , the islands of amorphous Sb_2S_3 (A) grow on the substrate (1) until they coalesce and fill in voids (2), resulting in a continuous planar film at a thickness of 70–90 nm after crystallization (3). (B) In case the Sb_2S_3 thin film crystallizes during deposition, separate grains are formed.

In literature, Sb_2S_3 thin films have predominantly formed via the island growth mechanism on planar substrates when grown by chemical [116], [181], [223] and physical deposition methods [224], [225].

According to the results presented in Table 3.2 and the views by SEM, achieving a uniform phase pure Sb_2S_3 thin film by USP has laid the foundation for the preparation of efficient planar Sb_2S_3 thin film solar cells.

3.1.6 Summary

To conclude, uniform and continuous Sb_2S_3 thin films, free of Cl, C, and secondary phases to the detection limit of the applied characterization techniques, were prepared by USP in air. The route to prepare these films involved the deposition of an amorphous Sb_2S_3 thin film with a thickness of 70–90 nm from a solution of $\text{SbCl}_3/\text{TU} = 1/3$ at 200–210°C. Thereafter, heat treatment in high vacuum at 170°C yielded crystalline Sb_2S_3 films with $E_g = 1.8$ eV, $S/\text{Sb} = 1.3$, and average lateral grain size $\approx 10 \mu\text{m}$.

In case of spraying the $\text{SbCl}_3/\text{TU} = 1/6$ solution at 200°C, the film thickness was not sufficient to achieve full coverage in the same procedure, although $S/\text{Sb} = 1.6$ was obtained instead. In general, films deposited from $\text{SbCl}_3/\text{TU} = 1/6$ solution showed close to stoichiometric composition.

Sb_2S_3 thin films were determined to form by the 3D Volmer-Weber growth mechanism when deposited by USP. Furthermore, it was proven that directly depositing crystalline Sb_2S_3 thin films results in the incomplete coverage of the substrate by preferentially vertically growing separate Sb_2S_3 grains. The onset of crystallization decreased from 220°C for $\text{SbCl}_3/\text{TU} = 1/3$ solution to 210°C for $\text{SbCl}_3/\text{TU} = 1/6$ likely due to an interaction resulting from the additional mass of liquid TU residing at the surface of the substrate during deposition.

3.2 Application of Sb_2S_3 thin films grown by ultrasonic spray pyrolysis in planar thin film solar cells

The Sb_2S_3 thin films deposited by USP from $\text{SbCl}_3/\text{TU} = 1/3$ solution were tested in planar glass/ITO/ TiO_2 / Sb_2S_3 /P3HT/Au solar cells. The results of this study are published in paper II. Solar cells were prepared based on 30 nm, 70 nm, 100 nm, and 150 nm thick Sb_2S_3 films, as estimated by SEM, grown onto glass/ITO/ TiO_2 substrates at the optimized conditions ($\text{SbCl}_3/\text{TU} = 1/3$, USP at 200°C, heat treatment at 170°C in vacuum, [II]). After capping the stack with P3HT/Au, the solar cells were tested for PV performance as a function of absorber thickness, cell area, storage time, and light intensity.

3.2.1 Influence of Sb_2S_3 film thickness on PV performance of solar cells

The solar cell stack is illustrated in Figure 3.5a. The cross-section of the most efficient solar cell with a 100 nm thick Sb_2S_3 film is presented in Figure 3.5b, and the photograph of a comparable back-contact-less glass/ITO/ TiO_2 / Sb_2S_3 stack is presented in Figure 3.5c.

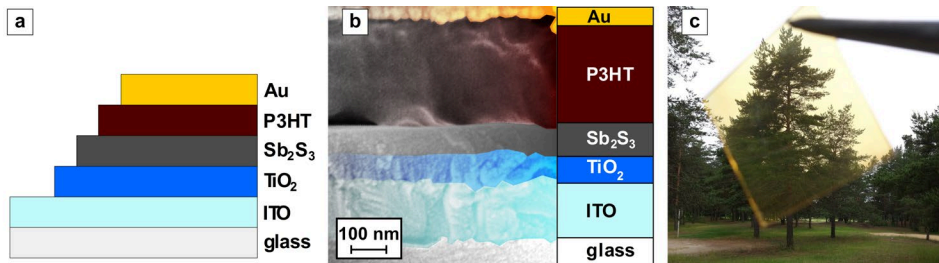


Figure 3.5. (a) Solar cell configuration. (b) SEM cross-section image of the best cell. (c) Photograph of a 100 nm thick crystalline Sb_2S_3 film on a 25 cm² square glass/ITO/ TiO_2 substrate.

Inspection of the J - V scans of the best cell at each absorber thickness (Figure 3.6a) reveals a parabolic trend, as $\eta = 1.6\%$ (30 nm), 4.4% (70 nm), 4.7% (100 nm absorber, cross section in Figure 3.6b), and 2.0% (150 nm) was achieved. Regarding transparency, as the thickness of the Sb_2S_3 film in the glass/ITO/ TiO_2 / Sb_2S_3 stack was increased from 70 nm to 100 nm (photograph in Figure 3.5c), and to 150 nm, the AVT of the back-contact-less stack decreased from 28% to 26%, and 16%, respectively (Figure 3.6b). Therefore, as $\text{AVT} \geq 20\%$ is required, solar cells with a 70–100 nm thick USP- Sb_2S_3 film would provide the optimal combination of η and AVT for semitransparent PV applications. Although, reduction of AVT is expected due to the back contact, as shown in ref. [197].

In literature, $\eta = 3.4\%$ and $\text{AVT} = 13\%$ for the complete stack was achieved with a planar solar cell of glass/ITO/30 nm TiO_2 /85 nm Sb_2S_3 /30 nm P3HT/10 nm Au, wherein Sb_2S_3 had been deposited by ALD [197].

The shape and magnitude of EQE provides insight on the spectral carrier collection efficiency in solar cells. The EQE spectra of the best solar cells with a 70 nm, 100 nm, and 150 nm thick Sb_2S_3 film (Figure 3.6b) convey that EQE decreases at longer wavelengths for solar cells with a 70 nm or 100 nm thick Sb_2S_3 film, and is level in the 350–650 nm wavelength range at an absorber thickness of 150 nm. EQE onset at 750 nm in all samples indicates $E_g \approx 1.65$ eV for the Sb_2S_3 film. In addition, the wavy shape of EQE at 350–500 nm wavelength is attributed to optical interference from ITO, TiO_2 and Sb_2S_3 in the solar cell stack, and to the parasitic absorption in P3HT at 500–650 nm wavelength, as described in ref. [137] and paper II, Figure 3c.

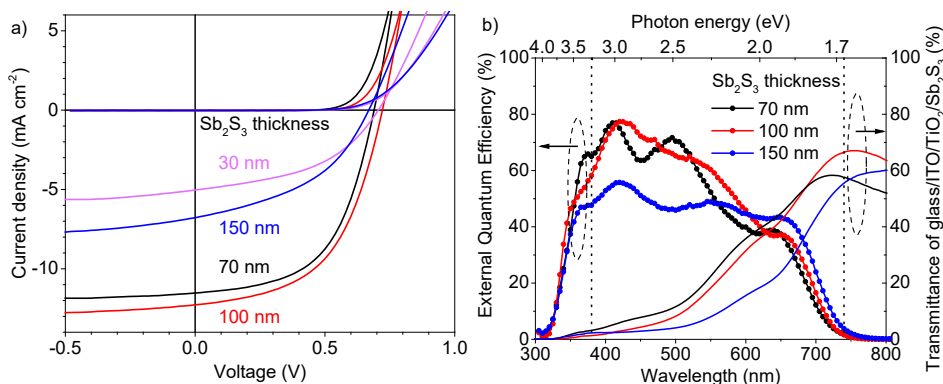


Figure 3.6. (a) Dark and light J - V curves of planar glass/ITO/TiO₂/Sb₂S₃/P3HT/Au solar cells with a 30, 70, 100, and 150 nm thick USP-grown Sb₂S₃ absorber layer. (b) EQE of solar cells and transmittance of glass/ITO/TiO₂/Sb₂S₃ reference samples with equivalent absorber thickness.

The increase in EQE at 550–750 nm wavelength is probably the result of increased light absorption capability in the 150 nm thick absorber. The simultaneous decrease in EQE at 350–550 nm wavelength could be partially caused by a decreased photogenerated hole diffusion capability from the region of the absorber near TiO₂ to the Sb₂S₃/P3HT interface. A decrease in EQE at 350–550 nm was reported for ALD-Sb₂S₃ based planar FTO/TiO₂/ZnS/Sb₂S₃/P3HT/Au solar cells after increasing absorber thickness from 90 nm to 162 nm, stating that the diffusion length of photogenerated holes is insufficient in thicker Sb₂S₃ films [148]. In a report on planar FTO/TiO₂/ALD-Sb₂S₃/P3HT/PEDOT:PSS/Au solar cells, EQE decreased at 350–550 nm to a value lower than at 550–750 nm wavelength when the absorber thickness had been increased from 90 nm to 120 nm [8]. Hence, the EQE results presented herein are consistent with literature.

Reduced carrier collection efficiency at longer wavelengths, as observed in the EQE spectra of the solar cells based on a 70 nm or a 100 nm thick USP-grown Sb₂S₃ film, has been generally linked to a limited lifetime of holes in the absorber bulk in thin film solar cells [12]. A flat low response at all wavelengths, as seen in the EQE spectrum of the solar cell based on a 150 nm thick USP-grown Sb₂S₃ film, has been associated with a high series resistance or a back contact barrier [12]. Furthermore, if the carrier concentration in the absorber is low (10^{12} cm⁻³ for CBD-Sb₂S₃ films [94] vs $\approx 10^{16}$ – 10^{17} cm⁻³ for CdTe, CIGS), a flat low response in EQE has also been ascribed to a detrimentally long drift distance for photogenerated electrons and holes in the absorber [12].

According to J - V scans (Table 3.3), average V_{oc} was similar (670–704 mV) when the absorber thickness was 30–100 nm, and decreased to 638 mV at an absorber thickness of 150 nm. As the absorber thickness was increased from 30 nm to 100 nm, average J_{sc} increased proportionally to 10.3 mA cm⁻² due to increased photogeneration capability in the absorber. Average J_{sc} was two times smaller at 150 nm vs 100 nm absorber thickness due to the three times larger R_s , in turn caused by the increased thickness of the resistive ($\rho = 2\text{--}3 \cdot 10^6$ Ω cm² in dark) Sb₂S₃ absorber. FF was optimal (57 %) at 70 nm absorber thickness due to the smallest R_s (7.4 Ω cm²) in combination with the largest R_{sh} (2.2 k Ω cm²). Less optimal R_s and R_{sh} at other absorber thicknesses resulted in a proportionally reduced FF . Consequently, average η peaked at 3.7 % in solar cells with a 100 nm thick Sb₂S₃ absorber.

Table 3.3. Solar cell output parameters depending on Sb_2S_3 film thickness.^a

Sb_2S_3 thickness, nm		V_{oc} , mV	J_{sc} , mA cm ⁻²	FF, %	η , %	R_s , Ω cm ²	R_{sh} , k Ω cm ²	No. of cells
30	Avg.	704±7 ^b	4.8±0.3	43±3	1.5±0.1	14±2.1	0.5±0.1	8
	Best	705	5.0	46	1.6	18	0.6	
70	Avg.	670±8	7.5±0.6	57±4	2.9±0.2	7.4±0.6	2.2±1.0	9
	Best	691	11.5	55	4.4	6.0	1.1	
100	Avg.	693±17	10.3±1.0	52±3	3.7±0.4	7.6±1.5	0.9±0.3	36
	Best	726	12.3	52	4.7	5.9	0.7	
150	Avg.	638±16	4.3±1.1	44±1	1.2±0.3	26±5.2	0.7±0.2	8
	Best	669	6.9	43	2.0	19	0.4	

^aMeasurement conditions: 100 mW cm⁻²; AM1.5G, Xe light source; cell area 7.1 mm².

^bStandard deviation.

3.2.2 Influence of cell area, storage time and light intensity on PV performance of Sb_2S_3 solar cells

The effect of varying cell area on the PV performance parameters of USP- Sb_2S_3 thin film solar cells was investigated to assess the area scalability of USP- Sb_2S_3 solar cells, and to identify any potential shortcomings that could be addressed in later investigations. Solar cells were fabricated with a back contact area ranging from 1.7 to 180 mm². The respective PV performance parameters were characterized via *J-V* scans in dark, and under light at AM1.5G (Figure 3.7a).

Increasing cell area caused V_{oc} , J_{sc} , FF, and η to decrease linearly, whereas R_s increased linearly. The best cells of 1.7 mm², 7.1 mm² area, and the singular cells of 88 mm² and 180 mm² area yielded η = 5.5 %, 4.7 %, 3.2 %, and 1.5 %. It is noteworthy that a threefold increase was achieved compared to the previous best for USP- Sb_2S_3 solar cells of a comparable area of 1.7 mm² and 100 mm² (see section 1.5, Table 1.1).

The decrease in PV parameter values as cell area is increased to 88 mm² and beyond is likely related to deviations in film uniformity and thickness of TiO₂, Sb_2S_3 , and P3HT, which is not as noticeable for contacts smaller than 10 mm². Decreased PV performance at a larger solar cell area is a common issue for emerging and commercial PV alike [14], [41]. Thus, further research is required to optimize performance of USP- Sb_2S_3 solar cells via tuning of the film uniformity, thickness, and properties of all constituent layers.

Solar cells must withstand operation in fluctuating weather conditions for decades. Thus, it is instrumental to identify and solve any design flaws before committing to any particular cell architecture. Therefore, the impact of storage time on the PV performance parameters of a USP- Sb_2S_3 solar cell of 88 mm² area was studied as a first approximation (see paper II, Figure 6). The unencapsulated cell was stored in ambient office conditions regulated by automated ventilation and air conditioning, and was exposed to cycles of fluorescent tube light and sunlight in V_{oc} condition.

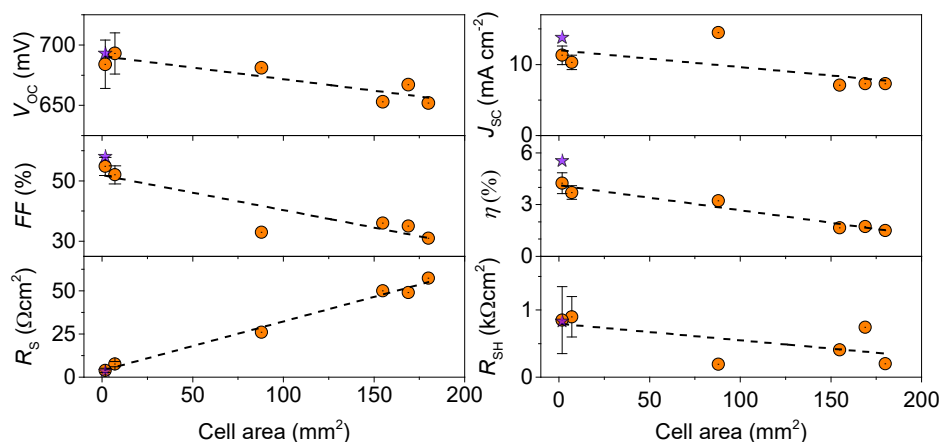


Figure 3.7. Effect of cell area on the photoconversion parameters of planar ITO/TiO₂/Sb₂S₃/P3HT/Au solar cells. Measurement: (a) Xe, AM1.5G, cell area 7.1 mm². The lines are linear fits on the shown axes. The violet star marks the best device and the error bars represent standard deviation.

In the span of one year in storage, V_{oc} remained stable, J_{sc} decayed linearly ($-0.014 \text{ mA cm}^{-2} \text{ d}^{-1}$) as R_s increased linearly over time, whereas R_{sh} was constant. The cell gained FF at 0.0078 \% d^{-1} , and η decayed from 3.2 \% at 0.0024 \% d^{-1} . In comparison, planar FTO/TiO₂/spin coated Sb₂S₃/spiro-OMeTAD/Au cells ($\eta = 4.3 \text{ \%}$, area 10 mm^2) kept in dark in dry N₂ at room temperature without encapsulation lost η at 0.026 \% d^{-1} on average in 100 days [145]. Moreover, planar FTO/TiO₂/spin coated Sb₂S₃/spiro-OMeTAD/Au cells ($\eta = 4.2 \text{ \%}$, area 10 mm^2) stored in dark in air at room temperature, RH 85 %, without encapsulation lost η at a rate of 0.074 \% d^{-1} on average in 45 days [147]. Therefore, leaving aside the different unstandardized storage conditions and preparation procedures, the USP-based cell appears to decay at least ≈ 10 times slower than the aforementioned solar cells based on a spin coated Sb₂S₃ absorber.

According to literature, efforts are underway to stabilize η of Sb₂S₃ solar cells via e.g. post-growth selenization of the Sb₂S₃ film [139], SbCl₃ treatment of the Sb₂S₃ film [147], or zinc halide treatment of the TiO₂ layer [145]. In retrospect of these studies, device stability clearly depends on the passivation of the ETL/Sb₂S₃ and Sb₂S₃/HTL interfaces. Thus, further studies are required to achieve long-term stability for Sb₂S₃ solar cells.

In order to evaluate the effect of daily variations in sunlight on PV performance parameters, the J - V curve of a freshly prepared ITO/TiO₂/USP-Sb₂S₃/P3HT/Au solar cell was measured at 3 – 100 mW cm^{-2} light intensity (see paper II, Figure 7).

The observed increase in η at reduced light intensity for the solar cell is mainly due to the relative increase in J_{sc} , and FF. The increase in FF is caused by increased R_{sh} , as R_s was constant. Light intensity dependent R_{sh} is characteristic to Sb₂S₃ based solar cells [6], [66], [97], [147], and is likely accentuated by the presence of the photosensitive P3HT layer [226].

The increased performance in dim light with or without the organic HTL emphasizes the prospect of installing Sb₂S₃ solar cells in regions shrouded by clouds, where light intensity is mostly below 100 mW cm^{-2} . Namely, according to satellite imagery, 67 % of the Earth is generally under cloud cover, and on average 55 % of land is covered by clouds [227]. Thus, developing PV dedicated to operation at reduced light intensity could be a target application for USP-Sb₂S₃ based solar cells.

3.2.3 Summary

As a proof of concept, it was demonstrated that a planar USP-Sb₂S₃ solar cell with $\eta = 5.5\%$ (1.7 cm²), 4.7% (7.1 mm²), and 3.2% (88 mm²) is achievable with a 100 nm thick USP-grown Sb₂S₃ thin film absorber by applying a two-step process to grow continuous phase pure Sb₂S₃ thin films. Thereby, it was proven that it is possible to prepare USP-Sb₂S₃ based solar cells that are comparable to in PV performance to the most efficient solar cells in literature.

Furthermore, the high resistivity of USP-grown Sb₂S₃ thin films manifested at a thickness of 150 nm, causing η of solar cells to decrease. Resistivity of the absorber could be reduced to a reasonable value via doping and grain growth engineering in the future.

The stack of glass/ITO/TiO₂/USP-Sb₂S₃ yielded AVT = 26% at an absorber thickness of 100 nm, proving that USP-Sb₂S₃ based solar cells are potentially applicable for semitransparent applications if combined with a suitably transparent back contact.

Increasing the cell area resulted in a steady loss of η likely due to variations in the thickness of the TiO₂, Sb₂S₃, and P3HT films. Finding the exact causes requires continued investigation, and optimization of the optoelectronic properties and morphology of the bulk phase and interfaces between the component layers.

The decay of η over time of the 88 mm² USP-Sb₂S₃ solar cell was ≈ 10 times slower compared to the degradation reported for solar cells based on a spin coated Sb₂S₃ film and spiro-OMeTAD, although the storage conditions were different in each study.

The magnified η of the ITO/TiO₂/USP-Sb₂S₃/P3HT/Au solar cell at light intensity below 100 mW cm⁻² indicates that this type of solar cell could be especially suitable for application in conditions where reduced intensity of sunlight or diffuse light is prevalent. Although, more comprehensive investigation is required to discover the origin of this phenomenon.

3.3 Thermal analysis of SbEX as an alternative precursor for depositing Sb₂S₃ thin films

In order to investigate the possibility of depositing uniform phase pure Sb₂S₃ thin films by USP from a halogenide-free precursor solution, reagents fitting the description were screened according to the conditions set in section 1.7.3. Moreover, as the lower limit for depositing Sb₂S₃ thin films from the SbCl₃/TU solution was $\approx 200^{\circ}\text{C}$, precursors that would decompose below 200°C were considered. A melting point of $\approx 70^{\circ}\text{C}$ and total decomposition into Sb₂S₃ at $\approx 160^{\circ}\text{C}$ had been reported for antimony ethyl xanthate (Sb(S₂COCH₂CH₃)₃; SbEX) [183]. SbEX was selected because its decomposition temperature was lower than for any other compound under consideration.

Notably, the thermal decomposition of SbEX had not been studied by thermal analysis combined with online *in situ* evolved gas analysis and intermediate solid decomposition product analysis. Thus, a TG/DTA-EGA-MS analysis was undertaken to definitively describe the thermal decomposition of SbEX in an inert and an oxidizing atmosphere. The results of this study are published in paper III.

3.3.1 Synthesis and identification of SbEX

The phase composition and purity of the SbEX powder synthesized in this study was determined by FTIR, Raman, nuclear magnetic resonance spectroscopy (NMR), EDX, and XRD. According to FTIR (see paper III, Figure 1, Table S1), several vibrational bands attributed to the functional groups of the EX ligand were detected. Bands attributed to SbEX were also detected by Raman (see paper III, Figure S1). According to qualitative 1D and 2D NMR, chemical shift values attributed to the functional groups in the sequence of S₂COCH₂CH₃, i.e. the EX ligand, were detected (see paper III, Table 1). According to quantitative ¹H(CH₂) NMR, the powder contained 95 mol% SbEX (see paper III, Table 2). An atomic ratio of S/Sb of 5.7 ± 0.1 (expected 6.0) was calculated from EDX data. The remainder was attributed to amorphous Sb₂S₃ based on Raman data. The XRD pattern of the synthesized powder matched the reference pattern of SbEX [228]. Thus, according to the combined data from FTIR, Raman, NMR, EDX, and XRD measurements, the composition of the substance was 95 mol% SbEX and 5 mol% amorphous Sb₂S₃.

3.3.2 Thermal analysis of SbEX

SbEX decomposed thermally in the temperature range of $90\text{--}800^{\circ}\text{C}$ in argon atmosphere in three steps or at $90\text{--}590^{\circ}\text{C}$ in air atmosphere in four steps. After melting at 85°C , SbEX decomposed into Sb₂S₃ in an endothermic decomposition step at $90\text{--}170^{\circ}\text{C}$ in argon (Figure 3.8a) and air (Figure 3.8b) atmosphere. A second, exothermic step occurred at $170\text{--}250^{\circ}\text{C}$ in both atmospheres that purified Sb₂S₃ from decomposition residues and crystallized it. In the first and second decomposition step, the evolution of CS₂, C₂H₅OH, CO, CO₂, COS, H₂O, and minor gases was detected proportionally to the mass loss of 66.3 % vs 2.1 % in argon, and 61.1 % vs 2.1 % in synthetic air (Table 3.4). Consequently, the proof provided in this study refutes a part of the explanation given for the thermal analysis of SbEX in two publications, wherein the mass loss in the second decomposition step has been unfoundedly attributed to the evolution of sulfur vapors [205], [219].

Furthermore, in argon atmosphere, the mass of Sb₂S₃ derived from SbEX remained stable until the characteristic melting point of Sb₂S₃ = 550°C , which reaffirmed the phase purity of Sb₂S₃ formed from SbEX. In argon atmosphere, the third decomposition step started at 590°C , ending with the total mass loss of the remaining material.

In air atmosphere, Raman analysis of the Sb_2S_3 product obtained at 170°C from SbEX confirmed oxidation of Sb_2S_3 in the form of Sb_2O_3 . In air atmosphere, the third decomposition step proceeded at $250\text{--}495^\circ\text{C}$ with an exothermic peak at 365°C . In addition, evolution of SO_2 was detected by EGA-MS in that step. The residue at the end of the third decomposition step in air was Sb_2O_4 , according to XRD. Heating SbEX to 350°C in air resulted in the formation of crystalline sulfates and oxides, according to XRD. In the fourth decomposition step in air in the range of $495\text{--}595^\circ\text{C}$ with an exothermic peak at 570°C , SO_2 continued to evolve. The residue at the end of the fourth decomposition step in air was Sb_2O_4 , according to XRD.

The main thermal decomposition reactions of SbEX are described in paper III, Scheme 1, according to EGA-MS data recorded in Ar and air (see paper III, Figure 3a-i), and according to FTIR data of intermediate solid decomposition products heated at 115°C , and 160°C in either N_2 or air (see paper III, Figure 4a, b).

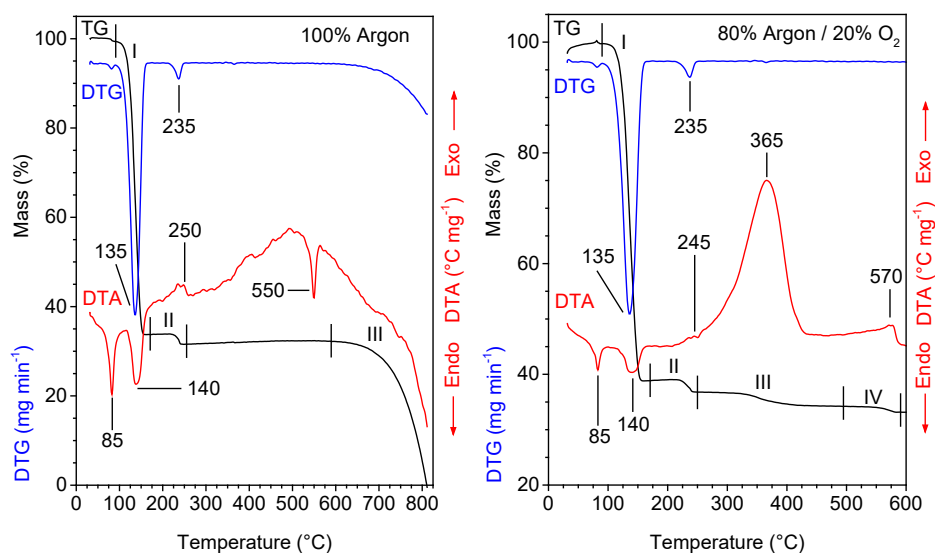


Figure 3.8. Thermal analysis curves (TG, DTG, DTA) of the SbEX powder in (a) argon (initial mass 11.6 mg), and (b) 80% argon / 20% oxygen (initial mass 13.9 mg). Gas flow: 60 mL min^{-1} . Measurement: *in situ* online coupled TG/DTA-MS system.

3.3.3 Summary

According to the TG/DTA-EGA-MS measurement results, SbEX decomposed thermally in the temperature range of $90\text{--}800^\circ\text{C}$ in argon atmosphere in three steps or at $90\text{--}590^\circ\text{C}$ in air atmosphere in four steps. In argon and air, SbEX decomposed by 170°C into amorphous Sb_2S_3 , according to Raman, and evolution of CS_2 , $\text{C}_2\text{H}_5\text{OH}$, CO , CO_2 , COS , H_2O was detected by EGA-MS. A second endothermic step occurred at $170\text{--}255^\circ\text{C}$ in argon, and $170\text{--}250^\circ\text{C}$ in air, accompanied by the evolution of the same gases as in the first step. However, Sb_2O_3 was additionally detected by Raman in the intermediate product exposed to 170°C in air. The Sb_2S_3 formed from SbEX in argon remained stable until its melting point of 550°C . At temperatures above 270°C in air, oxidation of Sb_2S_3 continued, resulting in Sb_2O_4 at 590°C . Thus, in principle, SbEX is considered a prospective and novel precursor for the preparation of Sb_2S_3 in air at around 170°C . In addition, as Sb_2S_3 is expected to oxidize at around 170°C , a method to prevent oxidation is required.

Table 3.4. Thermal decomposition steps, mass losses, DTA and DTG peak temperatures, evolved gases, and phase composition of SbEX and its decomposition products heated in inert or air atmosphere. TG/DTA-MS data recorded at a heating rate of $10^{\circ}\text{C min}^{-1}$ with open Al_2O_3 crucible.

Atmosphere ^a	Step	Temp. range, °C	Mass loss at end of step, %	DTA peak temp., °C	DTG peak temp., °C	Evolved gases by EGA-MS ^b	Intermediate decomposition product	
							Synth. temp., °C	Phase composition by XRD
Inert	Melt	70–90	0	85 endo	-		Initial	SbEX
	1	90–170	66.3	140 endo	135	CS₂, EtOH, CO, CO₂, COS, H₂O, EtSH, SO ₂	115	SbEX
		170	-					
	2	170–255	68.4	235 exo, 250 exo	240	270	Sb ₂ S ₃	
3	590–800	100	-	-	-	730	Sb ₂ S ₃ , Sb	
Air	Melt	70–90	0	85 endo	-		Initial	SbEX
	1	90–170	61.1	140 endo	135	CS₂, EtOH, CO, CO₂, COS, H₂O, EtSH, SO ₂	115	SbEX
		170	-					
	2	170–250	63.2	235 exo, 245 exo	235	270	Sb ₂ S ₃	
	3	250–495	65.8	365 exo	350	SO ₂	350	Sb ₂ (S ₂ O ₇) ₃ , Sb ₂ S ₃ , Sb ₂ O ₄
4	495–590	66.8	570 exo	570	SO ₂	600	Sb ₂ O ₄	

^aAr or 80 % Ar / 20 % O₂ for thermal analysis, N₂ or air for intermediate solid decomposition product analysis.

^bMajor gases in bold.

3.4 Deposition of Sb₂S₃ thin films from SbEX solutions by ultrasonic spray pyrolysis

Solutions of antimony ethyl xanthate (SbEX), and SbEX with thiourea (TU) or thioacetamide (TA) were used at different deposition temperatures with the aim to deposit uniform and conformal phase pure Sb₂S₃ thin films by USP. The results of this study are published in paper IV.

3.4.1 Deposition of Sb₂S₃ films from SbEX solution

Films were grown from a solution of SbEX by USP at 105°C, 135°C, and 165°C in air on a glass/ITO/TiO₂ substrate (Table 3.5). Some films were then heat treated at 225°C, 2·10⁻¹ Pa. At first, deposition at 105°C was pursued to determine whether the synthesis route from SbEX film to crystalline Sb₂S₃ film would yield a pure phase. A thin film of SbEX was grown at 105°C. Heat treatment converted the film into orthorhombic Sb₂S₃, according to XRD and Raman data (Table 3.5). Analysis of this sample by FTIR revealed bands positioned at 1025 cm⁻¹ and 1225 cm⁻¹, attributed to vibrations of SbEX. As presence of SbEX in the heat treated film is contrary to the aim of the thesis, these films were excluded from further discussion.

Table 3.5. Phase composition (XRD, Raman, FTIR) of films deposited from SbEX solution by USP. Substrate: glass/ITO/TiO₂. Heat treatment: 225°C, 2·10⁻¹ Pa, 30 min.

Deposition temperature, °C	Film state	Phase composition		
		XRD	Raman	FTIR
105	As-grown	SbEX	SbEX	SbEX
	Heat treated	Sb ₂ S ₃	Sb ₂ S ₃	SbEX
135	As-grown	–	amorph. Sb ₂ S ₃	–
	Heat treated	–	Sb ₂ S ₃	–
165	As-grown	Sb ₂ O ₃	N/M ^a	N/M

^aN/M – Not measured.

The thermal analysis results of paper III could not be directly converted for use with USP. Thus, films were grown by USP in air from a solution of SbEX at a deposition temperature of 135°C and 165°C, followed by heat treatment. As could be predicted based on the results of paper III, the film grown at 135°C contained amorphous Sb₂S₃, and the film grown at 165°C contained crystalline Sb₂O₃ (Table 3.5). The Sb₂S₃ layer grown at 135°C did not crystallize after heat treatment in vacuum at 225°C, likely due to an inhibiting effect of decomposition residues (atomic ratios of C/Sb = 0.6, S/Sb = 0.4 calculated from EDX data; see paper IV, section 3.1). Thus, the first preparation route in its form of implementation was not successful in achieving the aim of the thesis. Consequently, these negative results explicitly confirm that suppressing oxidation in this USP deposition process is absolutely necessary to achieve phase pure Sb₂S₃ thin films.

3.4.2 Deposition of Sb₂S₃ films from SbEX/thioamide solutions

Thiourea (TU) and thioacetamide (TA) were chosen for the role of liquid protective layer as simple thioamides. TU melts at $\approx 180^\circ\text{C}$ and loses 84.3 % of initial mass by 237°C [229], whereas TA is reported to melt at 110°C and decompose at $120\text{--}200^\circ\text{C}$ without leaving any solid residues [230]. Consequently, TU is expected to form a temporary liquid protective coating at $\approx 180\text{--}250^\circ\text{C}$, and TA at $\approx 120\text{--}220^\circ\text{C}$.

In addition, thermal analysis coupled with evolved gas analysis of TA was used to clarify its melting point, mass loss and gaseous products in the temperature range of interest ($100\text{--}300^\circ\text{C}$) in air. TA melts at 120°C , degrades into H₂S and CH₃CN at $150\text{--}210^\circ\text{C}$, and a black colored amorphous solid residue of 3.2 % of its initial mass remains by 210°C (see paper IV, Figure 4a, b). Some CH₃CN oxidizes into H₂O and N₂O. Evidently, TA decomposes at a suitable temperature after melting, fulfilling the requirements for use in USP with SbEX.

Solutions of SbEX/TU = 1/1 and 1/3, and SbEX/TA = 1/3 and 1/10 dissolved in acetonitrile were sprayed by USP in air at 135°C , 165°C , and 215°C with the aim to grow Sb₂S₃ thin films. The respective deposition conditions are outlined in Table 3.6 with the resultant phase composition, atomic ratio of S/Sb, and band gap of the Sb₂S₃ films.

Table 3.6. Phase composition (XRD, Raman), calculated S/Sb atomic ratio (EDX), and calculated band gap (UV-VIS) data of films deposited from SbEX/thioamide solution by USP. Substrate: glass/ITO/TiO₂. Heat treatment: 225°C , $2 \cdot 10^{-1}$ Pa, 30 min.

Solution comp.	Molar ratio in solution	Depos. temp., °C	Phase composition ^a		S/Sb, at%/at%	E _g , eV	
			As-grown	Heat treated	Heat treated	Heat treated	
SbEX/TU	1/1	165	a-Sb ₂ S ₃	c-Sb ₂ S ₃	1.1	1.8	
	1/3	135	a-Sb ₂ S ₃	c-Sb ₂ S ₃	N/M ^b	>2.5	
		165	a-Sb ₂ S ₃	c-Sb ₂ S ₃	1.3	1.8	
		215	a-Sb ₂ S ₃	c-Sb ₂ S ₃	1.5	1.8	
SbEX/TA	1/3	165	a-Sb ₂ S ₃	c-Sb ₂ S ₃ , c-Sb ₂ O ₃	N/M	1.8	
		1/10	135	a-Sb ₂ S ₃	c-Sb ₂ S ₃	1.2	1.8
			165	a-Sb ₂ S ₃	c-Sb ₂ S ₃	1.4	1.8
	215		a-Sb ₂ S ₃	c-Sb ₂ S ₃	1.4	1.8	

^aa-Sb₂S₃ – amorphous Sb₂S₃. c- Sb₂S₃ – crystalline Sb₂S₃.

^bN/M – Not measured.

The as-grown films contained only amorphous Sb₂S₃, as confirmed by Raman, XRD, and FTIR. The band gap calculated from UV-VIS data was in excess of 2.2 eV for as-grown Sb₂S₃ films, and ≈ 1.8 eV for heat treated Sb₂S₃ films (Table 3.6), in line with literature (see section 3.1.3). Spraying the SbEX/TU = 1/1 solution at 165°C yielded films with S/Sb = 1.1

after heat treatment. Hence, $SbEX/TU = 1/3$ was used thereafter. Increasing the deposition temperature from $165^{\circ}C$ to $215^{\circ}C$ caused the atomic ratio of S/Sb in the heat treated film to increase from 1.3 to 1.5. Thus, films grown at $215^{\circ}C$ are expected to contain fewer residues.

Spraying the $SbEX/TA = 1/3$ solution at $165^{\circ}C$ yielded films containing Sb_2O_3 after heat treatment, indicating a lack of thioamide. Thus, $SbEX/TA$ was increased to $1/10$ to avoid oxidation of the Sb_2S_3 film. The atomic ratio of S/Sb was calculated as 1.4 for films grown at $165^{\circ}C$ and $215^{\circ}C$. Thus, the concentration of residues is estimated to be similar, as TA decomposes readily above $150^{\circ}C$ [IV]. Impurities were not detected by EDX or FTIR in any heat treated film. Thus, all Sb_2S_3 films grown from either solution were phase pure after heat treatment to the detection limit of Raman, XRD, FTIR, and EDX.

As the aim was to obtain uniform and continuous phase pure Sb_2S_3 thin films, the morphology of films grown at $165^{\circ}C$ and $215^{\circ}C$ from $SbEX/TU = 1/3$ and $SbEX/TA = 1/10$ solution was examined by SEM (Figure 3.9). The films grown at $165^{\circ}C$ appeared in both cases porous and uneven after heat treatment (Figure 3.9a, c, e, g), indicating an incomplete decomposition of the reagents during deposition.

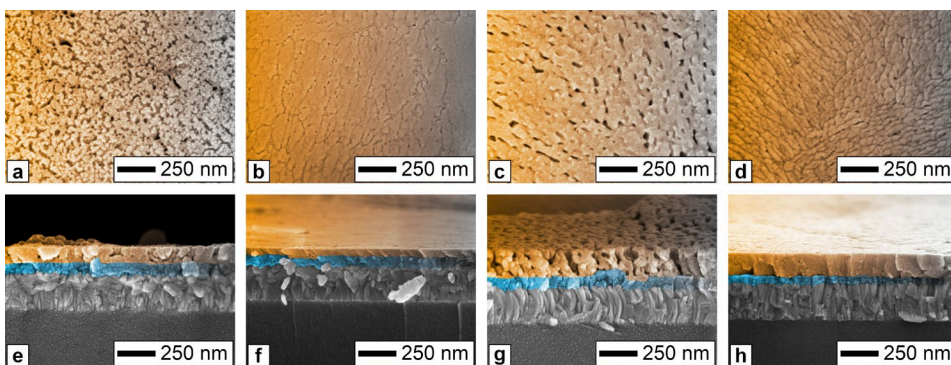


Figure 3.9. Top-down and cross-section SEM views of Sb_2S_3 films grown by USP from a solution of $SbEX/TU = 1/3$ at $165^{\circ}C$ (a, e), and $215^{\circ}C$ (b, f), or from a solution of $SbEX/TA = 1/10$ at $165^{\circ}C$ (c, g), and $215^{\circ}C$ (d, h), after heat treatment. Substrate: glass/ITO/ TiO_2 . Heat treatment: $225^{\circ}C$, $2 \cdot 10^{-1}$ Pa, 30 min.

After heat treatment, the films grown at $215^{\circ}C$ were compact, 50 nm thick, consisting of grains 40–280 nm by 30–130 nm ($SbEX/TU = 1/3$; Figure 3.9b, f), or 150 nm thick, consisting of grains 50–150 nm by 25–40 nm ($SbEX/TA = 1/10$; Figure 3.9d, h). Compared to Sb_2S_3 films grown from $SbCl_3/TU = 1/3$ solution at $200^{\circ}C$ after heat treatment (see paper II, Figure 1b), the lateral grain size of the films grown from $SbEX/TU = 1/3$ solution was smaller by about an order of magnitude, and mean crystallite size, calculated with respect to the reflection of the (2 0 2) crystallographic plane, was smaller by about a third (38 ± 6 nm vs 27 ± 4 nm). Therefore, the deposition of Sb_2S_3 thin films by USP from $SbEX$ solutions requires further optimization to achieve comparable results.

Three routes were identified for growing Sb_2S_3 films from $SbEX$ solutions by USP. First (Figure 3.10a), if there is a lack of thioamide to suppress oxidation of the growing film, Sb_2O_3 forms. Second (Figure 3.10b), if more thioamide reaches the substrate than can be decomposed in one USP cycle, solid residues accumulate within the growing film. During heat treatment, these trapped residues decompose into gaseous products, which carve voids into the film. Third (Figure 3.10c), if the concentration of thioamide is in the optimal

range at a deposition temperature of $\approx 215^\circ\text{C}$ to decompose SbEX, a balanced process ensues. Therein, the growing film is protected from oxidation by the liquid thioamide film, yet the precursor and the thioamide decompose sufficiently to allow to prepare a continuous phase pure crystalline Sb_2S_3 thin film after heat treatment.

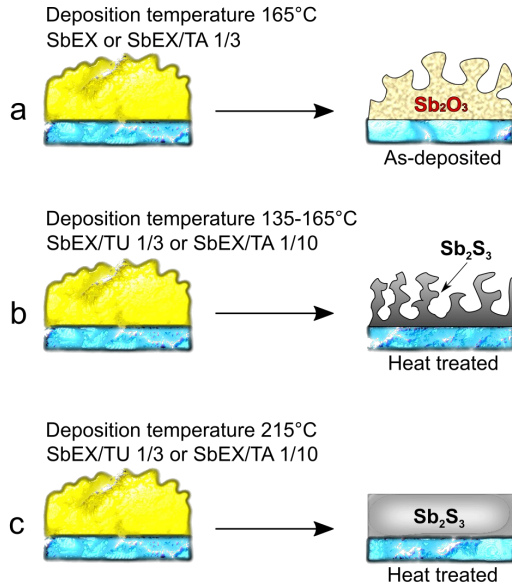


Figure 3.10. The growth of Sb-containing films from SbEX solutions by USP. (a) Deposition at 165°C with insufficient thioamide yields porous Sb_2O_3 . (b) Deposition from SbEX/TU = 1/3 or SbEX/TA = 1/10 solution at $135\text{--}165^\circ\text{C}$ yields porous Sb_2S_3 coatings after heat treatment due to leftover residues. (c) Deposition from SbEX/TU = 1/3 or SbEX/TA = 1/10 solution at 215°C yields compact and uniform Sb_2S_3 thin films after heat treatment due to an appropriate quantity of thioamide in solution.

3.4.3 Summary

The deposition of uniform phase pure Sb_2S_3 thin films from SbEX by USP in air was accomplished by adding an appropriate amount of thioamide to the spray solution (SbEX/TU = 1/3 or SbEX/TA = 1/10) at a deposition temperature of 215°C , and heat treating the resulting amorphous phase pure Sb_2S_3 layers in vacuum at 225°C .

Adding an insufficient quantity of thioamide, or none at all, to the spray solution causes the growing Sb_2S_3 layer to oxidize. According to FTIR, Raman, and XRD measurements of glass/ITO/ TiO_2 / Sb_2S_3 stacks, and the thermal analysis of TA, both TU and TA are liquid and decompose readily at $165\text{--}215^\circ\text{C}$, thereby forming a transient liquid barrier that blocks oxidation of the growing Sb_2S_3 layer.

In addition, if the amount of thioamide is excessive at the deposition temperature (165°C) that is required to completely decompose the byproducts, a porous Sb_2S_3 film is formed after heat treatment.

Conclusions

This thesis was focused on the development of the preparation process to obtain continuous uniform phase pure polycrystalline Sb_2S_3 thin films by ultrasonic spray pyrolysis (USP) for photovoltaic applications.

The novelty of this study is that the technological route was developed for preparing continuous phase pure Sb_2S_3 thin films on a planar substrate from $\text{Sb}(\text{TU})_3\text{Cl}_3$ formed in solution by a two-step process. The result was achieved by tuning the solution composition and USP deposition temperature, and the post-deposition heat treatment temperature. Furthermore, it was proven that these Sb_2S_3 thin films grown by USP are applicable for use in planar thin film solar cells, yielding up to 5.5 % power conversion efficiency after optimizing the thickness of the absorber. Moreover, thermal analysis and intermediate solid decomposition product analysis of antimony ethyl xanthate (SbEX) was done to assess its applicability as a precursor for depositing Sb_2S_3 thin films by USP. Finally, the technological route to deposit continuous phase pure Sb_2S_3 thin films by a two-step process from a solution of SbEX /thiourea (TU) or SbEX /thioacetamide (TA) was developed by tuning the deposition temperature and precursor solution composition.

The conclusions of this study are as follows:

- 1) Changing the deposition temperature and SbCl_3/TU molar ratio in solution was demonstrated to affect the phase composition, elemental composition and morphology of the Sb_2S_3 thin films deposited by USP in air at 200–220°C. Spraying a solution of $\text{SbCl}_3/\text{TU} = 1/6$ at a deposition temperature of 210°C or 220°C (or $\text{SbCl}_3/\text{TU} = 1/3$ at 220°C) yielded phase pure and crystalline (XRD, Raman), yet discontinuous (SEM) as-grown Sb_2S_3 thin films. Thus, continuous Sb_2S_3 thin films could not be prepared in one step by USP. Spraying a solution of $\text{SbCl}_3/\text{TU} = 1/6$ at 200°C or a solution of $\text{SbCl}_3/\text{TU} = 1/3$ at 200°C or 210°C yielded amorphous phase pure Sb_2S_3 thin films. In case of $\text{SbCl}_3/\text{TU} = 1/3$, the films were 70–90 nm thick and continuous, whereas in case of $\text{SbCl}_3/\text{TU} = 1/6$, the films were 50–70 nm thick and discontinuous. The amorphous Sb_2S_3 films grown from a solution of $\text{SbCl}_3/\text{TU} = 1/3$ at 200°C or 210°C were crystallized after heat treatment at the optimized conditions of 170°C, $5 \cdot 10^{-4}$ Pa, yielding a continuous morphology, an atomic ratio of $\text{S}/\text{Sb} = 1.3$, and $E_g \approx 1.8$ eV. Thus, the technological procedure to obtain continuous phase pure crystalline Sb_2S_3 thin films was achieved by applying a two-step process. It involved the deposition of a continuous amorphous Sb_2S_3 films by USP in air at 200–210°C, followed by post-growth heat treatment at 170°C, $5 \cdot 10^{-4}$ Pa.
- 2) Continuous crystalline Sb_2S_3 thin films grown by USP from a solution of $\text{SbCl}_3/\text{TU} = 1/3$ at 200°C in air, and heat treated at 170°C, $5 \cdot 10^{-4}$ Pa, were applicable as the absorber layer in planar ITO/ TiO_2 / Sb_2S_3 /P3HT/Au thin film solar cells, according to J - V and EQE. The optimal thickness of the Sb_2S_3 absorber film was 100 nm, based on η of solar cells. Accordingly, solar cells based on a 100 nm thick USP-grown Sb_2S_3 film yielded η of up to 5.5 % (1.7 mm^2), 4.7 % (7.1 mm^2), and 3.2 % (88 mm^2) at AM1.5G conditions, indicating PV performance approaching the state-of-the-art of planar Sb_2S_3 solar cells.

- 3) According to TG/DTA-EGA-MS, SbEX decomposed thermally in the temperature range of 90–800°C in argon atmosphere in three steps or at 90–590°C in air atmosphere in four steps. In argon and air, SbEX melted at 85°C, and decomposed by 170°C into amorphous Sb₂S₃, according to Raman, and evolution of CS₂, C₂H₅OH, CO, CO₂, COS, H₂O was detected by EGA-MS. A second endothermic step occurred at 170–255°C in argon, and 170–250°C in air, yielding crystalline Sb₂S₃, accompanied by the evolution of the same gases as in the first step. However, Sb₂O₃ was detected by Raman in the intermediate product exposed to 170°C in air. The Sb₂S₃ formed from SbEX in argon remained stable until its melting point of 550°C. At temperatures above 270°C in air, oxidation of Sb₂S₃ continued, resulting in Sb₂O₄ at 590°C. Thus, in principle, SbEX is considered a prospective and novel precursor for the preparation of Sb₂S₃ in air at around 170°C. Although, as partial oxidation of Sb₂S₃ is expected at ≈ 170°C, a method to prevent oxidation is required.
- 4) Spraying a solution of SbEX at 105°C or 165°C by USP on a planar glass/ITO/TiO₂ substrate in air yielded contaminated Sb₂S₃ after heat treatment at 225°C in vacuum, or crystalline Sb₂O₃, respectively. Thus, addition of thioamides to the spray solution and usage of a deposition temperature of 165°C was found to be necessary to prevent oxidation and contamination, according to XRD, Raman, and FTIR. Spraying a solution of SbEX/TU = 1/3 or SbEX/TA = 1/10 at 165°C by USP yielded phase pure, yet porous Sb₂S₃ thin films after heat treatment at 225°C in vacuum. Thus, increasing the deposition temperature to 215°C proved necessary to obtain continuous amorphous phase pure Sb₂S₃ thin films from a solution of SbEX by USP in air. Employing heat treatment at 225°C in vacuum yielded continuous phase pure crystalline Sb₂S₃ thin films with an atomic ratio of S/Sb = 1.5, E_g = 1.8 eV (SbEX/TU = 1/3) or an atomic ratio of S/Sb = 1.4, E_g = 1.8 eV (SbEX/TA = 1/10), respectively. Thus, the preparation of continuous phase pure Sb₂S₃ thin films by USP from SbEX was feasible, requiring a two-step approach, wherein amorphous Sb₂S₃ thin films were grown by USP in air with a thioamide additive, followed by crystallization at 225°C, 2·10⁻¹ Pa.

In all, it was proven that continuous phase pure thin films of Sb₂S₃ can be prepared by USP in air from a solution of Sb(TU)₃Cl₃, SbEX/TU = 1/3 or SbEX/TA = 1/10 after adapting a two-step preparation sequence. Depositing a sufficiently thick amorphous Sb₂S₃ film by USP allowed to obtain a continuous film after heat treatment. Thus, USP was demonstrated as a robust and broadly applicable method to deposit continuous phase pure Sb₂S₃ thin films. Furthermore, planar solar cells, based on a Sb₂S₃ thin film grown by USP in air from a solution of Sb(TU)₃Cl₃, with state-of-the-art power conversion efficiency were demonstrated, paving the way for future development of solar cells prepared in part, or fully, by USP in air. According to thermal analysis results, SbEX is a suitable precursor for USP as SbEX decomposes into Sb₂S₃ at 170°C in an inert atmosphere. Moreover, thermal analysis provided the insight that heating SbEX to 170°C in air causes the resultant Sb₂S₃ phase to oxidize. The two-step deposition approach developed herein could possibly be adapted to deposit continuous thin films of other metal sulfide or selenides in air at elevated temperatures from solutions of halide-containing or -free coordination complexes.

Future outlook

In parallel to the progression of this research, the knowledge base on tuning the morphology, phase composition and optoelectronic properties of Sb_2S_3 thin films and relevant highly efficient solar cells has expanded.

A vertically aligned grain structure in Sb_2S_3 films is beneficial for η of solar cells due to a shorter charge carrier extraction path and a reduction in horizontally aligned grain boundaries in the bulk of the absorber [166], [167]. Controllable grain growth and passivation of the ETL has been achieved by either modifying the surface of the ETL [144], [145], or by depositing a seed layer [149]–[151]. Thus, developing vertically aligned grain growth in Sb_2S_3 thin films by USP via engineering of the solution composition and substrate surface appears to have merit.

In addition, doping of Sb_2S_3 films has been attempted with less than a dozen elements so far, yielding an improvement in the morphology and electronic properties of the absorber and η of solar cells [108], [140], [141]. Thus, *in situ* doping of Sb_2S_3 thin films grown by USP is worth investigating after controllable grain growth has been achieved.

Furthermore, post-growth heat treatment in a sulfurizing or selenizing atmosphere should be applied for Sb_2S_3 films deposited by USP. Applying this type of treatment has been demonstrated to increase the phase purity, and decrease the concentration of deep level defects in the bulk of Sb_2S_3 coatings grown by other methods [6], [118], [137]. Alternatively, the optoelectronic properties of $\text{Sb}_2(\text{S},\text{Se})_3$ films have been tuned by optimizing the ratio of S/Se during deposition, yielding $\eta = 10.5\%$ in $\text{Sb}_2(\text{S},\text{Se})_3$ thin film solar cells [77].

In addition, the electronic properties of Sb_2S_3 thin films grown by USP have not yet been characterized systematically. Moreover, extensive characterization of the physical properties of USP- Sb_2S_3 films, including bulk and surface defects, is needed to provide feedback for technological parameters.

As semitransparent PV is likely to be the main application for Sb_2S_3 thin film solar cells, a suitably transparent and stable HTL and back contact have to be developed. In addition, stabilization of all interfaces in the stack, and encapsulation is required to sustain the PV performance of the USP- Sb_2S_3 thin film solar cells over reasonable periods of time for practical applications. Thus, passivation of surface defects at all interfaces should be a priority.

References

- [1] “Proposal for a REGULATION OF THE EUROPEAN PARLIAMENT AND OF THE COUNCIL establishing the framework for achieving climate neutrality and amending Regulation (EU) 2018/1999 (European Climate Law).” European Commission, Directorate-General for Climate Action, 03 2020. [Online]. Available: <https://eur-lex.europa.eu/legal-content/EN/TXT/?qid=1588581905912&uri=CELEX:52020PC0080>
- [2] “The Declaration of the Carbon Neutrality Coalition.” [Online]. Available: <https://carbon-neutrality.global/the-declaration/>
- [3] “Net Zero by 2050,” IEA, Paris, 2021. [Online]. Available: <https://www.iea.org/reports/net-zero-by-2050>
- [4] B. Burger *et al.*, “Photovoltaics report,” Fraunhofer Institute for Solar Energy Systems, ISE, Freiburg, Sep. 2020. Accessed: Jun. 08, 2021. [Online]. Available: <https://www.ise.fraunhofer.de/en/publications/studies/photovoltaics-report.html>
- [5] R. Kondrotas, C. Chen, and J. Tang, “Sb₂S₃ Solar Cells,” *Joule*, vol. 2, no. 5, pp. 857–878, May 2018, doi: 10.1016/j.joule.2018.04.003.
- [6] Y. C. Choi, D. U. Lee, J. H. Noh, E. K. Kim, and S. I. Seok, “Highly Improved Sb₂S₃ Sensitized-Inorganic–Organic Heterojunction Solar Cells and Quantification of Traps by Deep-Level Transient Spectroscopy,” *Adv. Funct. Mater.*, vol. 24, no. 23, pp. 3587–3592, Jun. 2014, doi: 10.1002/adfm.201304238.
- [7] X. Wang, J. Li, W. Liu, S. Yang, C. Zhu, and T. Chen, “A fast chemical approach towards Sb₂S₃ film with a large grain size for high-performance planar heterojunction solar cells,” *Nanoscale*, vol. 9, no. 10, pp. 3386–3390, 2017, doi: 10.1039/C7NR00154A.
- [8] D.-H. Kim *et al.*, “Highly reproducible planar Sb₂S₃-sensitized solar cells based on atomic layer deposition,” *Nanoscale*, vol. 6, no. 23, pp. 14549–14554, 2014, doi: 10.1039/C4NR04148H.
- [9] E. Kärber, A. Katerski, I. Oja Acik, A. Mere, V. Mikli, and M. Krunks, “Sb₂S₃ grown by ultrasonic spray pyrolysis and its application in a hybrid solar cell,” *Beilstein J. Nanotechnol.*, vol. 7, pp. 1662–1673, 2016, doi: 10.3762/bjnano.7.158.
- [10] R. Parize *et al.*, “ZnO/TiO₂/Sb₂S₃ Core–Shell Nanowire Heterostructure for Extremely Thin Absorber Solar Cells,” *J. Phys. Chem. C*, vol. 121, no. 18, pp. 9672–9680, May 2017, doi: 10.1021/acs.jpcc.7b00178.
- [11] J. L. Gray, “The Physics of the Solar Cell,” in *Handbook of Photovoltaic Science and Engineering*, John Wiley & Sons, Ltd, 2010, pp. 82–129. doi: 10.1002/9780470974704.ch3.
- [12] R. Scheer and H.-W. Schock, *Chalcogenide Photovoltaics: Physics, Technologies, and Thin Film Devices*, 1st ed. Wiley-VCH, 2011.
- [13] A. Romeo and E. Arregiani, “CdTe-Based Thin Film Solar Cells: Past, Present and Future,” *Energies*, vol. 14, no. 6, 2021, doi: 10.3390/en14061684.
- [14] M. Green, E. Dunlop, J. Hohl-Ebinger, M. Yoshita, N. Kopidakis, and X. Hao, “Solar cell efficiency tables (version 57),” *Prog. Photovoltaics*, vol. 29, no. 1, pp. 3–15, Jan. 2021, doi: 10.1002/pip.3371.
- [15] W. Shockley, “The theory of p-n junctions in semiconductors and p-n junction transistors,” *Bell Syst. Tech. J.*, vol. 28, no. 3, pp. 435–489, Jul. 1949, doi: 10.1002/j.1538-7305.1949.tb03645.x.

- [16] S. Rühle, "Tabulated values of the Shockley–Queisser limit for single junction solar cells," *Sol. Energy*, vol. 130, pp. 139–147, Jun. 2016, doi: 10.1016/j.solener.2016.02.015.
- [17] T. Kirchartz and U. Rau, "What Makes a Good Solar Cell?," *Adv. Energy Mater.*, vol. 8, no. 28, p. 1703385, Oct. 2018, doi: 10.1002/aenm.201703385.
- [18] R. Guerrero-Lemus, R. Vega, T. Kim, A. Kimm, and L. E. Shephard, "Bifacial solar photovoltaics – A technology review," *Renewable Sustainable Energy Rev.*, vol. 60, pp. 1533–1549, Jul. 2016, doi: 10.1016/j.rser.2016.03.041.
- [19] M. R. Khan, A. Hanna, X. Sun, and M. A. Alam, "Vertical bifacial solar farms: Physics, design, and global optimization," *Appl. Energy*, vol. 206, pp. 240–248, Nov. 2017, doi: 10.1016/j.apenergy.2017.08.042.
- [20] W. Gu, T. Ma, S. Ahmed, Y. Zhang, and J. Peng, "A comprehensive review and outlook of bifacial photovoltaic (bPV) technology," *Energy Convers. Manage.*, vol. 223, p. 113283, Nov. 2020, doi: 10.1016/j.enconman.2020.113283.
- [21] M. Takla, N. E. Kamfjord, H. Tveit, and S. Kjelstrup, "Energy and exergy analysis of the silicon production process," *Energy*, vol. 58, pp. 138–146, Sep. 2013, doi: 10.1016/j.energy.2013.04.051.
- [22] P. C. K. Vesborg and T. F. Jaramillo, "Addressing the terawatt challenge: scalability in the supply of chemical elements for renewable energy," *RSC Adv.*, vol. 2, no. 21, pp. 7933–7947, 2012, doi: 10.1039/C2RA20839C.
- [23] L. El Chaar, L. A. Lamont, and N. El Zein, "Review of photovoltaic technologies," *Renewable Sustainable Energy Rev.*, vol. 15, no. 5, pp. 2165–2175, Jun. 2011, doi: 10.1016/j.rser.2011.01.004.
- [24] G. Giacchetta, M. Leporini, and B. Marchetti, "Evaluation of the environmental benefits of new high value process for the management of the end of life of thin film photovoltaic modules," *J. Cleaner Prod.*, vol. 51, pp. 214–224, Jul. 2013, doi: 10.1016/j.jclepro.2013.01.022.
- [25] "DIRECTIVE 2011/65/EU OF THE EUROPEAN PARLIAMENT AND OF THE COUNCIL on the restriction of the use of certain hazardous substances in electrical and electronic equipment." THE EUROPEAN PARLIAMENT AND THE COUNCIL OF THE EUROPEAN UNION, Jun. 08, 2011. [Online]. Available: <https://eur-lex.europa.eu/legal-content/EN/TXT/?uri=CELEX:02011L0065-20210401>
- [26] G. Genchi, M. S. Sinicropi, G. Lauria, A. Carocci, and A. Catalano, "The Effects of Cadmium Toxicity," *Int. J. Environ. Res. Public Health*, vol. 17, no. 11, 2020, doi: 10.3390/ijerph17113782.
- [27] H. Steinberger, "Health, safety and environmental risks from the operation of CdTe and CIS thin-film modules," *Prog. Photovoltaics*, vol. 6, no. 2, pp. 99–103, Mar. 1998, doi: 10.1002/(SICI)1099-159X(199803/04)6:2<99::AID-PIP211>3.0.CO;2-Q.
- [28] "Mineral commodity summaries 2021," Reston, VA, Report, 2021. doi: 10.3133/mcs2021.
- [29] B. J. Stanbery, "Copper Indium Selenides and Related Materials for Photovoltaic Devices," *Crit. Rev. Solid State Mater. Sci.*, vol. 27, no. 2, pp. 73–117, Apr. 2002, doi: 10.1080/20014091104215.
- [30] M. Nakamura, K. Yamaguchi, Y. Kimoto, Y. Yasaki, T. Kato, and H. Sugimoto, "Cd-Free Cu(In,Ga)(Se,S)₂ Thin-Film Solar Cell With Record Efficiency of 23.35%," *IEEE J. Photovolt.*, vol. 9, no. 6, pp. 1863–1867, Nov. 2019, doi: 10.1109/JPHOTOV.2019.2937218.

- [31] D. Feldman and R. Margolis, "H₂ 2020 Solar Industry Update," National Renewable Energy Laboratory, NREL/PR-7A40-79758, Apr. 2021.
- [32] E. Biyik *et al.*, "A key review of building integrated photovoltaic (BIPV) systems," *Eng. Sci. Technol. Int. J.*, vol. 20, no. 3, pp. 833–858, Jun. 2017, doi: 10.1016/j.jestch.2017.01.009.
- [33] D.-J. van de Ven *et al.*, "The potential land requirements and related land use change emissions of solar energy," *Sci. Rep.*, vol. 11, no. 1, p. 2907, Feb. 2021, doi: 10.1038/s41598-021-82042-5.
- [34] "Best Research-Cell Efficiency Chart." National Renewable Energy Laboratory. Accessed: Jun. 17, 2021. [Online]. Available: <https://www.nrel.gov/pv/cell-efficiency.html>
- [35] J.-P. Correa-Baena *et al.*, "Promises and challenges of perovskite solar cells," *Science*, vol. 358, no. 6364, p. 739, Nov. 2017, doi: 10.1126/science.aam6323.
- [36] W. S. Yang *et al.*, "Iodide management in formamidinium-lead-halide-based perovskite layers for efficient solar cells," *Science*, vol. 356, no. 6345, p. 1376, Jun. 2017, doi: 10.1126/science.aan2301.
- [37] V. Consonni, J. Briscoe, E. Kärber, X. Li, and T. Cossuet, "ZnO nanowires for solar cells: a comprehensive review," *Nanotechnology*, vol. 30, no. 36, p. 362001, Jun. 2019, doi: 10.1088/1361-6528/ab1f2e.
- [38] A. A. F. Husain, W. Z. W. Hasan, S. Shafie, M. N. Hamidon, and S. S. Pandey, "A review of transparent solar photovoltaic technologies," *Renewable Sustainable Energy Rev.*, vol. 94, pp. 779–791, Oct. 2018, doi: 10.1016/j.rser.2018.06.031.
- [39] T. D. Lee and A. U. Ebong, "A review of thin film solar cell technologies and challenges," *Renewable Sustainable Energy Rev.*, vol. 70, pp. 1286–1297, Apr. 2017, doi: 10.1016/j.rser.2016.12.028.
- [40] W. Wang *et al.*, "Device Characteristics of CZTSSe Thin-Film Solar Cells with 12.6% Efficiency," *Adv. Energ. Mater.*, vol. 4, no. 7, p. 1301465, May 2014, doi: 10.1002/aenm.201301465.
- [41] A. Zakutayev *et al.*, "Emerging inorganic solar cell efficiency tables (version 2)," *J. Phys.: Energy*, vol. 3, no. 3, p. 032003, Apr. 2021, doi: 10.1088/2515-7655/abebca.
- [42] B. O'Regan and M. Grätzel, "A low-cost, high-efficiency solar cell based on dye-sensitized colloidal TiO₂ films," *Nature*, vol. 353, no. 6346, pp. 737–740, Oct. 1991, doi: 10.1038/353737a0.
- [43] A. Hagfeldt, G. Boschloo, L. Sun, L. Kloo, and H. Pettersson, "Dye-Sensitized Solar Cells," *Chem. Rev.*, vol. 110, no. 11, pp. 6595–6663, Nov. 2010, doi: 10.1021/cr900356p.
- [44] Y. Cao, Y. Liu, S. M. Zakeeruddin, A. Hagfeldt, and M. Grätzel, "Direct Contact of Selective Charge Extraction Layers Enables High-Efficiency Molecular Photovoltaics," *Joule*, vol. 2, no. 6, pp. 1108–1117, Jun. 2018, doi: 10.1016/j.joule.2018.03.017.
- [45] N. Kato *et al.*, "Degradation analysis of dye-sensitized solar cell module after long-term stability test under outdoor working condition," *Sol. Energy Mater. Sol. Cells*, vol. 93, no. 6, pp. 893–897, Jun. 2009, doi: 10.1016/j.solmat.2008.10.022.
- [46] S. Lepikko, K. Miettunen, A. Poskela, A. Tiihonen, and P. D. Lund, "Testing dye-sensitized solar cells in harsh northern outdoor conditions," *Energy Sci. Eng.*, vol. 6, no. 3, pp. 187–200, Jun. 2018, doi: 10.1002/ese3.195.

- [47] A. Poskela, K. Miettunen, A. Tiihonen, and P. D. Lund, "Extreme sensitivity of dye solar cells to UV-induced degradation," *Energy Sci. Eng.*, vol. 9, no. 1, pp. 19–26, Jan. 2021, doi: 10.1002/ese3.810.
- [48] M. Kaltenbrunner *et al.*, "Ultrathin and lightweight organic solar cells with high flexibility," *Nat. Commun.*, vol. 3, no. 1, p. 770, Apr. 2012, doi: 10.1038/ncomms1772.
- [49] J. E. Carlé *et al.*, "Overcoming the Scaling Lag for Polymer Solar Cells," *Joule*, vol. 1, no. 2, pp. 274–289, Oct. 2017, doi: 10.1016/j.joule.2017.08.002.
- [50] K. Kawano, R. Pacios, D. Poplavskyy, J. Nelson, D. D. C. Bradley, and J. R. Durrant, "Degradation of organic solar cells due to air exposure," *Sol. Energy Mater. Sol. Cells*, vol. 90, no. 20, pp. 3520–3530, Dec. 2006, doi: 10.1016/j.solmat.2006.06.041.
- [51] N. Bristow and J. Kettle, "Outdoor performance of organic photovoltaics: Diurnal analysis, dependence on temperature, irradiance, and degradation," *J. Renewable Sustainable Energy*, vol. 7, no. 1, p. 013111, Jan. 2015, doi: 10.1063/1.4906915.
- [52] N. Bristow and J. Kettle, "Outdoor organic photovoltaic module characteristics: Benchmarking against other PV technologies for performance, calculation of Ross coefficient and outdoor stability monitoring," *Sol. Energy Mater. Sol. Cells*, vol. 175, pp. 52–59, Feb. 2018, doi: 10.1016/j.solmat.2017.10.008.
- [53] R. R. Lunt and V. Bulovic, "Transparent, near-infrared organic photovoltaic solar cells for window and energy-scavenging applications," *Appl. Phys. Lett.*, vol. 98, no. 11, p. 113305, Mar. 2011, doi: 10.1063/1.3567516.
- [54] Y. Li *et al.*, "Color-neutral, semitransparent organic photovoltaics for power window applications," *Proc. Natl. Acad. Sci. U. S. A.*, vol. 117, no. 35, p. 21147, Sep. 2020, doi: 10.1073/pnas.2007799117.
- [55] W. Wang *et al.*, "Fused Hexacyclic Nonfullerene Acceptor with Strong Near-Infrared Absorption for Semitransparent Organic Solar Cells with 9.77% Efficiency," *Adv. Mater.*, vol. 29, no. 31, p. 1701308, Aug. 2017, doi: 10.1002/adma.201701308.
- [56] Z. Fan, K. Sun, and J. Wang, "Perovskites for photovoltaics: a combined review of organic–inorganic halide perovskites and ferroelectric oxide perovskites," *J. Mater. Chem. A*, vol. 3, no. 37, pp. 18809–18828, 2015, doi: 10.1039/C5TA04235F.
- [57] A. Kojima, K. Teshima, Y. Shirai, and T. Miyasaka, "Organometal Halide Perovskites as Visible-Light Sensitizers for Photovoltaic Cells," *J. Am. Chem. Soc.*, vol. 131, no. 17, pp. 6050–6051, May 2009, doi: 10.1021/ja809598r.
- [58] J. Jeong *et al.*, "Pseudo-halide anion engineering for α -FAPbI₃ perovskite solar cells," *Nature*, vol. 592, no. 7854, pp. 381–385, Apr. 2021, doi: 10.1038/s41586-021-03406-5.
- [59] H. Needleman, "Lead Poisoning," *Annu. Rev. Med.*, vol. 55, no. 1, pp. 209–222, Jan. 2004, doi: 10.1146/annurev.med.55.091902.103653.
- [60] U. Zulfiqar *et al.*, "Lead toxicity in plants: Impacts and remediation," *J. Environ. Manage.*, vol. 250, p. 109557, Nov. 2019, doi: 10.1016/j.jenvman.2019.109557.
- [61] A. Babayigit, A. Ethirajan, M. Muller, and B. Conings, "Toxicity of organometal halide perovskite solar cells," *Nat. Mater.*, vol. 15, no. 3, pp. 247–251, Mar. 2016, doi: 10.1038/nmat4572.

- [62] F. Sani, S. Shafie, H. N. Lim, and A. O. Musa, "Advancement on Lead-Free Organic-Inorganic Halide Perovskite Solar Cells: A Review," *Materials*, vol. 11, no. 6, 2018, doi: 10.3390/ma11061008.
- [63] P. Billen *et al.*, "Comparative evaluation of lead emissions and toxicity potential in the life cycle of lead halide perovskite photovoltaics," *Energy*, vol. 166, pp. 1089–1096, Jan. 2019, doi: 10.1016/j.energy.2018.10.141.
- [64] I. Kaiser *et al.*, "The eta-solar cell with CuInS₂: A photovoltaic cell concept using an extremely thin absorber (eta)," *Sol. Energy Mater. Sol. Cells*, vol. 67, no. 1, pp. 89–96, Mar. 2001, doi: 10.1016/S0927-0248(00)00267-1.
- [65] C. Lévy-Clément, R. Tena-Zaera, M. A. Ryan, A. Katty, and G. Hodes, "CdSe-Sensitized p-CuSCN/Nanowire n-ZnO Heterojunctions," *Adv. Mater.*, vol. 17, no. 12, pp. 1512–1515, Jun. 2005, doi: 10.1002/adma.200401848.
- [66] Y. Itzhaik, O. Niitsoo, M. Page, and G. Hodes, "Sb₂S₃-Sensitized Nanoporous TiO₂ Solar Cells," *J. Phys. Chem. C*, vol. 113, no. 11, pp. 4254–4256, Mar. 2009, doi: 10.1021/jp900302b.
- [67] K. Taretto and U. Rau, "Modeling extremely thin absorber solar cells for optimized design," *Prog. Photovoltaics*, vol. 12, no. 8, pp. 573–591, Dec. 2004, doi: 10.1002/pip.549.
- [68] P. H. Rekemeyer, S. Chang, C.-H. M. Chuang, G. W. Hwang, M. G. Bawendi, and S. Gradečak, "Enhanced Photocurrent in PbS Quantum Dot Photovoltaics via ZnO Nanowires and Band Alignment Engineering," *Adv. Energy Mater.*, vol. 6, no. 24, p. 1600848, Dec. 2016, doi: 10.1002/aenm.201600848.
- [69] E. H. Sargent, "Colloidal quantum dot solar cells," *Nat. Photonics*, vol. 6, no. 3, pp. 133–135, Mar. 2012, doi: 10.1038/nphoton.2012.33.
- [70] E. Georgitzikis *et al.*, "Optimization of Charge Carrier Extraction in Colloidal Quantum Dots Short-Wave Infrared Photodiodes through Optical Engineering," *Adv. Funct. Mater.*, vol. 28, no. 42, p. 1804502, Sep. 2018, doi: 10.1002/adfm.201804502.
- [71] T. K. Todorov *et al.*, "Ultrathin high band gap solar cells with improved efficiencies from the world's oldest photovoltaic material," *Nat. Commun.*, vol. 8, no. 1, p. 682, Sep. 2017, doi: 10.1038/s41467-017-00582-9.
- [72] T. Minami, Y. Nishi, and T. Miyata, "High-Efficiency Cu₂O-Based Heterojunction Solar Cells Fabricated Using a Ga₂O₃ Thin Film as N-Type Layer," *Appl. Phys. Express*, vol. 6, no. 4, p. 044101, Apr. 2013, doi: 10.7567/apex.6.044101.
- [73] P. Sinsermsuksakul *et al.*, "Overcoming Efficiency Limitations of SnS-Based Solar Cells," *Adv. Energy Mater.*, vol. 4, no. 15, p. 1400496, Oct. 2014, doi: 10.1002/aenm.201400496.
- [74] C. Chen, Y. Zhai, F. Li, and G. Yue, "Fabrication of silver sulfide thin films for efficient organic solar cells with high short-circuit currents based on double heterojunctions," *J. Power Sources*, vol. 298, pp. 259–268, Dec. 2015, doi: 10.1016/j.jpowsour.2015.08.066.
- [75] L. Wang *et al.*, "Stable 6%-efficient Sb₂Se₃ solar cells with a ZnO buffer layer," *Nat. Energy*, vol. 2, no. 4, p. 17046, Mar. 2017, doi: 10.1038/nenergy.2017.46.
- [76] L. Whittaker-Brooks, J. Gao, A. K. Hailey, C. R. Thomas, N. Yao, and Y.-L. Loo, "Bi₂S₃ nanowire networks as electron acceptor layers in solution-processed hybrid solar cells," *J. Mater. Chem. C*, vol. 3, no. 11, pp. 2686–2692, 2015, doi: 10.1039/C4TC02534B.

- [77] X. Wang *et al.*, “Manipulating the Electrical Properties of $\text{Sb}_2(\text{S,Se})_3$ Film for High-Efficiency Solar Cell,” *Advanced Energy Materials*, vol. 10, no. 40, p. 2002341, Oct. 2020, doi: 10.1002/aenm.202002341.
- [78] M. Mujahid, C. Chen, J. Zhang, C. Li, and Y. Duan, “Recent advances in semitransparent perovskite solar cells,” *InfoMat*, vol. 3, no. 1, pp. 101–124, Jan. 2021, doi: 10.1002/inf2.12154.
- [79] G. M. Kim and T. Tatsuma, “Semi-transparent Perovskite Solar Cells Developed by Considering Human Luminosity Function,” *Sci. Rep.*, vol. 7, no. 1, p. 10699, Sep. 2017, doi: 10.1038/s41598-017-11193-1.
- [80] S. Rahmany and L. Etgar, “Semitransparent Perovskite Solar Cells,” *ACS Energy Lett.*, vol. 5, no. 5, pp. 1519–1531, May 2020, doi: 10.1021/acscenergylett.0c00417.
- [81] B. Lee, L. Lahann, Y. Li, and S. R. Forrest, “Cost estimates of production scale semitransparent organic photovoltaic modules for building integrated photovoltaics,” *Sustainable Energy Fuels*, vol. 4, no. 11, pp. 5765–5772, 2020, doi: 10.1039/D0SE00910E.
- [82] H.-C. Kwon, A. Kim, H. Lee, D. Lee, S. Jeong, and J. Moon, “Parallelized Nanopillar Perovskites for Semitransparent Solar Cells Using an Anodized Aluminum Oxide Scaffold,” *Adv. Energy Mater.*, vol. 6, no. 20, p. 1601055, Oct. 2016, doi: 10.1002/aenm.201601055.
- [83] H. Lei, J. Chen, Z. Tan, and G. Fang, “Review of Recent Progress in Antimony Chalcogenide-Based Solar Cells: Materials and Devices,” *Solar RRL*, vol. 3, no. 6, p. 1900026, Jun. 2019, doi: 10.1002/solr.201900026.
- [84] J. Zhang *et al.*, “All Antimony Chalcogenide Tandem Solar Cell,” *Solar RRL*, vol. 4, no. 4, p. 2000048, Apr. 2020, doi: 10.1002/solr.202000048.
- [85] T. Jiménez, D. Seuret-Jiménez, O. Vigil-Galán, M. A. Basurto-Pensado, and M. Courel, “ $\text{Sb}_2(\text{S}_{1-x}\text{Se}_x)_3$ solar cells: the impact of radiative and non-radiative loss mechanisms,” *J. Phys. D: Appl. Phys.*, vol. 51, no. 43, p. 435501, Sep. 2018, doi: 10.1088/1361-6463/aaddea.
- [86] Y. Liu, K. T. Eddie Chua, T. C. Sum, and C. K. Gan, “First-principles study of the lattice dynamics of Sb_2S_3 ,” *Phys. Chem. Chem. Phys.*, vol. 16, no. 1, pp. 345–350, 2014, doi: 10.1039/C3CP53879F.
- [87] J. Ibáñez *et al.*, “Structural, Vibrational, and Electronic Study of Sb_2S_3 at High Pressure,” *J. Phys. Chem. C*, vol. 120, no. 19, pp. 10547–10558, May 2016, doi: 10.1021/acs.jpcc.6b01276.
- [88] A. Kyono, M. Kimata, M. Matsuhisa, Y. Miyashita, and K. Okamoto, “Low-temperature crystal structures of stibnite implying orbital overlap of $\text{Sb } 5s^2$ inert pair electrons,” *Phys. Chem. Miner.*, vol. 29, no. 4, pp. 254–260, May 2002, doi: 10.1007/s00269-001-0227-1.
- [89] A. Kyono, A. Hayakawa, and M. Horiki, “Selenium substitution effect on crystal structure of stibnite (Sb_2S_3),” *Phys. Chem. Miner.*, vol. 42, no. 6, pp. 475–490, Jun. 2015, doi: 10.1007/s00269-015-0737-x.
- [90] K. Momma and F. Izumi, “VESTA 3 for three-dimensional visualization of crystal, volumetric and morphology data,” *J. Appl. Crystallogr.*, vol. 44, pp. 1272–1276, 2011, doi: 10.1107/S0021889811038970.
- [91] A. Kyono and M. Kimata, “Structural variations induced by difference of the inert pair effect in the stibnite-bismuthinite solid solution series ($\text{Sb,Bi})_2\text{S}_3$,” *Am. Mineral.*, vol. 89, no. 7, pp. 932–940, Jul. 2004, doi: 10.2138/am-2004-0702.

- [92] P. Bohac and P. Kaufmann, "Zone refining of antimony trisulfide," *Mater. Res. Bull.*, vol. 10, no. 7, pp. 613–622, Jul. 1975, doi: 10.1016/0025-5408(75)90042-2.
- [93] Y. Zhou *et al.*, "Thin-film Sb₂Se₃ photovoltaics with oriented one-dimensional ribbons and benign grain boundaries," *Nat. Photonics*, vol. 9, no. 6, pp. 409–415, Jun. 2015, doi: 10.1038/nphoton.2015.78.
- [94] O. Savadogo and K. C. Mandal, "Studies on new chemically deposited photoconducting antimony trisulphide thin films," *Sol. Energy Mater. Sol. Cells*, vol. 26, no. 1, pp. 117–136, Mar. 1992, doi: 10.1016/0927-0248(92)90131-8.
- [95] O. Savadogo and K. C. Mandal, "Improved Schottky barrier on *n*-Sb₂S₃ films chemically deposited with silicotungstic acid," *Electron. Lett.*, vol. 28, no. 18, p. 1682–1683(1), Aug. 1992, doi: 10.1049/el:19921069.
- [96] O. Savadogo and K. C. Mandal, "Low Cost Schottky Barrier Solar Cells Fabricated on CdSe and Sb₂S₃ Films Chemically Deposited with Silicotungstic Acid," *J. Electrochem. Soc.*, vol. 141, no. 10, p. 2871, 1994, doi: 10.1149/1.2059248.
- [97] S.-J. Moon, Y. Itzhaik, J.-H. Yum, S. M. Zakeeruddin, G. Hodes, and M. Grätzel, "Sb₂S₃-Based Mesoscopic Solar Cell using an Organic Hole Conductor," *J. Phys. Chem. Lett.*, vol. 1, no. 10, pp. 1524–1527, May 2010, doi: 10.1021/jz100308q.
- [98] S. Messina, M. T. S. Nair, and P. K. Nair, "Solar cells with Sb₂S₃ absorber films," *Thin Solid Films*, vol. 517, no. 7, pp. 2503–2507, Feb. 2009, doi: 10.1016/j.tsf.2008.11.060.
- [99] S. Nezu *et al.*, "Light Soaking and Gas Effect on Nanocrystalline TiO₂/Sb₂S₃/CuSCN Photovoltaic Cells following Extremely Thin Absorber Concept," *J. Phys. Chem. C*, vol. 114, no. 14, pp. 6854–6859, Apr. 2010, doi: 10.1021/jp100401e.
- [100] S. Ito, K. Tsujimoto, D.-C. Nguyen, K. Manabe, and H. Nishino, "Doping effects in Sb₂S₃ absorber for full-inorganic printed solar cells with 5.7% conversion efficiency," *Int. J. Hydrogen Energy*, vol. 38, no. 36, pp. 16749–16754, Dec. 2013, doi: 10.1016/j.ijhydene.2013.02.069.
- [101] W. Lian *et al.*, "Revealing composition and structure dependent deep-level defect in antimony trisulfide photovoltaics," *Nat. Commun.*, vol. 12, no. 1, p. 3260, May 2021, doi: 10.1038/s41467-021-23592-0.
- [102] N. Fleck *et al.*, "How Oxygen Exposure Improves the Back Contact and Performance of Antimony Selenide Solar Cells," *ACS Appl. Mater. Interfaces*, vol. 12, no. 47, pp. 52595–52602, Nov. 2020, doi: 10.1021/acsami.0c14256.
- [103] K. C. Godel, B. Roose, A. Sadhanala, Y. Vaynzof, S. K. Pathak, and U. Steiner, "Partial oxidation of the absorber layer reduces charge carrier recombination in antimony sulfide solar cells," *Phys. Chem. Chem. Phys.*, vol. 19, no. 2, pp. 1425–1430, 2017, doi: 10.1039/C6CP07559B.
- [104] N. N. Greenwood and A. Earnshaw, *Chemistry of the Elements*, 2nd ed. Oxford, U.K.: Butterworth-Heinemann, 1997.
- [105] W. E. Thorneycroft, *Antimony And Bismuth*, vol. VI, Part V. London, U.K.: Charles Griffin & Co, Ltd, 1936. [Online]. Available: <https://archive.org/details/in.ernet.dli.2015.153746>
- [106] M. Liu, Y. Gong, Z. Li, M. Dou, and F. Wang, "A green and facile hydrothermal approach for the synthesis of high-quality semi-conducting Sb₂S₃ thin films," *Appl. Surf. Sci.*, vol. 387, pp. 790–795, Nov. 2016, doi: 10.1016/j.apsusc.2016.06.126.

- [107] M. Calixto-Rodriguez *et al.*, "A comparative study of the physical properties of Sb_2S_3 thin films treated with N_2 AC plasma and thermal annealing in N_2 ," *Appl. Surf. Sci.*, vol. 256, no. 8, pp. 2428–2433, Feb. 2010, doi: 10.1016/j.apsusc.2009.10.081.
- [108] E. Cárdenas, A. Arato, E. Perez-Tijerina, T. K. Das Roy, G. Alan Castillo, and B. Krishnan, "Carbon-doped Sb_2S_3 thin films: Structural, optical and electrical properties," *Sol. Energy Mater. Sol. Cells*, vol. 93, no. 1, pp. 33–36, Jan. 2009, doi: 10.1016/j.solmat.2008.02.026.
- [109] J. D. Desai and C. D. Lokhande, "Alkaline bath chemical deposition of antimony (III) sulphide thin films," *Thin Solid Films*, vol. 237, no. 1, pp. 29–31, Jan. 1994, doi: 10.1016/0040-6090(94)90234-8.
- [110] Z. Yang *et al.*, "Ultrafast self-trapping of photoexcited carriers sets the upper limit on antimony trisulfide photovoltaic devices," *Nat. Commun.*, vol. 10, no. 1, p. 4540, Oct. 2019, doi: 10.1038/s41467-019-12445-6.
- [111] S. Fan, C. Shi, K. Lv, Q. Wang, F. Guo, and W. Chen, "The low-temperature preparation for low-selenium $\text{Sb}_2\text{S}_x\text{Se}_y$ thin film solar cells with efficiency of > 5%," *J. Nanopart. Res.*, vol. 23, no. 2, p. 42, Feb. 2021, doi: 10.1007/s11051-021-05155-y.
- [112] V. Piacente, P. Scardala, and D. Ferro, "Study of the vaporization behaviour of Sb_2S_3 and Sb_2Te_3 from their vapour pressure measurements," *J. Alloys Compd.*, vol. 178, no. 1, pp. 101–115, Feb. 1992, doi: 10.1016/0925-8388(92)90251-4.
- [113] A. R. Kushkhov, D. S. Gaev, O. I. Rabinovich, and A. G. Stolyarov, "Growth and study of antimony selenide island films," *Crystallogr. Rep.*, vol. 58, no. 2, pp. 365–369, Mar. 2013, doi: 10.1134/S1063774513020132.
- [114] A. Mavlonov *et al.*, "A review of Sb_2Se_3 photovoltaic absorber materials and thin-film solar cells," *Sol. Energy*, vol. 201, pp. 227–246, May 2020, doi: 10.1016/j.solener.2020.03.009.
- [115] Y. C. Choi and S. I. Seok, "Efficient Sb_2S_3 -Sensitized Solar Cells Via Single-Step Deposition of Sb_2S_3 Using S/Sb-Ratio-Controlled SbCl_3 -Thiourea Complex Solution," *Adv. Funct. Mater.*, vol. 25, no. 19, pp. 2892–2898, May 2015, doi: 10.1002/adfm.201500296.
- [116] R. Parize, T. Cossuet, O. Chaix-Pluchery, H. Roussel, E. Appert, and V. Consonni, "In situ analysis of the crystallization process of Sb_2S_3 thin films by Raman scattering and X-ray diffraction," *Mater. Des.*, vol. 121, pp. 1–10, May 2017, doi: 10.1016/j.matdes.2017.02.034.
- [117] M. Leng *et al.*, "Selenization of Sb_2Se_3 absorber layer: An efficient step to improve device performance of $\text{CdS}/\text{Sb}_2\text{Se}_3$ solar cells," *Appl. Phys. Lett.*, vol. 105, no. 8, p. 083905, Aug. 2014, doi: 10.1063/1.4894170.
- [118] S. Yuan *et al.*, "Postsurface Selenization for High Performance Sb_2S_3 Planar Thin Film Solar Cells," *ACS Photonics*, vol. 4, no. 11, pp. 2862–2870, Nov. 2017, doi: 10.1021/acsp Photonics.7b00858.
- [119] Y. C. Choi *et al.*, " Sb_2Se_3 -Sensitized Inorganic–Organic Heterojunction Solar Cells Fabricated Using a Single-Source Precursor," *Angew. Chem., Int. Ed.*, vol. 53, no. 5, pp. 1329–1333, Jan. 2014, doi: 10.1002/anie.201308331.

- [120] Y. C. Choi *et al.*, “Efficient Inorganic–Organic Heterojunction Solar Cells Employing $\text{Sb}_2(\text{S}_x/\text{Se}_{1-x})_3$ Graded-Composition Sensitizers,” *Adv. Energy Mater.*, vol. 4, no. 7, p. 1301680, May 2014, doi: 10.1002/aenm.201301680.
- [121] Z. Li *et al.*, “9.2%-efficient core-shell structured antimony selenide nanorod array solar cells,” *Nat. Commun.*, vol. 10, no. 1, p. 125, Jan. 2019, doi: 10.1038/s41467-018-07903-6.
- [122] O. S. Hutter, L. J. Phillips, K. Durose, and J. D. Major, “6.6% efficient antimony selenide solar cells using grain structure control and an organic contact layer,” *Sol. Energy Mater. Sol. Cells*, vol. 188, pp. 177–181, Dec. 2018, doi: 10.1016/j.solmat.2018.09.004.
- [123] X. Wen *et al.*, “Vapor transport deposition of antimony selenide thin film solar cells with 7.6% efficiency,” *Nat. Commun.*, vol. 9, no. 1, p. 2179, Jun. 2018, doi: 10.1038/s41467-018-04634-6.
- [124] L. J. Phillips *et al.*, “Current Enhancement via a TiO_2 Window Layer for CSS Sb_2Se_3 Solar Cells: Performance Limits and High Voc,” *IEEE J. Photovolt.*, vol. 9, no. 2, pp. 544–551, Mar. 2019, doi: 10.1109/JPHOTOV.2018.2885836.
- [125] M. H. Braga, J. A. Ferreira, C. Lopes, and L. F. Malheiros, “Phase Transitions in the Cu–Sb–S System,” *Mater. Sci. Forum*, vol. 587–588, pp. 435–439, 2008, doi: 10.4028/www.scientific.net/MSF.587-588.435.
- [126] M. Richter, M. Hammer, T. Sonnet, and J. Parisi, “Bandgap extraction from quantum efficiency spectra of $\text{Cu}(\text{In,Ga})\text{Se}_2$ solar cells with varied grading profile and diffusion length,” *Thin Solid Films*, vol. 633, pp. 213–217, Jul. 2017, doi: 10.1016/j.tsf.2016.08.022.
- [127] J. Dong, Y. Liu, Z. Wang, and Y. Zhang, “Boosting V_{OC} of antimony chalcogenide solar cells: A review on interfaces and defects,” *Nano Sel.*, vol. 2, no. 10, pp. 1818–1848, Apr. 2021, doi: 10.1002/nano.202000288.
- [128] C. Ying, F. Guo, L. Xu, K. Lv, and C. Shi, “Ultra-thin CdS buffer layer for efficient Sb_2S_3 -sensitized TiO_2 nanorod array solar cells using Sb-thiourea complex solution,” *J. Nanopart. Res.*, vol. 23, no. 9, p. 200, Aug. 2021, doi: 10.1007/s11051-021-05321-2.
- [129] X. Jin *et al.*, “Solution processed NiO_x hole-transporting material for all-inorganic planar heterojunction Sb_2S_3 solar cells,” *Sol. Energy Mater. Sol. Cells*, vol. 185, pp. 542–548, Oct. 2018, doi: 10.1016/j.solmat.2018.06.017.
- [130] L. Zhang *et al.*, “ V_2O_5 as Hole Transporting Material for Efficient All Inorganic Sb_2S_3 Solar Cells,” *ACS Appl. Mater. Interfaces*, vol. 10, no. 32, pp. 27098–27105, Aug. 2018, doi: 10.1021/acsami.8b09843.
- [131] R. A. Miranda Gamboa, O. A. Jaramillo-Quintero, Y. A. Alarcón Altamirano, M. O. Concha-Guzmán, and M. E. Rincón, “A novel nanocomposite based on NiO_x -incorporated P3HT as hole transport material for Sb_2S_3 solar cells with enhanced device performance,” *J. Colloid Interface Sci.*, vol. 535, pp. 400–407, Feb. 2019, doi: 10.1016/j.jcis.2018.10.015.
- [132] J. P. Mitchell and D. G. Denure, “Electrical contacts on photoconductive Sb_2S_3 films,” *Thin Solid Films*, vol. 16, no. 3, pp. 285–296, Jun. 1973, doi: 10.1016/0040-6090(73)90082-5.
- [133] J. A. Chang *et al.*, “High-Performance Nanostructured Inorganic–Organic Heterojunction Solar Cells,” *Nano Lett.*, vol. 10, no. 7, pp. 2609–2612, Jul. 2010, doi: 10.1021/nl101322h.

- [134] C. P. Liu *et al.*, “Hybrid photovoltaic cells based on ZnO/Sb₂S₃/P3HT heterojunctions,” *Phys. Status Solidi B*, vol. 249, no. 3, pp. 627–633, Mar. 2012, doi: 10.1002/pssb.201147393.
- [135] B. Reeja-Jayan and A. Manthiram, “Effects of bifunctional metal sulfide interlayers on photovoltaic properties of organic–inorganic hybrid solar cells,” *RSC Adv.*, vol. 3, no. 16, pp. 5412–5421, 2013, doi: 10.1039/C3RA23055D.
- [136] J. A. Christians and P. V. Kamat, “Trap and Transfer. Two-Step Hole Injection Across the Sb₂S₃/CuSCN Interface in Solid-State Solar Cells,” *ACS Nano*, vol. 7, no. 9, pp. 7967–7974, Sep. 2013, doi: 10.1021/nn403058f.
- [137] E. Zimmermann *et al.*, “Toward High-Efficiency Solution-Processed Planar Heterojunction Sb₂S₃ Solar Cells,” *Adv. Sci. (Weinheim, Ger.)*, vol. 2, no. 5, p. 1500059, Apr. 2015, doi: 10.1002/advs.201500059.
- [138] M. S. You, C.-S. Lim, D. H. Kwon, J. H. Heo, S. H. Im, and K. J. Chae, “Oxide-free Sb₂S₃ sensitized solar cells fabricated by spin and heat-treatment of Sb(III)(thioacetamide)₂Cl₃,” *Org. Electron.*, vol. 21, no. Supplement C, pp. 155–159, Jun. 2015, doi: 10.1016/j.orgel.2015.02.015.
- [139] H. Deng *et al.*, “Efficient and stable TiO₂/Sb₂S₃ planar solar cells from absorber crystallization and Se-atmosphere annealing,” *Mater. Today Energy*, vol. 3, no. Supplement C, pp. 15–23, Mar. 2017, doi: 10.1016/j.mtener.2017.02.001.
- [140] R. Tang *et al.*, “n-Type Doping of Sb₂S₃ Light-Harvesting Films Enabling High-Efficiency Planar Heterojunction Solar Cells,” *ACS Appl. Mater. Interfaces*, vol. 10, no. 36, pp. 30314–30321, Sep. 2018, doi: 10.1021/acsami.8b08965.
- [141] C. Jiang, R. Tang, X. Wang, H. Ju, G. Chen, and T. Chen, “Alkali Metals Doping for High-Performance Planar Heterojunction Sb₂S₃ Solar Cells,” *Solar RRL*, vol. 3, no. 1, p. 1800272, Jan. 2019, doi: 10.1002/solr.201800272.
- [142] R. Tang *et al.*, “Vacuum assisted solution processing for highly efficient Sb₂S₃ solar cells,” *J. Mater. Chem. A*, vol. 6, no. 34, pp. 16322–16327, 2018, doi: 10.1039/C8TA05614E.
- [143] R. Nie, K. S. Lee, M. Hu, and S. I. Seok, “Strain Tuning via Larger Cation and Anion Codoping for Efficient and Stable Antimony-Based Solar Cells,” *Adv. Sci. (Weinheim, Ger.)*, vol. 8, no. 1, p. 2002391, Jan. 2021, doi: 10.1002/advs.202002391.
- [144] W. H. Kim, S. Woo, K.-P. Kim, S.-M. Kwon, and D.-H. Kim, “Efficient TiO₂ Surface Treatment Using Cs₂CO₃ for Solution-Processed Planar-Type Sb₂S₃ Solar Cells,” *Nanoscale Res. Lett.*, vol. 14, no. 1, p. 25, Jan. 2019, doi: 10.1186/s11671-019-2858-5.
- [145] J. Han *et al.*, “Synergistic Effect through the Introduction of Inorganic Zinc Halides at the Interface of TiO₂ and Sb₂S₃ for High-Performance Sb₂S₃ Planar Thin-Film Solar Cells,” *ACS Appl. Mater. Interfaces*, vol. 12, no. 39, pp. 44297–44306, Sep. 2020, doi: 10.1021/acsami.0c11550.
- [146] H. Ning *et al.*, “Enhancing the efficiency of Sb₂S₃ solar cells using dual-functional potassium doping,” *Sol. Energy Mater. Sol. Cells*, vol. 221, p. 110816, Mar. 2021, doi: 10.1016/j.solmat.2020.110816.
- [147] J. Han *et al.*, “Solution-Processed Sb₂S₃ Planar Thin Film Solar Cells with a Conversion Efficiency of 6.9% at an Open Circuit Voltage of 0.7 V Achieved via Surface Passivation by a SbCl₃ Interface Layer,” *ACS Appl. Mater. Interfaces*, vol. 12, no. 4, pp. 4970–4979, Jan. 2020, doi: 10.1021/acsami.9b15148.

- [148] P. Büttner *et al.*, "Adjusting Interfacial Chemistry and Electronic Properties of Photovoltaics Based on a Highly Pure Sb₂S₃ Absorber by Atomic Layer Deposition," *ACS Appl. Energy Mater.*, vol. 2, no. 12, pp. 8747–8756, Dec. 2019, doi: 10.1021/acsaem.9b01721.
- [149] P. Büttner *et al.*, "ZnS Ultrathin Interfacial Layers for Optimizing Carrier Management in Sb₂S₃-based Photovoltaics," *ACS Appl. Mater. Interfaces*, vol. 13, no. 10, pp. 11861–11868, Mar. 2021, doi: 10.1021/acsami.0c21365.
- [150] J. Chen *et al.*, "Preferentially oriented large antimony trisulfide single-crystalline cuboids grown on polycrystalline titania film for solar cells," *Commun. Chem.*, vol. 2, no. 1, p. 121, Oct. 2019, doi: 10.1038/s42004-019-0225-1.
- [151] L. Zhang, W. Lian, X. Zhao, Y. Yin, T. Chen, and C. Zhu, "Sb₂S₃ Seed-Mediated Growth of Low-Defect Sb₂S₃ on a TiO₂ Substrate for Efficient Solar Cells," *ACS Appl. Energy Mater.*, vol. 3, no. 12, pp. 12417–12422, Dec. 2020, doi: 10.1021/acsaem.0c02400.
- [152] S. H. Im *et al.*, "Toward Interaction of Sensitizer and Functional Moieties in Hole-Transporting Materials for Efficient Semiconductor-Sensitized Solar Cells," *Nano Lett.*, vol. 11, no. 11, pp. 4789–4793, Nov. 2011, doi: 10.1021/nl2026184.
- [153] K. Tsujimoto *et al.*, "TiO₂ Surface Treatment Effects by Mg²⁺, Ba²⁺, and Al³⁺ on Sb₂S₃ Extremely Thin Absorber Solar Cells," *J. Phys. Chem. C*, vol. 116, no. 25, pp. 13465–13471, Jun. 2012, doi: 10.1021/jp208937j.
- [154] C.-S. Lim, S. H. Im, H. Kim, J. A. Chang, Y. H. Lee, and S. I. Seok, "Enhancing the device performance of Sb₂S₃-sensitized heterojunction solar cells by embedding Au nanoparticles in the hole-conducting polymer layer," *Phys. Chem. Chem. Phys.*, vol. 14, no. 10, pp. 3622–3626, 2012, doi: 10.1039/C2CP23650H.
- [155] J. A. Chang *et al.*, "Panchromatic Photon-Harvesting by Hole-Conducting Materials in Inorganic–Organic Heterojunction Sensitized-Solar Cell through the Formation of Nanostructured Electron Channels," *Nano Lett.*, vol. 12, no. 4, pp. 1863–1867, Apr. 2012, doi: 10.1021/nl204224v.
- [156] J. C. Cardoso *et al.*, "Fabrication of coaxial TiO₂/Sb₂S₃ nanowire hybrids for efficient nanostructured organic-inorganic thin film photovoltaics," *Chem. Commun.*, vol. 48, no. 22, pp. 2818–2820, 2012, doi: 10.1039/C2CC17573H.
- [157] J. Zhong *et al.*, "High Efficiency Solar Cells As Fabricated by Sb₂S₃-Modified TiO₂ Nanofibrous Networks," *ACS Appl. Mater. Interfaces*, vol. 5, no. 17, pp. 8345–8350, Sep. 2013, doi: 10.1021/am401273r.
- [158] Z. Lan, X. Zhang, J. Wu, J. Lin, M. Huang, and H. Zhao, "A novel photoelectrochemical solar cell with high efficiency in converting ultraviolet light to electricity," *Electrochimica Acta*, vol. 108, pp. 337–342, Oct. 2013, doi: 10.1016/j.electacta.2013.06.121.
- [159] J. K. Kim, G. Veerappan, N. Heo, D. H. Wang, and J. H. Park, "Efficient Hole Extraction from Sb₂S₃ Heterojunction Solar Cells by the Solid Transfer of Preformed PEDOT:PSS Film," *J. Phys. Chem. C*, vol. 118, no. 39, pp. 22672–22677, Oct. 2014, doi: 10.1021/jp507652r.
- [160] R. Lindblad *et al.*, "Energy level alignment in TiO₂/metal sulfide/polymer interfaces for solar cell applications," *Phys. Chem. Chem. Phys.*, vol. 16, no. 32, pp. 17099–17107, 2014, doi: 10.1039/C4CP01581A.

- [161] K. C. Gödel *et al.*, "Efficient room temperature aqueous Sb_2S_3 synthesis for inorganic–organic sensitized solar cells with 5.1% efficiencies," *Chem. Commun.*, vol. 51, no. 41, pp. 8640–8643, 2015, doi: 10.1039/C5CC01966D.
- [162] N. Ali *et al.*, "Antimony sulphide, an absorber layer for solar cell application," *Appl. Phys. A: Mater. Sci. Process.*, vol. 122, no. 1, p. 23, Dec. 2015, doi: 10.1007/s00339-015-9542-0.
- [163] C. Lan *et al.*, "Microstructural and Optical Properties of Sb_2S_3 Film Thermally Evaporated from Antimony Pentasulfide and Efficient Planar Solar Cells," *Phys. Status Solidi RRL*, vol. 12, no. 6, p. 1800025, Mar. 2018, doi: 10.1002/pssr.201800025.
- [164] M. Y. Versavel and J. A. Haber, "Structural and optical properties of amorphous and crystalline antimony sulfide thin-films," *Thin Solid Films*, vol. 515, no. 18, pp. 7171–7176, Jun. 2007, doi: 10.1016/j.tsf.2007.03.043.
- [165] M. I. Medina-Montes, Z. Montiel-González, N. R. Mathews, and X. Mathew, "The influence of film deposition temperature on the subsequent post-annealing and crystallization of sputtered Sb_2S_3 thin films," *J. Phys. Chem. Solids*, vol. 111, no. Supplement C, pp. 182–189, Dec. 2017, doi: 10.1016/j.jpcs.2017.07.035.
- [166] H. Zhang *et al.*, "Controllable orientations for Sb_2S_3 solar cells by vertical VTD method," *Prog. Photovoltaics*, vol. 28, no. 8, pp. 823–832, Aug. 2020, doi: 10.1002/pip.3278.
- [167] Y. Zeng *et al.*, "Quasi-Vertically-Orientated Antimony Sulfide Inorganic Thin-Film Solar Cells Achieved by Vapor Transport Deposition," *ACS Appl. Mater. Interfaces*, vol. 12, no. 20, pp. 22825–22834, May 2020, doi: 10.1021/acsami.0c02697.
- [168] R. Wang *et al.*, "Improving the performance of Sb_2S_3 thin-film solar cells by optimization of VTD source-substrate proximity," *Sol. Energy*, vol. 220, pp. 942–948, May 2021, doi: 10.1016/j.solener.2021.03.052.
- [169] Y. Zeng, F. Liu, M. Green, and X. Hao, "Fabrication of Sb_2S_3 planar thin film solar cells with closed-space sublimation method," in *2018 IEEE 7th World Conference on Photovoltaic Energy Conversion (WCPEC) (A Joint Conference of 45th IEEE PVSC, 28th PVSEC & 34th EU PVSEC)*, Jun. 2018, pp. 0870–0872. doi: 10.1109/PVSC.2018.8547305.
- [170] L. Guo *et al.*, "Scalable and efficient Sb_2S_3 thin-film solar cells fabricated by close space sublimation," *APL Mater.*, vol. 7, no. 4, p. 041105, Apr. 2019, doi: 10.1063/1.5090773.
- [171] Ž. Živković, N. Štrbac, D. Živković, D. Grujičić, and B. Boyanov, "Kinetics and mechanism of Sb_2S_3 oxidation process," *Thermochim. Acta*, vol. 383, no. 1, pp. 137–143, Feb. 2002, doi: 10.1016/S0040-6031(01)00688-8.
- [172] W. A. West and A. W. C. Menzies, "The Vapor Pressures of Sulphur between 100° and 550° with related Thermal Data," *J. Phys. Chem.*, vol. 33, no. 12, pp. 1880–1892, Dec. 1929, doi: 10.1021/j150306a002.
- [173] M. T. S. Nair, Y. Peña, J. Campos, V. M. García, and P. K. Nair, "Chemically Deposited Sb_2S_3 and Sb_2S_3 -CuS Thin Films," *J. Electrochem. Soc.*, vol. 145, no. 6, pp. 2113–2120, Jun. 1998, doi: 10.1149/1.1838605.
- [174] S. Messina, M. T. S. Nair, and P. K. Nair, "Antimony sulphide thin film as an absorber in chemically deposited solar cells," *J. Phys. D: Appl. Phys.*, vol. 41, no. 9, p. 095112, Apr. 2008, doi: 10.1088/0022-3727/41/9/095112.

- [175] H. Maghraoui-Meherzi, T. Ben Nasr, N. Kamoun, and M. Dachraoui, "Structural, morphology and optical properties of chemically deposited Sb_2S_3 thin films," *Phys. B (Amsterdam, Neth.)*, vol. 405, no. 15, pp. 3101–3105, Aug. 2010, doi: 10.1016/j.physb.2010.04.020.
- [176] J. Ota and S. K. Srivastava, "Tartaric Acid Assisted Growth of Sb_2S_3 Nanorods by a Simple Wet Chemical Method," *Cryst. Growth Des.*, vol. 7, no. 2, pp. 343–347, Feb. 2007, doi: 10.1021/cg0605537.
- [177] H. Wedemeyer *et al.*, "Nanocrystalline solar cells with an antimony sulfide solid absorber by atomic layer deposition," *Energy Environ. Sci.*, vol. 6, no. 1, pp. 67–71, 2013, doi: 10.1039/C2EE23205G.
- [178] H.-J. Jo, S. H. Kim, J. S. Kim, S.-J. Lee, and D.-H. Kim, "Time-resolved photocurrent of an organic-inorganic hybrid solar cell based on Sb_2S_3 ," *J. Korean Phys. Soc.*, vol. 69, no. 4, pp. 541–546, Aug. 2016, doi: 10.3938/jkps.69.541.
- [179] M. K. S. Barr *et al.*, "Engineering a three-dimensional, photoelectrochemically active p-NiO/i- Sb_2S_3 junction by atomic layer deposition," *Electrochim. Acta*, vol. 179, pp. 504–511, Oct. 2015, doi: 10.1016/j.electacta.2015.07.016.
- [180] P. Sun *et al.*, "In-situ growth of antimony sulfide in carbon nanoparticle matrix: Enhanced electrocatalytic activity as counter electrode in dye-sensitized solar cells," *J. Power Sources*, vol. 319, pp. 219–226, Jul. 2016, doi: 10.1016/j.jpowsour.2016.04.002.
- [181] W. Wang, F. Strössner, E. Zimmermann, and L. Schmidt-Mende, "Hybrid solar cells from Sb_2S_3 nanoparticle ink," *Sol. Energy Mater. Sol. Cells*, vol. 172, pp. 335–340, Dec. 2017, doi: 10.1016/j.solmat.2017.07.046.
- [182] J. Rodriguez-Castro, P. Dale, M. F. Mahon, K. C. Molloy, and L. M. Peter, "Deposition of Antimony Sulfide Thin Films from Single-Source Antimony Thiolate Precursors," *Chem. Mater.*, vol. 19, no. 13, pp. 3219–3226, Jun. 2007, doi: 10.1021/cm070405j.
- [183] J. Rodriguez-Castro *et al.*, "Formation of antimony sulfide powders and thin films from single-source antimony precursors," *J. Mater. Chem.*, vol. 18, no. 44, pp. 5399–5405, 2008, doi: 10.1039/B810947H.
- [184] F. T. F. O'Mahony *et al.*, "Low-Temperature Solution Processing of Mesoporous Metal-Sulfide Semiconductors as Light-Harvesting Photoanodes," *Angew. Chem., Int. Ed.*, vol. 52, no. 46, pp. 12047–12051, Nov. 2013, doi: 10.1002/anie.201305276.
- [185] V. V. Killedar, K. Y. Rajpure, P. S. Patil, and C. H. Bhosale, "Transient photoconductivity measurements of spray deposited Sb_2S_3 and Bi_2S_3 thin films from non-aqueous medium," *Mater. Chem. Phys.*, vol. 59, no. 3, pp. 237–241, Jun. 1999, doi: 10.1016/S0254-0584(99)00044-9.
- [186] K. Y. Rajpure and C. H. Bhosale, "Effect of composition on the structural, optical and electrical properties of sprayed Sb_2S_3 thin films prepared from non-aqueous medium," *J. Phys. Chem. Solids*, vol. 61, no. 4, pp. 561–568, Apr. 2000, doi: 10.1016/S0022-3697(99)00240-1.
- [187] K. Y. Rajpure and C. H. Bhosale, "(Photo)electrochemical investigations on spray deposited n- Sb_2S_3 thin film/polyiodide/C photoelectrochemical solar cells," *Mater. Chem. Phys.*, vol. 63, no. 3, pp. 263–269, Mar. 2000, doi: 10.1016/S0254-0584(99)00233-3.

- [188] K. Y. Rajpure and C. H. Bhosale, "Preparation and characterization of spray deposited photoactive Sb_2S_3 and Sb_2Se_3 thin films using aqueous and non-aqueous media," *Mater. Chem. Phys.*, vol. 73, no. 1, pp. 6–12, Jan. 2002, doi: 10.1016/S0254-0584(01)00350-9.
- [189] M. Medles *et al.*, "Raman and Optical Studies of spray pyrolysed Sb_2S_3 thin films," *J. Optoelectron. Adv. Mater.*, vol. 16, no. 5–6, pp. 726–731, 2014.
- [190] R. Boughalmi, A. Boukhachem, M. Kahlaoui, H. Maghraoui, and M. Amlouk, "Physical investigations on Sb_2S_3 sprayed thin film for optoelectronic applications," *Mater. Sci. Semicond. Process.*, vol. 26, pp. 593–602, Oct. 2014, doi: 10.1016/j.mssp.2014.05.059.
- [191] D. R. Lide, Ed., *CRC Handbook of Chemistry and Physics*, 87th ed. Boca Raton, FL, U.S.A.: CRC Press, 2006.
- [192] I. I. Ozturk *et al.*, "Interaction of antimony(III) chloride with thiourea, 2-mercapto-5-methyl-benzimidazole, 3-methyl-2-mercaptobenzothiazole, 2-mercaptopyrimidine, and 2-mercaptopyridine," *J. Coord. Chem.*, vol. 64, no. 22, pp. 3859–3871, Nov. 2011, doi: 10.1080/00958972.2011.633603.
- [193] G. Q. Zhong, M. Gu, and Y. Q. Jia, "Solid-Solid Synthesis, Characterization and Thermal Decomposition of Thiourea Complex of Antimony Trichloride," *Adv. Mater. Res. (Durten-Zurich, Switz.)*, vol. 549, pp. 126–130, 2012, doi: 10.4028/www.scientific.net/AMR.549.126.
- [194] Y. Zhang *et al.*, "Phosphotungstic Acid Regulated Chemical Bath Deposition of Sb_2S_3 for High-Efficiency Planar Heterojunction Solar Cell," *Energy Technol. (Weinheim, Ger.)*, vol. 6, no. 11, pp. 2126–2131, Nov. 2018, doi: 10.1002/ente.201800238.
- [195] I. Grozdanov, "A simple and low-cost technique for electroless deposition of chalcogenide thin films," *Semicond. Sci. Technol.*, vol. 9, no. 6, p. 1234, 1994.
- [196] P. Büttner *et al.*, "Solid state interdigitated Sb_2S_3 based TiO_2 nanotube solar cells," *RSC Adv.*, vol. 10, no. 47, pp. 28225–28231, 2020, doi: 10.1039/D0RA04123H.
- [197] S.-J. Lee *et al.*, "Approach to Transparent Photovoltaics Based on Wide Band Gap Sb_2S_3 Absorber Layers and Optics-Based Device Optimization," *ACS Appl. Energy Mater.*, vol. 3, no. 12, pp. 12644–12651, Dec. 2020, doi: 10.1021/acsaem.0c02552.
- [198] K. P. Musselman *et al.*, "Improved Exciton Dissociation at Semiconducting Polymer:ZnO Donor:Acceptor Interfaces via Nitrogen Doping of ZnO," *Adv. Funct. Mater.*, vol. 24, no. 23, pp. 3562–3570, Jun. 2014, doi: 10.1002/adfm.201303994.
- [199] D. Muñoz-Rojas, V. H. Nguyen, C. Masse de la Huerta, S. Aghazadehchors, C. Jiménez, and D. Bellet, "Spatial Atomic Layer Deposition (SALD), an emerging tool for energy materials. Application to new-generation photovoltaic devices and transparent conductive materials," *C. R. Phys.*, vol. 18, no. 7, pp. 391–400, Sep. 2017, doi: 10.1016/j.crhy.2017.09.004.
- [200] David Muñoz-Rojas, "Spatial Atomic Layer Deposition," in *Chemical Vapor Deposition for Nanotechnology*, Viet Huong Nguyen, Ed. Rijeka: IntechOpen, 2019, p. Ch. 1. doi: 10.5772/intechopen.82439.

- [201] V. H. Nguyen, A. Sekkat, C. Jiménez, D. Muñoz, D. Bellet, and D. Muñoz-Rojas, "Impact of precursor exposure on process efficiency and film properties in spatial atomic layer deposition," *Chem. Eng. J. (Amsterdam, Neth.)*, vol. 403, p. 126234, Jan. 2021, doi: 10.1016/j.cej.2020.126234.
- [202] M. Pichumani, P. Bagheri, K. M. Poduska, W. González-Viñas, and A. Yethiraj, "Dynamics, crystallization and structures in colloid spin coating," *Soft Matter*, vol. 9, no. 12, pp. 3220–3229, 2013, doi: 10.1039/C3SM27455A.
- [203] Kaienburg, P., Klingebiel, B., and Kirchartz, T., "Spin-coated planar Sb₂S₃ hybrid solar cells approaching 5% efficiency," *Beilstein J. Nanotechnol.*, vol. 9, pp. 2114–2124, 2018, doi: 10.3762/bjnano.9.200.
- [204] Y. Liu, C. Chen, Y. Zhou, R. Kondrotas, and J. Tang, "Butyldithiocarbamate acid solution processing: its fundamentals and applications in chalcogenide thin film solar cells," *J. Mater. Chem. C*, vol. 7, no. 36, pp. 11068–11084, 2019, doi: 10.1039/C9TC02837D.
- [205] J. Li, X. Liu, and J. Yao, "The Enhanced Photovoltaic Performance of Sb₂S₃ Solar Cells by Thermal Decomposition of Antimony Ethyl Xanthate with Thiourea Doping," *Energy Technol. (Weinheim, Ger.)*, vol. 8, no. 4, p. 1900841, Apr. 2020, doi: 10.1002/ente.201900841.
- [206] N. Sahu, B. Parija, and S. Panigrahi, "Fundamental understanding and modeling of spin coating process: A review," *Indian J. Phys.*, vol. 83, no. 4, pp. 493–502, Apr. 2009, doi: 10.1007/s12648-009-0009-z.
- [207] R. Tang *et al.*, "Hydrothermal deposition of antimony selenosulfide thin films enables solar cells with 10% efficiency," *Nat. Energy*, vol. 5, no. 8, pp. 587–595, Aug. 2020, doi: 10.1038/s41560-020-0652-3.
- [208] F. Yang *et al.*, "Improved charge transfer and photoelectrochemical performance of CuI/Sb₂S₃/TiO₂ heterostructure nanotube arrays," *Journal of Colloid and Interface Science*, vol. 464, pp. 1–9, Feb. 2016, doi: 10.1016/j.jcis.2015.11.004.
- [209] G. Peng *et al.*, "Substrate placement angle-dependent growth of dandelion-like TiO₂ nanorods for solid-state semiconductor-sensitized solar cells," *RSC Adv.*, vol. 4, no. 95, pp. 53335–53343, 2014, doi: 10.1039/C4RA10611C.
- [210] D. Perednis and L. J. Gauckler, "Thin Film Deposition Using Spray Pyrolysis," *Journal of Electroceramics*, vol. 14, no. 2, pp. 103–111, Mar. 2005, doi: 10.1007/s10832-005-0870-x.
- [211] S. Rahemi Ardekani, A. Sabour Rouh Aghdam, M. Nazari, A. Bayat, E. Yazdani, and E. Saievar-Iranizad, "A comprehensive review on ultrasonic spray pyrolysis technique: Mechanism, main parameters and applications in condensed matter," *Journal of Analytical and Applied Pyrolysis*, vol. 141, p. 104631, Aug. 2019, doi: 10.1016/j.jaap.2019.104631.
- [212] R. J. Lang, "Ultrasonic Atomization of Liquids," *The Journal of the Acoustical Society of America*, vol. 34, no. 1, pp. 6–8, Jan. 1962, doi: 10.1121/1.1909020.
- [213] P. Majerič and R. Rudolf, "Advances in Ultrasonic Spray Pyrolysis Processing of Noble Metal Nanoparticles—Review," *Materials*, vol. 13, no. 16, 2020, doi: 10.3390/ma13163485.
- [214] M. Krunk *et al.*, "Composition and structure of CuInS₂ films prepared by spray pyrolysis," *Thin Solid Films*, vol. 361–362, pp. 61–64, Feb. 2000, doi: 10.1016/S0040-6090(99)00835-4.

- [215] S. Polivtseva, I. O. Acik, A. Katerski, A. Mere, V. Mikli, and M. Krunks, "Spray Pyrolysis Deposition of Sn_xS_y Thin Films," *Energy Procedia*, vol. 60, pp. 156–165, Jan. 2014, doi: 10.1016/j.egypro.2014.12.358.
- [216] M. Kriisa, M. Krunks, I. Oja Acik, E. Kärber, and V. Mikli, "The effect of tartaric acid in the deposition of Sb_2S_3 films by chemical spray pyrolysis," *Mater. Sci. Semicond. Process.*, vol. 40, pp. 867–872, Dec. 2015, doi: 10.1016/j.mssp.2015.07.049.
- [217] J. Rodriguez-Castro, M. F. Mahon, and K. C. Molloy, "Aerosol-Assisted CVD of Antimony Sulfide from Antimony Dithiocarbamates," *Chem. Vap. Deposition*, vol. 12, no. 10, pp. 601–607, Oct. 2006, doi: 10.1002/cvde.200506369.
- [218] M. A. Khwaja, T. J. Cardwell, and R. J. Magee, "Thermal studies on arsenic, antimony and bismuth alkylxanthate complexes," *Analytica Chimica Acta*, vol. 64, no. 1, pp. 9–17, Mar. 1973, doi: 10.1016/S0003-2670(00)86887-7.
- [219] T. Alqahtani, M. D. Khan, D. J. Kelly, S. J. Haigh, D. J. Lewis, and P. O'Brien, "Synthesis of $\text{Bi}_{2-2x}\text{Sb}_{2x}\text{S}_3$ ($0 \leq x \leq 1$) solid solutions from solventless thermolysis of metal xanthate precursors," *J. Mater. Chem. C*, vol. 6, no. 46, pp. 12652–12659, 2018, doi: 10.1039/C8TC02374C.
- [220] A. J. Vreugdenhil, S. H. R. Brienne, I. S. Butler, J. A. Finch, and R. D. Markwell, "Infrared spectroscopic determination of the gas-phase thermal decomposition products of metal-ethylidithiocarbonate complexes," *Spectrochimica Acta Part A: Molecular and Biomolecular Spectroscopy*, vol. 53, no. 12, pp. 2139–2151, Oct. 1997, doi: 10.1016/S1386-1425(97)00144-3.
- [221] S. Kharbish, E. Libowitzky, and A. Beran, "Raman spectra of isolated and interconnected pyramidal XS_3 groups ($X = \text{Sb, Bi}$) in stibnite, bismuthinite, kermesite, stephanite and bournonite," *Eur. J. Mineral.*, vol. 21, no. 2, pp. 325–333, Apr. 2009, doi: 10.1127/0935-1221/2009/0021-1914.
- [222] V. Janošević, M. Mitrić, N. Bundaleski, Z. Rakočević, and I. L. Validžić, "High-efficiency Sb_2S_3 -based hybrid solar cell at low light intensity: cell made of synthesized Cu and Se-doped Sb_2S_3 ," *Prog. Photovoltaics*, vol. 24, no. 5, pp. 704–715, May 2016, doi: 10.1002/pip.2724.
- [223] L. Zheng *et al.*, "Solid-state nanocrystalline solar cells with an antimony sulfide absorber deposited by an in situ solid-gas reaction," *J. Mater. Chem. A*, vol. 5, no. 10, pp. 4791–4796, 2017, doi: 10.1039/C7TA00291B.
- [224] J. Escorcia-García, D. Becerra, M. T. S. Nair, and P. K. Nair, "Heterojunction $\text{CdS/Sb}_2\text{S}_3$ solar cells using antimony sulfide thin films prepared by thermal evaporation," *Thin Solid Films*, vol. 569, pp. 28–34, Oct. 2014, doi: 10.1016/j.tsf.2014.08.024.
- [225] M. Kamruzzaman, L. Chaoping, F. Yishu, A. K. M. Farid Ul Islam, and J. A. Zapien, "Atmospheric annealing effect on $\text{TiO}_2/\text{Sb}_2\text{S}_3/\text{P3HT}$ heterojunction hybrid solar cell performance," *RSC Adv.*, vol. 6, no. 101, pp. 99282–99290, 2016, doi: 10.1039/C6RA20378G.
- [226] S. Ryu, N. Y. Ha, Y. H. Ahn, J.-Y. Park, and S. Lee, "Light intensity dependence of organic solar cell operation and dominance switching between Shockley–Read–Hall and bimolecular recombination losses," *Scientific Reports*, vol. 11, no. 1, p. 16781, Aug. 2021, doi: 10.1038/s41598-021-96222-w.
- [227] M. D. King, S. Platnick, W. P. Menzel, S. A. Ackerman, and P. A. Hubanks, "Spatial and Temporal Distribution of Clouds Observed by MODIS Onboard the Terra and Aqua Satellites," *IEEE Trans. Geosci. Electron.*, vol. 51, no. 7, pp. 3826–3852, Jul. 2013, doi: 10.1109/TGRS.2012.2227333.

- [228] G. Gottardi, "The crystal structure of xanthates II. Antimonious xanthate," *Z. Kristallogr. - Cryst. Mater.*, vol. 115, no. 1–6, pp. 451–459, 1961, doi: 10.1524/zkri.1961.115.16.451.
- [229] J. Madarász and G. Pokol, "Comparative evolved gas analyses on thermal degradation of thiourea by coupled TG-FTIR and TG/DTA-MS instruments," *J. Therm. Anal. Calorim.*, vol. 88, no. 2, pp. 329–336, May 2007, doi: 10.1007/s10973-006-8058-4.
- [230] F. Cornea, L. Ivan, C. Pentică, and E. Segal, "On the thermal stability of some thioamides," *Thermochim. Acta*, vol. 86, pp. 25–32, Apr. 1985, doi: 10.1016/0040-6031(85)87030-1.

Acknowledgements

I acknowledge my supervisors Prof. Malle Krunks, PhD, and Prof. Ilona Oja Acik, PhD, for their contribution and guidance.

I appreciate the collaborative input of past and present members of the Lab. of Thin Film Chemical Technologies at Tallinn University of Technology, and the co-authors from other institutions. I am grateful to Dr. Atanas Katerski for guidance on the experimental aspects of this study. Moreover, I am grateful to Dr. Erki Kärber for discussion on interpreting measurement results, XES measurements, and advice on academic writing.

I am thankful to Dr. Jasper Adamson from the National Institute of Chemical Physics and Biophysics for the introduction to 1D and 2D NMR analysis. I thank Dr. Kaia Tõnsuaadu from the Lab. of Inorganic Materials at Tallinn University of Technology for the introduction to TG/DTA-EGA-MS analysis.

I am grateful to Dr. Valdek Mikli, Dr. Olga Volobujeva from the Lab. of Optoelectronic Materials at Tallinn University of Technology for SEM and EDX measurements, Eng. Jekaterina Kozlova from the Institute of Physics at Tartu University for SEM measurements, and Prof. Maarja Grossberg, PhD, from the Lab. of Optoelectronic Materials at Tallinn University of Technology for access to Raman measurements.

I would like to thank the following funding sources for financial support during the course of the work in my thesis: the Estonian Ministry of Education and Research project IUT19-4, the Estonian Research Council grant PRG627, the European Regional Development Fund project TK141 “Advanced materials and high-technology devices for energy recuperation systems”, the project ETAG21014 “Development of Semi-Transparent Bifacial Thin Film Solar Cells for Innovative Applications” contract with the Research Council of Lithuania (LMTLT), No S-BMT-21-1(LT08-2-LMT-K-01-003) financed by Iceland, Liechtenstein and Norway through the EEA Grants, and the European Council grant H2020 ERA Chair Emerging next generation photovoltaics, 5GSOLAR (2020–2026) Grant agreement ID: 952509. The research in this thesis was also partially supported by ASTRA “TUT Institutional Development Programme for 2016–2022” Graduate School of Functional Materials and Technologies. DoRa+ 1.1 travel scholarships to international conferences were financed by the Archimedes Foundation.

Finally, I offer my sincerest gratitude to my family whose support throughout the progression of this thesis was paramount.

Abstract

Deposition of Sb_2S_3 thin films by ultrasonic spray pyrolysis for photovoltaic applications

Converting sunlight to useable energy is one of the major processes that can satisfy the ever increasing global demand for electricity, while abiding by the conditions for climate neutrality. Evidently, converting sunlight to electricity does not pollute the environment or cause global warming. In addition, emerging technologies are based on affordable and available raw materials in order to intensify energy independence, and to decrease the environmental impact of freighting. However, environmentally friendly production of solar cells does entail a frugal consumption of materials and energy. To that end, novel solar cell concepts are being developed for various fields of application to produce pollution free energy. Some of these applications are, for example, semitransparent solar windows, tandem and bifacial solar cells. In addition to roof-mounted installations, building and product integrated devices, e.g. photovoltaic greenhouse glass, are also being developed.

As the outlined applications require stable performance of photovoltaics for decades, research on solar cells based on a stable inorganic absorber, e.g. Sb_2S_3 , has become relevant. Ensuring the formation of a continuous Sb_2S_3 film with an appropriate thickness is the most basic requirement to create a solar cell with appreciable power conversion efficiency. However, continuous phase pure Sb_2S_3 thin films, and corresponding solar cells have not been prepared by ultrasonic spray pyrolysis. Ultrasonic spray pyrolysis is an appropriate method for the task, as it is established, applicable in air, robust, rapid, and area-scalable.

Therefore, the topic of this thesis is to prepare continuous phase pure Sb_2S_3 thin films for photovoltaic applications by ultrasonic spray pyrolysis in air to assess whether these films could be applied as the absorber in planar solar cells. In order to achieve the aim of the study, the effect of deposition temperature, precursor solution composition and concentration on the phase composition, elemental composition, optical properties and morphology of the prepared Sb_2S_3 thin films was investigated. In addition, solar cells were prepared based on the Sb_2S_3 thin films grown by ultrasonic spray pyrolysis, and the respective physical output parameters were studied.

Films grown by spraying a solution of SbCl_3 and thiourea in a molar ratio of 1/3 or 1/6 were investigated. Spraying a solution of SbCl_3 and thiourea in a molar ratio of 1/3 at a temperature of 220°C or a solution of SbCl_3 and thiourea in a molar ratio of 1/6 at 210°C or 220°C yielded discontinuous crystalline phase pure Sb_2S_3 films. On the contrary, spraying a solution of SbCl_3 and thiourea in a molar ratio of 1/6 at a temperature of 200°C yielded a discontinuous amorphous phase pure Sb_2S_3 thin film, which crystallized, yet did not change in morphology after heat treatment in vacuum at 170°C. Spraying a solution of SbCl_3 and thiourea in a molar ratio of 1/3 at a temperature of 200°C or 210°C yielded a continuous amorphous 70–90 nm thick phase pure Sb_2S_3 thin film. Heat treatment of these films in vacuum at 170°C resulted in continuous crystalline phase pure Sb_2S_3 thin films. Thus, a two-step process proved suitable to deposit continuous uniform phase pure Sb_2S_3 thin films.

Sb_2S_3 thin film that had been deposited from a solution of SbCl_3 and thiourea in a molar ratio of 1/3 at a temperature of 200°C, and heat treated, were tested in planar thin film solar cells. According to the results of this study, the power conversion efficiency of solar cells depends on the thickness of the Sb_2S_3 absorber film. The highest power conversion

efficiency of up to 5.5 % was achieved in planar solar cells of ITO/TiO₂/Sb₂S₃/P3HT/Au by employing a 100 nm thick Sb₂S₃ thin film. Preliminary results indicate that, in principle, the Sb₂S₃ thin films grown by ultrasonic spray pyrolysis are applicable as the absorber film in planar solar cells. However, further research and development is needed, because the films were not sufficiently uniform. The results of the storage time test indicate that the power conversion efficiency of an unencapsulated Sb₂S₃ solar cell is more stable over time compared to organic or perovskite photovoltaics.

According to the knowledge at the time, it was unknown whether and how phase pure Sb₂S₃ thin films could be deposited from solutions of other coordination complexes. The suitability of antimony ethyl xanthate as a precursor for ultrasonic spray pyrolysis was assessed based on the results of the thermal analysis study. Antimony ethyl xanthate decomposed below 170°C into Sb₂S₃ in an inert atmosphere, but oxidized in air. Therefore, a two-step process was applied to deposit uniform continuous Sb₂S₃ thin films. Amorphous Sb₂S₃ thin films were deposited at a temperature of 215°C by ultrasonic spray pyrolysis in air from a solution of antimony ethyl xanthate and thiourea or thioacetamide in a molar ratio of 1/3 or 1/10. Heat treatment at a temperature of 225°C in vacuum proved appropriate to crystallize these thin films. The crystallized Sb₂S₃ thin films had $E_g = 1.8$ eV and $S/Sb = 1.5$ (thiourea based) or $S/Sb = 1.4$ (thioacetamide based).

In conclusion, the preparation of compact phase pure Sb₂S₃ thin films by ultrasonic spray pyrolysis in air from a halogenide-containing and -free coordination complex solution was reported for the first time in the scope of this study. It was proven that highly efficient planar solar cells can be prepared from continuous Sb₂S₃ thin films grown by ultrasonic spray pyrolysis in air. In addition, it was demonstrated that the back-contact-less stack of glass/ITO/TiO₂/Sb₂S₃ is in principle suitable for semitransparent photovoltaic applications, e.g. solar windows, bifacial tandem devices, as well as building and product integrated devices. Thus, the results of this study are useful for the preparation of continuous phase pure Sb₂S₃ thin films in an air environment, and also for the research and development of conventional and semitransparent solar cells and products based thereon.

Lühikokkuvõte

Päikesepatareides rakendatavate Sb_2S_3 õhukeste kilede sadestamine ultrahelipihustuspürolüüsi meetodil

Päikesevalgusest energia tootmine on üks peamisi tehnoloogiad, millega täita pidevalt kasvavat ülemaailmset elektrienergia nõudlust kliimaneutraalsel viisil. Teatavasti ei saasta päikesevalgusest energia tootmine keskkonda ega põhjusta kliimasoojenemist. Lisaks põhinevad uued arendamisjärgus tehnoloogiad soodsal ja kättesaadaval toormel, et suurendada energiatootmise iseseisvust ja vähendada transpordi mõju keskkonnale. Selleks, et toota päikesepatareid keskkonnasõbralikul viisil, on eeldatud, et materjali ja energiat tarbitakse säästlikult. Seetõttu kavandatakse ka uusi päikesepatareilahendusi erinevate kasutusvaldkondade jaoks. Uudsete rakenduste sekka kuulub näiteks päikesepatareide integreerimine läbipaistvates aknaklaasides, paaris- ja kahepoolsetes seadistes. Lisaks katusepaigaldistele on arendamisel ka ehitis- ja tooteintegreeritud seadised, nt päikesepatareiga kaetud kasvuhooneklaas.

Päikesepatareide tööviime peab püsima aastakümnete vältel, mistõttu on oluline arendada vastupidavatel anorgaanilistel neeldumiskihtidel, nt Sb_2S_3 , põhinevaid päikesepatareid. Selleks, et valmistada arvestatava kasuteguriga päikesepatarei, peab Sb_2S_3 kile olema eelkõige pidev ja sobiva paksusega. Seni pole pidevaid faasipuhtaid Sb_2S_3 õhukesti kilesid ega asjakohaseid päikesepatareid ultrahelipihustuspürolüüsi meetodit rakendades valmistatud. Ultrahelipihustuspürolüüs sobib antud ülesande täitmiseks, sest see on kauaaegse arengu läbinud kiire võimekas ja suure tootmismahuga meetod, mida saab õhus rakendada.

Käesoleva doktoritöö eesmärgiks oli valmistada faasipuhtad pidevad Sb_2S_3 õhukest kiled ultrahelipihustuspürolüüsi meetodil, et hinnata, kuivõrd rakendatavad need on päikesepatareides. Töö eesmärgi saavutamiseks uuriti, kuidas sadestustemperatuur, lähteaine lahuse koostis ja lähteainete kontsentratsioon mõjutavad Sb_2S_3 õhukeste kilede faasi- ja elementkoostist, optilisi omadusi ja morfoloogiat. Lisaks valmistati ultrahelipihustuspürolüüsi meetodil sadestatud Sb_2S_3 õhukestest kiledest päikesepatareid ja uuriti nende füüsikalisi väljundparameetreid.

Töös uuriti kilesid, mis olid sadestatud $SbCl_3$ ja tiourea moolsuhtes 1/3 ja 1/6 lahuse pihustamisel. Pihustades $SbCl_3$ ja tiourea moolsuhtes 1/3 lahust temperatuuril 220°C või moolsuhtes 1/6 lahust temperatuuril 210°C või 220°C tekkis kristalne ja faasipuhas, kuid ebaühtlane Sb_2S_3 kile. Seevastu, pihustades $SbCl_3$ ja tiourea moolsuhtes 1/6 lahust temperatuuril 200°C kasvas katkendlik amorfne faasipuhas Sb_2S_3 kile, mis kristalliseerus, kuid ei muutnud kuju pärast kuumutamist vaakumis temperatuuril 170°C. Pihustades $SbCl_3$ ja tiourea moolsuhtes 1/3 lahust õhus temperatuuril 200°C või 210°C tekkis ühtlane amorfne 70–90 nm paksune faasipuhas Sb_2S_3 kile. Kuumutades neid amorfseid kilesid vaakumis temperatuuril 170°C tekkis pidev kristalne faasipuhas Sb_2S_3 kile. Seega osutus, et kaheastmeline protsess sobis pidevate ja ühtlaste faasipuhaste Sb_2S_3 õhukeste kilede valmistamiseks.

Sb_2S_3 kilesid, mis olid sadestatud $SbCl_3$ ja tiourea moolsuhtes 1/3 lahusest õhus temperatuuril 200°C, katsetati tasastes päikesepatareides. Töös selgus, et päikesepatarei kasutegur sõltub Sb_2S_3 neeldumiskihi paksusest. Parim kasuteguri väärtus 5.5 % saavutati ITO/TiO₂/Sb₂S₃/P3HT/Au päikesepatareides, kui Sb_2S_3 kile paksus oli 100 nm. Esialgse katse tulemustest avaldub, et sisuliselt on ultrahelipihustuspürolüüsi meetodil sadestatud Sb_2S_3 kilesid võimalik kasutada tasase päikesepatarei neeldumiskihina.

Uurimis- ja arendustööga on siiski vaja jätkata, sest kiled ei olnud veel piisavalt ühtlased. Hoiustamiskatse tulemustest on näha, et kaitsekihtideta Sb_2S_3 päikesepatarei kasutegur on ajas püsivam kui orgaanilistel või perovskiit-päikesepatareidel.

Senise teadmuse põhjal ei olnud kindel, kas ja kuidas on võimalik ultrahelipihustuspürolüüsiga sadestada faasipuhtaid Sb_2S_3 kilesid teiste kompleksühendite lahustest. Termilise analüüsi tulemuste põhjal hinnati, kas antimonetüülksantaat sobib ultrahelipihustuspürolüüsi lähteaineks. Antimonetüülksantaat lagunes temperatuuril alla $170^\circ C$, moodustades Sb_2S_3 , mis säilitas inertkeskkonnas puhtusastme, kuid oksüdeerus õhus. Seetõttu rakendati ühtlaste pidevate Sb_2S_3 õhukeste kilede valmistamiseks kaheastmelist protsessi. Amorfseid Sb_2S_3 kiled sadestati temperatuuril $215^\circ C$ ultrahelipihustuspürolüüsi meetodil õhus antimonetüülksantaadi ja tiouurea või tioatseetamiidi lahusest, mis oli vastavalt moolsuhtes 1/3 või 1/10. Kilede kristallimiseks osutus sobivaks neid kuumutada vaakumis temperatuuril $225^\circ C$. Kristalliseerunud Sb_2S_3 kiledele arvutati $E_g = 1.8$ eV ja aatomsuhe S/Sb = 1.5 (tiouurea-põhine) või S/Sb = 1.4 (tioatseetamiidi-põhine).

Kokkuvõtteks sadestati selle uurimustöö raames esmakordselt ultrahelipihustuspürolüüsi meetodil õhukeskkonnas halogeniidi-põhise, kuid ka -vaba kompleksühendi lahusest pidevad faasipuhtad Sb_2S_3 õhukesed kiled. Tõestati, et ultrahelipihustuspürolüüsi meetodil õhukeskkonnas sadestatud pidevatest Sb_2S_3 kiledest saab valmistada arvestatava kasuteguriga päikesepatareisisid. Lisaks näidati, et tagakontaktita klaas/ITO/TiO₂/Sb₂S₃ struktuur sobib põhimõtteliselt poolläbipaistva päikesepatarei rakendustes, nt päikesepatareiakendes, paaris-, kahepoolsetes ja ehitis- või tooteintegreeritud seadistes rakendamiseks. Seetõttu on antud uurimistöö tulemustest kasu nii pidevate puhtafaasiliste Sb_2S_3 kilede valmistamisel õhukeskkonnas, kui ka tavapäraste ja poolläbipaistvate õhukesekileliste päikesepatareide ning nendel põhinevate toodete edaspidisel arendamisel.

Appendix

Publication I

J. S. Eensalu, A. Katerski, E. Kärber, I. Oja Acik, A. Mere, M. Krunks. "Uniform Sb₂S₃ optical coatings by chemical spray method," *Beilstein Journal of Nanotechnology*, vol. 10, pp. 198–210, Jan. 2019, doi: 10.3762/bjnano.10.18.



Uniform Sb₂S₃ optical coatings by chemical spray method

Jako S. Eensalu^{*}, Atanas Katerski, Erki Kärber, Ilona Oja Acik, Arvo Mere and Malle Krunks^{*}

Full Research Paper

[Open Access](#)**Address:**

Laboratory of Thin Film Chemical Technologies, Department of Materials and Environmental Technology, Tallinn University of Technology, Ehitajate tee 5, Tallinn 19086, Estonia

Email:

Jako S. Eensalu^{*} - jako.eensalu@taltech.ee; Malle Krunks^{*} - malle.krunks@taltech.ee

^{*} Corresponding author

Keywords:

antimony sulfide; thin films; ultrasonic spray; vacuum annealing; Volmer–Weber growth

Beilstein J. Nanotechnol. **2019**, *10*, 198–210.

doi:10.3762/bjnano.10.18

Received: 22 September 2018

Accepted: 04 December 2018

Published: 15 January 2019

This article is part of the thematic issue "Chemical thin coating methods for functional nanomaterials".

Guest Editor: J. Bachmann

© 2019 Eensalu et al.; licensee Beilstein-Institut.

License and terms: see end of document.

Abstract

Antimony sulfide (Sb₂S₃), an environmentally benign material, has been prepared by various deposition methods for use as a solar absorber due to its direct band gap of ≈ 1.7 eV and high absorption coefficient in the visible light spectrum (1.8×10^5 cm⁻¹ at 450 nm). Rapid, scalable, economically viable and controllable in-air growth of continuous, uniform, polycrystalline Sb₂S₃ absorber layers has not yet been accomplished. This could be achieved with chemical spray pyrolysis, a robust chemical method for deposition of thin films. We applied a two-stage process to produce continuous Sb₂S₃ optical coatings with uniform thickness. First, amorphous Sb₂S₃ layers, likely forming by 3D Volmer–Weber island growth through a molten phase reaction between SbCl₃ and SC(NH₂)₂, were deposited in air on a glass/ITO/TiO₂ substrate by ultrasonic spraying of methanolic Sb/S 1:3 molar ratio solution at 200–210 °C. Second, we produced polycrystalline uniform films of Sb₂S₃ (E_g 1.8 eV) with a post-deposition thermal treatment of amorphous Sb₂S₃ layers in vacuum at 170 °C, $< 4 \times 10^{-6}$ Torr for 5 minutes. The effects of the deposition temperature, the precursor molar ratio and the thermal treatment temperature on the Sb₂S₃ layers were investigated using Raman spectroscopy, X-ray diffraction, scanning electron microscopy, energy dispersive X-ray spectroscopy and UV–vis–NIR spectroscopy. We demonstrated that Sb₂S₃ optical coatings with controllable structure, morphology and optical properties can be deposited by ultrasonic spray pyrolysis in air by tuning of the deposition temperature, the Sb/S precursor molar ratio in the spray solution, and the post-deposition treatment temperature.

Introduction

Antimony sulfide (Sb₂S₃) is an environmentally benign material. As Sb and S are abundant elements in the Earth's crust, enough raw materials can be supplied to manufacture large

quantities of Sb₂S₃ in the long term. Sb₂S₃ can be applied as the inorganic absorber in solar cells due to its direct band gap of ≈ 1.7 eV [1,2].

Sb₂S₃, prepared by a chemical bath deposition (CBD) [3,4], spin coating [5], atomic layer deposition (ALD) [6] or chemical spray pyrolysis (CSP) [7] method, has been applied in extremely thin absorber (ETA) solar cells due to its excellent absorption coefficient in the visible light spectrum ($1.8 \times 10^5 \text{ cm}^{-1}$ at 450 nm) [1,2]. Improvements in photocurrent density have been sought by utilizing a transparent, nanostructured window layer instead of planar window layers with the ETA Sb₂S₃ absorber layer [4,7]. Previous studies show that achieving sufficient repeatability alongside optimization of the component layers, i.e., transparent (structured) window layer, Sb₂S₃ absorber layer, and hole transport material layer, and their respective interfaces, is a tremendous undertaking [4].

Attention has surged toward planar heterojunction Sb₂S₃ solar cells due to their simpler structure, less intricate production, and enhanced repeatability vs structured solar cells [8]. Planar $\approx 1.7 \text{ eV}$ absorber layers can be applied in semitransparent solar cells as well as in tandem solar cells.

Chemical spray pyrolysis (CSP) is a robust and industrially scalable chemical method for rapid deposition of thin films [9]. Our research group first investigated spray-deposited Sb₂S₃ by pneumatically spraying aqueous solutions (tartaric acid added as complexing agent to prevent hydrolysis [10], akin to studies by Rajpure et al. [11]) or methanolic solutions of SbCl₃. Following, we studied the effect of the Sb/S precursor molar ratio in solution on ultrasonically sprayed Sb₂S₃ layers and presented the first planar TiO₂/Sb₂S₃/P3HT solar cells comprising ultrasonically sprayed Sb₂S₃ (power conversion efficiency $\eta \leq 1.9\%$) [12].

SbCl₃ and thiourea (SC(NH₂)₂) are often used in the field to deposit Sb₂S₃ thin films. Spraying the SbCl₃/SC(NH₂)₂ (henceforth Sb/S) 1:6 molar ratio solution at 250 °C in air yielded separate Sb₂S₃ grains, which did not cover the TiO₂ substrate entirely, whereas spraying the Sb/S 1:3 solution yielded an inhomogeneous mix of amorphous and polycrystalline Sb₂S₃ [12]. We learned to produce continuous uniform layers of polycrystalline Sb₂S₃ by a two-step process on ZnO nanorod/TiO₂ substrates [7]. In this study, we applied this two-step process, i.e., depositing amorphous Sb₂S₃ layers on planar substrates, followed by post-deposition crystallization.

The aim of this study was to produce crystalline, continuous, Sb₂S₃ optical coatings with uniform thickness to be applied as a photovoltaic absorber by ultrasonic spraying on planar glass/ITO/TiO₂ substrates, followed by a post-deposition treatment. To this end, we studied the effect of the deposition temperature (T_D), the molar ratio of precursors SbCl₃ and thiourea (SC(NH₂)₂) in the spray solution, and the post-deposition treat-

ment temperature on the structure, morphology and optical properties of ultrasonically sprayed Sb₂S₃ thin films.

Results and Discussion

Two sequential operations were used to obtain homogeneous Sb₂S₃ optical coatings with uniform thickness on planar TiO₂ substrates. First, we tuned the deposition temperature and molar ratio of Sb/S precursors in spray solution to deposit continuous amorphous Sb₂S₃ layers. An intimate contact, which is a prerequisite for high power conversion efficiency in solar cells [13], is formed at the interface between TiO₂ and Sb₂S₃ during deposition of amorphous Sb₂S₃ layers. Second, all layers were thermally treated in an inert environment (vacuum, $<4 \times 10^{-6}$ Torr) to induce crystallization, without oxidation.

Preliminary experiments at deposition temperatures lower than 182 °C (decomposition of SC(NH₂)₂ [14,15]) yielded inhomogeneous red-brown layers. Furthermore, in our previous paper, 250 °C was found to be too high a deposition temperature to obtain sufficient coverage of TiO₂ substrate by polycrystalline Sb₂S₃ thin films, despite the suitable band gap of 1.6 eV and high phase purity [12]. Restricted to deposition temperatures in the range 182–250 °C, we sprayed Sb/S 1:3 and 1:6 molar ratio precursor solutions at $T_D = 200, 210, \text{ and } 220 \text{ °C}$. We varied the aforementioned parameters to attain the conditions to deposit dense and homogeneous layers of amorphous Sb₂S₃, which we then crystallized by a post-deposition thermal treatment.

Based on the scanning electron microscopy (SEM) images, preliminary experiments revealed that spraying Sb/S 1:6 solutions consistently yielded twice thinner layers compared to layers deposited from Sb/S 1:3 solutions. Sb₂S₃ layers of comparable thickness were deposited by spraying Sb/S 1:6 solutions for 40 minutes and Sb/S 1:3 solutions for 20 minutes.

The samples are named in the text as follows: A-B-C, where A is the S/Sb molar ratio in solution, B is the deposition temperature, and C is the specification of the treatment. [Sb/S molar ratio in solution: “3” for Sb/S 1:3 or “6” for Sb/S 1:6]-[deposition temperature: “200”, “210” or “220” (°C)]-[treatment: “As-dep.” for as-deposited and “170”, “200” or “250” (°C) for samples thermally treated in vacuum].

The samples in which Sb₂S₃ layers were deposited from either Sb/S 1:3 or 1:6 solution at $T_D = 200 \text{ °C}$, followed by thermal treatment in vacuum at 200 °C (3-200-200, 6-200-200), contain no Sb₂S₃, as it likely volatilized completely during the vacuum thermal treatment. Likewise, treating the Sb₂S₃ layers at temperatures higher than 200 °C caused Sb₂S₃ to completely volatilize during treatment. Photographs of the samples (Figure S1) and the description of the vapor pressure calculations

(Comment S1) are provided in the Supporting Information File 1. Consequently, only as-deposited samples and samples thermally treated in vacuum at 170 °C and 200 °C are eligible for discussion.

Structure of as-deposited and thermally treated Sb_2S_3 layers

Raman spectroscopy provides quantitative and qualitative information on the vibrational modes in solids. The wide Raman band centered at 290 cm^{-1} [12,16] associated with metastibnite, i.e., amorphous Sb_2S_3 , is characteristic of as-deposited orange colored (photograph in Supporting Information File 1, Figure S1) samples (3-200-As-dep., 3-210-As-dep., Figure 1A; 6-200-As-dep., Figure 1B). The band centered at 145 cm^{-1} is a low frequency E_g vibrational mode of anatase- TiO_2 [17], which is observed due to the laser beam penetrating to the substrate [12,16] through the discontinuous Sb_2S_3 layers. The TiO_2

vibrational band is absent in spectra of Sb_2S_3 layers containing less pinholes, as the signal is captured only from Sb_2S_3 .

The narrower bands, attributed to orthorhombic Sb_2S_3 [16,18–20], are present in the spectra of as-deposited and thermally treated lustrous gray (photograph in Supporting Information File 1, Figure S1) samples (3-200-170, 3-210-170, 3-210-200, 3-220-As-dep., 3-220-170, 3-220-200, Figure 1A; 6-200-170, 6-210-As-dep., 6-210-170, 6-210-200, 6-220-As-dep., 6-220-170, 6-220-200, Figure 1B; photograph in Supporting Information File 1, Figure S1). According to group theory, orthorhombic Sb_2S_3 has 30 predicted Raman active modes: $\Gamma_{\text{Raman}} = 10A_g + 5B_{1g} + 10B_{2g} + 5B_{3g}$ [18,20]. The Raman spectra were deconvoluted using Lorentzian fitting into vibrational bands of Sb_2S_3 based on the literature [12,16,21,22]. The centers of the bands of Sb_2S_3 in the deconvoluted Raman spectra (Table 1, symmetries taken from [20,21]) are similar to

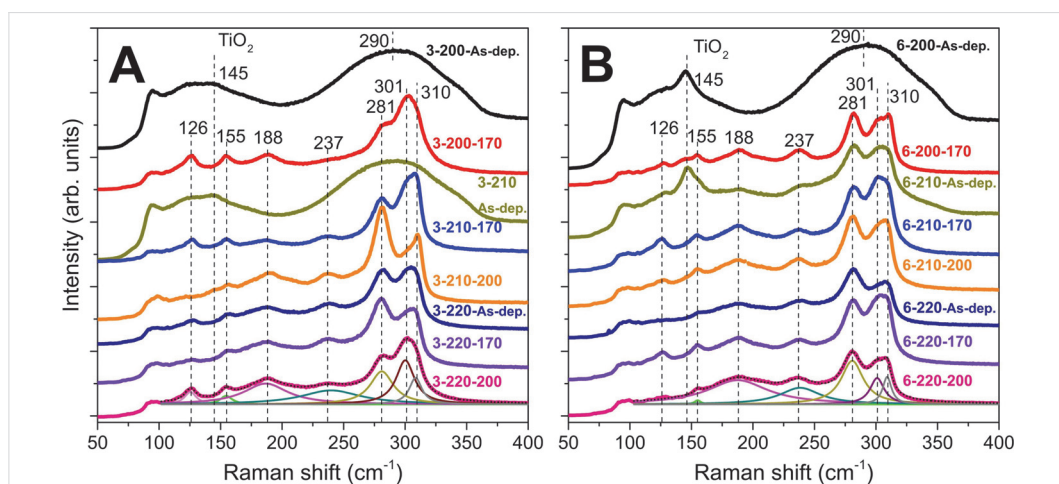


Figure 1: Raman spectra (shifted for visibility) of the as-deposited and thermally treated Sb_2S_3 films deposited from Sb/S 1:3 (A) or 1:6 (B) solution at 200, 210, 220 °C. Examples of deconvoluted fitted band curves are presented for the lowermost spectra. Sample names in figures: [S/Sb molar ratio in solution]-[deposition temperature]-[thermal treatment temperature].

Table 1: Raman band centers and assigned active modes for the studied Sb_2S_3 layers.

This study	Center of Raman band, cm^{-1}			Symmetry	Vibrational mode, [21–23]
	Ref. [21]	Ref. [20]	Ref. [21]		
126	125	129	A_g	A_g	lattice mode
155	156	158	A_g	A_g/B_{2g}	lattice mode
188	189	186	B_{1g}	B_{1g}	antisym. S–Sb–S bending
237	237	239	B_{1g}	B_{1g}/B_{3g}	symmetric S–Sb–S bending
281	281	282	A_g	A_g/B_{2g}	antisym. S–Sb–S stretching
301	300	299	A_g	A_g/B_{2g}	antisym. S–Sb–S stretching
310	310	312	A_g	A_g/B_{2g}	symmetric S–Sb–S stretching

values reported in our previous studies [7,12]. Band centers, relative single peak intensities and full widths at half maximum (FWHM) of the narrow bands centered at 281, 301 and 310 cm^{-1} can be respectively found in Tables S1, S2, and S3 of Supporting Information File 1.

The FWHM of the vibrational band centered at 281 cm^{-1} narrows from $\approx 24 \text{ cm}^{-1}$ to 21–23 cm^{-1} after vacuum thermal treatment of the samples deposited at 210–220 °C from both Sb/S 1:3 and Sb/S 1:6 solutions (3-210-170, 3-220-170, 6-210-170 and 6-220-170) at 170 °C (3-210-170, 3-220-170, 6-210-170 and 6-220-170) and narrows by 5 cm^{-1} at most after vacuum thermal treatment at 200 °C (3-210-200). The narrowing of the Raman bands due to thermal treatment leads us to suppose that crystallization continues during the vacuum thermal treatment and proceeds further at higher thermal treatment temperatures [16]. The vibrational bands corresponding to Sb_2O_3 were not detected by Raman spectroscopy in any of the studied glass/ITO/ $\text{TiO}_2/\text{Sb}_2\text{S}_3$ samples.

X-ray diffraction (XRD) provides qualitative information on the phase composition and crystal structure. XRD patterns of reference glass/ITO/ TiO_2 samples and samples containing XRD-amorphous Sb_2S_3 (3-200-As-dep., 3-210-As-dep., Figure 2A; 6-200-As-dep., Figure 2B) show only diffraction peaks corresponding to cubic In_2O_3 ($2\theta = 21.3^\circ, 30.4^\circ, 35.3^\circ, 37.4^\circ, 41.4^\circ, 45.3^\circ$, ICDD PDF 03-065-3170) and anatase- TiO_2 ($25.3^\circ, 48.2^\circ$, ICDD PDF 00-016-0617). The diffraction peaks of orthorhombic Sb_2S_3 (ICDD PDF 01-075-4012), space group $Pnma$ (D_{2h}^{16}) [20,24,25], appear in XRD patterns of lustrous gray as-deposited and thermally treated Sb_2S_3 samples (3-200-170, 3-210-170, 3-210-200, 3-220-As-dep., 3-220-170, 3-220-200, Figure 2A; 6-200-170, 6-210-As-dep., 6-210-170, 6-210-200, 6-220-As-dep., 6-220-170, 6-220-200, Figure 2B). The 2θ angles of observed Sb_2S_3 diffraction peaks and corresponding crystal plane indices are presented in Supporting Information File 1, Table S4. Experimentally determined mean lattice constants a , b and c of Sb_2S_3 are $11.25 \pm 0.07 \text{ \AA}$, $3.810 \pm 0.025 \text{ \AA}$ and $11.16 \pm 0.07 \text{ \AA}$, respectively. Our experimentally deter-

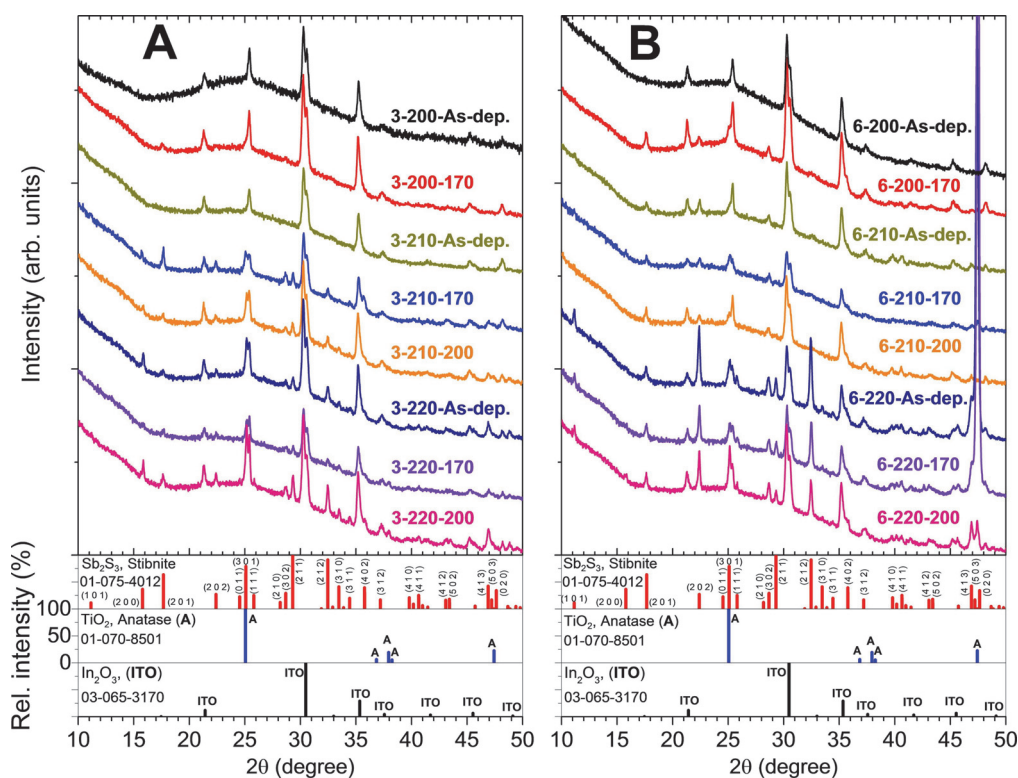


Figure 2: XRD patterns (shifted for visibility) of as-deposited and vacuum treated (170 °C or 200 °C, 5 minutes) Sb_2S_3 layers deposited on glass/ITO/ TiO_2 substrate from Sb/S 1:3 (A) or 1:6 (B) solution at $T_s = 200, 210, 220$ °C. Sample names in figures: [S/Sb molar ratio in solution]-[deposition temperature]-[thermal treatment temperature].

mined mean unit cell volume ($479 \pm 4 \text{ \AA}^3$) lies between the experimentally determined volume (486.7 \AA^3) and the theoretically determined volume (470.5 \AA^3) calculated from orthorhombic Sb_2S_3 powder (>99.99 wt %) data presented by Ibáñez et al. [20].

Sb_2S_3 layers deposited from Sb/S 1:6 solution at 210 °C (6-210-As-dep., Figure 2B) are polycrystalline, whereas layers deposited from Sb/S 1:3 solution (3-210-As-dep., Figure 2A) are XRD-amorphous. Sb_2S_3 layers deposited at 220 °C from both Sb/S 1:3 (3-220-As-dep., Figure 2A) and 1:6 (6-220-As-dep., Figure 2B) solution are polycrystalline. Several diffraction peaks corresponding to orthorhombic Sb_2S_3 were detected in these samples. No additional phases were detected by XRD in any studied samples. The presence or absence of amorphous Sb_2O_3 as a minor phase in the Sb_2S_3 layers, as it is difficult to ascertain by Raman or XRD analyses, has not been conclusively demonstrated.

The diffraction peak of the (2 0 0)/(0 0 2) plane of Sb_2S_3 is absent in most samples deposited from Sb/S 1:6 solution. Conversely, the diffraction peak of the (1 0 1) plane of Sb_2S_3 is absent in all samples deposited from Sb/S 1:3 solution. Sb_2S_3 crystallites in most of our samples have no preferred orientation. Only crystallites in as-deposited and vacuum treated (170 °C) samples deposited from Sb/S 1:6 solution (6-220-As-dep., 6-220-170, Figure 2B) show a preferred orientation parallel to the substrate surface along the (0 2 0) plane normal of Sb_2S_3 . Interestingly, this preferred orientation of crystallites does not extend to the sample with Sb_2S_3 deposited in the same conditions, but thermally treated in vacuum at 200 °C (6-220-200, Figure 2B).

The larger crystallite size is a boon to the power conversion efficiency of all solar absorber materials because decreasing the amount of grain boundaries likely increases charge carrier mobility [26]. The crystallite sizes of as-deposited and thermally treated Sb_2S_3 layers are presented in Table 2. The effect of the deposition temperature is observed in Sb/S 1:3 Sb_2S_3

layers, as the crystallite size increases after vacuum annealing at 170 °C from $19 \pm 8 \text{ nm}$ to $100 \pm 23 \text{ nm}$ by raising T_D from 200 to 220 °C. The crystallite size in Sb/S 1:6 Sb_2S_3 layers ($42 \pm 15 \text{ nm}$) does not change significantly with T_D or vacuum treatment. Furthermore, vacuum treatment at 200 °C vs 170 °C does not substantially affect the crystallite size of Sb_2S_3 layers.

In comparison, the largest crystallites in Sb_2S_3 layers grown on TiO_2 substrates via CBD and annealed at 270 °C in N_2 for 30 min oriented along the (2 0 0) plane parallel to the substrate were 74 nm in size [16]. The crystallites oriented along the (2 0 1) plane were 24 nm in size in Sb_2S_3 layers grown on SnO_2/F (FTO) coated glass substrates via thermal evaporation [27]. The crystallite size was 52 nm along the (3 0 1) plane in Sb_2S_3 layers grown on glass substrates at 250 °C via spray pyrolysis [28], similar to the crystallite size in some of our samples. We conclude that the mean crystallite size in our Sb_2S_3 layers is in the general range of values obtained in the literature using both chemical and physical methods.

Morphology of as-deposited and thermally treated Sb_2S_3 layers

Influence of deposition temperature on morphology of Sb_2S_3 layers

The aim of this study was to obtain uniform Sb_2S_3 layers, which continuously coat the TiO_2 substrate. According to SEM surface studies, layers deposited from both Sb/S 1:3 and Sb/S 1:6 solutions at 200 and 210 °C (3-200-As-dep., 3-210-As-dep., Figure 3G,H, Supporting Information File 1, Figure S2A,B, Figure S3A,B; 6-200-As-dep., Figure 3A,B; 6-210-As-dep., Figure 3C,D) cover the substrate almost entirely. Grain boundaries and larger clusters of grains have formed in layers deposited from Sb/S 1:6 solutions for 40 minutes at 210 °C (6-210-As-dep., Figure 3C,D, Figure S5C,D). Cap-shaped islands ($\varnothing 70 \text{ nm}$) in Sb_2S_3 layers deposited from Sb/S 1:6 solution at $T_D = 210 \text{ °C}$ for 20 minutes (Figure S4A,B), have grown ($\varnothing 100 \text{ nm}$) and coalesced further after 40 minutes of deposition at 200–210 °C (6-200-As-dep., Figure 3A,B, Figure S5A,B; 6-210-As-dep., Figure 3C,D, Figure S5C,D, Figure

Table 2: Crystallite size (D) of as-deposited and vacuum treated Sb_2S_3 thin films. The crystallite size was calculated by the Scherrer equation from the (2 0 2) diffraction peak of as-deposited and vacuum treated (170 °C, 200 °C, 5 minutes) Sb_2S_3 thin films deposited on glass/ITO/ TiO_2 substrates from Sb/S 1:3 and 1:6 precursor solution at $T_D = 200, 210, 220 \text{ °C}$.

Sb/S in sol.	D , nm					
	1:3			1:6		
T_D , °C	200	210	220	200	210	220
as-dep.	amorph.	amorph.	33 ± 10	amorph.	39 ± 4	47 ± 1
vac. 170 °C	19 ± 8	38 ± 6	100 ± 23	37 ± 8	35 ± 4	49 ± 3
vac. 200 °C	no layer ^a	32 ± 8	67 ± 12	no layer ^a	45 ± 6	52 ± 3

^aNo Sb_2S_3 was detected by XRD or Raman.

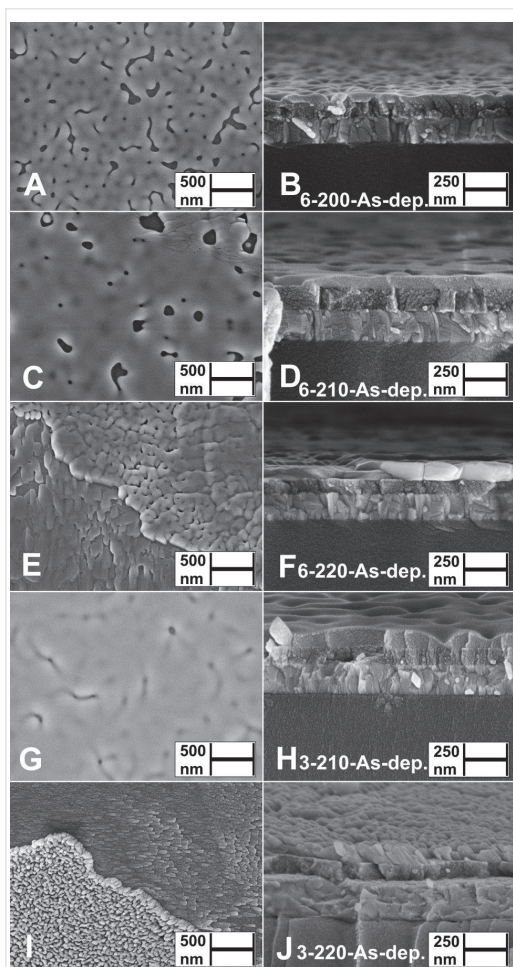


Figure 3: Surface and cross-sectional views by SEM study of as-deposited Sb_2S_3 layers deposited from Sb/S 1:6 solution at $T_D = 200$ °C (A, B), 210 °C (C, D) or 220 °C (E, F) and from Sb/S 1:3 solution at $T_D = 210$ °C (G, H) or 220 °C (I, J) on glass/ITO/ TiO_2 substrate. Sample names in figures: [S/Sb molar ratio in solution]-[deposition temperature]-[as-deposited].

S6A,B), thereby covering the TiO_2 substrate to a greater extent. The layers deposited from Sb/S 1:6 solution at 220 °C for 40 minutes (6-220-As-dep., Figure S5E,F, Figure S5E,F) consist of various agglomerates, separated by pinholes, and grains flowing randomly along the partially exposed TiO_2 substrate (lower left, Figure 3E).

Increasing the deposition temperature from 210 to 220 °C significantly transforms the surface morphology in Sb/S 1:3 layers, as instead of the planar grains (3-210-As-dep., Figure 3G,H) domains of elongated rod-shaped grains (length ≈ 100 nm)

appear either upright or sideways on the substrate (3-220-As-dep., Figure 3I,J, Figure S3C,D). Rod-shaped Sb_2S_3 grains were able to grow due to the nature of the material as well as due to complex interactions between the substrate and the turbulence of the spray during deposition [29].

Increasing the sulfur precursor concentration in the spray solution from Sb/S 1:3 to 1:6 (and deposition time from 20 to 40 minutes) yields Sb_2S_3 layers consisting of agglomerated grains (6-220-As-dep., Figure 3E,F). As the deposition time was simultaneously increased from 20 to 40 minutes, it is uncertain whether the morphology of the Sb_2S_3 layers is affected more by the Sb/S molar ratio in solution or by the deposition time. Sb_2S_3 tends to yield different morphologies in similar deposition conditions, possibly due to liquid phase reactions between molten-boiling SbCl_3 (mp 73.4 °C, bp 223.5 °C [30]) and molten thiourea (TU, mp 182 °C [14,15]) catalyzed by the highly active surface of the TiO_2 substrate [31].

We have consistently observed twice slower growth of Sb_2S_3 by spraying solutions with Sb/S 1:6 (Supporting Information File 1, Figure S4A,B) vs Sb/S 1:3 (Figure 3G,H) molar ratio at 200–220 °C. We speculate that doubling the concentration of TU could sterically inhibit the formation of solid Sb_2S_3 nuclei on the surface of the active TiO_2 substrate due to more intense bubbling of volatile TU decomposition products (CS_2 , NH_3 , HCN , COS , SO_2 , HCl , HNCS) at 200–220 °C in air based on decomposition studies of pure TU [14], $\text{Cu}(\text{TU})_3\text{Cl}$ [32], $\text{Zn}(\text{TU})_2\text{Cl}_2$ [33], and $\text{Sn}(\text{TU})_2\text{Cl}_2$ [34]) in the surrounding liquid phase.

In summary, the most uniform and continuous Sb_2S_3 thin films were deposited from Sb/S 1:3 solution at 200–210 °C.

Influence of vacuum treatment temperature on morphology of Sb_2S_3 layers

The thermal treatment of X-ray amorphous Sb_2S_3 layers (6-200-As-dep., Figure 3A,B; 3-200-As-dep.; 3-210-As-dep., Figure 3G,H, Supporting Information File 1, Figure S2A,B) in vacuum at 170 °C for 5 minutes yields enhanced substrate coverage at the expense of decreased layer thickness due to coalescence of grains and film formation (6-200-170, Figure 4A,B; 3-200-170, Figure 4G,H; 3-210-170, Figure 4I,J). Complete substrate coverage is observed in the Sb_2S_3 layers deposited at 210 °C from Sb/S 1:3 solution as coalescence is facilitated during treatment in vacuum at 170 °C due to the near-continuous coverage of the TiO_2 substrate in the as-deposited layers (3-210-170, Figure 4G,H, Figure S2C,D, Figure S7A,B).

Planar grain agglomerates in thermally treated Sb_2S_3 layers (3-210-170, Figure 4G,H, Supporting Information File 1, Figure

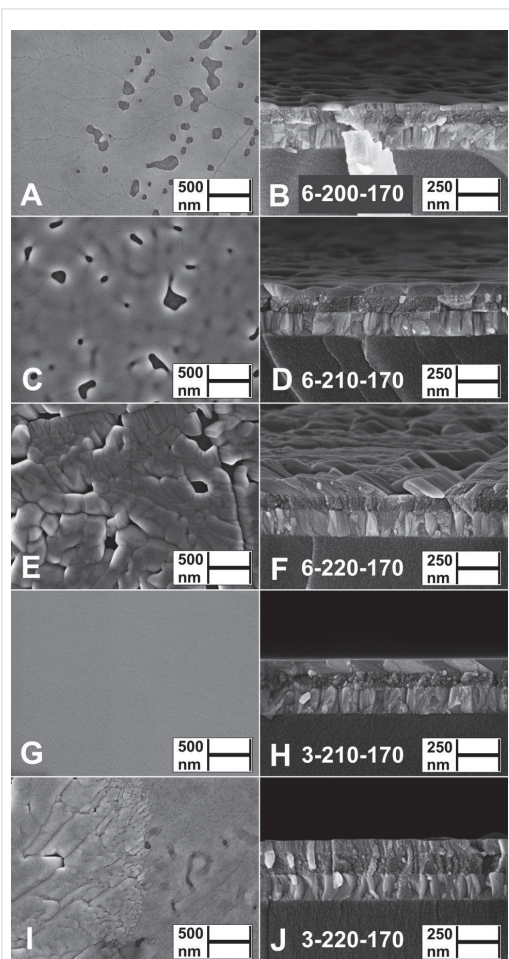


Figure 4: Surface and cross-sectional views by SEM study of thermally treated (170 °C, 5 minutes) Sb_2S_3 layers deposited from Sb/S 1:6 solution at $T_D = 200$ °C (A, B), 210 °C (C, D) or 220 °C (E, F) and from Sb/S 1:3 solution at $T_D = 210$ °C (G, H) or 220 °C (I, J) on glass/ITO/ TiO_2 substrates. Sample names in figures: [S/Sb molar ratio in solution]-[deposition temperature]-[thermal treatment temperature].

S7A,B; 6-200-170, Figure 4A,B, Figure S9A,B; 6-210-170, Figure 4C,D, Figure S9C,D) range from 100 nm to over 10 μm in size. These agglomerates, consisting of smaller grains separated by ridges, resemble the surface morphology of 300 nm thick polycrystalline Sb_2S_3 films grown via thermal evaporation and annealed for 10 min at 300 °C in N_2 [35], and that of metal halide perovskites obtained by Volmer–Weber growth via hot casting [36]. The layers deposited at 220 °C from both Sb/S 1:3 and Sb/S 1:6 solutions, and thermally treated at 170 °C, consist of numerous grains and pinholes (3-220-170, Figure 4I,J; 6-220-170, Figure 4E,F).

Sb_2S_3 layers deposited at 210 °C from both Sb/S 1:3 and Sb/S 1:6 solutions, and thermally treated in vacuum at 200 °C (3-210-200, Figure 5A,B, Supporting Information File 1, Figure S8A,C,E; 6-210-200, Figure 5C,D, Figure S8B,D,F), are porous, inhomogeneous and ≈ 20 nm thinner (Table 3) vs the uniform in thickness layers after treatment at 170 °C (3-210-170, Figure 4I,J; 6-210-170, Figure 4C,D).

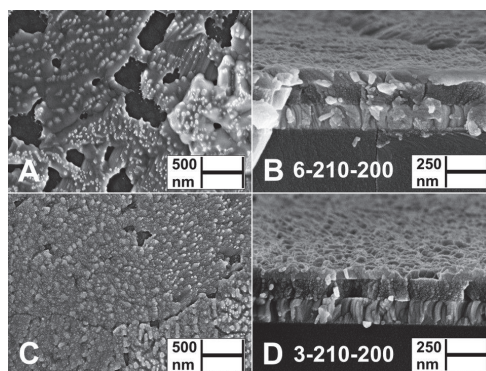


Figure 5: Surface and cross-sectional views by SEM study of vacuum treated (200 °C, 5 minutes) Sb_2S_3 layers deposited from Sb/S 1:6 solution (A, B) and from Sb/S 1:3 solution (C, D) at $T_D = 210$ °C on glass/ITO/ TiO_2 substrates. Sample names in figures: [S/Sb molar ratio in solution]-[deposition temperature]-[thermal treatment temperature].

Table 3: Thicknesses of Sb_2S_3 layers estimated from SEM images.

	Sb_2S_3 layer thickness, nm					
	Sb/S 1:3 in sol., 20 min dep.			Sb/S 1:6 in sol., 40 min dep.		
T_D , °C	200	210	220	200	210	220
as-dep.	70–90	80–100	60/150 ^a	50–70	60/400 ^a	40/400 ^a
vac., 170 °C	70–90	70–90	80/150 ^a	30–40	60/400 ^a	40/400 ^a
vac., 200 °C	no layer ^b	60–70	N/A	no layer ^b	60–70	N/A

^aThickness of formations shown in the Supporting Information File 1 in Figures S5, S7, S8 and S9. ^bNo Sb_2S_3 was detected by XRD or Raman.

The decreasing layer thickness indicates that approximately a quarter of Sb_2S_3 by volume has either evaporated or sublimated, i.e., volatilized. Incongruent evaporation, i.e., depletion of sulfur in Sb_2S_3 during evaporation, may cause the change in Sb_2S_3 layer morphology, as volatilization of the planar regions around the nucleating islands has been reported during thermal treatment of both Sb_2Se_3 layers grown via thermal evaporation [37] and oxide containing Sb_2S_3 layers grown via CBD [16].

The calculated vapor pressure of Sb_2S_3 is $\approx 2 \times 10^{-10}$ Torr at 170 °C, 7×10^{-9} Torr at 200 °C and 9×10^{-7} Torr at 250 °C [38], whereas the dynamic system pressure is $\approx 4 \times 10^{-6}$ Torr. The calculated partial pressure of Sb_2S_3 is $\approx 0.0050\%$ at 170 °C, 0.18% at 200 °C and 23% at 250 °C (Comment S1 in Supporting Information File 1). The loss of a quarter of the Sb_2S_3 layer thickness in samples that were vacuum annealed at 200 vs 170 °C (Table 3) correlates with the exponential increase in Sb_2S_3 vapor pressure in the 170–250 °C range.

In conclusion, the most uniform and continuous Sb_2S_3 thin films were produced by vacuum treatment at 170 °C for 5 min of Sb_2S_3 layers deposited from Sb/S 1:3 solution at 200–210 °C.

Elemental composition of as-deposited and thermally treated Sb_2S_3 layers

The elemental composition of Sb_2S_3 in as-deposited and thermally treated glass/ITO/ TiO_2 / Sb_2S_3 samples was determined using energy dispersive X-ray spectroscopy (EDX). The EDX results of studied Sb_2S_3 layers in terms of S to Sb atomic ratio (S/Sb) are presented in Table 4. S/Sb in both as-deposited and vacuum annealed polycrystalline Sb_2S_3 layers deposited at $T_D = 220$ °C is close to the stoichiometric value of 1.5 of Sb_2S_3 , whereas the S/Sb ratio of as-deposited and thermally treated Sb_2S_3 layers (Sb/S 1:3 in solution, T_D 200–210 °C, 3-200-As-dep., 3-210-As-dep., 3-200-170, 3-210-170) is ≈ 1.3 . S/Sb is ≈ 1.5 – 1.6 in layers deposited from Sb/S 1:6 solution at 200–220 °C.

Table 4: S/Sb atomic ratio of as-deposited and thermally treated Sb_2S_3 layers calculated from EDX data.

Sb/S in sol.	S/Sb in layer					
	1:3			1:6		
T_D , °C	200	210	220	200	210	220
as-dep.	1.3	1.3	1.5	1.6	1.5	1.5
vac., 170 °C	1.3	1.3	1.5	1.6	1.6	1.5
vac., 200 °C	N/A	1.4	N/A	N/A	1.5	N/A

We note that interpretation of EDX spectra of very thin layers is difficult. Most of our Sb_2S_3 layers are thinner than 100 nm,

which could explain the divergence in the elemental composition of our Sb_2S_3 layers. Therefore, future studies by more surface sensitive methods are required. Overall, S/Sb in most studied samples approximates the stoichiometric value of 1.5 of Sb_2S_3 .

Oxygen could not be quantified by EDX due to the thin layers and high concentration of O in the glass/ITO/ TiO_2 substrate. In addition, C and Cl levels were below the detection limit of the used EDX setup in all studied Sb_2S_3 layers, meaning most C and Cl species exit the growing Sb_2S_3 layer during deposition in open environment (Supporting Information File 1, Figure S11). We believe that this reinforces our claim that formation of Sb_2S_3 proceeds through a molten phase reaction between SbCl_3 and TU, where the denser (4562 kg/m^3 [39]) Sb_2S_3 precipitates and nucleates, while the remainder of the volatile compounds (SbCl_3 , and various decomposition products of TU) exit the system [14,15,38,40].

Growth mechanism of Sb_2S_3 layers by spray pyrolysis

The three most common growth mechanisms of solids can be described by the following equations [41]:

$$\sigma_{\text{SG}} > \sigma_{\text{LG}} + \sigma_{\text{SL}} \quad (1)$$

$$\sigma_{\text{SG}} < \sigma_{\text{LG}} + \sigma_{\text{SL}} \quad (2)$$

$$\sigma_{\text{SG}} \approx \sigma_{\text{LG}} + \sigma_{\text{SL}} \quad (3)$$

Where σ_{SG} is the surface free energy of the substrate–gas interface (TiO_2 –air), σ_{LG} is the surface free energy of the layer–gas interface (Sb_2S_3 –air) and σ_{SL} is the surface free energy of the substrate–layer interface (TiO_2 – Sb_2S_3). The surface free energy (σ) is the driving force of fluids and solids to seek a condition of minimum energy by contracting interfacial surface area [41]. Separate 3D islands grow if Equation 1 is valid, a.k.a. Volmer–Weber growth; 2D layer-by-layer growth occurs if Equation 2 is valid, a.k.a. Frank–Van der Merwe growth; combined 2D layer-by-layer and 3D island growth occurs if Equation 3 is valid, a.k.a. Stranski–Krastranov growth [36,41–43].

Furthermore, SEM surface studies show cap-shaped islands indicative of Volmer–Weber growth in Sb_2S_3 layers deposited on Si/ SiO_2 alternative substrates by ultrasonic spraying (Supporting Information File 1, Figure S10A,B). Metastibnite- Sb_2S_3 forms when formation of stibnite- Sb_2S_3 is halted by insufficient reaction time and energy [44–46]. Volmer–Weber island growth of amorphous Sb_2S_3 (and in some cases leaf-like grains of polycrystalline Sb_2S_3) have been observed in Sb_2S_3 layers

grown by chemical bath deposition on glass [47,48], $\text{In}_2\text{O}_3/\text{Sn}$ (ITO) [49], planar TiO_2 [16] and TiO_2 nanotube arrays [50], by sequential deposition [51] and spin coating [8,52] on planar TiO_2 , by photochemical deposition on mesoporous TiO_2 [53], by thermal evaporation on planar CdS [27] and planar TiO_2 [54]. Supported by these numerous observations, we consider the Volmer–Weber growth characteristic of Sb_2S_3 , given that the substrate and deposition conditions are met. Indeed, metastibnite, the naturally occurring mineral form of amorphous Sb_2S_3 , has the botryoidal characteristic, preferentially forming globular clusters [55]. We have also observed 3D growth of extremely thin TiO_2 layers by spray pyrolysis [56]. Therefore, 3D island growth may partially be imposed by the use of the spray pyrolysis method as well.

Based on the above observations, the morphology and crystallinity of as-deposited layers seems to determine the nature of Sb_2S_3 layer morphology as formed during vacuum thermal treatment. Our proposed growth mechanism of Sb_2S_3 by ultrasonic spraying in air is illustrated in Figure 6.

Optical properties of as-deposited and thermally treated Sb_2S_3 layers

The absorption coefficient (α) and band gap (E_g) values of Sb_2S_3 in both as-deposited and thermally treated glass/ITO/ $\text{TiO}_2/\text{Sb}_2\text{S}_3$ samples were determined using an approximated Sb_2S_3 layer thickness of 100 nm derived from SEM images (Table 3). The absorption coefficient α was determined as

$$\alpha = d^{-1} \ln \left[(1 - R) T^{-1} \right], \quad (4)$$

where d is the layer thickness, R is the total reflectance, included to compensate for thin film interference, and T is the total transmittance.

The band gap of Sb_2S_3 layers was determined by plotting $(\alpha h\nu)^{1/r}$ vs $h\nu$, where h is the Planck constant, ν is the frequency and $r = 1/2$ is the exponent corresponding to the assumed direct optical transition [57]. Extrapolating the linear region of this curve to the $h\nu$ -axis yields the optical band gap. Thin film interference could not be completely removed by accounting for reflectance in α calculations. Thus, the absolute values of α may deviate from the expected values with the uncertainty introduced by using a constant layer thickness in calculations.

The α vs wavelength plots of samples, which contain as-deposited or vacuum-treated Sb_2S_3 layers deposited from Sb/S 1:3 solution, are shown in Figure 7A. Likewise, α vs wavelength plots of Sb/S 1:6 samples are shown in Figure 7B. The α in samples containing amorphous Sb_2S_3 increases steadily from 10^3 – 10^4 cm^{-1} at 600–800 nm to 10^5 cm^{-1} at around 400 nm. The α increases significantly faster in samples containing as-grown crystalline Sb_2S_3 or vacuum crystallized Sb_2S_3 . The value of α surges by an order of magnitude from around 10^4 cm^{-1} to 10^5 cm^{-1} as the wavelength decreases from 750 nm to 650 nm due to the onset of absorption in crystalline Sb_2S_3 . At shorter wavelengths beyond the absorption edge, α increases at a slower rate, from around 10^5 cm^{-1} at 650 nm to more than $5 \times 10^5 \text{ cm}^{-1}$ at 300 nm. The optical absorption results are in agreement with XRD, which shows that these samples (3-220-As-dep., 3-210-170, 6-210-As-dep. and 6-200-170) contain orthorhombic Sb_2S_3 (Figure 2A,B). Comparing the α spectra of samples containing amorphous and crystalline

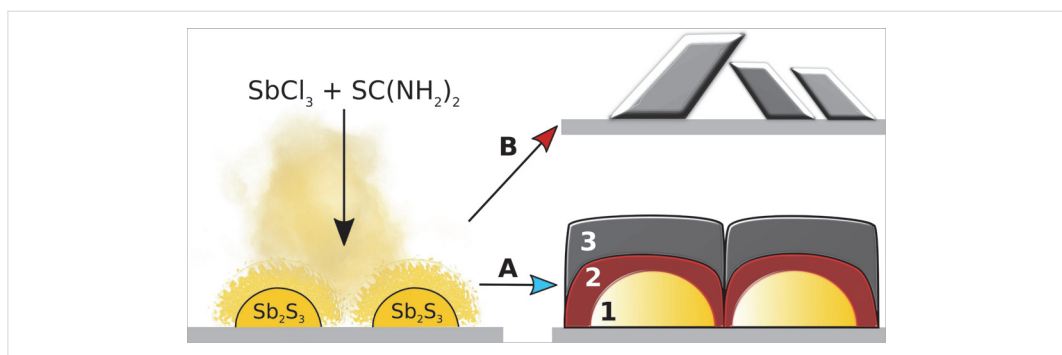


Figure 6: Proposed growth mechanism paths of Sb_2S_3 by Volmer–Weber growth during ultrasonic spraying of methanolic solution of SbCl_3 – $\text{SC}(\text{NH}_2)_2$ in excess of sulfur precursor in aerosol. Amorphous Sb_2S_3 nucleates after precipitation from a molten SbCl_3 – $\text{SC}(\text{NH}_2)_2$ mixture: A – Amorphous Sb_2S_3 islands nucleate on the rigid TiO_2 substrate and grow by 3D Volmer–Weber growth, surrounded by a protective bubbling liquid film of volatile SbCl_3 and TU decomposition products (1), eventually interconnecting by coalescence of sufficiently large islands to minimize Sb_2S_3 –air interfacial free surface energy (2), and form grain boundaries during crystallization in vacuum or inert environment (3). B – Sb_2S_3 crystallizes into separate grains if either the deposition temperature, the deposition time or the excess of TU in Sb/S precursor molar ratio exceed a critical value before or during process A, i.e., the energetic threshold for crystallization is surpassed.

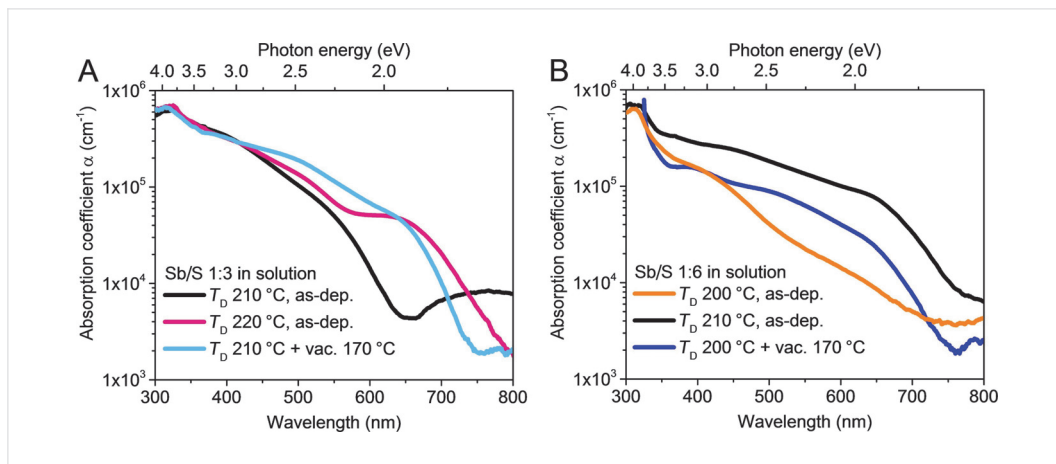


Figure 7: Absorption coefficient (α) vs wavelength of glass/ITO/TiO₂/Sb₂S₃ samples incorporating as-deposited and vacuum treated (170 °C, 5 minutes) Sb₂S₃ layers. The α of glass/ITO/TiO₂ substrates is not shown as it is negligible at the presented wavelengths. Sb₂S₃ layers were deposited from Sb/S 1:3 solution at 210 °C, 220 °C (A) and from Sb/S 1:6 solution at 200 °C and 210 °C (B).

Sb₂S₃ further confirms that the Sb₂S₃ layers deposited from Sb/S 1:3 solution at 200–210 °C, and from Sb/S 1:6 solution at 200 °C, are indeed amorphous. Namely, α is an order of magnitude smaller at around 600 nm in samples containing amorphous Sb₂S₃ layers (3-210-As-dep. and 6-200-As-dep.).

The experimentally determined E_g are ≈ 2.7 and 1.8 eV for amorphous and polycrystalline Sb₂S₃, respectively (Table 5, Tauc plots in Supporting Information File 1, Figure S12). In comparison, E_g of amorphous CBD-Sb₂S₃ on glass substrates is ≈ 2.5 eV [58] and E_g of polycrystalline Sb₂S₃ prepared by physical and chemical methods is commonly reported as 1.6–1.8 eV [1,22,58–60]. As such, we find the E_g of our polycrystalline Sb₂S₃ layers lies satisfactorily in the range of published values.

Table 5: Band gap (E_g) of as-deposited and thermally treated Sb₂S₃ layers, as estimated assuming direct optical transition and Tauc plots^a of optical transmittance spectra of glass/ITO/TiO₂/Sb₂S₃ samples.

Sb/S in sol.	E_g , eV					
	1:3			1:6		
T_D , °C	200	210	220	200	210	220
as-dep.	2.6	2.7	1.8	2.7	1.8	1.8
vac. 170 °C	1.8	1.8	1.8	1.8	1.8	1.8
vac. 200 °C	no layer ^b	1.8	1.8	no layer ^b	1.8	1.8

^aSupporting Information File 1, Figure S12A,B. ^bNo Sb₂S₃ was detected by XRD or Raman.

Conclusion

The structure, the morphology, and the optical properties of Sb₂S₃ layers could be controlled by varying the spray deposi-

tion temperature and the molar ratio of precursors in spray solution. Nonuniform, discontinuous layers of polycrystalline Sb₂S₃ (E_g 1.8 eV) were deposited by ultrasonic spray pyrolysis of SbCl₃/SC(NH₂)₂ 1:3 solution at $T_D \geq 220$ °C or 1:6 solution at $T_D \geq 210$ °C on glass/ITO/TiO₂ substrates in air. Increasing the concentration of the sulfur precursor in spray solution from Sb/S 1:3 to 1:6 reduced the crystallization temperature of Sb₂S₃ layers by ≈ 10 °C. Uniform layers of amorphous Sb₂S₃ ($E_g \approx 2.7$ eV, S/Sb 1:3) were deposited on glass/ITO/TiO₂ substrates in air by ultrasonic spray pyrolysis of Sb/S 1:3 solution at $T_D = 200$ –210 °C. High quality, uniform, pinhole-free coatings of polycrystalline orthorhombic Sb₂S₃ (E_g 1.8 eV, S/Sb 1.3) with lateral grain size as large as 10 μ m were produced by crystallization of amorphous Sb₂S₃ layers in vacuum at 170 °C for 5 minutes. Such Sb₂S₃ optical coatings are very attractive for future application as low-cost absorber layers in solar cells.

Experimental Materials

Commercial 1.1 mm thick soda-lime glass coated with 150 nm 25 Ω ·sq⁻¹ tin doped indium oxide (ITO) from ZSW was used as a substrate. The substrates were rinsed with deionized water, methanol (99.9 vol %), deionized water, dipped in aqueous room temperature H₂SO₄ (1 vol %), rinsed again with deionized water, and dried at 105 °C in air.

TiO₂ was prepared by methods used in our previous papers [7,12]. The TiO₂ film thickness was ≈ 80 nm based on SEM images. The Sb₂S₃ layers were deposited from 30 mM SbCl₃ (99 wt %) and SC(NH₂)₂ (99 wt %) methanolic (99.9 vol %)

solutions at molar ratios of Sb/S 1:3 and Sb/S 1:6. All chemicals were purchased from Sigma-Aldrich and used without any additional processing. The precursor solutions were prepared inside a glovebox with controlled humidity (<14 ppm).

The solutions were ultrasonically nebulized and guided by compressed air at a flow rate of 5 L·min⁻¹ onto glass/ITO/TiO₂ substrates at deposition temperatures of 200, 210, and 220 °C for 20 min (Sb/S 1:3) or 40 min (Sb/S 1:6). After deposition, some of the samples were thermally treated in dynamic vacuum (<4 × 10⁻⁶ Torr) at 170, 200 or 250 °C for 5 min. The average heating and cooling rate was ≈8 °C·min⁻¹.

Characterization

The elemental composition of the films was determined by energy dispersive X-ray spectroscopy (EDX) using a Bruker spectrometer with ESPRIT 1.8 system at the Zeiss HR FESEM Ultra 55 scanning electron microscope (SEM) operating at an accelerating voltage of 7 kV. The surface and cross-sectional morphologies of the layers were recorded by the same SEM system at an electron beam accelerating voltage of 4 kV.

Unpolarized micro-Raman measurements were conducted at room temperature using a Horiba Jobin Yvon Labram HR 800 spectrometer in backscattering geometry. The laser intensity was attenuated to ca. 143 μW·μm⁻² over a focal area of Ø 5 μm to prevent oxidation of the Sb₂S₃ layers, a common oversight according to Kharbush et al. [21]. Deconvoluted band centers in Raman shift, band intensities and full widths at half maximum (FWHM) were fitted using a Lorentzian function [61].

X-ray diffraction (XRD) patterns were recorded on a Rigaku Ultima IV powder diffractometer in θ-2θ mode (Cu Kα₁ λ = 1.5406 Å, 40 kV, 40 mA, step 0.02°, 5°/min, silicon strip detector D/teX Ultra). The crystal structure and phase composition were analyzed using Rigaku PDXL 2 software.

Optical total transmittance and total reflectance spectra of glass/ITO/TiO₂ reference and glass/ITO/TiO₂/Sb₂S₃ samples were measured in the 250–1600 nm range vs air as a reference using a Jasco V-670 UV-VIS-NIR spectrophotometer equipped with a 40 mm integrating sphere and Spectra Manager II software.

Supporting Information

Supporting Information File 1

Additional XRD, EDX data, SEM images, Lorentzian fitting of Sb₂S₃ Raman vibrational bands, and Tauc plots.

[<https://www.beilstein-journals.org/bjnano/content/supplementary/2190-4286-10-18-S1.pdf>]

Acknowledgements

We acknowledge Dr. Valdek Mikli from the Laboratory of Optoelectronic Materials Physics at Tallinn University of Technology for recording SEM images and EDX measurements, Estonian Research Council project IUT19-4 “Thin films and nanomaterials by wet-chemical methods for next-generation photovoltaics” and European Regional Development Fund project TK141 “Advanced materials and high-technology devices for sustainable energetics, sensorics and nanoelectronics” for funding.

ORCID® IDs

Jako S. Eensalu - <https://orcid.org/0000-0002-4312-0227>

Atanas Katerski - <https://orcid.org/0000-0003-1980-3391>

Erki Kärber - <https://orcid.org/0000-0001-6157-3070>

Ilona Oja Acik - <https://orcid.org/0000-0002-1870-3543>

Arvo Mere - <https://orcid.org/0000-0001-9070-3970>

Malle Krunk - <https://orcid.org/0000-0003-4658-4403>

References

- Versavel, M. Y.; Haber, J. A. *Thin Solid Films* **2007**, *515*, 7171–7176. doi:10.1016/j.tsf.2007.03.043
- Messina, S.; Nair, M. T. S.; Nair, P. K. *Thin Solid Films* **2007**, *515*, 5777–5782. doi:10.1016/j.tsf.2006.12.155
- Itzhaik, Y.; Niitsoo, O.; Page, M.; Hodes, G. *J. Phys. Chem. C* **2009**, *113*, 4254–4256. doi:10.1021/jp900302b
- Choi, Y. C.; Lee, D. U.; Noh, J. H.; Kim, E. K.; Seok, S. I. *Adv. Funct. Mater.* **2014**, *24*, 3587–3592. doi:10.1002/adfm.201304238
- Choi, Y. C.; Seok, S. I. *Adv. Funct. Mater.* **2015**, *25*, 2892–2898. doi:10.1002/adfm.201500296
- Wedemeyer, H.; Michels, J.; Chmielowski, R.; Bourdais, S.; Muto, T.; Sugiura, M.; Denler, G.; Bachmann, J. *Energy Environ. Sci.* **2013**, *6*, 67–71. doi:10.1039/c2ee23205g
- Parize, R.; Katerski, A.; Gromyko, I.; Rapenne, L.; Roussel, H.; Kärber, E.; Appert, E.; Krunk, M.; Consonni, V. *J. Phys. Chem. C* **2017**, *121*, 9672–9680. doi:10.1021/acs.jpcc.7b00178
- Sung, S.-J.; Gil, E. K.; Lee, S.-J.; Choi, Y. C.; Yang, K.-J.; Kang, J.-K.; Cho, K. Y.; Kim, D.-H. *J. Ind. Eng. Chem. (Amsterdam, Neth.)* **2017**, *56*, 196–202. doi:10.1016/j.jiec.2017.07.012
- Patil, P. S. *Mater. Chem. Phys.* **1999**, *59*, 185–198. doi:10.1016/s0254-0584(99)00049-8
- Kriisa, M.; Krunk, M.; Oja Acik, I.; Kärber, E.; Mikli, V. *Mater. Sci. Semicond. Process.* **2015**, *40*, 867–872. doi:10.1016/j.mssp.2015.07.049
- Rajpure, K. Y.; Bhosale, C. H. *Mater. Chem. Phys.* **2002**, *73*, 6–12. doi:10.1016/s0254-0584(01)00350-9
- Kärber, E.; Katerski, A.; Oja Acik, I.; Mere, A.; Mikli, V.; Krunk, M. *Beilstein J. Nanotechnol.* **2016**, *7*, 1662–1673. doi:10.3762/bjnano.7.158
- Kim, D.-H.; Lee, S.-J.; Park, M. S.; Kang, J.-K.; Heo, J. H.; Im, S. H.; Sung, S.-J. *Nanoscale* **2014**, *6*, 14549–14554. doi:10.1039/c4nr04148h
- Madarász, J.; Pokol, G. *J. Therm. Anal. Calorim.* **2007**, *88*, 329–336. doi:10.1007/s10973-006-8058-4
- Timchenko, V. P.; Novozhilov, A. L.; Slepysheva, O. A. *Russ. J. Gen. Chem.* **2004**, *74*, 1046–1050. doi:10.1023/b:rugc.0000045862.69442.aa

16. Parize, R.; Cossuet, T.; Chaix-Pluchery, O.; Roussel, H.; Appert, E.; Consonni, V. *Mater. Des.* **2017**, *121*, 1–10. doi:10.1016/j.matdes.2017.02.034
17. Chang, H.; Huang, P. J. *J. Raman Spectrosc.* **1998**, *29*, 97–102. doi:10.1002/(sici)1097-4555(199802)29:2<97::aid-jrs198>3.0.co;2-e
18. Liu, Y.; Eddie Chua, K. T.; Sum, T. C.; Gan, C. K. *Phys. Chem. Chem. Phys.* **2014**, *16*, 345–350. doi:10.1039/c3cp53879f
19. Makreski, P.; Petruševski, G.; Ugarković, S.; Jovanovski, G. *Vib. Spectrosc.* **2013**, *68*, 177–182. doi:10.1016/j.vibspec.2013.07.007
20. Ibáñez, J.; Sans, J. A.; Popescu, C.; López-Vidrier, J.; Elvira-Betanzos, J. J.; Cuenca-Gotor, V. P.; Gomis, O.; Manjón, F. J.; Rodríguez-Hernández, P.; Muñoz, A. *J. Phys. Chem. C* **2016**, *120*, 10547–10558. doi:10.1021/acs.jpcc.6b01276
21. Kharbush, S.; Libowitzky, E.; Beran, A. *Eur. J. Mineral.* **2009**, *21*, 325–333. doi:10.1127/0935-1221/2009/0021-1914
22. Medles, M.; Benramdane, N.; Bouzidi, A.; Sahraoui, K.; Miloua, R.; Desfeux, R.; Mathieu, C. *J. Optoelectron. Adv. Mater.* **2014**, *16*, 726–731. <https://joam.inoe.ro/index.php?option=magazine&op=view&idu=3498&catid=84>
23. Nakamoto, K. *Infrared and Raman Spectra of Inorganic and Coordination Compounds*, 6th ed.; Wiley-Blackwell: São Paulo, Brazil, 2008. doi:10.1002/9780470405888
24. Hofmann, W. Z. *Kristallogr.* **1933**, *86*, 225–245. doi:10.1524/zkri.1933.86.1.225
25. Petzelt, J.; Grigas, J. *Ferroelectrics* **1973**, *5*, 59–68. doi:10.1080/00150197308235780
26. Grovonor, C. R. M. *J. Phys. C: Solid State Phys.* **1985**, *18*, 4079–4119. doi:10.1088/0022-3719/18/21/008
27. Escoria-García, J.; Becerra, D.; Nair, M. T. S.; Nair, P. K. *Thin Solid Films* **2014**, *569*, 28–34. doi:10.1016/j.tsf.2014.08.024
28. Boughalmi, R.; Boukhachem, A.; Kahlaoui, M.; Maghraoui, H.; Amlouk, M. *Mater. Sci. Semicond. Process.* **2014**, *26*, 593–602. doi:10.1016/j.mssp.2014.05.059
29. Birkholz, M.; Selle, B.; Fuhs, W.; Christiansen, S.; Strunk, H. P.; Reich, R. *Phys. Rev. B* **2001**, *64*, 085402. doi:10.1103/physrevb.64.085402
30. Greenwood, N. N.; Earnshaw, A. *Chemistry of the Elements*, 2nd ed.; Butterworth-Heinemann: Oxford, United Kingdom, 1997. doi:10.1016/c2009-0-30414-6
31. Fujishima, A.; Zhang, X.; Tryk, D. A. *Surf. Sci. Rep.* **2008**, *63*, 515–582. doi:10.1016/j.surfrep.2008.10.001
32. Madarász, J.; Krunks, M.; Niinistö, L.; Pokol, G. *J. Therm. Anal. Calorim.* **2015**, *120*, 189–199. doi:10.1007/s10973-015-4481-8
33. Madarász, J.; Krunks, M.; Niinistö, L.; Pokol, G. *J. Therm. Anal. Calorim.* **2004**, *78*, 679–686. doi:10.1023/b:jtan.0000046127.69336.90
34. Politseva, S.; Oja Acik, I.; Krunks, M.; Tõnsuaadu, K.; Mere, A. *J. Therm. Anal. Calorim.* **2015**, *121*, 177–185. doi:10.1007/s10973-015-4580-6
35. Lan, C.; Liang, G.; Lan, H.; Peng, H.; Su, Z.; Zhang, D.; Sun, H.; Luo, J.; Fan, P. *Phys. Status Solidi RRL* **2018**, *12*, 1800025. doi:10.1002/pssr.201800025
36. Zheng, Y. C.; Yang, S.; Chen, X.; Chen, Y.; Hou, Y.; Yang, H. G. *Chem. Mater.* **2015**, *27*, 5116–5121. doi:10.1021/acs.chemmater.5b01924
37. Kushkhov, A. R.; Gaev, D. S.; Rabinovich, O. I.; Stolyarov, A. G. *Crystallogr. Rep.* **2013**, *58*, 365–369. doi:10.1134/s1063774513020132
38. Piacente, V.; Scardala, P.; Ferro, D. J. *Alloys Compd.* **1992**, *178*, 101–115. doi:10.1016/0925-8388(92)90251-4
39. Lide, D. R., Ed. *CRC Handbook of Chemistry and Physics*, 87th ed.; CRC Press: Boca Raton, FL, U.S.A., 2006.
40. Ozturk, I. I.; Kourkoumelis, N.; Hadjikakou, S. K.; Manos, M. J.; Tasiopoulos, A. J.; Butler, I. S.; Balzarini, J.; Hadjiiladis, N. *J. Coord. Chem.* **2011**, *64*, 3859–3871. doi:10.1080/00958972.2011.633603
41. Rohrer, G. S. *Metall. Mater. Trans. A* **2010**, *41*, 1063–1100. doi:10.1007/s11661-010-0215-5
42. Volmer, M.; Weber, A. Z. *Phys. Chem., Stoechiom. Verwandtschaftsl.* **1926**, *119*, 277–301. doi:10.1515/zpch-1926-11927
43. Abraham, D. B.; Newman, C. M. *EPL* **2009**, *86*, 16002–16007. doi:10.1209/0295-5075/86/16002
44. Ostwald, W. *The Principles of Inorganic Chemistry*, 2nd ed.; Macmillan and Co., Ltd.: London, United Kingdom, 1904.
45. Brookins, D. G. *Econ. Geol.* **1972**, *67*, 369–372. doi:10.2113/gsecongeo.67.3.369
46. Clouet, E. Modeling of Nucleation Processes. In *ASM Handbook, Fundamentals of Modeling for Metals Processing*; Furrer, D. U.; Semiatin, S. L., Eds.; ASM International: Materials Park, OH, U.S.A., 2009; Vol. 22A, pp 203–219.
47. Lokhande, C. D.; Sankapal, B. R.; Mane, R. S.; Pathan, H. M.; Muller, M.; Giersig, M.; Ganesan, V. *Appl. Surf. Sci.* **2002**, *193*, 1–10. doi:10.1016/s0169-4332(01)00819-4
48. Krishnan, B.; Arato, A.; Cardenas, E.; Roy, T. K. D.; Castillo, G. A. *Appl. Surf. Sci.* **2008**, *254*, 3200–3206. doi:10.1016/j.apsusc.2007.10.098
49. Zhu, G.; Huang, X.; Hojamberdiev, M.; Liu, P.; Liu, Y.; Tan, G.; Zhou, J.-p. *J. Mater. Sci.* **2011**, *46*, 700–706. doi:10.1007/s10853-010-4797-5
50. Bessegato, G. G.; Cardoso, J. C.; Silva, B. F. d.; Zanon, M. V. B. *J. Photochem. Photobiol., A* **2014**, *276*, 96–103. doi:10.1016/j.jphotochem.2013.12.001
51. Zheng, L.; Jiang, K.; Huang, J.; Zhang, Y.; Bao, B.; Zhou, X.; Wang, H.; Guan, B.; Yang, L. M.; Song, Y. *J. Mater. Chem. A* **2017**, *5*, 4791–4796. doi:10.1039/c7ta00291b
52. Wang, W.; Strössner, F.; Zimmermann, E.; Schmidt-Mende, L. *Sol. Energy Mater. Sol. Cells* **2017**, *172*, 335–340. doi:10.1016/j.solmat.2017.07.046
53. Kozytskiy, A. V.; Stroyuk, O. L.; Skoryk, M. A.; Dzhagan, V. M.; Kuchmiy, S. Y.; Zahn, D. R. T. *J. Photochem. Photobiol., A* **2015**, *303–304*, 8–16. doi:10.1016/j.jphotochem.2015.02.005
54. Kamruzzaman, M.; Chaoping, L.; Yishu, F.; Farid Ul Islam, A. K. M.; Zapien, J. A. *RSC Adv.* **2016**, *6*, 99282–99290. doi:10.1039/c6ra20378g
55. Morteani, G.; Ruggieri, G.; Möller, P.; Preinfalk, C. *Miner. Deposita* **2011**, *46*, 197–210. doi:10.1007/s00126-010-0316-5
56. Oja Acik, I.; Junolainen, A.; Mikli, V.; Danilson, M.; Krunks, M. *Appl. Surf. Sci.* **2009**, *256*, 1391–1394. doi:10.1016/j.apsusc.2009.08.101
57. Tauc, J.; Grigorovici, R.; Vancu, A. *Phys. Status Solidi* **1966**, *15*, 627–637. doi:10.1002/pssb.19660150224
58. Grozdanov, I. *Semicond. Sci. Technol.* **1994**, *9*, 1234–1241. doi:10.1088/0268-1242/9/6/013
59. Grozdanov, I.; Ristov, M.; Sinadinovski, G.; Mitreski, M. *J. Non-Cryst. Solids* **1994**, *175*, 77–83. doi:10.1016/0022-3093(94)90317-4

60. Medina-Montes, M. I.; Montiel-González, Z.; Paraguay-Delgado, F.; Mathews, N. R.; Mathew, X. *J. Mater. Sci.: Mater. Electron.* **2016**, *27*, 9710–9719. doi:10.1007/s10854-016-5033-0
61. Wojdyr, M. *J. Appl. Crystallogr.* **2010**, *43*, 1126–1128. doi:10.1107/s0021889810030499

License and Terms

This is an Open Access article under the terms of the Creative Commons Attribution License (<http://creativecommons.org/licenses/by/4.0>). Please note that the reuse, redistribution and reproduction in particular requires that the authors and source are credited.

The license is subject to the *Beilstein Journal of Nanotechnology* terms and conditions: (<https://www.beilstein-journals.org/bjnano>)

The definitive version of this article is the electronic one which can be found at:
[doi:10.3762/bjnano.10.18](https://doi.org/10.3762/bjnano.10.18)

Publication II

J. S. Eensalu, A. Katerski, E. Kärber, L. Weinhardt, M. Blum, C. Heske, W. Yang, I. Oja Acik, M. Krunk. "Semitransparent Sb_2S_3 thin film solar cells by ultrasonic spray pyrolysis for use in solar windows," *Beilstein Journal of Nanotechnology*, vol. 10, pp. 2396–2409, Dec. 2019, doi: 10.3762/bjnano.10.230.



Semitransparent Sb_2S_3 thin film solar cells by ultrasonic spray pyrolysis for use in solar windows

Jako S. Eensalu^{*1}, Atanas Katerski¹, Erki Kärber^{1,2}, Lothar Weinhardt^{2,3}, Monika Blum⁴, Clemens Heske^{2,3}, Wanli Yang⁴, Ilona Oja Acik¹ and Malle Krunk^{*1}

Full Research Paper

[Open Access](#)**Address:**

¹Department of Materials and Environmental Technology, Tallinn University of Technology, Ehitajate tee 5, 19086, Estonia, ²Department of Chemistry and Biochemistry, University of Nevada, Las Vegas (UNLV), 4505 Maryland Parkway, Las Vegas, NV 89154-4003, USA, ³Institute for Photon Science and Synchrotron Radiation (IPS), Karlsruhe Institute of Technology (KIT), 76344 Eggenstein-Leopoldshafen, Germany and ⁴Advanced Light Source, Lawrence Berkeley National Laboratory, 1 Cyclotron Road, Berkeley, California, 94720, USA

Email:

Jako S. Eensalu^{*} - jako.eensalu@taltech.ee; Malle Krunk^{*} - malle.krunk@taltech.ee

^{*} Corresponding author

Keywords:

antimony sulfide; semitransparent solar cells; solar windows; thin films; ultrasonic spray pyrolysis

Beilstein J. Nanotechnol. **2019**, *10*, 2396–2409.

doi:10.3762/bjnano.10.230

Received: 18 July 2019

Accepted: 08 November 2019

Published: 06 December 2019

Associate Editor: N. Motta

© 2019 Eensalu et al.; licensee Beilstein-Institut.

License and terms: see end of document.

Abstract

The integration of photovoltaic (PV) solar energy in zero-energy buildings requires durable and efficient solar windows composed of lightweight and semitransparent thin film solar cells. Inorganic materials with a high optical absorption coefficient, such as Sb_2S_3 ($>10^5 \text{ cm}^{-1}$ at 450 nm), offer semitransparency, appreciable efficiency, and long-term durability at low cost. Oxide-free throughout the Sb_2S_3 layer thickness, as confirmed by combined studies of energy dispersive X-ray spectroscopy and synchrotron soft X-ray emission spectroscopy, semitransparent Sb_2S_3 thin films can be rapidly grown in air by the area-scalable ultrasonic spray pyrolysis method. Integrated into a ITO/ TiO_2 / Sb_2S_3 /P3HT/Au solar cell, a power conversion efficiency (PCE) of 5.5% at air mass 1.5 global (AM1.5G) is achieved, which is a record among spray-deposited Sb_2S_3 solar cells. An average visible transparency (AVT) of 26% of the back-contact-less ITO/ TiO_2 / Sb_2S_3 solar cell stack in the wavelength range of 380–740 nm is attained by tuning the Sb_2S_3 absorber thickness to 100 nm. In scale-up from mm^2 to cm^2 areas, the Sb_2S_3 hybrid solar cells show a decrease in efficiency of only 3.2% for an 88 mm^2 Sb_2S_3 solar cell, which retains 70% relative efficiency after one year of non-encapsulated storage. A cell with a PCE of 3.9% at 1 sun shows a PCE of 7.4% at 0.1 sun, attesting to the applicability of these solar cells for light harvesting under cloud cover.

Introduction

Modern buildings, especially high-rise buildings, have a large window area available for building-integrated photovoltaics (BIPV). Covering the windows with semitransparent thin film solar cells creates energy-producing solar windows. In addition to current BIPV technology, solar windows could provide advantageous features: they are mountable during construction, they promise an effective utilization of building space, as well as cost and weight savings, and about half of the building electricity demand can be produced on site [1]. Solar windows can be split into two groups: perforated grids of opaque solar cells, such as silicon, or one continuous semitransparent thin film solar cell (dye-sensitized, perovskite, quantum dot, etc.) [1]. Perforated solar windows, comprised of fragments of crystalline Si (c-Si) solar cells, have shown a tendency to overheat and underperform in efficiency (PCE) [2,3]. C-Si grids are also considered visually unappealing for solar windows [4]. Accordingly, thin film solar cells, even with lower PCE, are considered more promising for applications in solar windows [1,4].

The fundamental issue of semitransparent solar cells is a tradeoff between high PCE and high average visible transparency (AVT). The AVT of solar cells must be over 20% to qualify as semitransparent [4]. The PCE and AVT of semitransparent thin film solar cells are listed in the following for reference: dye-sensitized – PCE of 9.2% at 60% AVT [5]; polymer – PCE of 4.0% at 66% AVT [6]; halide perovskite – PCE of 6.4% at 30% AVT [7]. Dye-sensitized, organic, and halide perovskite absorbers are generally sensitive to moisture, especially in combination with sunlight and air [8–10]. At present, tremendous research efforts have been allocated worldwide to increase the long-term stability of these solar cells [11]. As minimizing fabrication cost is crucial for commercialization, solar windows would benefit from a fully inorganic absorber that has superior stability towards moisture and air as well as sunlight.

Sb₂S₃ has attractive properties ($E_g \approx 1.7$ eV, absorption coefficient $\alpha \approx 1.8 \times 10^5$ cm⁻¹ at 450 nm, anisotropic structure, inorganic) as a light absorber for conventional and semitransparent photovoltaic use [12–14]. Sb₂S₃ has been incorporated as a solar absorber in photo-electrochemical cells, thin film cells, extremely thin absorber (ETA) cells, and hybrid solar cells based on a planar underlay or on nano- or mesostructured scaffolds [15–22]. Studies on ETA Sb₂S₃ cells, which became the basis for respective hybrid solar cells, were pioneered by the teams of Nair, Nezu, and Hodes in the mid-2000s [19,23,24]. The record PCE of 7.5%, achieved with solar cells based on Sb₂S₃ grown by chemical bath deposition (CBD) into mesoporous TiO₂, shows the excellent potential of Sb₂S₃ as a PV

absorber, and the suitability of its fabrication by chemical methods [20]. Until now, semitransparency aspects of Sb₂S₃ solar cells have only been studied by Zimmermann et al., who reported a PCE of 4.25% for a tin-doped indium oxide (ITO)/TiO₂/Sb₂S₃/poly(3-hexylthiophene-2,5-diyl) (P3HT)/Ag solar cell with a 50–70 nm thick Sb₂S₃ absorber and a nontransparent 125 nm Ag back contact [21].

TiO₂ is the most commonly used electron transport material (ETM) in Sb₂S₃ solar cells [18,25–32]. SnO₂ and ZnO have also been employed as the planar ETM, with varying success [33,34]. Conjugated polymers, e.g., P3HT, Spiro-OMeTAD (2,2',7,7'-tetrakis[*N,N*-di(4-methoxyphenyl)amino]-9,9'-spirobifluorene), and poly[2,6-(4,4-bis(2-ethylhexyl)-4*H*-cyclopenta[2,1-*b*;3,4-*b'*]dithiophene)-*alt*-4,7-(2,1,3-benzothiadiazole)] (PCPDTBT), are the most popular organic hole transport materials (HTMs) in Sb₂S₃ solar cell studies because of the high PCE values [17,18,25,27–31,35]. However, planar cells with inorganic HTMs (which are chemically and thermally more stable and have lower cost), such as CuSCN, NiO_x, and V₂O₅, have also shown comparable efficiencies [26,36,37].

As the performance of PV cells highly depends on the quality of the absorber, the development of fabrication techniques to produce high quality Sb₂S₃ absorber layers, with few grain boundaries and intra-grain defects is essential to enable commercialization of Sb₂S₃-based solar cells [14,38]. The record PCE of 5.77% was achieved with a planar TiO₂/Sb₂S₃/P3HT cell by employing an 87 nm thick Sb₂S₃ thin film absorber grown by atomic layer deposition (ALD) [18], whereas a PCE of 4.25% was reported when using Sb₂S₃ layers grown by CBD [21]. Unfortunately, the Sb₂O₃ impurity phase, which is considered detrimental to PV performance, unavoidably forms in the bulk of the Sb₂S₃ thin film when it is grown by CBD from an aqueous solution [18]. In 2018, PCE \approx 5.7% was achieved for a cell based on a spin-coated Sb₂S₃ absorber, and the same group further increased the PCE of this cell to 6.4% by Zn doping during spin-coating of Sb₂S₃ [39,40]. Soon after, by doping Sb₂S₃ with CsOH, the PCE of planar Sb₂S₃ solar cells was boosted from 4.3% to 6.6% [41]. When looking forward to mass production on meter-sized substrates, however, spin-coating cannot be upscaled due to design limitations [42]. Industrialization is feasible only for low-cost, upscalable methods, to the detriment of both conventional ALD and CBD that require several hours to deposit 100 nm thick Sb₂S₃ films [18,20,21]. Regarding vacuum deposition methods, a PCE of 3.5% was achieved by thermally evaporating 700 nm of Sb₂S₃ onto planar CdS. The main drawbacks of thermal evaporation and conventional ALD as vacuum techniques are the high

energy demand and the need for batch processing, which inflates production costs.

As a potent solution-based chemical deposition method, ultrasonic chemical spray pyrolysis (USP) is capable of rapid, area-scalable, roll-to-roll and low-cost in-air deposition of Sb_2S_3 layers without imposing limitations on the substrate size [43,44]. A recent paper showed a PCE of 4.6% in solar cells based on $\text{Sb}_2(\text{S},\text{Se})_3$ grown onto planar CdS by USP, followed by Se vapor annealing at ≈ 400 °C. However, pristine Sb_2S_3 solar cells consistently yielded a PCE below 0.1% [45]. This clearly illustrates the difficulty of preparing high quality Sb_2S_3 absorber layers by USP. A comparative overview of HTMs, deposition methods and PV parameters of solar cells of planar $\text{TiO}_2/\text{Sb}_2\text{S}_3/\text{HTM}$ configuration of relevant studies is provided in Table S1 in Supporting Information File 1.

Previously, we observed that the moderate photocurrent density and PCE (of 1.9%) in solar cells based on Sb_2S_3 layers grown by USP was due to a discontinuity of the Sb_2S_3 layer [28]. In our recent study, we showed that the discontinuity of Sb_2S_3 films grown by USP, and likely other chemical methods, is a result of 3D island growth [46]. We demonstrated that by adapting a two-step sequence, whereby amorphous Sb_2S_3 layers are first deposited by USP and then crystallized by thermal annealing, compact Sb_2S_3 thin films with uniform thickness can be fabricated [46]. Similarly, a two-step procedure to grow compact Sb_2S_3 thin films has become common practice for many deposition techniques [18–20,27,29,31,35,47]. To summarize: in order to achieve progress in the various areas of PV applications, e.g., BIPV, and to increase the availability of PV beyond the state-of-the-art in compliance with ever stricter safety and health regulations, novel thin film solar cell designs are required, using abundant non-toxic materials and implementing cost-effective solar cell fabrication technologies.

The aim of this study was to fabricate state-of-the art hybrid solar cells, based on compact thin films of Sb_2S_3 deposited by USP in air, by optimizing the thickness of the Sb_2S_3 layer, and to consider the influence of cell area, storage time and light intensity on PV performance to investigate their potential for application in semitransparent solar windows. In this study, hybrid solar cells with a maximum PCE of 5.5% at AM1.5G and an AVT of 26% without back contact were fabricated. A PCE of 3.2% was recorded for a solar cell with 88 mm² area. This is the highest PCE in this size category; so far, the PCE of planar Sb_2S_3 solar cells has only been reported for ≈ 1 cm² area (by our group). A solar cell with a PCE of 3.9% at AM1.5G (1 sun) showed a PCE of 7.4% at 0.1 sun, and 10.2% at 0.03 sun, demonstrating the suitability of this solar cell for operation in direct sunlight, as well as under full cloud cover.

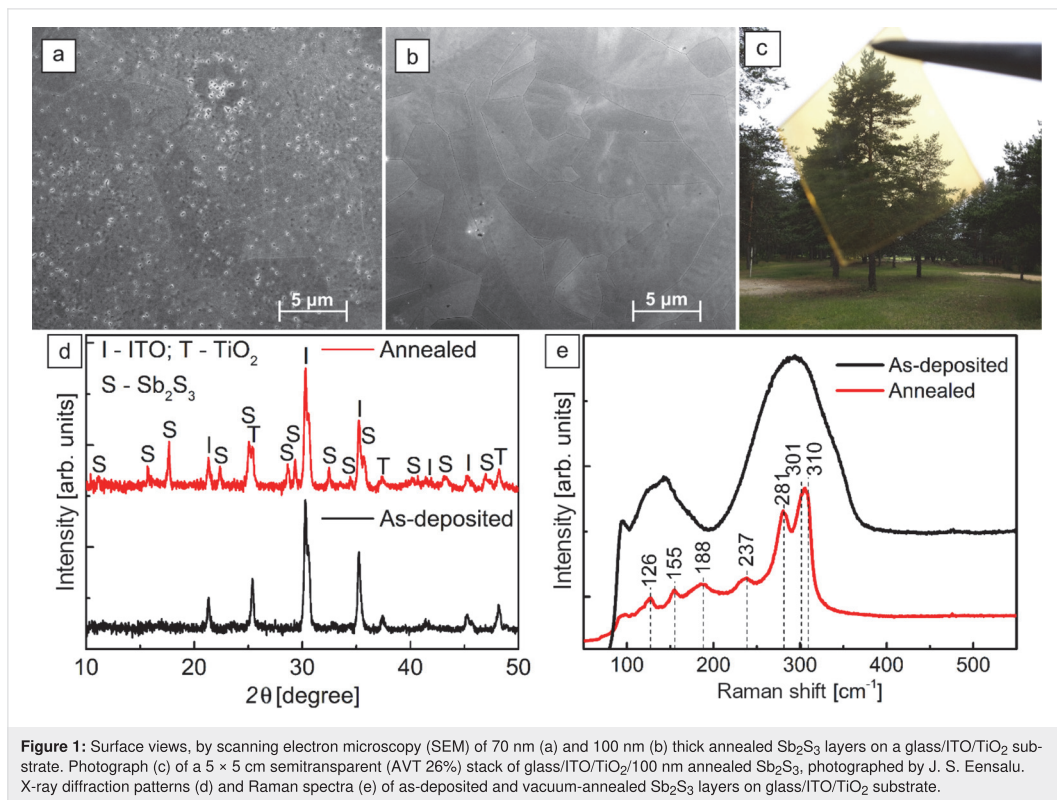
Results and Discussion

Quality assessment of USP- Sb_2S_3 thin films

The substrate coverage of Sb_2S_3 layers on a glass/ITO/ TiO_2 substrate, annealed in vacuum, depends on the quantity of Sb_2S_3 deposited by USP [46]. Thinner (≤ 70 nm) Sb_2S_3 layers contain pin-holes (Figure 1a), whereas thicker (≥ 100 nm) Sb_2S_3 layers fully cover the TiO_2 ETM (Figure 1b). As the Sb_2S_3 film thickness is increased from 70 to 100 nm, the average lateral grains size increases from ≈ 5 μm (Figure 1a) to ≈ 10 μm (Figure 1b). An increase in grain size with Sb_2S_3 film thickness has been observed by using both physical deposition techniques and chemical deposition techniques [16,32,48]. For reference, the semitransparency of a 5×5 cm glass/ITO/ $\text{TiO}_2/100$ nm Sb_2S_3 stack, showing an AVT of 26%, is illustrated in a photograph in Figure 1c. The initial results show the excellent perspective of this type of solar cell. However, it should be noted that the AVT requirement for semitransparent solar cells generally refers to the complete stack. Thus, further optimization of the HTM and back contact is needed to attain an AVT in excess of 20% for the complete solar cell.

As-deposited Sb_2S_3 layers on glass/ITO/ TiO_2 substrate were amorphous (Figure 1d), as only signals of anatase- TiO_2 and In_2O_3 from the substrate were detected by X-ray diffraction (XRD). In contrast, the XRD pattern of the vacuum-annealed sample matched orthorhombic Sb_2S_3 (ICDD PDF 01-075-4012). The Raman spectrum of the as-deposited Sb_2S_3 layer contains two broad bands (Figure 1e), which are characteristic of amorphous Sb_2S_3 [28,46]. After vacuum annealing, characteristic narrower bands of Sb_2S_3 are detected, which is an expected result when crystalline Sb_2S_3 is formed [28,46,49]. No traces of additional phases were detected by either XRD or Raman in any glass/ITO/ $\text{TiO}_2/\text{Sb}_2\text{S}_3$ samples. Chlorine, which could originate from the SbCl_3 precursor, was not detected by energy-dispersive X-ray spectroscopy (EDX) in any sample. Furthermore, the atomic ratio of S to Sb in the annealed Sb_2S_3 layers was close to the stoichiometric value of 1.5, as estimated using EDX (Figure S1 in Supporting Information File 1).

Soft X-ray emission spectroscopy (XES) is an element- and site-specific method that allows for the study of the electronic structure and chemical bonding in materials [50–53]. The attenuation length (e^{-1}) of ≈ 180 eV soft X-rays in Sb_2S_3 is ≈ 83 nm [54], which makes XES an excellent tool for non-destructively studying the near-surface regions and bulk of thin films [55]. For 50 nm thick Sb_2S_3 layers, the XES spectra (Figure 2) probe the chemical states in the entire Sb_2S_3 film. The S $L_{2,3}$ XES data in Figure 2 allows three transitions for the Sb_2S_3 films and the reference (denoted as “S 3s”, “Sb 5s”, and UVB – upper valence band) to be clearly distinguished. These transitions stem from electronic transitions from valence bands into the



S 2p core holes ($S L_{2,3}$) created as the initial state of XES. The transition centered at 147.5 eV is predominantly due to S 3s-derived electronic valence states and appears as the main transition of sulfides [50]. Another peak, as a shoulder for the former, is found at 151 eV and ascribed to Sb 5s-derived states by comparison with band structure and density of states calculations [50]. Lastly, transitions from the upper valence band of Sb_2S_3 can be found centered at around 156 eV. These transitions were identified in line with atom-decomposed density of states prediction in the valence band of Sb_2S_3 , calculated from first principles [56].

The overall spectral shape of the Sb_2S_3 thin films, as-prepared and after annealing, agree very well with the Sb_2S_3 reference powder. In contrast, no evidence for S–O bonds can be found in the Sb_2S_3 thin film spectra, as can be seen by comparing with the reference spectra of $\text{Sb}_2(\text{SO}_4)_3$. Sulfate spectra have characteristic line shapes [53]. Thus, the XES study suggests that S is exclusively bonded to Sb in the Sb_2S_3 films, throughout its thickness, in the entirety of the analyzed spot size, and both as-deposited and after annealing. The XES study, in addition to the EDX results that showed a S to Sb atomic ratio of 1.5 in the

layers, provides further assurance that inclusion of O in the form of a minor impurity phase in the Sb_2S_3 layers is likely negligible. Thus, even without further scrutinizing the layer composition, these results already give USP a distinct advantage over aqueous CBD, wherein the inclusion of oxygen is inevitable and traceable [57–59].

To summarize the thin film characterization, we have fabricated polycrystalline, chlorine-free (below EDX detection limit), and oxygen-free (EDX and XES analysis) Sb_2S_3 thin films by USP in air. To our knowledge, this is the first report on XES experiments for Sb_2S_3 thin films, which, for us, provided the indispensable support of evidence for the claim of the exclusion of oxygen in Sb_2S_3 thin films grown by USP in air.

Development of USP- Sb_2S_3 semitransparent solar cells

Influence of Sb_2S_3 thickness on PV performance of semitransparent Sb_2S_3 solar cells

To investigate the effect of Sb_2S_3 film thickness on PV performance of solar cells, we applied 30, 70, 100, and 150 nm thick films of USP- Sb_2S_3 . By increasing the Sb_2S_3 layer thickness

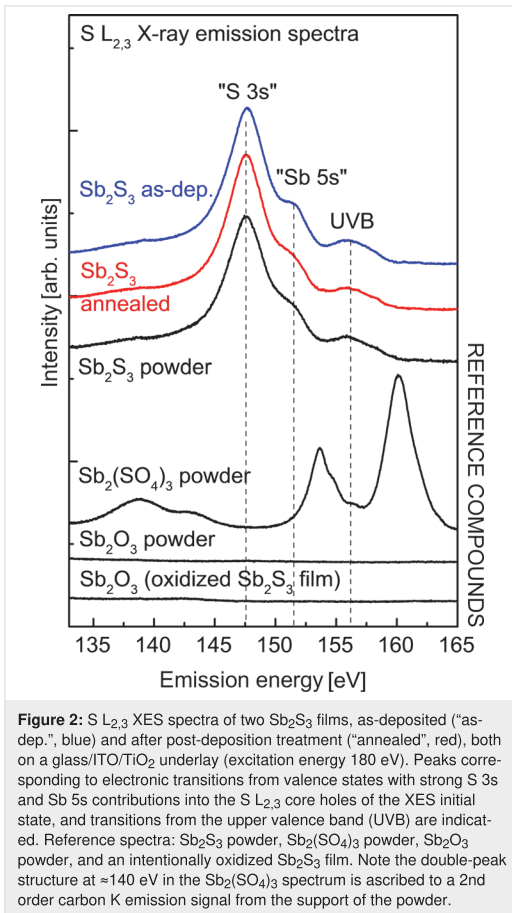


Figure 2: S $L_{2,3}$ XES spectra of two Sb_2S_3 films, as-deposited (“as-dep.”, blue) and after post-deposition treatment (“annealed”, red), both on a glass/ITO/ TiO_2 underlay (excitation energy 180 eV). Peaks corresponding to electronic transitions from valence states with strong S 3s and Sb 5s contributions into the S $L_{2,3}$ core holes of the XES initial state, and transitions from the upper valence band (UVB) are indicated. Reference spectra: Sb_2S_3 powder, $Sb_2(SO_4)_3$ powder, Sb_2O_3 powder, and an intentionally oxidized Sb_2S_3 film. Note the double-peak structure at ≈ 140 eV in the $Sb_2(SO_4)_3$ spectrum is ascribed to a 2nd order carbon K emission signal from the support of the powder.

from 30 to 100 nm in glass/ITO/ TiO_2 / Sb_2S_3 /P3HT/Au solar cell (Figure 3a), the open-circuit voltage (V_{OC}) decreased slightly (704 ± 7 mV vs 693 ± 17 mV), the short-circuit current (J_{SC}) doubled (4.8 ± 0.3 mA cm^{-2} vs 10.3 ± 1.0 mA cm^{-2}), the fill factor (FF) increased moderately ($43 \pm 3\%$ vs $52 \pm 3\%$), and consequently, the PCE increased by a factor of ≈ 2.5 ($1.5 \pm 0.1\%$ vs $3.7 \pm 0.4\%$). The highest V_{OC} of 726 mV observed in this study is comparable to the highest V_{OC} of 732 mV reported for planar TiO_2 / Sb_2S_3 solar cells, where Sb_2S_3 was grown by chemical bath deposition [21]. Increasing the Sb_2S_3 layer thickness further to 150 nm causes all photoconversion parameters to plummet; an expected result in the case of increased recombination losses in the bulk of the Sb_2S_3 absorber layer [60]. The FF is adversely affected by large values of series resistance (R_S) and by small values of shunt resistance (R_{SH}) [61]. The cells with 70 nm thick Sb_2S_3 had the highest FF of $57 \pm 4\%$, incidentally coinciding with the smallest of R_S and the largest of R_{SH} , whereas the FF was slightly smaller in cells with 100 nm thick-

ness, mostly due to a smaller R_{SH} . Compared to cells with 70–100 nm thick Sb_2S_3 layers, the FF was smaller by around 10% in cells with both the thinnest (30 nm) and the thickest (150 nm) Sb_2S_3 layers. The decrease in the FF in these cells could mainly be attributed to the occurrence of R_S over $10 \Omega cm^2$ (Table 1). In particular, R_S could be inflated in cells with thin (30 nm) Sb_2S_3 layers, because the mobility of charge carriers is likely impeded by numerous grain boundaries owing to the smaller grain size in thinner films. On the other end, R_S is also over $10 \Omega cm^2$ in the cells with overly thick Sb_2S_3 layers (150 nm), which is ascribed to the ohmic resistance of the thicker absorber. In this study, the resistivity (ρ) of 100–150 nm thick Sb_2S_3 films on glass/ TiO_2 substrate was measured by the collinear four-wire technique and by van der Pauw measurements to be in the range of $2\text{--}3 \times 10^6 \Omega cm$, as anticipated.

Figure 3b shows the external quantum efficiency (EQE) of solar cells with 70, 100 and 150 nm thick Sb_2S_3 thin films and transmittance of solar cells without P3HT/Au back contact. The AVT of the stacks of glass/ITO/ TiO_2 / Sb_2S_3 with 70, 100, and 150 nm of Sb_2S_3 is 28%, 26%, and 16%, respectively in the 380–740 nm wavelength range (Figure 3b). Thus, the 150 nm thick Sb_2S_3 film is already too opaque for it to qualify as a semitransparent absorber layer. According to the EQE, appreciable photoelectric conversion in these cells occurs in the 320–750 nm wavelength range. The observed EQE onset at 750 nm corresponds to a band gap of 1.65 eV of crystalline Sb_2S_3 . Cells with 70 and 100 nm thick Sb_2S_3 film showed the best EQE values, reaching almost 80% EQE at around 425 nm wavelength, which is almost the maximum realistically attainable EQE. The decreased EQE at higher wavelengths is common for solar cells with a chemically deposited Sb_2S_3 absorber [18,21]. The average and best photoconversion parameters calculated from the J – V curves and EQE are presented in Table 1. Compared to J – V -derived PV parameters of planar TiO_2 / Sb_2S_3 /HTM solar cells (Supporting Information File 1, Table S1), the PCE achieved in this study for a 1.7 mm^2 cell area (5.5%) and 7.1 mm^2 cell area (4.7%) is among the top values achieved in the last five years, and close to the record PCE of planar solar cells based on pristine Sb_2S_3 . The mismatch in J_{SC} calculated from J – V and EQE likely stems from the difference in light intensity during J – V and EQE measurements, coupled with a strong dependence of photoelectric conversion efficiency on light intensity in these solar cells, as will be discussed later on. The EQE shoulder at around 650 nm (Figure 3b), indicates the presence of a beneficial phenomenon called the optical spacer effect, which can occur in solar cells with a very thin absorber [21,62,63]. The optical spacer effect increases the EQE at above 650 nm, where P3HT does not absorb light. The magnitude of the gain in EQE due to this effect depends on the thickness of the HTM and that of the

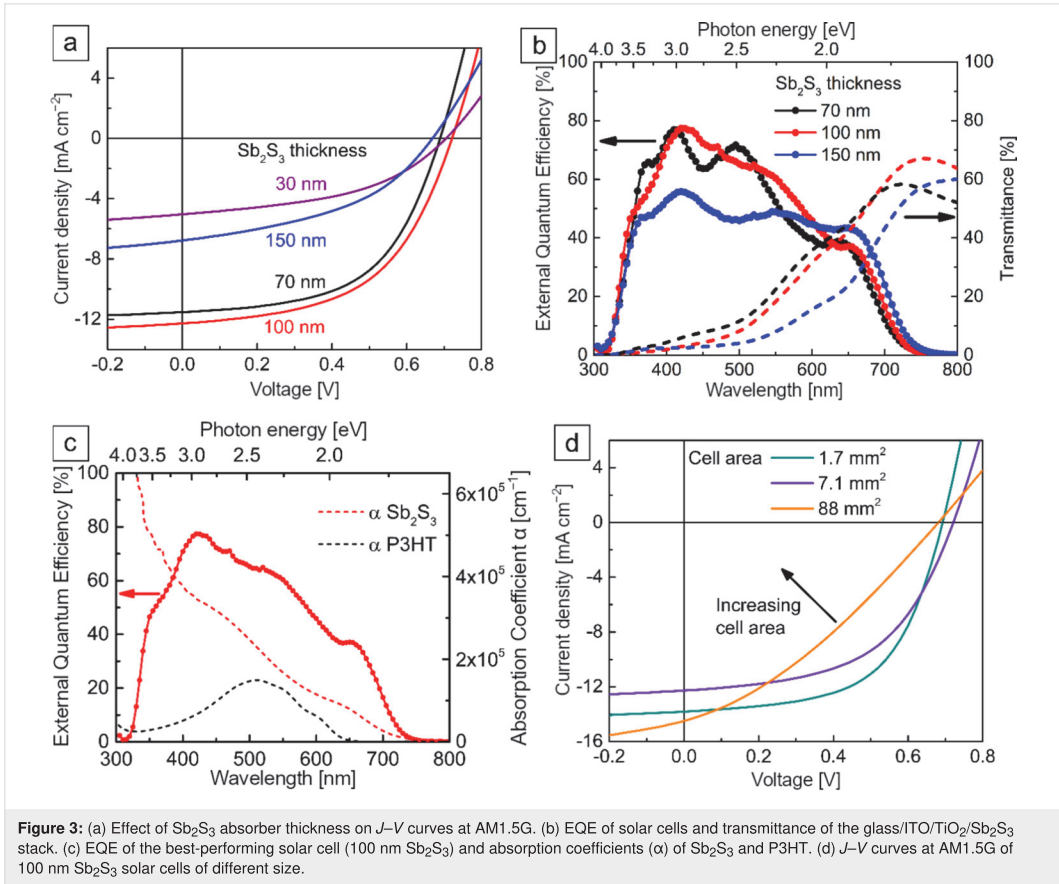


Table 1: Photoconversion parameters^a of solar cells as a function of Sb_2S_3 film thickness. The best results are given in parentheses.

Sb_2S_3 [nm]	V_{OC} [mV]	$J_{\text{SC},I-V}$ [mA cm^{-2}]	$J_{\text{SC,EQE}}$	FF [%]	PCE [%]	R_{S} [$\Omega \text{ cm}^2$]	R_{SH} [$\text{k}\Omega \text{ cm}^2$]	N^{b}
30	$704 \pm 7^{\text{c}}$ (705)	4.8 ± 0.3 (5.00)	– (6.78)	43 ± 3 (46)	1.5 ± 0.1 (1.6)	14 ± 2.1 (18)	0.5 ± 0.1 (0.6)	8
70	670 ± 8 (691)	7.5 ± 0.6 (11.5)	– (10.3)	57 ± 4 (55)	2.9 ± 0.2 (4.4)	7.4 ± 0.6 (6.0)	2.2 ± 1.0 (1.1)	9
100	693 ± 17 (726)	10.3 ± 1.0 (12.3)	– (10.9)	52 ± 3 (52)	3.7 ± 0.4 (4.7)	7.6 ± 1.5 (5.9)	0.9 ± 0.3 (0.7)	36
150	638 ± 16 (669)	4.3 ± 1.1 (6.88)	– (9.60)	44 ± 1 (43)	1.2 ± 0.3 (2.0)	26 ± 5.2 (19)	0.7 ± 0.2 (0.4)	8

^aMeasurement conditions: 100 mW cm^{-2} , AM1.5G, cell active area 7.1 mm^2 ; ^bNumber of measured cells; ^cStandard deviation.

absorber [21]. The optical spacer effect can have a strong influence on the EQE when the thickness of the absorber is around 100 nm or less [62]. Otherwise, most of the incident light is absorbed before reaching the optical spacer layer and the optical spacer effect is not seen. The optical spacer effect is illustrated in the EQE spectrum (Figure 3c) of one of the best-performing

devices (100 nm Sb_2S_3 , 7.1 mm^2) coupled with the absorption coefficient curves of Sb_2S_3 and P3HT. The transmittance of light to the absorber is limited at higher photon energies by the onset of absorption of TiO_2 at 3.0 eV and ITO at 3.6 eV. The P3HT layer, however, does not contribute to the generation of photocurrent [14,21]. On the contrary, any photogeneration

within the P3HT is known to have an adverse effect on J_{SC} and FF [14,21]. Lastly, the EQE of cells with 150 nm thick Sb_2S_3 indicates a decline of the collection of photogenerated carriers in the 350–600 nm wavelength range (Figure 3b). The decrease is more drastic at lower wavelengths, which are more rapidly dampened in Sb_2S_3 , as evident from the absorption coefficient (Figure 3c), and related photoexcitation in the Sb_2S_3 occurs closer to the side of incidence, i.e., the ETM/ Sb_2S_3 interface. Hence, we are led to conclude that the holes photogenerated near the ETM/ Sb_2S_3 interface, which must travel the farthest towards the HTM, face mobility issues when traversing the thickest (150 nm) absorber layer. On the other end, at wavelengths above 600 nm, the benefit of using layers thicker than 100 nm to absorb more light is clearly seen through increased EQE, as expected. For reference, the penetration depth for light of 600 nm wavelength is about 100 nm, assuming $\alpha = 1 \times 10^5 \text{ cm}^{-1}$ (Figure 3c). Electron mobility tends to be greater in semiconductors when compared to hole mobility, although the efficacy of electron transport is also subject to change when the absorber thickness is varied. In this particular case, however, the spacer effect also occurs in the EQE spectra at wavelengths above 600 nm, for which the light reaches deepest into Sb_2S_3 and closer to the back electrode. Hence, more sophisticated analyses might be appropriate for the complete depiction of the impact of Sb_2S_3 thickness on electron transport. The existence of the optical spacer effect can also have a negative impact. Even some tens of nanometers off of the optimum HTM thickness at constant absorber layer thickness could drastically decrease the J_{SC} ; thus it is crucial to ensure uniform thickness of P3HT throughout the whole area of the solar cell [62].

Influence of cell area on PV performance of semitransparent Sb_2S_3 solar cells

To investigate the effect of enlarging cell area on PV performance, we fabricated cells with active area ranging from 1.7 to 180 mm^2 and calculated the photoconversion parameters from I - V curves measured at 100 mW cm^{-2} with AM1.5G (Figure 3d). The cross-sectional SEM view of the best solar cell with 100 nm of Sb_2S_3 is presented in Figure 4 alongside the

corresponding device schematic. As the cell area was increased from 1.7 to 180 mm^2 , V_{OC} , J_{SC} , FF, and R_{SH} all decreased linearly at different rates, but at the same time, R_S increased substantially (Figure 5). As a result, the PCE decreased from

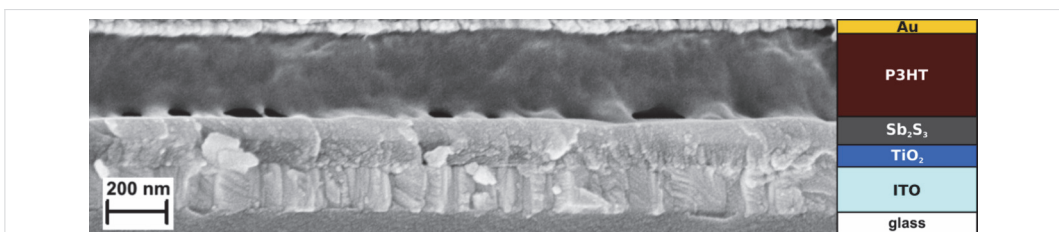
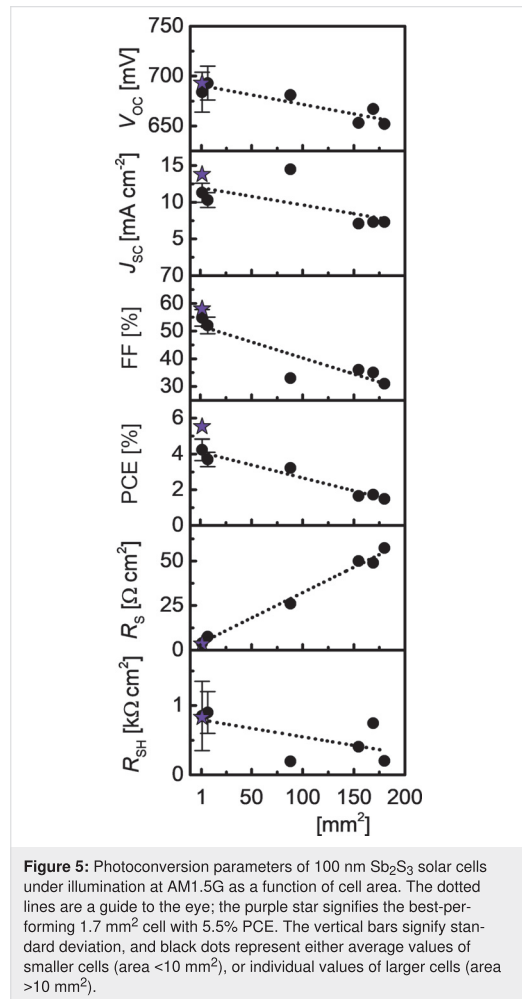


Figure 4: SEM cross-section of the best-performing 5.5% PCE solar cell (100 nm Sb_2S_3) and the corresponding device schematic.

4.2 ± 0.6% to 1.6%. The highest PCE of 5.5%, 4.7%, and 3.2% at AM1.5G (Table 2) was obtained in the three best-performing cells with 1.7 mm², 7.1 mm² and 88 mm² area, respectively. The statistical variance of photoconversion parameters (V_{OC} , J_{SC} , FF, PCE, R_S , R_{SH}) of 36 cells of 7.1 mm² active area with 100 nm Sb₂S₃ is presented in Figure S2 in Supporting Information File 1.

Despite commendable V_{OC} (682 mV) and J_{SC} (14.5 mA cm⁻²), the FF is substantially smaller (33%) in larger (≈100 mm²) cells when compared to <10 mm² cells (Table 2) due to about three times larger R_S (26 Ω mm²) and about three times smaller R_{SH} (190 Ω mm²) under both illuminated (Figure 3d) and dark conditions (Figure S3 in the Supporting Information File 1). Also, the photocurrent loss in larger cells originates from the increase in R_S alongside the decrease in R_{SH} (Table 2). In addition, the probability of a given cell to exhibit photocurrent loss, and a resulting decrease in FF, increases proportionally with area due to unforeseen thickness fluctuations and a resultant mismatch in the thicknesses of TiO₂, Sb₂S₃, and P3HT layers, assuming to be primarily due to a uniform distribution of defects. Upon scribing large cells (>100 mm²) into several smaller ≈0.1 mm² cells, all photoconversion parameters of the cells with USP-grown Sb₂S₃ ended up showing values like those of individual cells with similar sizes, as has previously been demonstrated for structured ETA-Sb₂S₃ cells [14]. In a study of SnO:F/CdS/Sb₂(S,Se)₃/C/Ag solar cells of 20–80 mm² area, a similar trend of lower PCE in larger cells was described (from 6.2% at 20 mm² to 5.7% at 60 mm²) [64]. We perceive the most concerning issues with up-scaling of planar solar cells with Sb₂S₃ grown by USP as the following: (1) enlarging the cell area causes FF loss, possibly because of minute, nontrivial discrepancies in layer thickness of Sb₂S₃, and particularly P3HT; (2) enlarging the cell area introduces loss in J_{SC} and loss in FF due to the large resistivity of the absorber layer. It appears that the PCE on the level of small cells (<10 mm²) can only be achieved in larger cells (>100 mm²) if the TiO₂, Sb₂S₃ and P3HT layers are uniform to the precision of a few nanometers

in thickness [14,21,34,62]. Therefore, device performance is not only highly dependent on the deposition technique for its ability to produce pure phase Sb₂S₃, but also on the capability of the specific deposition equipment to produce films with superior uniformity in thickness, i.e., nanometer precision, which USP can provide after some optimization.

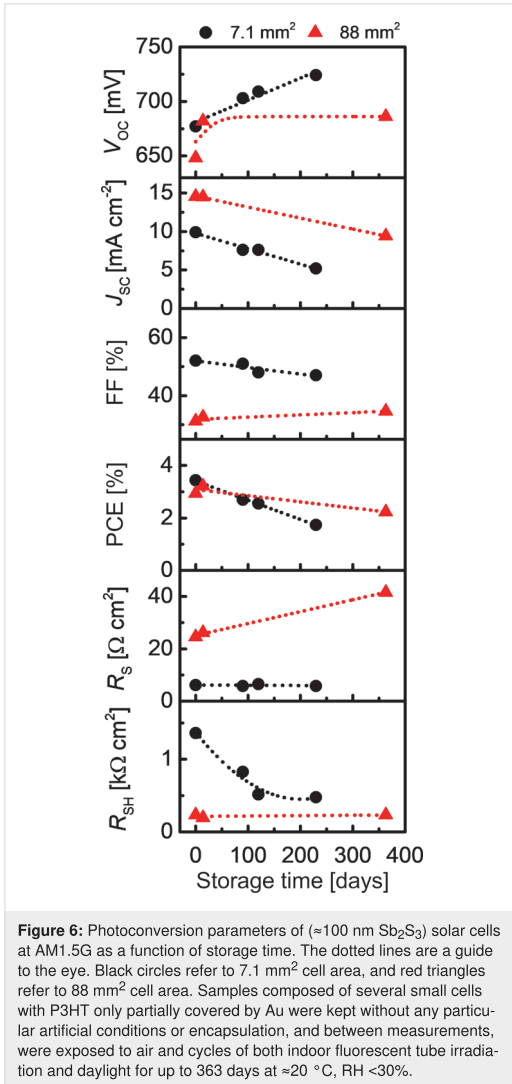
Influence of storage time on PV performance of semitransparent Sb₂S₃ solar cells

The stability of solar cells is paramount to ensure long-term performance under operation conditions, in turn maximizing return on investment. We investigated the stability of photoconversion parameters of cells of 7.1 mm² and 88 mm² area with USP-grown Sb₂S₃ by keeping the cells at rest in V_{OC} condition for 230 days at room temperature (RT), relative humidity (RH) <30%, and exposed to both indoor light and daylight incident through the laboratory windows (Figure 6). In the 7.1 mm² cell, over 230 days, V_{OC} increased slightly, whereas J_{SC} was halved, FF decreased slightly due to three times smaller R_{SH} , and, as a result PCE was halved in the tested 7.1 mm² cell (Figure 5, numeric data in Table S2 in the Supporting Information File 1), whereas R_S remained constant. In comparison, a trend of PCE decreasing from 3.7% to 1.5% after 300 days of aging was observed in ETA cells with a TiO₂/Sb₂S₃/CuSCN structure [24]. The V_{OC} of the 88 mm² cell increased from 648 mV to 682 mV after 14 days (Figure 5), and remained constant after 363 days of storage, unlike the linear increase of 20 mV per 100 days observed in the 7.1 mm² cell. The reason for this discrepancy is still under question and requires further study. A partially reversible increase of V_{OC} over time due to humidity in air is common for solar cells containing organic materials [9]. J_{SC} declines linearly at a similar rate in both cells, 2.0 mA cm⁻² per 100 days for the small cell, and 1.4 mA cm⁻² per 100 days for the 88 mm² cell, independent of the initial J_{SC} value. The linear decrease of J_{SC} during aging in light or dark conditions correlates with the general trend in organic PV [9], meaning the stability of Sb₂S₃ hybrid solar cell hinges on the stability of the chosen HTM. The FF increased slightly in the 88 mm² cell,

Table 2: Photoconversion parameters^a of solar cells as a function of active area. The best results are given in parentheses.

Area [mm ²]	V_{OC} [mV]	$J_{SC,I-V}$ [mA cm ⁻²]	FF [%]	PCE [%]	R_S [Ω cm ²]	R_{SH} [kΩ cm ²]	N ^b
1.7	684 ± 20 ^c (693)	11.3 ± 1.3 (13.8)	55 ± 3 (58)	4.3 ± 0.6 (5.53)	3.9 ± 1.2 (3.3)	0.8 ± 0.5 (0.8)	37
7.1	693 ± 17 (726)	10.3 ± 1.0 (12.3)	52 ± 3 (52)	3.7 ± 0.4 (4.67)	7.6 ± 1.5 (5.9)	0.9 ± 0.3 (0.7)	36
88	681	14.5	33	3.22	26	0.2	1
155	653	7.1	36	1.65	50	0.4	1
169	667	7.3	35	1.72	49	0.8	1
180	652	7.3	31	1.49	57	0.2	1

^aMeasurement conditions: 100 mW cm⁻², AM1.5G, Sb₂S₃ thickness 100 nm; ^bNumber of measured cells; ^cStandard deviation.

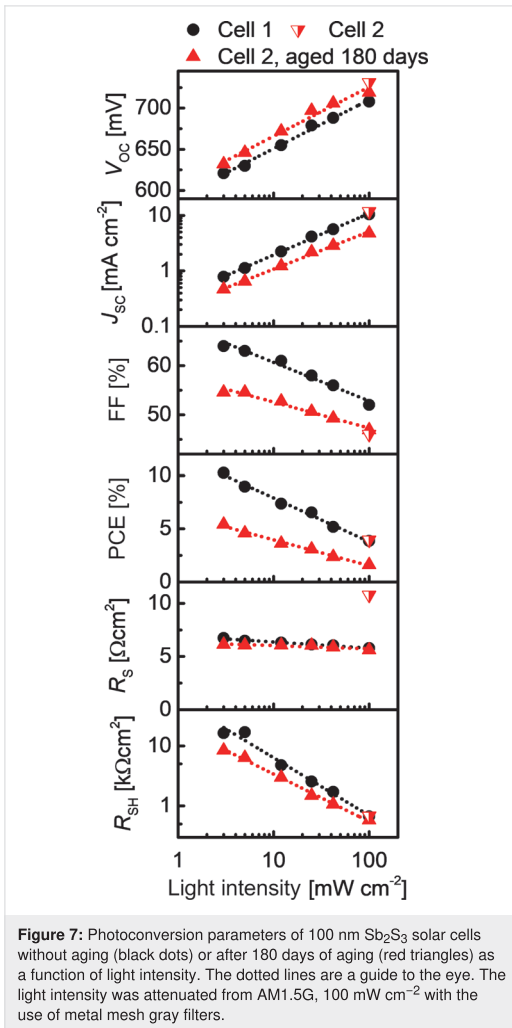


opposite to the slight decrease in the smaller cell. Consequently, the PCE of the larger cell decreases by $\approx 0.2\%$ per 100 days, that is at a slower rate compared to the decrease of 0.7% per 100 days for the small cell. According to Hintz et al., the in-flux of moisture and oxygen from air presumably leads to degradation of P3HT [65]. We suppose that this process occurs more slowly in the larger cell, which could explain why the larger cell retains more PCE over time compared to the smaller cell. Another discrepancy appears when examining the R_S and R_{SH} . The R_S of the large cell increases linearly by $4.5 \Omega \text{ cm}^2$ per 100 days, whereas R_S is constant for the small cell. The opposite occurs for R_{SH} , where the small cell rapidly loses R_{SH} over

the first 120 days, but the initial R_{SH} in the large cell is retained after one year. The decrease in PCE over time observed in both 7.1 mm 2 and 88 mm 2 area solar cells is probably due to moisture-assisted oxidation of P3HT [65]. Thus, to inhibit loss of PCE over time, encapsulation of the solar cell from moisture and oxygen is advised. Deng et al. studied the effect of storage time on the PCE of ITO/TiO $_2$ /as-deposited Sb_2S_3 /P3HT/Au, and ITO/TiO $_2$ / Sb_2S_3 (Se-annealed)/Au solar cells under continuous illumination by measuring J - V every 24 h [66]. The Se-annealed sample experienced a net gain in PCE in the first 24 h, which was retained over 400 hours of illumination [66]. The sample containing P3HT lost all PCE after 150 hours of illumination, mainly because of the loss of J_{SC} [66]. In the same study, it was shown that solar cells without the P3HT layer, with both as-deposited and Se-annealed Sb_2S_3 absorber, did not experience a quantifiable loss of PCE over six months of storage in air [66]. Assuming that the materials properties of the layers in these solar cells are similar to the corresponding layers in this study, we argue that the loss of PCE after storage in air is probably caused by the organic P3HT layer. In conclusion, we have demonstrated that increasing the active area of the cell helps to retain PCE of the solar cell based on USP-grown Sb_2S_3 absorber over extended periods of time, and this dependence on cell area certainly warrants more thorough investigation.

Influence of light intensity on PV performance of semitransparent Sb_2S_3 solar cells

The intensity of incident light in real working conditions of solar cells is not constant and is rarely at standard brightness, requiring solar cells to perform well at standard light intensity as well as at attenuated light intensities. In addition, close inspection of the dependence of photoconversion parameters on light intensity could provide valuable information about the cause of J_{SC} and FF losses in the solar cell [47]. We investigated the I - V output of cells with a USP-grown Sb_2S_3 absorber at a number of different illumination intensities between 3 and 100 mW cm^{-2} . A constant device temperature was maintained to avoid introduction of additional uncertainty to the measurements. The light intensity was attenuated by using metal mesh gray filters. By decreasing the incident light intensity from 100 to 3 mW cm^{-2} , V_{OC} and J_{SC} decreased, as expected, whereas R_{SH} , R_S and FF increased (Figure 7). Overall, the PCE increased from 3.9% at 100 mW cm^{-2} , AM1.5G, to over 10% at 3 mW cm^{-2} . The increase in PCE when lowering light intensity is hereby taken as characteristic of Sb_2S_3 -based solar cells [19,47]. Curiously, the tendency of change in PCE for Sb_2S_3 solar cells is opposite to that of monocrystalline Si solar cells at lower light intensity [67]. In comparison, after aging a solar cell under ambient light and RT for 180 days, in the same conditions as in the storage time test (Figure 5), the PV parameters follow similar trends depending on light intensity (Figure 6).



The elevated PCE in freshly prepared and aged cells with USP-grown Sb_2S_3 is related to an associative gain of FF and R_{SH} at decreased light intensity. The exact reasons for this dependence are yet to be clarified. An investigation on the low light intensity behavior of Cu- and Se-doped Sb_2S_3 -based hybrid solar cells showed that the PCE of these cells was also significantly higher at lower light intensity (2.12% at 25 mW cm^{-2} and 9.03% at 5 mW cm^{-2}), and it was concluded that the behavior was similar to amorphous Si solar cells [68]. In the case of amorphous Si solar cells, the decrease in FF at increasing light intensity was connected to the increasing electric field inside the solar cell [69]. Essentially, if the quality of the solar cell is improved, the PCE at higher light intensity will increase and approach the PCE at low light intensity [69]. While the explanations for

many phenomena in this structure are still under discussion, inorganic ETM/ Sb_2S_3 /organic HTM solar cells demonstrate excellent applicability for $1\text{--}10 \text{ mW cm}^{-2}$ light harvesting, a commonly observed range of light intensity when partial or full cloud cover is present. The durability of these solar cells is expected to be a manageable concern under attenuated light.

Conclusion

Semitransparent and oxide-free thin films of crystalline Sb_2S_3 were fabricated at low temperature using two steps, an initial non-vacuum growth by facile spray pyrolysis (USP) at $200 \text{ }^\circ\text{C}$, followed by a low-temperature annealing in a non-oxygen containing environment at $170 \text{ }^\circ\text{C}$. This process is compatible with existing window glass manufacturing technology. By integrating semitransparent thin films of Sb_2S_3 with optimized thickness of 100 nm in the planar ITO/ TiO_2 / Sb_2S_3 /P3HT/Au hybrid solar cell, a PCE of 5.5% and an AVT of 26% in ITO/ TiO_2 / Sb_2S_3 were achieved. The PCE and AVT combinations obtained in this study are similar to those reported for other semitransparent thin film solar cell configurations. The feasibility of fabricating large-area lab-scale Sb_2S_3 solar cells by the USP method is demonstrated by achieving a PCE of 3.2% at 88 mm^2 solar cell area, laying the foundation for further improvements in scalability. Furthermore, over the span of a year, the 88 mm^2 non-encapsulated solar cell stored under standard office conditions showed half the rate of aging and an increased stability towards humidity and air when compared to smaller cells ($<10 \text{ mm}^2$ area). We consider the trend of increased PCE at decreased light intensity observed in USP- Sb_2S_3 solar cells favorable for light conversion under cloud cover. It is clear that the key to further increase the efficiency, area-scalability, and durability of opaque and semitransparent Sb_2S_3 solar cells lies in tuning of the layers and interfaces of the ETM/ Sb_2S_3 /HTM stack. Considering the potential benefits of the capability of USP for large-scale production, extensive cost-savings could be achieved by depositing all component layers in the Sb_2S_3 -solar cell by ultrasonic spray pyrolysis, further accentuating facile integration in solar window glass production.

Experimental

Solar cell fabrication

All chemicals were sourced from Sigma-Aldrich and used as-purchased without further processing. ITO covered ($25 \text{ } \Omega \text{ sq}^{-1}$, ZSW) soda-lime glass substrates were cleaned with deionized water, ethanol, deionized water, H_2SO_4 (1% w/w), and rinsed with deionized water before drying at $105 \text{ }^\circ\text{C}$ in air. Then, a dense, compact TiO_2 layer was grown on glass/ITO by ultrasonic spray pyrolysis in air from 0.1 M titanium tetraisopropoxide (98% v/v) and 0.4 M acetylacetonone (99% v/v) dissolved in ethanol (96.6% v/v) according to a previously published procedure [28,46,70]. After deposition, the glass/

ITO/TiO₂ stack was annealed at 450 °C for 30 min in air to form anatase.

Amorphous layers of Sb₂S₃ were deposited by ultrasonic spray pyrolysis in air from a solution of SbCl₃ (99% w/w) and SC(NH₂)₂ (98% w/w), Sb/S molar ratio 1:3, dissolved in methanol (99.8% v/v), according to a previously published procedure [46]. The Sb₂S₃ thin film thickness was controlled by varying the concentration of SbCl₃ and SC(NH₂)₂ (1:3) in methanol. The Sb₂S₃ thin films were crystallized by annealing in vacuum ($\leq 4 \times 10^{-6}$ torr) at 170 °C for 5 min.

We observed that without annealing of Sb₂S₃, the solar cells of the same structure showed a V_{OC} of about 700 mV, but virtually no J_{SC} , producing PCE <0.1%. All solar cells henceforth were based on annealed Sb₂S₃ thin films.

P3HT, as the hole transport material (HTM), was applied by immersing samples into a room-temperature solution of regioregular P3HT (2% w/w) dissolved in chlorobenzene (99.5% v/v), then dried at 50 °C for 10 min in air, and further dried in vacuum ($\leq 4 \times 10^{-6}$ torr) for 5 min. The solar cells were completed by depositing the Au counter electrode by thermal evaporation in vacuum ($< 2 \times 10^{-4}$ torr). The cells with areas of 1.7 mm² and 7.1 mm² were prepared with the use of perforated metal masks. The area of cells larger than 7.1 mm² was defined by mechanically scribing contacts after Au deposition.

Thin film characterization

The characterization methods employed in this study, except for XRD and XES, have already been described in detail elsewhere [28]. The structure and phase composition were characterized by XRD (Rigaku Ultima IV, θ -2 θ , Cu K α_1 λ = 1.5406 Å, 40 kV, 40 mA, step 0.02°, 5° min⁻¹, Si strip detector D/teX Ultra) and Raman spectroscopy (Horiba Labram HR 800, backscattering mode, $\approx 143 \mu\text{W} \mu\text{m}^{-2}$). The elemental composition of glass/ITO/TiO₂/Sb₂S₃ samples and solar cell cross sections were recorded in the combined energy dispersive X-ray spectrometer (Bruker spectrometer, ESPRIT 1.8, 7 kV) and scanning electron microscope (Zeiss HR FESEM Ultra 55, 4 kV) system. The surface morphology of glass/ITO/TiO₂/Sb₂S₃ samples was recorded in a HR-SEM (Helios NanoLab 600, FEI Company). The optical properties were measured using a UV–vis–NIR spectrophotometer (Jasco V-670, integrating sphere, air reference). The AVT was calculated as the arithmetic average of total transmittance of the glass/ITO/TiO₂/Sb₂S₃ stack in the 380–740 nm wavelength range by using Equation 1 [71]:

$$\text{AVT}(\%) = \frac{\int_{380}^{740} T(\lambda) d(\lambda)}{740 - 380}, \quad (1)$$

where λ is the wavelength, and $T(\lambda)$ (%) is the total transmittance at λ . The resistivity of Sb₂S₃ layers on glass/TiO₂ substrate was measured at room temperature in dark by using the van der Pauw technique (MMR Technologies H50) and collinear four-wire I - V sensing (Eco Chemie BV, AutoLab PGSTAT302). The contact material for both measurements was deposited from an aqueous graphite ink from Alfa Aesar. S L_{2,3} soft X-ray emission spectra of Sb₂S₃ were measured using the SALSA endstation [72], at the open port of Beamline 8.0.1 of the Advanced Light Source (ALS), at Lawrence Berkeley National Laboratory (LBNL). The Sb₂S₃ films were excited with a photon energy of 180 eV, and the emitted X-rays at the S L_{2,3} edge were recorded as a function of energy. The reference chemicals for XES measurements were purchased from Alfa Aesar (Sb₂S₃ and Sb₂O₃ powders, both 99.999% w/w) and Sb₂(SO₄)₃ powder (99.91% w/w) from Chemsavers.

Solar cell characterization

The current–voltage (I - V) curves of the solar cells were measured by using a factory-calibrated solar simulator (Newport Oriel Sol3A class AAA) that provided AM1.5G, 100 mA cm⁻² light intensity, a metal mask with adjustable aperture area, and a source meter. The light intensity was regulated for the light intensity dependence measurements using gray filters (metal meshes with varied hole size). The external quantum efficiency (EQE) spectra were measured using a monochromatized light source (Newport 300 W Xenon lamp, 69911 with a monochromator Newport Cornerstone 260), a digital lock-in detector (Merlin) and a factory-calibrated Si reference detector. The integrated short-circuit current density (J_{SC}) from EQE was calculated in AM1.5G conditions with the online tool Open Photovoltaics Analysis Platform and compared with the J_{SC} obtained from the I - V measurements.

Supporting Information

Additional literature data of Sb₂S₃ solar cells, EDX data, statistical data of PV parameters of the optimized solar cell, dark J - V scans, and numeric data of the solar cell aging experiment.

Supporting Information File 1

Additional data.

[<https://www.beilstein-journals.org/bjnano/content/supplementary/2190-4286-10-230-S1.pdf>]

Acknowledgements

The authors thank Dr. Valdek Mikli from the Laboratory of Optoelectronic Materials Physics at Tallinn University of Technology (TUT) for recording the cross-section SEM image of the

solar cell and for EDX measurements, and Eng. Jekaterina Kozlova from the Institute of Physics at Tartu University for recording surface SEM images of glass/ITO/TiO₂/Sb₂S₃ samples. For valuable discussions, J. S. E. thanks Dr. Arvo Mere from the Department of Cybernetics and Dr. Nicolae Spalatu from the Laboratory of Thin Film Chemical Technologies (TUT).

Funding

This work was supported by the Estonian Research Council project IUT19-4 “Thin films and nanomaterials by wet-chemical methods for next-generation photovoltaics” and European Regional Development Fund project TK141 (TAR16016EK) “Advanced materials and high-technology devices for energy recuperation systems”. This research used resources of the Advanced Light Source, which is a DOE Office of Science User Facility under contract no. DE-AC02-05CH11231. The Baltic-American Freedom Foundation (BAFF) is acknowledged for a personal research grant of E. K. at the University of Nevada, Las Vegas.

ORCID® iDs

Jako S. Eensalu - <https://orcid.org/0000-0002-4312-0227>

Atanas Katerski - <https://orcid.org/0000-0003-1980-3391>

Wanli Yang - <https://orcid.org/0000-0003-0666-8063>

References

- Husain, A. A. F.; Hasan, W. Z. W.; Shafie, S.; Hamidon, M. N.; Pandey, S. S. *Renewable Sustainable Energy Rev.* **2018**, *94*, 779–791. doi:10.1016/j.rser.2018.06.031
- Dubey, S.; Sarvaiya, J. N.; Seshadri, B. *Energy Procedia* **2013**, *33*, 311–321. doi:10.1016/j.egypro.2013.05.072
- van Dyk, E. E.; Meyer, E. L.; Leitch, A. W. R.; Scott, B. J. S. *Afr. J. Sci.* **2000**, *96*, 198–200.
- Shin, D.; Choi, S.-H. *Coatings* **2018**, *8*, 329–358. doi:10.3390/coatings8100329
- Ito, S.; Chen, P.; Comte, P.; Nazeeruddin, M. K.; Liska, P.; Péchy, P.; Grätzel, M. *Prog. Photovoltaics* **2007**, *15*, 603–612. doi:10.1002/pip.768
- Chen, K.-S.; Salinas, J.-F.; Yip, H.-L.; Huo, L.; Hou, J.; Jen, A. K.-Y. *Energy Environ. Sci.* **2012**, *5*, 9551–9557. doi:10.1039/c2ee22623e
- Roldán-Carmona, C.; Malinkiewicz, O.; Betancur, R.; Longo, G.; Mombiona, C.; Jaramillo, F.; Camacho, L.; Bolink, H. J. *Energy Environ. Sci.* **2014**, *7*, 2968–2973. doi:10.1039/c4ee01389a
- Wang, D.; Wright, M.; Elumalai, N. K.; Uddin, A. *Sol. Energy Mater. Sol. Cells* **2016**, *147*, 255–275. doi:10.1016/j.solmat.2015.12.025
- Jørgensen, M.; Norrman, K.; Gevorgyan, S. A.; Tromholt, T.; Andreasen, B.; Krebs, F. C. *Adv. Mater. (Weinheim, Ger.)* **2012**, *24*, 580–612. doi:10.1002/adma.201104187
- Bristow, N.; Kettle, J. *Sol. Energy Mater. Sol. Cells* **2018**, *175*, 52–59. doi:10.1016/j.solmat.2017.10.008
- Correa-Baena, J.-P.; Saliba, M.; Buonassisi, T.; Grätzel, M.; Abate, A.; Tress, W.; Hagfeldt, A. *Science* **2017**, *358*, 739–744. doi:10.1126/science.aam6323
- Greenwood, N. N.; Earnshaw, A. *Chemistry of the Elements*, 2nd ed.; Applied Organometallic Chemistry, Vol. 12; Butterworth-Heinemann: Oxford, United Kingdom, 1997.
- Versavel, M. Y.; Haber, J. A. *Thin Solid Films* **2007**, *515*, 7171–7176. doi:10.1016/j.tsf.2007.03.043
- Kondrotas, R.; Chen, C.; Tang, J. *Joule* **2018**, *2*, 857–878. doi:10.1016/j.joule.2018.04.003
- Rajpure, K. Y.; Bhosale, C. H. *Mater. Chem. Phys.* **2000**, *63*, 263–269. doi:10.1016/s0254-0584(99)00233-3
- Escorcia-García, J.; Becerra, D.; Nair, M. T. S.; Nair, P. K. *Thin Solid Films* **2014**, *569*, 28–34. doi:10.1016/j.tsf.2014.08.024
- Parize, R.; Katerski, A.; Gromyko, I.; Rapenne, L.; Roussel, H.; Kärber, E.; Appert, E.; Krunk, M.; Consonni, V. J. *Phys. Chem. C* **2017**, *121*, 9672–9680. doi:10.1021/acs.jpcc.7b00178
- Kim, D.-H.; Lee, S.-J.; Park, M. S.; Kang, J.-K.; Heo, J. H.; Im, S. H.; Sung, S.-J. *Nanoscale* **2014**, *6*, 14549–14554. doi:10.1039/c4nr04148h
- Itzhak, Y.; Niitsoo, O.; Page, M.; Hodes, G. J. *Phys. Chem. C* **2009**, *113*, 4254–4256. doi:10.1021/jp900302b
- Choi, Y. C.; Lee, D. U.; Noh, J. H.; Kim, E. K.; Seok, S. I. *Adv. Funct. Mater.* **2014**, *24*, 3587–3592. doi:10.1002/adfm.201304238
- Zimmermann, E.; Pfadler, T.; Kalb, J.; Dorman, J. A.; Sommer, D.; Hahn, G.; Weickert, J.; Schmidt-Mende, L. *Adv. Sci.* **2015**, *2*, 1500059. doi:10.1002/advs.201500059
- Kim, J. K.; Veerappan, G.; Heo, N.; Wang, D. H.; Park, J. H. *J. Phys. Chem. C* **2014**, *118*, 22672–22677. doi:10.1021/jp507652r
- Rodríguez-Lazcano, Y.; Nair, M. T. S.; Nair, P. K. J. *Electrochem. Soc.* **2005**, *152*, G635–G638. doi:10.1149/1.1945387
- Nezu, S.; Larramona, G.; Choné, C.; Jacob, A.; Delatouche, B.; Péré, D.; Moisan, C. J. *Phys. Chem. C* **2010**, *114*, 6854–6859. doi:10.1021/jp100401e
- Reeja-Jayan, B.; Manthiram, A. *RSC Adv.* **2013**, *3*, 5412–5421. doi:10.1039/c3ra23055d
- Christians, J. A.; Kamat, P. V. *ACS Nano* **2013**, *7*, 7967–7974. doi:10.1021/nm403058f
- You, M. S.; Lim, C.-S.; Kwon, D. H.; Heo, J. H.; Im, S. H.; Chae, K. J. *Org. Electron.* **2015**, *21*, 155–159. doi:10.1016/j.orgel.2015.02.015
- Kärber, E.; Katerski, A.; Oja Acik, I.; Mere, A.; Mikli, V.; Krunk, M. *Beilstein J. Nanotechnol.* **2016**, *7*, 1662–1673. doi:10.3762/bjnano.7.158
- Lan, C.; Liang, G.; Lan, H.; Peng, H.; Su, Z.; Zhang, D.; Sun, H.; Luo, J.; Fan, P. *Phys. Status Solidi RRL* **2018**, *12*, 1800025. doi:10.1002/pssr.201800025
- Ye, Q.; Xu, Y.; Chen, W.; Yang, S.; Zhu, J.; Weng, J. *Appl. Surf. Sci.* **2018**, *440*, 294–299. doi:10.1016/j.apsusc.2018.01.090
- Kaienburg, P.; Klingebiel, B.; Kirchartz, T. *Beilstein J. Nanotechnol.* **2018**, *9*, 2114–2124. doi:10.3762/bjnano.9.200
- Wang, X.; Li, J.; Liu, W.; Yang, S.; Zhu, C.; Chen, T. *Nanoscale* **2017**, *9*, 3386–3390. doi:10.1039/c7nr00154a
- Lei, H.; Yang, G.; Guo, Y.; Xiong, L.; Qin, P.; Dai, X.; Zheng, X.; Ke, W.; Tao, H.; Chen, Z.; Li, B.; Fang, G. *Phys. Chem. Chem. Phys.* **2016**, *18*, 16436–16443. doi:10.1039/c6cp02072k
- Liu, C. P.; Wang, H. E.; Ng, T. W.; Chen, Z. H.; Zhang, W. F.; Yan, C.; Tang, Y. B.; Bello, I.; Martinu, L.; Zhang, W. J.; Jha, S. K. *Phys. Status Solidi B* **2012**, *249*, 627–633. doi:10.1002/pssb.201147393
- Wang, W.; Strössner, F.; Zimmermann, E.; Schmidt-Mende, L. *Sol. Energy Mater. Sol. Cells* **2017**, *172*, 335–340. doi:10.1016/j.solmat.2017.07.046

36. Jin, X.; Yuan, Y.; Jiang, C.; Ju, H.; Jiang, G.; Liu, W.; Zhu, C.; Chen, T. *Sol. Energy Mater. Sol. Cells* **2018**, *185*, 542–548. doi:10.1016/j.solmat.2018.06.017
37. Zhang, L.; Jiang, C.; Wu, C.; Ju, H.; Jiang, G.; Liu, W.; Zhu, C.; Chen, T. *ACS Appl. Mater. Interfaces* **2018**, *10*, 27098–27105. doi:10.1021/acsami.8b09843
38. Darga, A.; Mencaraglia, D.; Longeaud, C.; Savenije, T. J.; O'Regan, B.; Bourdais, S.; Muto, T.; Delatouche, B.; Dennler, G. *J. Phys. Chem. C* **2013**, *117*, 20525–20530. doi:10.1021/jp4072394
39. Tang, R.; Wang, X.; Jiang, C.; Li, S.; Liu, W.; Ju, H.; Yang, S.; Zhu, C.; Chen, T. *ACS Appl. Mater. Interfaces* **2018**, *10*, 30314–30321. doi:10.1021/acsami.8b08965
40. Zhang, L.; Wu, C.; Liu, W.; Yang, S.; Wang, M.; Chen, T.; Zhu, C. *J. Mater. Chem. A* **2018**, *6*, 21320–21326. doi:10.1039/c8ta08296k
41. Jiang, C.; Tang, R.; Wang, X.; Ju, H.; Chen, G.; Chen, T. *Sol. RRL* **2019**, *3*, 1800272. doi:10.1002/solr.201800272
42. Carlé, J. E.; Helgesen, M.; Hagemann, O.; Hösel, M.; Heckler, I. M.; Bundgaard, E.; Gevorgyan, S. A.; Søndergaard, R. R.; Jørgensen, M.; García-Valverde, R.; Chaouki-Almagro, S.; Villarejo, J. A.; Krebs, F. C. *Joule* **2017**, *1*, 274–289. doi:10.1016/j.joule.2017.08.002
43. Patil, P. S. *Mater. Chem. Phys.* **1999**, *59*, 185–198. doi:10.1016/s0254-0584(99)00049-8
44. López Ibáñez, R.; Martín, F.; Ramos-Barrado, J. R.; Leinen, D. *Surf. Coat. Technol.* **2008**, *202*, 2408–2412. doi:10.1016/j.surfcoat.2007.09.016
45. Cheng, J.; Hu, R.; Wang, K.; Meng, X.; Li, Y.; Yang, X.; Liao, X.; Li, L.; Chong, K. B. *Sol. RRL* **2019**, *3*, 1800346. doi:10.1002/solr.201800346
46. Eensalu, J. S.; Katerski, A.; Kärber, E.; Oja Acik, I.; Mere, A.; Krunks, M. *Beilstein J. Nanotechnol.* **2019**, *10*, 198–210. doi:10.3762/bjnano.10.18
47. Moon, S.-J.; Itzhaik, Y.; Yum, J.-H.; Zakeeruddin, S. M.; Hodes, G.; Grätzel, M. J. *Phys. Chem. Lett.* **2010**, *1*, 1524–1527. doi:10.1021/jz100308q
48. Medina-Montes, M. I.; Montiel-González, Z.; Paraguay-Delgado, F.; Mathews, N. R.; Mathew, X. J. *Mater. Sci.: Mater. Electron.* **2016**, *27*, 9710–9719. doi:10.1007/s10854-016-5033-0
49. Parize, R.; Cossuet, T.; Chaix-Pluchery, O.; Roussel, H.; Appert, E.; Consonni, V. *Mater. Des.* **2017**, *121*, 1–10. doi:10.1016/j.matdes.2017.02.034
50. Heske, C.; Groh, U.; Fuchs, O.; Umbach, E.; Franco, N.; Bostedt, C.; Terminello, L. J.; Perera, R. C. C.; Hallmeier, K. H.; Preobrajenski, A.; Szargan, R.; Zweigart, S.; Riedl, W.; Karg, F. *Phys. Status Solidi A* **2001**, *187*, 13–24. doi:10.1002/1521-396x(200109)187:1<13::aid-sssa13>3.0.co;2-d
51. Weinhardt, L.; Gleim, T.; Fuchs, O.; Heske, C.; Umbach, E.; Bär, M.; Muffler, H.-J.; Fischer, C.-H.; Lux-Steiner, M. C.; Zubavichus, Y.; Niesen, T. P.; Karg, F. *Appl. Phys. Lett.* **2003**, *82*, 571–573. doi:10.1063/1.1539553
52. Weinhardt, L.; Fuchs, O.; Peter, A.; Umbach, E.; Heske, C.; Reichardt, J.; Bär, M.; Lauermaier, I.; Kötschau, I.; Grimm, A.; Sokoll, S.; Lux-Steiner, M. C.; Niesen, T. P.; Visbeck, S.; Karg, F. *J. Chem. Phys.* **2006**, *124*, 074705. doi:10.1063/1.2168443
53. Duncan, D. A.; Kephart, J. M.; Horsley, K.; Blum, M.; Mezher, M.; Weinhardt, L.; Häming, M.; Wilks, R. G.; Hofmann, T.; Yang, W.; Bär, M.; Sampath, W. S.; Heske, C. *ACS Appl. Mater. Interfaces* **2015**, *7*, 16382–16386. doi:10.1021/acsami.5b03503
54. Center for X-ray Optics (CXRO), Lawrence Berkeley National Laboratory. X-Ray Attenuation Length. http://henke.lbl.gov/optical_constants/atten2.html (accessed Jan 15, 2019).
55. Bär, M.; Schubert, B.-A.; Marsen, B.; Wilks, R. G.; Blum, M.; Krause, S.; Pookpanratana, S.; Zhang, Y.; Unold, T.; Yang, W.; Weinhardt, L.; Heske, C.; Schock, H.-W. *J. Mater. Res.* **2012**, *27*, 1097–1104. doi:10.1557/jmr.2012.59
56. Koc, H.; Mamedov, A. M.; Deligoz, E.; Ozisik, H. *Solid State Sci.* **2012**, *14*, 1211–1220. doi:10.1016/j.solidstatesciences.2012.06.003
57. Lokhande, C. D.; Sankapal, B. R.; Mane, R. S.; Pathan, H. M.; Muller, M.; Giersig, M.; Ganesan, V. *Appl. Surf. Sci.* **2002**, *193*, 1–10. doi:10.1016/s0169-4332(01)00819-4
58. Krishnan, B.; Arato, A.; Cardenas, E.; Roy, T. K. D.; Castillo, G. A. *Appl. Surf. Sci.* **2008**, *254*, 3200–3206. doi:10.1016/j.apsusc.2007.10.098
59. Wedemeyer, H.; Michels, J.; Chmielowski, R.; Bourdais, S.; Muto, T.; Sugiura, M.; Dennler, G.; Bachmann, J. *Energy Environ. Sci.* **2013**, *6*, 67–71. doi:10.1039/c2ee23205g
60. Jo, H.-J.; Kim, S. H.; Kim, J. S.; Lee, S.-J.; Kim, D.-H. *J. Korean Phys. Soc.* **2016**, *69*, 541–546. doi:10.3938/jkps.69.541
61. Servaites, J. D.; Yeganeh, S.; Marks, T. J.; Ratner, M. A. *Adv. Funct. Mater.* **2010**, *20*, 97–104. doi:10.1002/adfm.200901107
62. Andersen, P. D.; Skårhøj, J. C.; Andreasen, J. W.; Krebs, F. C. *Opt. Mater.* **2009**, *31*, 1007–1012. doi:10.1016/j.optmat.2008.11.014
63. Georgitzikis, E.; Malinowski, P. E.; Maes, J.; Hadjipour, A.; Hens, Z.; Heremans, P.; Cheyns, D. *Adv. Funct. Mater.* **2018**, *28*, 1804502. doi:10.1002/adfm.201804502
64. De Bray Sánchez, F.; Nair, M. T. S.; Nair, P. K. *Appl. Surf. Sci.* **2018**, *454*, 305–312. doi:10.1016/j.apsusc.2018.05.076
65. Hintz, H.; Egelhaaf, H.-J.; Lüer, L.; Hauch, J.; Peisert, H.; Chasse, T. *Chem. Mater.* **2011**, *23*, 145–154. doi:10.1021/cm102373k
66. Deng, H.; Yuan, S.; Yang, X.; Cai, F.; Hu, C.; Qiao, K.; Zhang, J.; Tang, J.; Song, H.; He, Z. *Mater. Today Energy* **2017**, *3*, 15–23. doi:10.1016/j.mtener.2017.02.001
67. Gong, C.; Posthuma, N.; Dross, F.; Kerschaver, E. V.; Giovanni, F.; Beaucarne, G.; Poortmans, J.; Hoofman, R. J. O. M. Comparison of n- and p-type high efficiency silicon solar cell performance under low illumination conditions. In *2008 33rd IEEE Photovoltaic Specialists Conference*, 2008; pp 1–4. doi:10.1109/pvsc.2008.4922441
68. Janošević, V.; Mitrić, M.; Bundaleski, N.; Rakočević, Z.; Validžić, I. L. *Prog. Photovoltaics* **2016**, *24*, 704–715. doi:10.1002/pip.2724
69. Nath, M.; Chakraborty, S.; Kim, K. H.; Johnson, E. V.; Roca i Cabarrocas, P.; Chatterjee, P. *Phys. Status Solidi C* **2010**, *7*, 1105–1108. doi:10.1002/pssc.200982726
70. Dundar, I.; Krichevskaya, M.; Katerski, A.; Acik, I. O. R. *Soc. Open Sci.* **2019**, *6*, 181578. doi:10.1098/rsos.181578
71. Kim, G. M.; Tsuma, T. *Sci. Rep.* **2017**, *7*, 10699. doi:10.1038/s41598-017-11193-1
72. Blum, M.; Weinhardt, L.; Fuchs, O.; Bär, M.; Zhang, Y.; Weigand, M.; Krause, S.; Pookpanratana, S.; Hofmann, T.; Yang, W.; Denlinger, J. D.; Umbach, E.; Heske, C. *Rev. Sci. Instrum.* **2009**, *80*, 123102. doi:10.1063/1.3257926

License and Terms

This is an Open Access article under the terms of the Creative Commons Attribution License (<http://creativecommons.org/licenses/by/4.0>). Please note that the reuse, redistribution and reproduction in particular requires that the authors and source are credited.

The license is subject to the *Beilstein Journal of Nanotechnology* terms and conditions: (<https://www.beilstein-journals.org/bjnano>)

The definitive version of this article is the electronic one which can be found at:
[doi:10.3762/bjnano.10.230](https://doi.org/10.3762/bjnano.10.230)

Publication III

J. S. Eensalu, K. Tõnsuaadu, J. Adamson, I. Oja Acik, M. Krunk. "Thermal decomposition of *tris*(O-ethylthiocarbonato)-antimony(III)—a single-source precursor for antimony sulfide thin films," *Journal of Thermal Analysis and Calorimetry*, Jun. 2021, doi: 10.1007/s10973-021-10885-1.



Thermal decomposition of tris(O-ethylthiocarbonato)-antimony(III)—a single-source precursor for antimony sulfide thin films

Jako S. Eensalu¹ · Kaia Tõnsuaadu² · Jasper Adamson³ · Ilona Oja Acik¹ · Malle Krunks¹

Received: 31 July 2020 / Accepted: 2 May 2021
© The Author(s) 2021

Abstract

Thermal decomposition of tris(O-ethylthiocarbonato)-antimony(III) (**1**), a precursor for Sb₂S₃ thin films synthesized from an acidified aqueous solution of SbCl₃ and KS₂COCH₂CH₃, was monitored by simultaneous thermogravimetry, differential thermal analysis and evolved gas analysis via mass spectroscopy (TG/DTA-EGA-MS) measurements in dynamic Ar, and synthetic air atmospheres. **1** was identified by Fourier transform infrared spectroscopy (FTIR) and nuclear magnetic resonance (NMR) measurements, and quantified by NMR and elemental analysis. Solid intermediates and final decomposition products of **1** prepared in both atmospheres were determined by X-ray diffraction (XRD), Raman spectroscopy, and FTIR. **1** is a complex compound, where Sb is coordinated by three ethylthiocarbonate ligands via the S atoms. The thermal degradation of **1** in Ar consists of three mass loss steps, and four mass loss steps in synthetic air. The total mass losses are 100% at 800 °C in Ar, and 66.8% at 600 °C in synthetic air, where the final product is Sb₂O₄. **1** melts at 85 °C, and decomposes at 90–170 °C into mainly Sb₂S₃, as confirmed by Raman, and an impurity phase consisting mostly of CSO₂²⁻ ligands. The solid-phase mineralizes fully at ≈240 °C, which permits Sb₂S₃ to crystallize at around 250 °C in both atmospheres. The gaseous species evolved include CS₂, C₂H₅OH, CO, CO₂, COS, H₂O, SO₂, and minor quantities of C₂H₅SH, (C₂H₅)₂S, (C₂H₅)₂O, and (S₂COCH₂CH₃)₂. The thermal decomposition mechanism of **1** is described with chemical reactions based on EGA-MS and solid intermediate decomposition product analysis.

Keywords Antimony ethyl xanthate · Thermal degradation · Evolved gas analysis · Antimony sulfide · Decomposition mechanism

Introduction

Antimony sulfide (Sb₂S₃) is a material naturally suitable for application as the absorber layer in thin film solar cells. The crustal abundance and price of Sb (0.2 ppm; \$8.6 kg⁻¹), and S (340 ppm; \$0.05 kg⁻¹), which form the nontoxic Sb₂S₃, attest to its long-term economic viability as a strategic resource [1–3]. The anisotropic Sb₂S₃ has a bandgap of ≈1.7 eV, a high absorption coefficient of 1·10⁵ cm⁻¹ at 450 nm, a melting point of 550 °C, and is stable toward moisture, UV, and oxidation in air below 150 °C, being etched only by concentrated acid [4–7]. A bandgap of 1.7 eV makes Sb₂S₃ a prime candidate for application as the top cell absorber in tandem solar cells [8, 9], and as the thinner than 200 nm absorber in IR inactive semitransparent solar cells [10, 11].

Sb₂S₃ thin films have been fabricated from colloidal or metal–organic precursors by a number of solution-based

✉ Jako S. Eensalu
jako.eensalu@taltech.ee

✉ Malle Krunks
malle.krunks@taltech.ee

¹ Laboratory of Thin Film Chemical Technologies, Department of Materials and Environmental Technology, Tallinn University of Technology, Ehitajate tee 5, 19086 Tallinn, Estonia

² Laboratory of Inorganic Materials, Department of Materials and Environmental Technology, Tallinn University of Technology, Ehitajate tee 5, 19086 Tallinn, Estonia

³ Laboratory of Chemical Physics, National Institute of Chemical Physics and Biophysics, Akadeemia tee 23, 12618 Tallinn, Estonia

chemical methods, e.g., chemical bath (CBD) [12–14], atomic layer deposition (ALD) [15–17], spin-coating [18, 19], spray pyrolysis [11, 20–22], and by physical methods, e.g., thermal evaporation (TE) from inorganic targets [23], mainly for application as absorber in thin film solar cells. The highest power conversion efficiency achieved for planar Sb_2S_3 thin film solar cell is 6.6% by spin-coating a metal–organic complex of Sb, followed by annealing and Cs-doping [19], whereas the top power conversion efficiency of Sb_2S_3 solar cells is 7.5% [24]. Mass production of Sb_2S_3 solar cells with consistent power conversion efficiency requires use of simple and cost-effective methods, e.g., spray pyrolysis, as other methods are likely too expensive (vacuum, inert gas, specialty reagents for ALD, TE), too time consuming and waste-generating (CBD), or too small-scale (spin-coating) [25].

In order to fabricate Sb_2S_3 thin films from organometallic precursors, it is crucial to understand their decomposition mechanisms in oxidizing and inert atmosphere. Our laboratory has experience in analysis of formation of CuS , In_2S_3 , CuInS_2 , ZnS , and SnS thin films by employing TG/DTA-EGA for thiourea-based precursors to estimate the appropriate deposition conditions for spray pyrolysis in air [26–31]. The resulting thin films contained C and Cl impurities, except in case of Sb_2S_3 , where uniform thin films of Sb_2S_3 , free of C and Cl to detectable limits, were deposited at 210 °C by spray pyrolysis, wherein a liquid-phase reaction occurred due to a favorably low melting point of the precursors [22]. As lowering the deposition and annealing temperature of Sb_2S_3 thin films is critical for application as the ≈ 1.7 eV top absorber in tandem solar cells, the processing temperature must be decreased further. Moreover, lower processing temperature and shorter processing time would decrease the energy budget, ergo, the cost of producing Sb_2S_3 thin film-based solar cells and other devices, and increase the selection of usable substrates.

Metal xanthates, *i.e.*, alkoxy- or aryldithiocarbonates, tend to decompose at low temperatures (100–250 °C) [32, 33], which is suitable to deposit metal chalcogenide thin films onto polymer substrates for flexible applications, and to fabricate the top cell for tandem solar cells. However, the decomposition mechanism and temperature of each xanthate depend significantly on the combination of cation [34], and ligand [33], meaning that TG/DTA-EGA could be of use. Xanthates, e.g., potassium ethyl xanthate ($\text{KS}_2\text{COCH}_2\text{CH}_3$, KEX) were discovered by W. C. Zeise in 1822 [4]. Since then, xanthates and related organometallic compounds are being used in ore flotation, in organic chemistry, in analytical chemistry, in biochemistry, in coordination chemistry, and in materials science to fabricate metal chalcogenide powders and layers, e.g., ZnS , NiS , Fe_2S_3 , Cu_2S , PbS , As_2S_3 , Sb_2S_3 , Bi_2S_3 , and lead-free perovskites [4, 32, 34–44]. Antimony ethyl xanthate (SbEX) has risen to prominence in the last

decade as a single-source precursor to fabricate Sb_2S_3 powders for various applications, or to make porous layers for use as the absorber in solar cells by solution-based chemical methods, e.g., solvothermal, or spin-coating coupled with post-deposition annealing at 160–240 °C [33, 39, 45].

A comprehensive thermal decomposition study of SbEX, where TG/DTA is coupled with evolved gas analysis and intermediate solid decomposition product analysis, has not been published. Sporadic studies of TG curves of SbEX have been published with contradictory and vague statements regarding the temperature required to produce phase pure Sb_2S_3 [32, 33, 39, 45]. Therefore, a comparative study of the TG/DTA-EGA-MS of SbEX in inert and oxidizing atmosphere is required to determine its suitability for depositing phase pure Sb_2S_3 thin films for application in semitransparent, bifacial, and as the top cell absorber in tandem solar cells, in addition to other semiconductor applications.

Aiming to determine the viability of SbEX as a single-source precursor for depositing Sb_2S_3 thin films by ultrasonic spray pyrolysis, we investigate the thermal decomposition of SbEX in inert and synthetic air atmosphere in this study by TG/DTA-EGA-MS coupled with analysis of the solid intermediate decomposition products of SbEX, and describe the mechanism of thermal decomposition of SbEX.

Experimental

Synthesis

Potassium ethyldithiocarbonate (potassium ethyl xanthate, KEX) (> 97 mass%, Acros) and antimony(III)chloride (SbCl_3) (99 mass%, Sigma-Aldrich), deionized water (18.2 $\text{M}\Omega\text{cm}^{-1}$), and HCl (≥ 37 vol%, Sigma-Aldrich) were employed for the synthesis of the precursor for thermal analysis. All chemicals were used as-bought without further purification. The precursor for thermal analysis was synthesized according to the literature [40], with some modifications.

The precursor was synthesized at room temperature by pouring 375 mM of KEX to 200 mL of 125 mM SbCl_3 , acidified beforehand with HCl to retain SbCl_3 , while stirring. A bright yellow substance started precipitating immediately upon mixing. The solution was stirred for 60 min. The precipitate was rinsed with deionized water, diethyl ether (99.5 vol%, Sigma-Aldrich), and acetone (99.8 vol%, Merck), then recrystallized from acetone and rinsed with water at 83% yield. This product, named **1** going forward, was used for further analysis.

Elemental analysis

The elemental composition of **1** was analyzed by energy-dispersive X-ray spectroscopy (EDX) on a Zeiss Ultra 55 FEG HR-SEM setup equipped with a Bruker ESPRIT 1.8 system. The atomic ratio of S/Sb was found to be 5.7 ± 0.1 , which is 93–97% of the expected stoichiometric atomic ratio of S to Sb of 6.0 in SbEX.

Nuclear magnetic resonance analysis

The nuclear magnetic resonance (NMR) analysis was carried out on a 800 MHz Bruker Avance III setup connected with a 18.8 T magnet/ 54 mm heat opening diameter at 25 °C. Samples of **1** were weighed, and dissolved in CDCl₃ (99.8 vol%, Eurisotop) for 1D qualitative ¹H, 1D quantitative ¹³C, 2D homonuclear correlation spectroscopy (COSY), heteronuclear single-quantum correlation spectroscopy (HSQC), and heteronuclear multiple-bond correlation spectroscopy (HMBC) NMR. For 1D quantitative ¹H analysis, **1** and 2-Propanol (99.9 vol%, Sigma-Aldrich) were weighed in a fixed molar ratio on a microbalance after antistatic screening, and co-dissolved in CD₃OD (MeOD, 99.8 vol%, Eurisotop). Chemical shifts in ppm were calibrated relative to CDCl₃ and MeOD. The residual mass of **1** in the weighing tray was subtracted before quantification. NMR data were analyzed, and figures were generated using Mestrelab MNova software.

Vibrational analysis

The FTIR spectra of KEX and **1** were measured on a FTIR setup (Perkin Elmer GX 2000), 400–4000 cm⁻¹, 4 cm⁻¹ resolution, 32 scans, by the KBr pellet method, using the FTIR spectrum of the KBr pellet as background. 1.0 mass% of sample per 200 mg of KBr, pre-dried in air at 150 °C for 1 h, was pressed into a 13 mm-diameter pellet after grinding the mixture with a corundum pestle and mortar.

The FTIR spectra of **1**, and its intermediate decomposition products prepared at 115 °C, and at 160 °C in flowing N₂, and air were measured on a Bruker Alpha FTIR setup, equipped with a diamond anvil in absorbance mode, 24 scans, resolution 4 cm⁻¹.

In addition, Raman spectra of **1** and its intermediate solid decomposition products were measured on a micro-Raman setup (Horiba LabRam 800, 15 μW μm⁻², 532 nm He–Ne, Ø 5 μm), calibrated with 546.1 nm Hg line. Raman data were analyzed with Fityk software [46]. FTIR and Raman figures were generated with OriginLab software.

Thermal analysis

The simultaneous TG/DTA/EGA-MS measurement of **1** was performed in a Setaram LabSys EVO apparatus, using a heating rate of 10 °C min⁻¹, purge gas (Ar or 80% Ar, 20% O₂-synthetic air) with a flow rate of 60 mL min⁻¹, sample mass 14.2 mg (in Ar), and 13.5 mg (in synthetic air) in open Al₂O₃ crucible. The gaseous species were guided into a ThermoStar GSD320 quadrupole mass spectrometer through a heated capillary tube kept at 180 °C. Data were collected in multiple ion detection mode (MID) monitoring 21 channels between $m/z = 1-89$. Collection time was 1 s for each channel. EGA-MS figures were generated with OriginLab software.

The evolved gases were identified based on their MS reference spectra available in the public domain spectral library of NIST [47]. Reaction schemes were generated with ACD ChemSketch freeware.

Intermediate decomposition product preparation

Intermediate decomposition products of **1** were prepared in inert atmosphere in laboratory test as follows: after purging the quartz tube inside the two-zone tube furnace to $1 \cdot 10^{-3}$ mbar at room temperature, 99.999% N₂ flow of 60 mL min⁻¹, and heating rate of 10 °C min⁻¹ were used, while retaining the ceramic crucible at 170 °C, 270 °C, 400 °C, or 730 °C for 10 min before cooling in ambient to ≈40 °C and withdrawing. Intermediate decomposition products of **1** in air were prepared in laboratory test at 170 °C, 270 °C, and 480 °C by inserting **1** into a preheated muffle furnace, and retaining the specified temperature in the crucible for 10 min before withdrawing. At 600 °C, the residue from TG/DTA in synthetic air was used.

For FTIR analysis of the products of the first decomposition step, intermediate decomposition products of **1** were prepared in inert atmosphere in the same two-zone tube furnace as follows: after purging to $1 \cdot 10^{-3}$ mbar at room temperature, 99.999% N₂ flow of 30 mL min⁻¹, and heating rate of 5 °C min⁻¹ were used, while retaining the crucible at 115 °C, or 160 °C for 3 min before cooling in ambient to ≈40 °C and withdrawing. For FTIR analysis of the first decomposition step, intermediate decomposition products of **1** in air were prepared as follows: **1** was inserted into a preheated muffle furnace and heated in a semi-closed crucible, to prevent the solid from surging out, at the specified temperature for 3 min before withdrawal, and immediately cooled in a cold water bath to room temperature.

Structural analysis

The phase composition of **1**, its intermediate and final decomposition products were analyzed with a powder XRD (Rigaku Ultima IV, Si strip detector D/teX Ultra), Cu $K_{\alpha 1}$ λ 1.5406 Å, θ -2 θ mode, 5°min⁻¹, step 0.02°, 40 kV, 40 mA. XRD data were analyzed using Rigaku PDXL 2 software. Figures were generated with OriginLab software.

Results and discussion

Identification of **1**

The FTIR spectra of potassium ethyl xanthate (KS₂COC₂H₅ – KEX) and antimony ethyl xanthate (Sb(S₂COC₂H₅)₃ – SbEX) have been published before, being only presented in this study to identify and demonstrate the purity of KEX and **1**. FTIR spectra of KEX and **1**, as measured by the KBr technique, are shown in Fig. 1. The list of possible assignments of FTIR bands of KEX and **1**, based on the literature [36, 38, 41–43, 48, 49], is presented in Table S1 in the electronic Supporting File.

According to FTIR, the spectra of KEX and **1** were similar, although bands had shifted in the range of 1300 cm⁻¹–1000 cm⁻¹ in **1** vs KEX, showing that the complex with Sb seems to have formed. The C=S stretching modes shifted from 1006 cm⁻¹ and 1050 cm⁻¹ in KEX to 1001 cm⁻¹, and 1024 cm⁻¹ in **1**, indicating the formation of longer C-S bonds as a result of the stronger electron pull toward Sb in the Sb-S bond than in the K-S bond due to Sb being more electronegative than K. The symmetric C–O–C stretching (1103 cm⁻¹, 1118 cm⁻¹) in KEX, shifted to 1112 cm⁻¹, and 1135 cm⁻¹ in **1**. The asymmetric C–O–C stretching (1158 cm⁻¹, 1173 cm⁻¹) in KEX, merged into a

strong band at 1230 cm⁻¹ in **1**. C–O–C stretching modes shifting to higher wavenumbers likely points to a shortening of C–O–C bonds in the ligand. Weaker bands appearing at 3000–2870 cm⁻¹, 1468 cm⁻¹, 1448 cm⁻¹, 1075 cm⁻¹ and 813 cm⁻¹ attributed to CH₃ and CH₂ stretching and bending modes did not shift considerably, revealing that the interaction between the ethyl group and the cation (K, Sb) is weak, as expected. Therefore, the ethyl group is the farthest, and the CS₂ group is probably the closest to Sb, connected to each other by the C–O–C bridge. The wide band positioned at 3650–3300 cm⁻¹ in both KEX and **1** is attributed to adsorbed H₂O.

The Raman spectrum of **1** is shown in Fig. S1. So far, the Raman spectrum of SbEX is unindexed, though 35 Raman active optical modes in the range of 50–3000 cm⁻¹ were observed in the Raman spectrum of **1**. The most intense Raman bands of **1** are centered at 91, 167, 232, 339, 406, 439, 665, 845, 998, and 1029 cm⁻¹. Raman band centers of **1**, with possible assignments from compounds similar to SbEX [43, 48, 50], are listed in Table S2. Raman bands attributed to only **1** were found above the limit of detection.

The crystal structure of SbEX is rhombohedral, space group R $\bar{3}$, $a = 10.13$ Å, $\alpha = 103^\circ 30'$, six units in the unit cell, and each Sb atom is known to be surrounded by three S atoms at 2.52 Å, and another three at 3.00 Å, which altogether form a distorted octahedron, extending into the planar S₂C–O group [51, 52]. The XRD pattern of rhombohedral SbEX is available in the CSD database under SBXANT, and the XRD pattern of **1** is presented only to confirm its identity as SbEX (Fig. S2, numeric data in Table S3). According to XRD, additional phases above the limit of detection were not found in **1**.

The 1D NMR analysis results are presented in Table 1. Minor traces of acetone and ethanol were found in **1**. Evidently, the acquired ¹H and ¹³C NMR data correspond to

Fig. 1 FTIR spectra of potassium ethyl xanthate (KEX) and **1** recorded with 4 cm⁻¹ resolution in KBr pellet

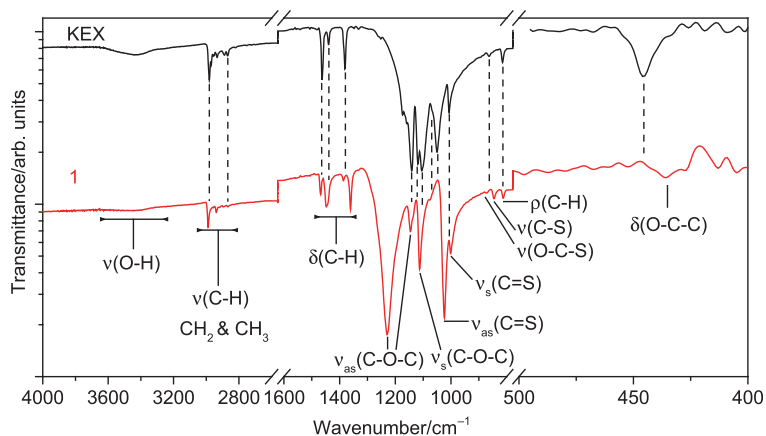


Table 1 ^1H and ^{13}C spectral data of **1** in comparison to the literature [33, 53]

Compound	^1H / ppm			^{13}C / ppm			Integral of ^1H		Functional group
	Found in 1	Literature	Ref	Found in 1	Literature	Ref	1	2-PrOH	
CDCl_3	7.26, s	7.26	[53]	77.16	77.16	[53]	–	–	CHCl_3
CH_3COCH_3	2.17, s	2.17	[53]	–	30.92	[53]	–	0.01	$-\text{CH}_3$
2-PrOH	1.20, d	1.22	[53]	25.48	25.14	[53]	–	6.26	$-\text{CH}_3$
	4.01, sept	4.04	[53]	64.53	64.50	[53]	–	1.00	$-\text{CH}-$
1	1.47, t	1.40	[33]	14.00	12.40	[33]	3.00	4.18	$-\text{CH}_3$
	4.64, q	4.55	[33]	72.17	71.00	[33]	2.00	2.15 ^a	$-\text{CH}_2-$
	–	–	–	222.60	221.40	[33]	–	–	$-\text{O}-\text{C}-\text{S}_2$

^aThe CH_2 functional group was used to calculate the purity of **1** with respect to the known amount of 2-PrOH. There was overlap between the signals for the CH_3 functional group of 2-PrOH and the CH_3 functional group of **1**, which prevented accurate integration of these proton peaks

Table 2 COSY, HSQC and HMBC spectral data of **1**

Method	^1H / ppm		^{13}C / ppm	Functional groups ^a
COSY	1.43	4.65	–	$-\text{CH}_2-\text{CH}_3$
	4.60	1.48	–	
HSQC	1.46		14.04	$-\text{CH}_3$
	4.64		72.16	$-\text{CH}_2-$
HMBC	4.64		14.04	$-\text{CH}_2-\text{CH}_3$
	1.46		72.16	$-\text{CH}_2-\text{CH}_3$
	4.64		222.60	$\text{S}_2-\text{C}-\text{O}-\text{CH}_2-$

^aHMBC correlated nuclei are in bold

relevant values in the literature [33, 53], thereby complementing the FTIR data in identification of **1**.

According to quantitative ^1H of CH_3 , the analyte contained the equivalent of 95 mol% of $(\text{EX})_3$ versus 2-PrOH (Table 1). The remaining 5 mol% of **1** precipitated in the NMR test tube. According to XRD, the red precipitate was amorphous, as no reflections were observed. The Raman spectrum of the precipitate contained a single broad band, stretching from 200–360 cm^{-1} , and centered at 290 cm^{-1} , characteristic of amorphous Sb_2S_3 [21, 22]. Thus, the results of quantitative NMR, XRD, and Raman support the observations made in EDX analysis of **1** regarding its slight deficiency of sulfur (S/Sb of 1.42) vs stoichiometric composition of S/Sb of 1.50. Indeed, it is known that SbEX can change from light yellow to dark yellow, then to orange by decomposing over time to amorphous Sb_2S_3 [36].

Based on the liquid NMR COSY analysis (Table 2), **1** contains mutually J-bonded CH_3 and CH_2 groups. HSQC analysis revealed that the two observed peaks at (^1H 1.46; ^{13}C 14.04) and (^1H 4.64; ^{13}C 72.16) correlate with one another, proving that the CH_3 and CH_2 functional groups are directly bonded in **1**. According to HMBC analysis, three cross-peaks appeared (Table 2; Fig. S3). Thus, the CH_2 functional group is bonded to both the CH_3 , and the OCS_2 functional group and the sequence of functional groups in **1**

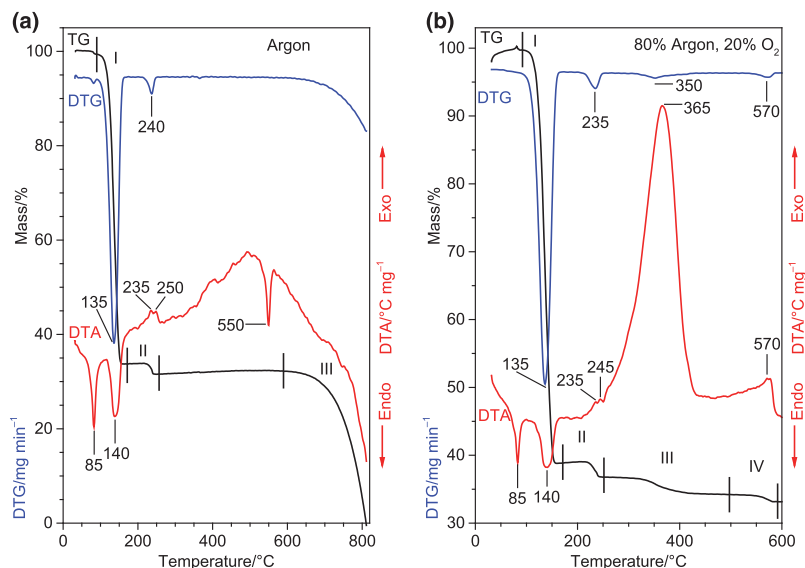
can be derived as $\text{CH}_3-\text{CH}_2-\text{O}-\text{CS}_2-$. The quantitative 1D ^1H NMR experiment showed that the molar ratio of CH_3 functional groups in **1** to 2-PrOH is 1.42 (expected 1.50, *i.e.*, 3/2). As ≈ 5 mol% of **1** is Sb_2S_3 , then the molar ratio of CH_3 in the EX ligand to Sb^{3+} is close to the expected stoichiometric value of 3.

In summary, FTIR showed that the vibrational modes of **1** correspond to only SbEX, and the main bands had shifted in comparison to KEX, indicating the formation of a complex with a more electronegative metal. XRD showed that only rhombohedral SbEX was detected in **1**. Raman showed that bands attributed to only **1** were detected. Further investigation by NMR showed that there are approximately three ligands per molecule of **1** with the structure of $-\text{S}_2\text{COCH}_2\text{CH}_3$, *i.e.*, the EX ligand. According to quantitative ^1H NMR, **1** contains approximately 95 mol% of SbEX. The slight deficiency of S was also observed by EDX (95 \pm 2 mol% of theoretical value). The remaining 5 mol% was identified as amorphous Sb_2S_3 by Raman. Therefore, **1** has been identified as 95 mol% $\text{Sb}(\text{S}_2\text{COCH}_2\text{CH}_3)_3 - \text{SbEX}$, and 5 mol% of amorphous Sb_2S_3 .

Thermal analysis

According to TG curves of **1** (Fig. 2), the thermal decomposition occurred in three mass loss steps in argon in the range of 90–800 $^\circ\text{C}$, whereas in synthetic air, four mass loss steps were observed in the range of 90–590 $^\circ\text{C}$. The endothermic step at 85 $^\circ\text{C}$ in both atmospheres is the melting point of **1**, because in laboratory test, a melting point of **1** of 77 ± 1 $^\circ\text{C}$ was measured on slow heating in air (*cf.* 75 $^\circ\text{C}$ in [32], 68–70 $^\circ\text{C}$ in [33]), wherein a viscous adhesive clear yellow liquid formed. The first mass loss step was endothermic in both atmospheres, as DTA peaked at 140 $^\circ\text{C}$, preceding the DTG maximum at 135 $^\circ\text{C}$. Similarly, in both atmospheres, two consecutive exothermic effects occurred in the second mass loss step at 235 $^\circ\text{C}$ and 250 $^\circ\text{C}$ in argon, and 235 $^\circ\text{C}$ and 245 $^\circ\text{C}$ in synthetic air, together with a DTG maximum

Fig. 2 TG, DTG, and DTA curves of **1** in **a** argon, flow 60 mL min^{-1} , heating rate 10°min^{-1} , initial mass 11.6 mg , and **b** synthetic air, flow 60 mL min^{-1} , heating rate 10°min^{-1} , initial mass 13.9 mg , as measured in situ by the online coupled TG/DTA-MS system



positioned at 240°C in argon, and 235°C in synthetic air, respectively.

Mass was constant in argon between 250 and 590°C , although a sharp endothermic effect occurred at 550°C . A broad endothermic effect occurred throughout the third mass loss step in argon beginning at 600°C . An intense exothermic effect appeared in the third mass loss step in synthetic air, peaking at 365°C , trailing the DTG peak at 350°C . A weaker exothermic effect occurred in the fourth mass loss

step in synthetic air at 570°C simultaneously with the DTG peak at 570°C .

The first mass loss step in both atmospheres was in the range of 90 – 170°C with mass losses of 66.3% in argon, and 61.1% in synthetic air. The second mass loss step was in the range of 170°C – 255°C in argon, and 170°C – 250°C in synthetic air, with mass loss of 2.1% in both cases. The third mass loss step started in argon at 590°C , proceeding until 810°C , where all of the remaining mass was lost. The mass

Table 3 Decomposition steps, mass losses, temperatures of DTA and DTG peaks, evolved gases, and detected crystalline phases of **1**. TG/DTA-MS data recorded using a heating rate of $10^\circ\text{C min}^{-1}$ in argon,

and synthetic air atmosphere with open Al_2O_3 crucible on a Setaram LabSys EVO instrument

Atmosphere	Step	Temperature range/ $^\circ\text{C}$	Mass loss at the end of the decomposition step /%	DTA peak temp./ $^\circ\text{C}$	DTG max temp./ $^\circ\text{C}$	Evolved gases from MS ^a	Crystalline phases at the end of the decomposition step (XRD data), ICDD PDF No
Ar	1	90–170	66.3	140 endo	135	CS_2, EtOH, CO, CO_2, COS H_2O, EtSH, SO_2	None
	2	170–255	68.4	235 exo, 250 exo	240		Sb_2S_3 (stibnite, 01–075-4012)
	3	590–800	100	–	–		Sb_2S_3 , Sb (05–0562) at 730°C
	Final	800°C	100	–	–		no solid residue
Ar + O_2	1	90–170	61.1	140 endo	135	CS_2, EtOH, CO, CO_2, COS H_2O, EtSH, SO_2	None
	2	170–250	63.2	235 exo, 245 exo	235		Sb_2S_3
	3	250–495	65.8	365 exo	350		Sb_2O_4 (cervantite, 01–074-8714)
	4	495–590	66.8	570 exo	570		Sb_2O_4 (600°C)
	Final	600°C	66.8	–	–		Sb_2O_4

^aMajor gases in bold

loss of **1** in argon above 590 °C is the result of incongruent evaporation of liquid Sb_2S_3 per the Sb-S phase diagram [5, 7, 54], as the product collected at 730 °C consisted of crystalline Sb_2S_3 and metallic Sb according to XRD (Table 3).

In synthetic air, the third mass loss step was in the range of 250–495 °C with mass loss of 2.6%. The fourth mass loss step in synthetic air was in the range of 495–590 °C with mass loss of 1.0%. Final mass loss was 100% in argon at 800 °C, and 66.8% in synthetic air at 600 °C. The theoretical mass loss in argon at 600 °C is 65.0% (experimental 68.3%), assuming pure Sb_2S_3 phase. The theoretical mass loss in air is 68.3%, as the final product in synthetic air was Sb_2O_4 . The final mass loss of **1** in synthetic air was lower than calculated due to presence of Sb_2S_3 in **1**.

Evolved gas analysis in argon and synthetic air atmosphere by online EGA-MS

The evolution curves of gases as ion currents of characteristic mass fragments of the identified gaseous species vs temperature evolved from **1** in argon, and in synthetic air in comparison, as recorded by online EGA-MS, are shown in Fig. 3. Peak centers and assignments of all measured EGA-MS channels are listed in Table S4.

According to EGA-MS in argon, the evolution of gases started at 50 °C with the evolution of adsorbed moisture as water (H_2O) with characteristic ion fragment of m/z 18, peaking at 82 °C. Evolution of water below 100 °C was not detected in synthetic air likely because the sample was purged for an extended period of time vs the sample in argon before commencing the EGA-MS run.

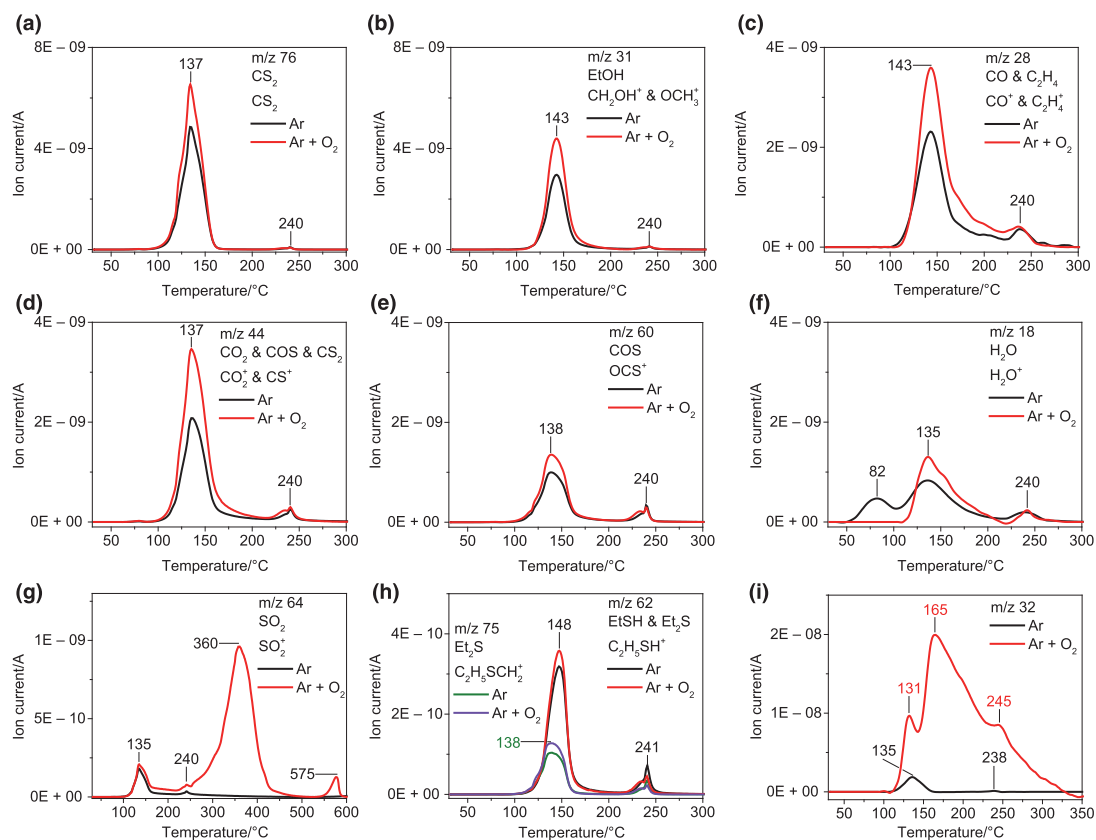


Fig. 3 Gas evolution profiles of CS_2 **a**, EtOH **b**, CO and C_2H_4 **c**, CO_2 , CS_2 , and COS **d**, COS **e**, H_2O **f**, SO_2 **g**, EtSH and Et_3S **h**, and unknown m/z 32 **i**, represented by their characteristic mass spectroscopic ion fragments, from **1** in argon (in black or green), flow

60 mL min^{-1} , heating rate 10°min^{-1} , initial mass 11.6 mg, and in synthetic air (in red or violet), flow 60 mL min^{-1} , heating rate 10°min^{-1} , initial mass 13.9 mg, as measured by in situ online coupled TG/DTA-EGA-MS system. (Color figure online)

The first decomposition step (90–170 °C) began similarly in argon and synthetic air with the evolution of several gases: carbon disulfide (CS₂, *m/z* 76, Fig. 3a), ethanol (EtOH, *m/z* 31, Fig. 3b), carbon monoxide (CO, *m/z* 28, Fig. 3c; possibly partially attributable to C₂H₄), carbon dioxide (CO₂, *m/z* 44, Fig. 3d; partially attributable to CS⁺ from CS₂ and COS), carbonyl sulfide (COS, *m/z* 60, Fig. 3e), water (*m/z* 18, Fig. 3f), and sulfur dioxide (SO₂, *m/z* 64, Fig. 3g). Substantial evolution of gaseous fragments corresponding to the methyl group (CH₃, *m/z* 15, Fig. S4a), and the ethyl or formyl group (C₂H₅ or CHO, *m/z* 29, Fig. S4b) was also detected. Evolution of some minor gases was also detected, *e.g.*, ethanethiol (EtSH, *m/z* 62, Fig. 3h), diethyl sulfide (Et₂S, *m/z* 75, Fig. 3h), diethyl ether (Et₂O, *m/z* 74, Fig. S4c) and dixanthogen ((EX)₂, *m/z* 89, Fig. S4d).

In argon, the evolution curve of the tentatively unassigned *m/z* 32 corresponded to CS₂, COS, and SO₂, with a maximum at 135 °C. Thus, in argon, *m/z* 32 is attributed to the S⁺ fragment of CS₂, COS, and SO₂, and possibly to molecular MeOH. The evolution curve of *m/z* 32 in synthetic air is a conundrum, because after 131 °C the curve is unlike any of the monitored *m/z* channels, its intensity looming over other gases by an order of magnitude without mass loss nor any DTA effects. This strange phenomenon was observed in experiments run in synthetic air with Al₂O₃ and Pt crucible (not shown), where the shape and intensity of the evolution curve were similarly anomalous. In synthetic air, *m/z* 32 could correspond to S⁺ (COS, CS₂, H₂S, S₈), or MeOH, but comparison to other *m/z* curves disproved this possibility. Therefore, *m/z* 32 in synthetic air remained unresolved in this study.

The second decomposition step (170–255 °C in argon, 170–250 °C in synthetic air) proceeded with the evolution of CS₂, EtOH, CO, CO₂, COS, H₂O, SO₂, EtSH, Et₂S, Et₂O, and (EX)₂ in a proportionally smaller quantity, reflecting the ≈30 times smaller mass loss in the second decomposition step compared to the first (2.1% vs. 66.3% in argon; 2.1% vs. 61.1% in synthetic air). In the second decomposition step in argon, and synthetic air the evolution curves of gases were asymmetric, tailing toward lower temperatures, peaking at 240 °C. The asymmetric evolution curve in EGA-MS supports the TG/DTA results in that two consecutive exothermic processes occur in the second decomposition step, peaking at 235 °C and 250 °C in argon, and at 235 °C and 245 °C in synthetic air (Fig. 2). The evolution of most gaseous species ceased by the end of the second decomposition step at ≈270 °C, indicating complete decomposition of organic material. In argon, no evolution of gases was detected beyond 270 °C, whereas in synthetic air, only SO₂ and *m/z* 32 continued to evolve.

In the third decomposition step in synthetic air (250–495 °C), SO₂ evolved in a significantly larger amount

than in the first and second step, peaking at 360 °C. In the fourth decomposition step in synthetic air (495–590 °C), SO₂ evolved from 530 to 590 °C, peaking at 575 °C. The evolution curve of SO₂ in synthetic air closely resembles the DTA curve (Fig. 2b), and follows the DTG peak positions in the temperature range of 200–600 °C, indicating that the exothermic DTA effects in that temperature range in synthetic air are directly related to the evolution of SO₂.

Discussion of thermal analysis results

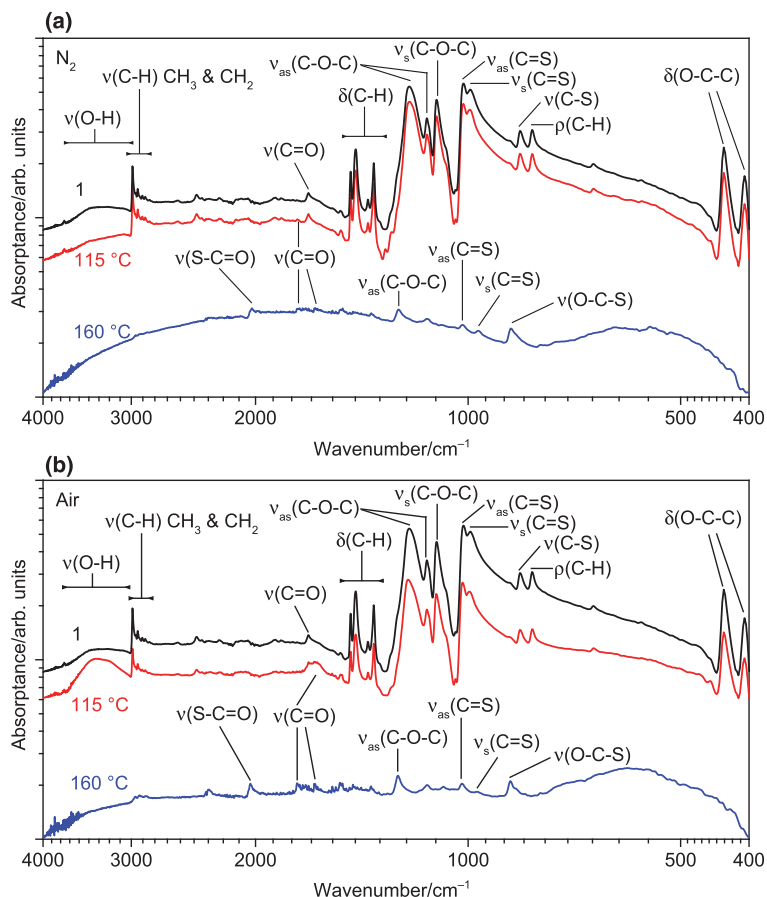
To establish the basis for describing the decomposition mechanism of **1**, laboratory tests were made to investigate the phase composition of the *solid* intermediate decomposition products of **1** at various temperatures in inert and air atmosphere. These intermediate decomposition products of **1** were characterized by FTIR, XRD, and Raman to determine the phase composition at various stages of the decomposition process.

The slight difference in FTIR spectra of some band positions of **1** in respect to measurements by KBr method is attributed to differences in instrument setup and measurement mode (Fig. 1 vs. Fig. 4). Tentative FTIR assignments in the following discussion are based on the literature [36, 38, 41–43, 48–50, 55–57]. According to FTIR, the vibrational modes of the intermediate decomposition product prepared at 115 °C in N₂ are nearly identical to those of **1** (Fig. 4a).

By 160 °C, the FTIR spectrum has changed significantly, as bands attributed to CH₃ and CH₂ stretching (2800–3000 cm⁻¹), scissoring (1386 cm⁻¹, 1443 cm⁻¹, 1468 cm⁻¹), twisting (1075 cm⁻¹), and rocking (813 cm⁻¹) modes have disappeared, indicating that the ethyl group (CH₃CH₂-) has been cleaved, and has exited into the gas phase. Furthermore, the O–C–C scissoring (407 cm⁻¹, 436 cm⁻¹) of the ethyl group has disappeared, in correlation with EGA-MS results, where evolution of EtOH peaked at 143 °C, and ended by 160–165 °C (Fig. 3b). Adsorbed water has evolved by 160 °C in N₂, because the broad band (O–H stretching, 3000–3700 cm⁻¹) is not present in the spectrum of the solid intermediate (Fig. 4a). Moreover, by 160 °C in N₂, bands have shifted from 995 cm⁻¹ to 967 cm⁻¹ (C=S symmetric stretching; bond elongation), from 1230 cm⁻¹ to 1254 cm⁻¹ (C–O–C asymmetric stretching; bond shortening), and from 1682 cm⁻¹ to 1643 cm⁻¹ (conjugated C=O stretching; bond elongation) (Fig. 4a). The shift in band positions and new bands at 870 cm⁻¹ (O–C–S stretching), and 2021 cm⁻¹ (S–C=O stretching) likely indicates the formation of a monothiocarbonate ligand (CSO₂²⁻).

The FTIR spectrum of the solid intermediate prepared at 115 °C in air is similar to the spectra of **1** and the solid intermediate prepared at 115 °C in N₂, although some features differ: a C=O stretching band at 1643 cm⁻¹ in air vs 1742 cm⁻¹ in N₂, and a more intense band between

Fig. 4 FTIR spectra of **1** and its intermediate decomposition products prepared in laboratory tests in N₂ **a**, and in air **b** in the first decomposition step at 115 °C and 160 °C, as measured with diamond anvil in reflectance mode at resolution of 4 cm⁻¹, 24 scans

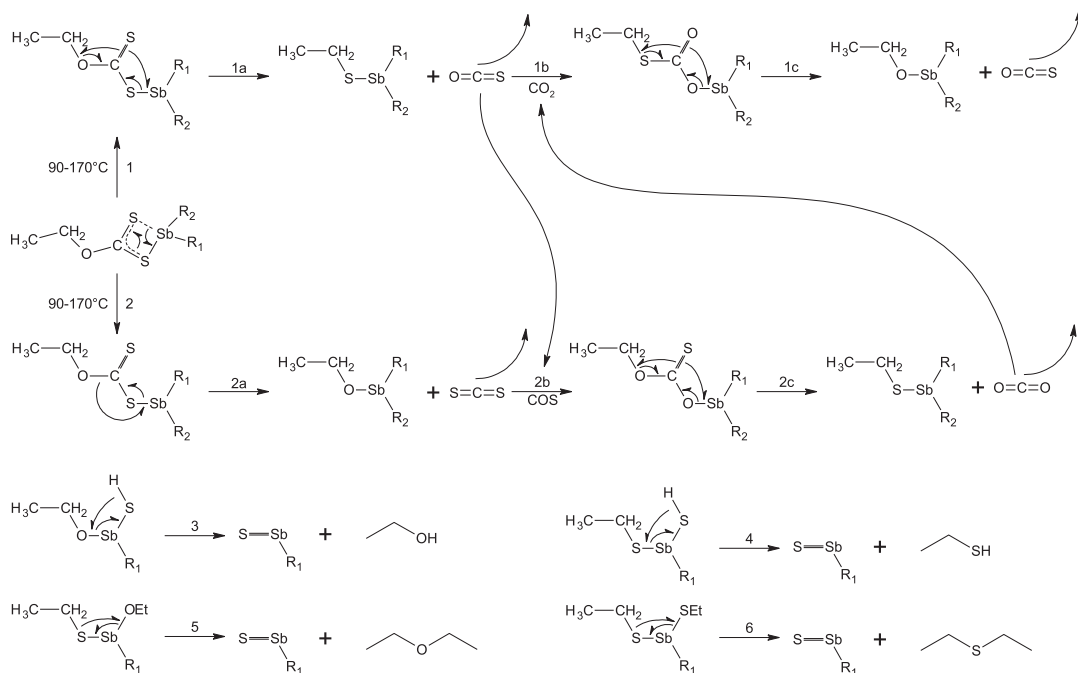


3000–3700 cm⁻¹ than in **1** (O–H stretching), showing that free water has formed during the decomposition of **1** due to air oxidation of the ethyl group. The FTIR spectrum of the solid intermediate prepared at 160 °C in air is similar to the spectrum of the residue prepared at 160 °C in N₂, except a weak residual of the ethyl group at 2800–3000 cm⁻¹ (CH₃, CH₂ stretching) possibly due to insufficient time for decomposition of **1** in laboratory test. In summary, the intermediate decomposition products prepared at 160 °C in N₂, and in air appear to contain one or more ligands composed of C=O, C–S, O=C–S, O–C–S, and possibly C–O–C fragments, with traces of ethyl group.

The main gases CS₂, EtOH, CO, CO₂, COS, and H₂O co-evolve in the first decomposition step, thus, the decomposition of SbEX cannot proceed merely by direct cleavage of the EX ligand, and must proceed through one or more parallel reactions. As SbEX is liquid before and during the decomposition, liquid-phase radical and ionic reactions that are common for xanthate reactions should occur [35, 37].

COS, CS₂ and EtOH likely form via competing reactions, where one Sb–S coordination bond is broken, followed by intramolecular rearrangement of bonds between the alkoxy and dithiocarbonyl group (Scheme 1, reaction 1 and reaction 2). With rotation of the dithiocarbonyl group, followed by cleavage of COS that evolves as a gas, Sb(R₁)(R₂)SCH₂CH₃ is produced (Scheme 1, reaction 1a). Without rotation of the dithiocarbonyl group, CS₂ is cleaved, evolving as a gas, and Sb(R₁)(R₂)OCH₂CH₃ (Scheme 1, reaction 2a) is produced. Reaction 2 and reaction 2a in Scheme 1 is most likely the main reaction, as this sequence is the most straightforward and credible source of CS₂—the main evolved gas. Reaction 2a is likely thermodynamically preferred over reaction 1a in Scheme 1, as rotation of the dithiocarbonyl group, and redistribution of twice as many bonds in reaction 1a vs reaction 2a requires overcoming a higher activation energy barrier.

In Scheme 1, Reaction 1a accounts for COS, and reaction 2a for CS₂. Thus, further reactions are needed to explain the evolution of CO₂, CO, EtOH, and H₂O. Also, EtSH as a

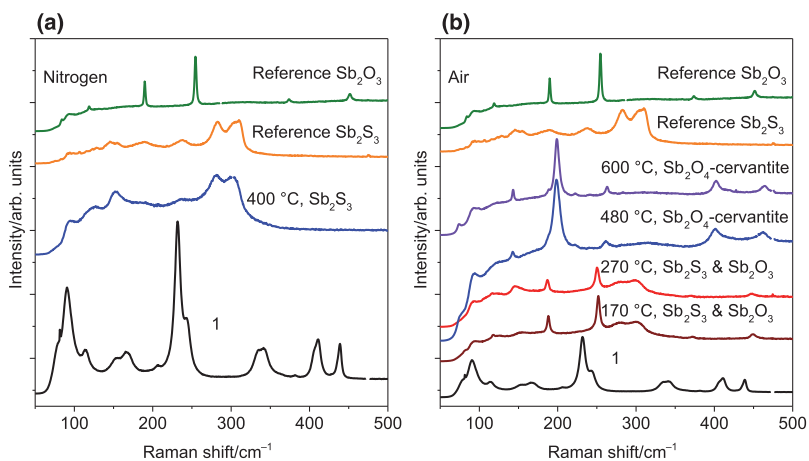


Scheme 1 Proposed decomposition reactions of SbEX occurring in the first decomposition step. $R_1, R_2 = \text{EX} / \text{EtO} / \text{EtS} / \text{CSO}_2 / \text{CSO}_2\text{Et} / \text{SH}$

minor gas probably forms in two reaction steps because of steric inhibition of interaction between S and CH_3CH_2 - in the EX ligand, as evinced by NMR and EGA-MS results. Mirroring reaction 1a, CO_2 and EtSH could be produced by reaction 2c in Scheme 1, whereby COS is injected into $\text{Sb}(R_1)(R_2)\text{OEt}$ ($R = \text{EX} / \text{SH} / \text{EtO} / \text{EtS}$), followed by

rearrangement of the COS moiety to yield $\text{Sb}(R_1)(R_2)\text{SET}$ and CO_2 . Reactions like 1b and 2b in Scheme 1, where the metal hydroxide, thiol, alkoxide, or mercaptane reacts as a Lewis base with CS_2 , COS, or CO_2 anhydride as Lewis acid, are known to form carbonates, thiocarbonates, and their alkyl-substituted derivatives [58].

Fig. 5 Raman spectra of **1** and its intermediate decomposition products in laboratory tests in **a** N_2 , flow 60 mL min^{-1} , heating rate 10°min^{-1} after pre-purging to $1 \cdot 10^{-2}$ mbar, heating time 10 min, and in **b** air, where **1** was inserted into a preheated furnace and heated at the specified temperature for 10 min before withdrawal and cooling



Considering the sizeable and rapid mass loss in the first decomposition step, $\text{Sb}(\text{EX})_2\text{OEt}$ could degrade further by decomposition of the remaining EX ligands, followed by evolution of EtOH, *e.g.*, reaction 3 in Scheme 1, while retaining enough Sb-S bonds to form Sb_2S_3 , as confirmed by Raman (Fig. 5b), because no intermediate decomposition products of **1** in inert atmosphere with Sb-O bonding were detected by neither Raman (Fig. 5a) nor XRD (Fig. 6a). By analogy to reaction 3, the remaining EX ligands of $\text{Sb}(\text{EX})_2\text{SEt}$ could decompose, followed by evolution of EtSH (*e.g.*, reaction 4 in Scheme 1).

Judging by EGA-MS evolution intensity (Fig. 3), the evolution of EtSH is an order of magnitude smaller compared to EtOH, meaning the EtS ligand likely undergoes further reactions, acting as a supply of S for Sb_2S_3 , *i.e.*, reaction 5 and reaction 6 in Scheme 1, whereas EtOH evolves directly, *i.e.*, reaction 3 in Scheme 1. Reactions 3–6 in Scheme 1 should proceed, as the interaction between ligands is not sterically inhibited, and because the ligands are small, single-bonded throughout, and therefore able to rotate around the axis of the single coordination bond with Sb. Another possible explanation for the sparse evolution of EtSH could be that reaction 2b is the rate determining step: first, because $\text{Sb}(\text{R}_1)(\text{R}_2)\text{OEt}$ is probably consumed mainly in reaction 3 in Scheme 1 to produce EtOH; second, because the insertion of COS into $\text{Sb}(\text{R}_1)(\text{R}_2)\text{OEt}$ is a gas–liquid reaction limited by the concentration of COS dissolved or dispersed in the liquid mixture.

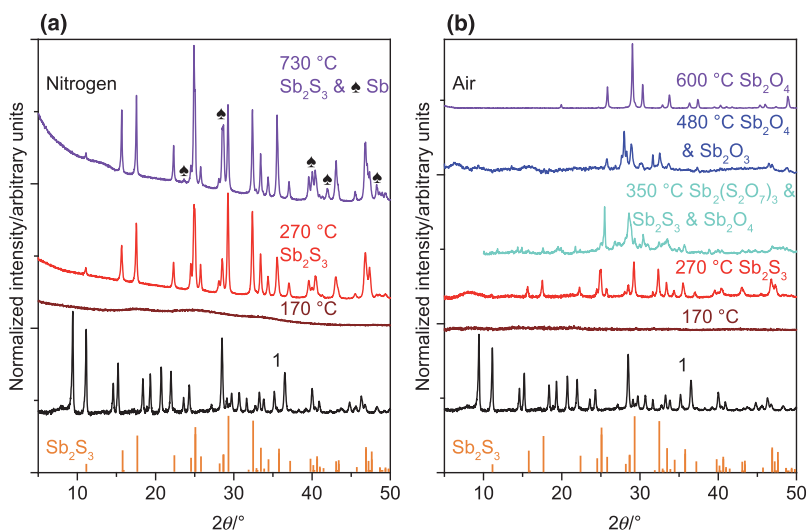
The combined intensity of evolving CO, COS and CO_2 in EGA-MS is similar to the intensity of evolving CS_2 , which could indicate that reaction 2b in Scheme 1 is supplied with COS by reaction 1a or reaction 1c, and with $\text{Sb}(\text{R}_1)(\text{R}_2)\text{OEt}$

by reaction 2a or reaction 1c in Scheme 1. Reaction 1c in Scheme 1 is unlikely to contribute significantly to the thermal decomposition of **1**, because it requires gaseous CO_2 as reactant, which forms in reaction 2c, in turn dependent on COS produced in reaction 1a. Consequently, reaction 1c in Scheme 1 has 6 prerequisite reaction steps before it can occur.

Et_2O and Et_2S are minor byproducts, probably forming via proton transfer between intermediate neighbor ligands and subsequent cleavage from Sb, *e.g.*, reaction 4 and reaction 6 in Scheme 1. SO_2 as a minor gas likely forms in argon by hydrolysis of COS or CS_2 to H_2S and CO_2 or CO, ending with H_2S oxidizing to SO_2 and H_2O [59]. As the quantity of protons is limited in **1** to the ethyl group in the EX ligand above 90 °C, the formation of EtOH, EtSH, and H_2O in argon (and air) requires the formation of an equivalent quantity of ethylene (C_2H_4) via proton transfer to supply the protons. Therefore, the EGA-MS of m/z 28 attributed to CO could be in part attributed to the evolution of C_2H_4 in addition to CO, albeit without definitive proof, as characteristic m/z of C_2H_4 overlap with EtOH and other evolved gases. C_2H_4 could react in air with O_2 to form oxirane ($\text{C}_2\text{H}_4(\text{O})$) or acetaldehyde [4], although neither can be confirmed with EGA-MS due to overlap with m/z of main gases. Water evolves as a product of various decomposition and condensation reactions of intermediate products in the thermal decomposition of SbEX with the atmosphere having no significant effect on its evolution. Finally, CO could evolve from hydrolysis of CS_2 or COS [59], or via incomplete oxidation of EtOH.

The results of this study show that the Chugaev elimination, which is often used to describe xanthate

Fig. 6 XRD patterns of **1** and its intermediate decomposition products in laboratory tests in a N_2 , flow 60 mL min^{-1} , heating rate $10^\circ \text{ min}^{-1}$ after pre-purging to $1 \cdot 10^{-2}$ mbar, heating time 10 min, and in b air, where **1** was inserted into a preheated furnace and heated at the specified temperature for 10 min before withdrawal and cooling



decomposition [35, 37], does not apply for **1** at all, because in it only COS and C₂H₄ are formed – neither the dominant gas in the first decomposition step of **1** (Fig. 3). Clearly, as the Chugaev elimination cannot explain the co-evolution of CS₂, CO, CO₂, H₂O, EtOH, EtSH, Et₂S, and Et₂O in inert and oxidizing atmospheres, the reaction is not valid.

At the end of the first decomposition step at 170 °C in argon, and air, about 3 mass% of the initial mass of organic species is retained in amorphous Sb₂S₃ (Table 3). The solid intermediate prepared at 170 °C in both N₂ and air was amorphous according to XRD, as seen in Fig. 6. However, according to Raman (Fig. 5b), a mixture of Sb₂S₃ and Sb₂O₃ (senarmontite) had formed in air at 170 °C by direct oxidation of Sb₂S₃. The asymmetric shape of the EGA-MS (Fig. 3) curves in addition to the two successive exothermic effects witnessed in DTA (Fig. 2) signifies that either more stable inorganic or organic ligands, *e.g.*, CSO₂²⁻, EtOCOS⁻, EtS⁻, EtO⁻, or a separate dispersed phase has formed inside the amorphous Sb₂S₃ phase, as seen from the FTIR spectra of solid intermediates prepared at 160 °C (Fig. 4). Presumably, the residual organic species are expelled as the gases seen in EGA-MS (Fig. 3), followed by crystallization of purified Sb₂S₃ (Fig. 6), as its nucleation is no longer inhibited. Elucidating the precise composition of this residual impurity in Sb₂S₃, which persists in the solid phase over 100 °C above the first decomposition, warrants further investigation.

The second decomposition step occurred in the range of 170–255 °C in Ar and 170–250 °C in synthetic air, with a mass loss of 2.1% in both cases, evolution of minor amount of CS₂, EtOH, CO, CO₂, COS, H₂O, SO₂, EtSH, Et₂S, Et₂O, and (EX)₂ (Fig. 3), and orthorhombic Sb₂S₃ was the final solid product in inert atmosphere, and a mixture of Sb₂S₃ and cubic Sb₂O₃ in air, as determined by Raman (Fig. 5b). Based on the FTIR analysis of the solid intermediate products (Fig. 4), antimony monothiocarbonate (Sb₂(CSO₂)₃), a trace of antimony ethyl monothiocarbonate (Sb(SOCOCH₂CH₃)₃), and possibly other (thio)carbonyl ligands persist until 240 °C. According to EGA-MS, trace quantities of presumed Sb-SEt, Sb-OEt, or Sb-OSCOEt ligands survive, evolving as EtOH, EtSH, Et₂O, and Et₂S by 250 °C (Fig. 3, Fig. S4). No FTIR bands were observed in any residue prepared at or above 270 °C in either atmosphere (not shown), meaning that all carbonaceous matter had mineralized or evolved by that point, in correlation with the results of EGA-MS (Fig. 3, Fig. S4).

The third decomposition step in synthetic air occurred in the range of 250–495 °C, with a mass loss of 1.0%, accompanied by evolution of SO₂ (Fig. 3), and a mix of Sb₂O₄ and Sb₂O₃ as the final product (Table 3). As seen in Fig. 6b, at 350 °C in air the gray residue contained at least one sulfate of antimony (Sb₂(S₂O₇)₃) in addition to Sb₂S₃, and Sb₂O₄ (cervantite), indicating that in the third decomposition step, any remaining Sb₂S₃ is first oxidized to

a mixture of Sb₂(S_nO_{3n+1})₃ (*n* = 1; 2; 3; 4), *e.g.*, Sb₂(S₂O₇)₃, ICDD 1–070–2198, and Sb₂(SO₄)₂(S₂O₇), 1–083–2537, then to Sb₂O₃, and finally to Sb₂O₄ with vigorous exothermic evolution of SO₂. Therefore, the formation of sulfates above 300 °C in the third decomposition step in air initially caused a slight mass gain that was masked by the net mass loss of 2.6% from the energetic SO₂ evolution. The oxidation rate and oxidation product of Sb₂S₃ at 350–500 °C is strongly dependent on temperature, and particle size [60], which explains the simultaneous detection of antimony compounds in progressive stages of oxidation in the residue.

In the fourth decomposition step in synthetic air in the range of 495–590 °C, the exothermic mass loss at 570 °C coupled with evolution of SO₂ at 575 °C is caused by purification of residual sulfate via transition of senarmontite-Sb₂O₃ into valentinite-Sb₂O₃ at 570 °C (*cf.* 570 °C in [5], 581 °C in [54]), followed by oxidation into Sb₂O₄, as seen by the difference in XRD patterns of residues prepared at 480 °C (senarmontite-Sb₂O₃ & cervantite-Sb₂O₄) and 600 °C (cervantite-Sb₂O₄) in air (Fig. 6b). The intermediate residue prepared in N₂ at 730 °C was composed of Sb₂S₃ and Sb (Fig. 6a). The incongruent evaporation of Sb₂S₃ proceeding above its melting point at 550 °C is complete by 800 °C, which is consistent with results of previous studies [54], where total mass loss of Sb₂S₃ was observed in inert atmosphere.

Similarly to thiourea–metal chloride complexes that we used to deposit SnS, ZnS, CuInS₂, In₂S₃, and Sb₂S₃ thin films by spray pyrolysis for photovoltaic applications [11, 20–22, 61–64], SbEX appears to be an excellent single-source precursor for producing phase pure Sb₂S₃ thin films by spray pyrolysis.

Conclusions

It was shown that, according to FTIR and NMR, **1**, synthesized from KEX and SbCl₃ in molar ratio of Sb/S of 1/3, contains a coordination complex, wherein three -S₂COCH₂CH₃ – ethyl xanthate ligands are coordinated to Sb atom via S atoms. According to elemental analysis and quantitative ¹H NMR, **1** contains approximately 95 mol% of Sb(S₂COCH₂CH₃)₃, and 5 mol% of amorphous Sb₂S₃, as identified by Raman.

The thermal decomposition of **1** consists of three mass loss steps in argon in the temperature range of 90–800 °C, whereas in synthetic air, four mass loss steps occurred in the temperature range of 90–590 °C with mass loss of 100% and 66.8%, respectively. The first and second thermal decomposition steps proceed similarly in argon and synthetic air in the temperature range of 90–170 °C. In argon, amorphous Sb₂S₃ formed as the product of the first decomposition step by 170 °C alongside a minor amount of possibly antimony monothiocarbonate

Sb(CSO₂)₃, Sb(OEt)₃, Sb(SET)₃ or a mixed ligand compound containing these ligands, identified by EGA-MS and FTIR of intermediate decomposition products. In synthetic air, amorphous senarmontite-Sb₂O₃ formed by 170 °C in addition to the aforementioned compounds, as identified by Raman. In the first decomposition step, CS₂, EtOH, CO, CO₂, COS, H₂O, and SO₂ evolved as main gases. Evolution of minor gases EtSH, Et₂S, Et₂O, and (EX)₂ was also detected.

Chemical reactions occurring in the first decomposition step in the temperature range of 90–170 °C were proposed for the first time for SbEX, describing formation of CS₂, COS, CO₂, EtOH, EtSH, Et₂S, Et₂O, and intermediate decomposition product ligands, *e.g.*, EtS, EtO, and (mono-thio)carbonyl-based unsubstituted and the respective alkyl-substituted ligands. Furthermore, the results of this study show that the Chugaev elimination reaction is inadequate to describe the thermal decomposition of SbEX.

In the second thermal decomposition step in argon, the solid phase was purified from the remaining ligands, and thereafter Sb₂S₃ crystallized, as confirmed by XRD and Raman. In synthetic air, the solid phase contained amorphous senarmontite-Sb₂O₃, as confirmed by XRD and Raman. The evolved gases in the second thermal decomposition step were the same as in the first step, although evolution of CS₂ and EtOH had diminished considerably. In argon, the third and final thermal decomposition step began at 590 °C, after melting of Sb₂S₃ at 550 °C, and proceeded apace until total mass loss at 800 °C. In air, the third decomposition step began at 250 °C, and ended at 495 °C with the formation of cervantite-Sb₂O₄, proceeding through formation and oxidation of a mixture of antimony sulfates coupled with vigorous evolution of SO₂ (EGA-MS), as shown for the first time for SbEX through solid-phase intermediate decomposition product analysis in this study by XRD and Raman. In the fourth decomposition step in synthetic air, remaining antimony sulfates oxidized into cervantite-Sb₂O₄, as confirmed by XRD of the final product remaining at 600 °C, coupled with evolution of SO₂ according to EGA-MS. Neither evolution of carbonaceous species, nor any presence in the solid state in either atmosphere in intermediate decomposition products prepared at or above 270 °C was detected, indicating that the solid state is free of carbon residues.

Results on the thermal decomposition of *tris*-ethylthiocarbonato-antimony(III) (**1**) in inert and oxidative atmospheres yielded valuable data serving as basis for determining the atmosphere and processing temperatures to be used to deposit phase pure Sb₂S₃ thin films. The fact that SbEX allows to deposit Sb₂S₃ at significantly lower temperatures in comparison to other single-source precursors, and is purified from C containing residues at very low temperatures, makes SbEX a suitable precursor for depositing phase pure Sb₂S₃ thin films by the spray pyrolysis method.

Electronic Supporting Material

The electronic Supplementary File contains the tabulated list of tentative FTIR vibrational assignments from the literature used in this study, the Raman spectrum of **1** in the range of 50–3000 cm⁻¹, and the corresponding tabulated list of tentative Raman vibrational assignments from the literature, the powder XRD pattern of **1**, and the corresponding numeric XRD data, the HMBC plot of **1**, EGA-MS gas evolution curves of additional gaseous species, and peak centers and proposed assignments of all *m/z* channels used in the EGA-MS.

Supplementary Information The online version contains supplementary material available at <https://doi.org/10.1007/s10973-021-10885-1>.

Acknowledgements The authors thank Dr. Valdek Mikli from the Laboratory of Optoelectronic Materials Physics at Tallinn University of Technology for EDX measurements. This study was funded by the Estonian Research Council project PRG627 “Antimony chalcogenide thin films for next-generation semitransparent solar cells applicable in electricity producing windows,” European Regional Development Fund Centre of Excellence project TK141 (TAR16016EK) “Advanced materials and high-technology devices for energy recuperation systems,” and European Regional Development Fund Centre of Excellence project TK134 “Emerging orders in quantum and nanomaterials.”

Author contributions All authors contributed to the study conception and design. Material preparation was performed by J.S. Eensalu. Data collection was performed by J.S. Eensalu, K. Tõnsuaadu and J. Adamson. All authors participated in the data analysis. The first draft of the manuscript was written by J.S. Eensalu and all authors commented on previous versions of the manuscript. All authors read and approved the final and the revised manuscript.

Funding This study was funded by the Estonian Research Council project PRG627 “Antimony chalcogenide thin films for next-generation semitransparent solar cells applicable in electricity producing windows,” European Regional Development Fund Centre of Excellence project TK141 (TAR16016EK) “Advanced materials and high-technology devices for energy recuperation systems,” and European Regional Development Fund Centre of Excellence project TK134 “Emerging orders in quantum and nanomaterials.”

Data availability Data and materials are available upon request from the authors.

Declarations

Conflict of interest The authors declare that they have no conflict of interest.

Open Access This article is licensed under a Creative Commons Attribution 4.0 International License, which permits use, sharing, adaptation, distribution and reproduction in any medium or format, as long as you give appropriate credit to the original author(s) and the source, provide a link to the Creative Commons licence, and indicate if changes were made. The images or other third party material in this article are included in the article’s Creative Commons licence, unless indicated otherwise in a credit line to the material. If material is not included in the article’s Creative Commons licence and your intended use is not

permitted by statutory regulation or exceeds the permitted use, you will need to obtain permission directly from the copyright holder. To view a copy of this licence, visit <http://creativecommons.org/licenses/by/4.0/>.

References

- Klochko K. Antimony Data Sheet. In: Mineral commodity summaries. U. S. Geological Survey. 2020. Available from: <https://pubs.usgs.gov/periodicals/mcs2020/mcs2020-antimony.pdf>. Accessed 13 May 2020.
- Apodaca LE. Sulfur Data Sheet. In: Mineral commodity summaries. U. S. Geological Survey; 2020. Available from: <https://pubs.usgs.gov/periodicals/mcs2020/mcs2020-sulfur.pdf>. Accessed 13 May 2020.
- Alharbi F, Bass JD, Salhi A, Alyamani A, Kim H-C, Miller RD. Abundant non-toxic materials for thin film solar cells: alternative to conventional materials. *Renew Energy*. 2011;36:2753–8.
- Greenwood NN, Earnshaw A. Chemistry of the elements. 2nd ed. Oxford: Butterworth-Heinemann; 1997.
- Thornycroft WE. Antimony and bismuth. London: Charles Griffin & Co Ltd; 1936.
- Rinkevichius V, Mikalkevichius M. Pyroelectric effect in antimony trisulfide single crystals. *Sov Phys Solid State USSR*. 1967;9:2360.
- Živković Ž, Štrbac N, Živković D, Grujičić D, Boyanov B. Kinetics and mechanism of Sb_2S_3 oxidation process. *Thermochim Acta*. 2002;383:137–43.
- Leijtens T, Bush KA, Prasanna R, McGehee MD. Opportunities and challenges for tandem solar cells using metal halide perovskite semiconductors. *Nat Energy*. 2018;3:828–38.
- Kondrotas R, Chen C, Tang J. Sb_2S_3 Solar cells. *Joule*. 2018;2:857–78.
- Shin HD, Choi S-H. Recent studies of semitransparent solar cells. *Coatings*. 2018;8:329–58.
- Eensalu JS, Katerski A, Kärber E, Weinhardt L, Blum M, Heske C, et al. Semitransparent Sb_2S_3 thin film solar cells by ultrasonic spray pyrolysis for use in solar windows. *Beilstein J Nanotechnol*. 2019;10:2396–409.
- SavadoGO O, Mandal KC. Studies on new chemically deposited photoconducting antimony trisulphide thin films. *Sol Energ Mat Sol Cells*. 1992;26:117–36.
- Zimmermann E, Pfadler T, Kalb J, Dorman JA, Sommer D, Hahn G, et al. Toward high-efficiency solution-processed planar heterojunction Sb_2S_3 solar cells. *Adv Sci (Weinheim, Ger)*. 2015;2:1500059.
- Parize R, Cossuet T, Chaix-Pluchery O, Roussel H, Appert E, Consonni V. In situ analysis of the crystallization process of Sb_2S_3 thin films by Raman scattering and X-ray diffraction. *Mater Des*. 2017;121:1–10.
- Wedemeyer H, Michels J, Chmielowski R, Bourdais S, Muto T, Sugiura M, et al. Nanocrystalline solar cells with an antimony sulfide solid absorber by atomic layer deposition. *Energy Environ Sci*. 2013;6:67–71.
- Kim D-H, Lee S-J, Park MS, Kang J-K, Heo JH, Im SH, et al. Highly reproducible planar Sb_2S_3 -sensitized solar cells based on atomic layer deposition. *Nanoscale*. 2014;6:14549–54.
- Büttner P, Scheler F, Pointer C, Döhler D, Barr MKS, Koroleva A, et al. Adjusting interfacial chemistry and electronic properties of photovoltaics based on a highly pure Sb_2S_3 absorber by atomic layer deposition. *ACS Appl Energy Mater*. 2019;2:8747–56.
- Kaiburg P, Klingebiel B, Kirchartz T. Spin-coated planar Sb_2S_3 hybrid solar cells approaching 5% efficiency. *Beilstein J Nanotechnol*. 2018;9:2114–24.
- Jiang C, Tang R, Wang X, Ju H, Chen G, Chen T. Alkali metals doping for high-performance planar heterojunction Sb_2S_3 solar cells. *Solar RRL*. 2019;3:1800272.
- Kriisa M, Krunks M, Oja Acik I, Kärber E, Mikli V. The effect of tartaric acid in the deposition of Sb_2S_3 films by chemical spray pyrolysis. *Mater Sci Semicond Process*. 2015;40:867–72.
- Kärber E, Katerski A, Oja Acik I, Mere A, Mikli V, Krunks M. Sb_2S_3 grown by ultrasonic spray pyrolysis and its application in a hybrid solar cell. *Beilstein J Nanotechnol*. 2016;7:1662–73.
- Eensalu JS, Katerski A, Kärber E, Oja Acik I, Mere A, Krunks M. Uniform Sb_2S_3 optical coatings by chemical spray method. *Beilstein J Nanotechnol*. 2019;10:198–210.
- Deng H, Yuan S, Yang X, Cai F, Hu C, Qiao K, et al. Efficient and stable $\text{TiO}_2/\text{Sb}_2\text{S}_3$ planar solar cells from absorber crystallization and Se-atmosphere annealing. *Mater Today Energy*. 2017;3:15–23.
- Choi YC, Lee DU, Noh JH, Kim EK, Seok SI. Highly improved Sb_2S_3 sensitized-inorganic-organic heterojunction solar cells and quantification of traps by deep-level transient spectroscopy. *Adv Funct Mater*. 2014;24:3587–92.
- Patil PS. Versatility of chemical spray pyrolysis technique. *Mater Chem Phys*. 1999;59:185–98.
- Krunks M, Leskelä T, Mutikainen I, Niinistö L. A Thermoanalytical study of copper(I) thiocarbamide compounds. *J Therm Anal Calorim*. 1999;56:479–84.
- Otto K, Oja Acik I, Tõnsuaadu K, Mere A, Krunks M. Thermoanalytical study of precursors for In_2S_3 thin films deposited by spray pyrolysis. *J Therm Anal Calorim*. 2011;105:615–23.
- Oja Acik I, Otto K, Krunks M, Tõnsuaadu K, Mere A. Thermal behaviour of precursors for CuInS_2 thin films deposited by spray pyrolysis. *J Therm Anal Calorim*. 2013;113:1455–65.
- Krunks M, Madarász J, Leskelä T, Mere A, Niinistö L, Pokol G. Study of zinc thiocarbamide chloride, a single-source precursor for zinc sulfide thin films by spray pyrolysis. *J Therm Anal Calorim*. 2003;72:497–506.
- Madarász J, Krunks M, Niinistö L, Pokol G. Evolved gas analysis of dichlorobis(thiourea)zinc(II) by coupled TG-FTIR and TG/DTA-MS techniques. *J Therm Anal Calorim*. 2004;78:679–86.
- Polvitseva S, Oja Acik I, Krunks M, Tõnsuaadu K, Mere A. Thermoanalytical study of precursors for tin sulfide thin films deposited by chemical spray pyrolysis. *J Therm Anal Calorim*. 2015;121:177–85.
- Khwaja MA, Cardwell TJ, Magee RJ. Thermal studies on arsenic, antimony and bismuth alkylxanthate complexes. *Anal Chim Acta*. 1973;64:9–17.
- Rodríguez-Castro J, Molloy KC, Liu Y, Lai CS, Dong Z, White TJ, et al. Formation of antimony sulfide powders and thin films from single-source antimony precursors. *J Mater Chem*. 2008;18:5399–405.
- Vreugdenhil AJ, Brienne SHR, Butler IS, Finch JA, Markwell RD. Infrared spectroscopic determination of the gas-phase thermal decomposition products of metal-ethyldithiocarbonate complexes. *Spectrochim Acta, Part A*. 1997;53:2139–51.
- DePuy CH, King RW. Pyrolytic cis eliminations. *Chem Rev*. 1960;60:431–57.
- Chakrabarty T, De AK. Liquid-liquid extraction of arsenic(III), antimony(III) and bismuth(III) with potassium ethyl xanthate. *Fresenius' J Anal Chem*. 1968;242:152–9.
- Zard SZ. On the trail of xanthates: some new chemistry from an old functional group. *Angew Chem, Int Ed Engl*. 1997;36:672–85.
- Talonen P, Sundholm G, Li WH, Floate S, Nichols RJ. A combined in situ infrared spectroscopy and scanning tunnelling

- microscopy study of ethyl xanthate adsorption on Au(111). *Phys Chem Chem Phys*. 1999;1:3661–6.
39. Li J, Liu X, Yao J. The enhanced photovoltaic performance of Sb_2S_3 solar cells by thermal decomposition of antimony ethyl xanthate with thiourea doping. *Energy Technol (Weinheim, Ger)*. 2020;8:1900841.
 40. Garje SS, Jain VK. Chemistry of arsenic, antimony and bismuth compounds derived from xanthate, dithiocarbamate and phosphorus based ligands. *Coord Chem Rev*. 2003;236:35–56.
 41. Ray A, Sathyanarayana DN, Prasad GD, Patel CC. Infrared spectral assignments of methyl and ethyl xanthato complexes of nickel(II). *Spectrochim Acta, Part A*. 1973;29:1579–84.
 42. Buchmaier C, Glänzer M, Torvisco A, Poelt P, Wewerka K, Kunert B, et al. Nickel sulfide thin films and nanocrystals synthesized from nickel xanthate precursors. *J Mater Sci*. 2017;52:10898–914.
 43. Barreca D, Gasparotto A, Maragno C, Seraglia R, Tondello E, Venzo A, et al. Synthesis and characterization of zinc bis(O-isopropylxanthate) as a single-source chemical vapor deposition precursor for ZnS. *Appl Organomet Chem*. 2005;19:1002–9.
 44. Vigneshwaran M, Ohta T, Iikubo S, Kapil G, Ripolles TS, Ogomi Y, et al. Facile synthesis and characterization of sulfur doped low bandgap bismuth based perovskites by soluble precursor route. *Chem Mater*. 2016;28:6436–40.
 45. Bansal N, O'Mahony FTF, Lutz T, Haque SA. Solution processed polymer–inorganic semiconductor solar cells employing Sb_2S_3 as a light harvesting and electron transporting material. *Adv Energy Mater*. 2013;3:986–90.
 46. Wojdyr M. Fityk: a general-purpose peak fitting program. *J Appl Crystallogr*. 2010;43:1126–8.
 47. NIST chemistry webbook. National Institute of Standards and Technology. <https://webbook.nist.gov/chemistry/>. Accessed 28 July 2020.
 48. Juncal LC, Cozzarín MV, Romano RM. Conformational and spectroscopic study of xanthogen ethyl formates, $ROC(S)SC(O)OCH_2CH_3$. Isolation of $CH_3CH_2OC(O)SH$. *Spectrochim Acta, Part A*. 2015;139:346–55.
 49. Chandra AP, Puskar L, Simpson DJ, Gerson AR. Copper and xanthate adsorption onto pyrite surfaces: implications for mineral separation through flotation. *Int J Miner Process*. 2012;114–117:16–26.
 50. Woods R, Hope GA. Spectroelectrochemical investigations of the interaction of ethyl xanthate with copper, silver and gold: I. FT-Raman and NMR spectra of the xanthate compounds. *Colloids Surf A*. 1998;137:319–28.
 51. Gottardi G. The crystal structure of xanthates II Antimonious xanthate. *Z Kristallogr Cryst Mater*. 1961;115:451–9.
 52. Hoskins BF, Tiekink ERT, Winter G. The crystal and molecular structure of O-ethylxanthato-bis(quinolin-8-olato)antimony(III) and a redetermination for tris(O-ethylxanthato)antimony(III). *Inorg Chim Acta*. 1985;97:217–22.
 53. Fulmer GR, Miller AJM, Sherden NH, Gottlieb HE, Nudelman A, Stoltz BM, et al. NMR chemical shifts of trace impurities: common laboratory solvents, organics, and gases in deuterated solvents relevant to the organometallic chemist. *Organometallics*. 2010;29:2176–9.
 54. Padilla R, Ramírez G, Ruiz MC. High-temperature volatilization mechanism of stibnite in nitrogen-oxygen atmospheres. *Metall Mater Trans B*. 2010;41:1284–92.
 55. IR spectrum table & chart. Merck KGaA. <https://www.sigmaaldrich.com/technical-documents/articles/biology/ir-spectrum-table.html>. Accessed 10 Jul 2020.
 56. Fisher NG, Dunn JG. Identifying organic foulants on activated carbon from gold processing plants. *Miner Eng*. 2000;13:1581–8.
 57. Fan H-T, Sun W, Jiang B, Wang Q-J, Li D-W, Huang C-C, et al. Adsorption of antimony(III) from aqueous solution by mercapto-functionalized silica-supported organic–inorganic hybrid sorbent: Mechanism insights. *Chem Eng J (Amst, Neth)*. 2016;286:128–38.
 58. Stueber D, Patterson D, Mayne CL, Orendt AM, Grant DM, Parry RW. Carbonates, thiocarbonates, and the corresponding mono-alkyl derivatives. 1. Their preparation and isotropic ^{13}C NMR chemical shifts. *Inorg Chem*. 2001;40:1902–11.
 59. Ferm RJ. The chemistry of carbonyl sulfide. *Chem Rev*. 1957;57:621–40.
 60. Padilla R, Aracena A, Ruiz MC. Kinetics of stibnite (Sb_2S_3) oxidation at roasting temperatures. *J Min Metall Sect B*. 2014;50:127–32.
 61. Polivtseva S, Katerski A, Kärber E, Oja Acik I, Mere A, Mikli V, Krunks M. Post-deposition treatment of sprayed SnS films. *Thin Solid Films*. 2017;633:179–84.
 62. Dedova T, Krunks M, Gromyko I, Mikli V, Sildos I, Utt K, et al. Effect of Zn:S molar ratio in solution on the properties of ZnS thin films and the formation of ZnS nanorods by spray pyrolysis. *Phys Status Solidi A*. 2014;211:514–21.
 63. Otto K, Katerski A, Mere A, Volobujeva O, Krunks M. Spray pyrolysis deposition of indium sulphide thin films. *Thin Solid Films*. 2011;519:3055–60.
 64. Krunks M, Mikli V, Bijakina O, Rebane H, Mere A, Varema T, Mellikov E. Composition and structure of $CuInS_2$ films prepared by spray pyrolysis. *Thin Solid Films*. 2000;361–362:61–4.

Publisher's Note Springer Nature remains neutral with regard to jurisdictional claims in published maps and institutional affiliations.

Publication IV

J. S. Eensalu, K. Tõnsuaadu, I. Oja Acik, M. Krunks. "Sb₂S₃ thin films by ultrasonic spray pyrolysis of antimony ethyl xanthate," *Materials Science in Semiconductor Processing*, vol. 137, p. 106209, Jan. 2022, doi: 10.1016/j.mssp.2021.106209.



Contents lists available at ScienceDirect

Materials Science in Semiconductor Processing

journal homepage: www.elsevier.com/locate/msspSb₂S₃ thin films by ultrasonic spray pyrolysis of antimony ethyl xanthateJako S. Eensalu^{a,*}, Kaia Tõnsuaadu^b, Ilona Oja Acik^a, Malle Krunks^{a,**}^a Laboratory of Thin Film Chemical Technologies, Department of Materials and Environmental Technology, Tallinn University of Technology, Ehitajate tee 5, 19086, Estonia^b Laboratory of Inorganic Materials, Department of Materials and Environmental Technology, Tallinn University of Technology, Ehitajate tee 5, 19086, Estonia

ARTICLE INFO

Keywords:

Antimony ethyl xanthate
Antimony sulfide
Spray pyrolysis
Thin film
Thioacetamide
Thiourea

ABSTRACT

Synthesis of antimony chalcogenides, especially Sb₂S₃, by facile and area scalable in-air chemical methods, such as spray pyrolysis, from cost-effective chemicals is certain to accelerate development of the related thin film solar cell technology. In this study, antimony ethyl xanthate, a scarcely studied halogenide-free precursor, is proven to be suitable for the deposition of conformal phase pure crystalline Sb₂S₃ thin films via ultrasonic spray pyrolysis in air by a two-step process. First, a solution of antimony ethyl xanthate with thiourea in a molar ratio of 1/3, or with thioacetamide in a molar ratio of 1/10 was sprayed onto a glass/ITO/TiO₂ substrate by ultrasonic spray pyrolysis at 215°C to yield amorphous phase pure Sb₂S₃ thin films. Second, performing post-growth heat treatment in vacuum at 225°C, was the key to produce phase pure conformal thin films of crystalline Sb₂S₃ (E_g 1.8 eV) with S/Sb atomic ratio of 1.46 by using thiourea, and 1.41 by using thioacetamide, respectively. Spraying solutions of antimony ethyl xanthate at $\geq 135^\circ\text{C}$ resulted in the formation of the Sb₂O₃ phase. Adding thiourea or thioacetamide to the spray solution prevented the oxidation of the growing Sb₂S₃ layer during deposition at 135°C, 165°C, and 215°C. The suppressed oxidation of Sb₂S₃ layers is attributed to the liquid state of thiourea and thioacetamide in these conditions.

1. Introduction

Antimony chalcogenides, *i.e.* Sb₂(S,Se)₃, continue to fascinate the scientific community with a tunable band gap of 1.1–1.7 eV, an absorption coefficient of 10⁵ cm⁻¹ in visible light, and an anisotropic 1D-ribbon-like structure, which facilitates charge carrier transport along the ribbons, and inhibits recombination between rows of ribbons [1]. Sb₂S₃ with an E_g of 1.7 eV is applicable as the absorber in single junction solar cells, or as the front absorber in two cell tandem solar cells, or even as a semitransparent absorber for solar glass or bifacial solar cells [1–8]. Also, Sb₂S₃ is chemically and physically stable, and environmentally benign [9]. These properties drive research of Sb₂S₃ as a light absorber in various solar cell architectures [2–5,10–14].

The current record power conversion efficiency (PCE) of Sb₂S₃ thin film solar cells is 7.1%, achieved by depositing a thin film of Sb₂S₃ using spin-coating from a halogenide-free precursor [15]. The uniform, conformal and compact Sb₂S₃ coating was paramount to achieving the aforementioned PCE. Smooth conformal coatings of Sb₂S₃ have been

grown on various substrate configurations by chemical methods, *e.g.* chemical bath deposition (CBD) [3,4,16,17], spin-coating [5,12,18], atomic layer deposition (ALD) [10,11], hydro- and solvothermal [19], chemical vapor deposition (CVD) [20], spray pyrolysis [21–23], successive ionic layer adsorption reaction [24], and by physical methods, *e.g.* thermal evaporation [14], sputtering [25], and vapor transport deposition [13]. Furthermore, Sb₂S₃ thin films have also been synthesized from Sb₂S₃ nanoparticles in a two-stage process [26–29]. As the melting point of 550°C [9], and the high vapor pressure of Sb₂S₃ set a hard limit on precursors and deposition conditions for physical methods [30], chemical methods are more commonly used to deposit Sb₂S₃ thin films. Furthermore, to ensure that Sb₂S₃ solar cells can be prepared at a competitive \$ kWh⁻¹, inexpensive and area-scalable methods that elicit no special requirements should be prioritized.

In comparison to the chemical deposition methods listed above, ultrasonic spray pyrolysis (USP) is advantageous for depositing uniform Sb₂S₃ coatings, for it is a robust, in-air, low maintenance, continuous production method for rapidly coating large area substrates [31].

Abbreviations: SbEX, antimony ethyl xanthate; USP, ultrasonic spray pyrolysis; TU, thiourea; TA, thioacetamide; PCE, power conversion efficiency; TG, thermogravimetry; DTG, differential thermogravimetry; DTA, differential thermal analysis; EGA-MS, evolved gas analysis via mass spectrometry.

* Corresponding author.

** Corresponding author.

E-mail addresses: jako.eensalu@taltech.ee (J.S. Eensalu), kaia.tonsuaadu@taltech.ee (K. Tõnsuaadu), malle.krunks@taltech.ee (M. Krunks).

<https://doi.org/10.1016/j.mssp.2021.106209>

Received 31 May 2021; Received in revised form 6 September 2021; Accepted 13 September 2021

Available online 22 September 2021

1369-8001/© 2021 The Authors. Published by Elsevier Ltd. This is an open access article under the CC BY license (<http://creativecommons.org/licenses/by/4.0/>).

Despite these capabilities, the challenge of USP is that the growing Sb_2S_3 film has to be protected against oxidation in air at the deposition temperature [23,32].

Metal chloride thiourea (TU) complexes are commonly used to grow phase pure layers of a wide range of metal sulfides, e.g. CuInS_2 , In_2S_3 , SnS_x , and Sb_2S_3 , by spray pyrolysis [23,32–37]. The suitability of these complexes for use in spray pyrolysis has been ascertained by coupled thermal and evolved gas analysis [35,38–43]. In case of TU complexes, extra TU in the spray solution functioned as a liquid shield against oxidation of the nascent sulfide layer during deposition [23,32,33,36,37,44]. Continuing from previous experience [23,32,45], phase pure conformal and uniform Sb_2S_3 thin films were prepared from a solution of SbCl_3/TU using USP in air, which resulted in a PCE of 5.5% in a planar solar cell [46], and a PCE of 2.3% in a ZnO nanowire core-shell extremely thin absorber solar cell [22].

In addition to TU based metal halogenide complex solutions, employing thioacetamide (TA) in the $\text{Sb}(\text{TA})_2\text{Cl}_3$ complex by spin-coating [12,18], and CBD [47], or as a source of H_2S in post-growth heat treatment [16], has been found to improve the phase purity of the Sb_2S_3 absorber. TA has not been applied as an additive in USP deposition of Sb_2S_3 layers. To gauge its compatibility with USP, the thermal decomposition of TA should be investigated.

Similarly to halogenide-thiourea complexes of antimony, Sb-alkyldithiocarbonate complexes are non-hygroscopic, and stable in air and water at ambient conditions [7,48,49]. Among these, antimony ethyldithiocarbonate, or, ethyl xanthate (SbEX), decomposes into Sb_2S_3 by $\sim 160^\circ\text{C}$, lower than any other antimony xanthate [7,48,50–52]. To date, Sb_2S_3 layers have been prepared from SbEX by aerosol-assisted chemical vapor deposition [48], spin-coating [49,51], and doctor blade [7], whereas conformal uniform thin films of Sb_2S_3 have not been prepared from it by any method. Lately, a layer of Sb_2S_3 was spin coated from a solution of SbEX and TU onto a mesoporous TiO_2 scaffold, which resulted in a more chemically pure Sb_2S_3 phase, and culminated in a solar cell with promising PCE of 3.7% [51]. Nevertheless, the effect of directly producing Sb_2S_3 thin films from a solution of SbEX with thioamide additives by in-air processes has not been investigated.

The thermal degradation of SbEX was studied in advance to assess its suitability as a precursor for USP [52]. As the nonvolatile SbEX melts at 80°C , and decomposes by $\sim 160^\circ\text{C}$ [52], thereby forming Sb_2S_3 , it is likely a suitable precursor for depositing thin films of Sb_2S_3 by USP.

The aim of this study is to develop the procedure to prepare phase pure conformal thin films of Sb_2S_3 from antimony ethyl xanthate by ultrasonic spray pyrolysis with suitable properties for application in solar cells. Thiourea and thioacetamide were used to investigate the possibility of deterring oxidation during the USP deposition of thin films of Sb_2S_3 from solutions of SbEX in air. The thermal decomposition of thioacetamide was studied by TG/DTA/EGA-MS to assess its suitability as an additive for the deposition of Sb_2S_3 thin films from SbEX by in-air wet chemical methods such as USP.

2. Materials and methods

Reagents $\text{KS}_2\text{COCH}_2\text{CH}_3$ (KEX, 97%, Acros), SbCl_3 (99%, Aldrich), HCl (37%, Aldrich), diethyl ether (99.5%, Aldrich), acetone (99.8%, Merck), ethanol (96.6%, Estonian Spirit Ltd), methanol (99.8%, Honeywell), titanium(IV)isopropoxide (98%, Acros), acetylacetone (99%, Acros), acetonitrile (99.9%, Honeywell), thiourea (TU, 99%, Alfa Aesar), and thioacetamide (TA, 99%, Merck) were used without further purification. SbEX was synthesized according to the procedure described in Ref. [52]. The SbEX phase was confirmed by powder X-ray diffraction and FTIR analysis [52].

2.1. Sample preparation

Samples were prepared using glass/ITO/ TiO_2 substrates by growing Sb_2S_3 layers in conditions that we use for preparation of solar cells [46],

as the choice of substrate can affect the materials properties of the deposited layer.

First, 1 mm thick ITO-covered soda lime glass (PGO, $10 \pm 3 \Omega/\text{sq}$) substrates were washed consecutively with ethanol, methanol, and deionized water. Then, the dried substrates were subjected to a boiling deionized water bath for 15 min before drying with compressed air.

A compact film of TiO_2 was deposited onto the ITO-covered glass at a deposition temperature of 340°C from a solution of 0.1 M titanium (IV) isopropoxide and 0.4 M acetylacetone dissolved in ethanol. The crystalline anatase phase was detected by XRD after heat treating the samples at 450°C for 30 min in air [46].

The SbEX solution was prepared by dissolving 60 mM of SbEX in acetonitrile, followed by stirring at 40°C for 30 min in a water bath to completely dissolve SbEX. The SbEX/thioamide solutions were prepared in the same way, at a molar ratio of SbEX/TU of 1/1, and 1/3, and SbEX/TA of 1/3, and 1/10. Solutions containing SbEX were sprayed onto heated substrates at 105°C , 135°C , and 165°C in case of SbEX, whereas 135°C , 165°C , and 215°C were used for SbEX/TU 1/3 and SbEX/TA 1/10.

During the ultrasonic spray pyrolysis (USP) of SbEX based solutions, the nozzle moved over an area of 50 cm^2 on the hot plate in a cyclical pattern at a scanning speed of 3 cm s^{-1} and a spray rate of 5.0 mL min^{-1} [23,32]. The flow rate of compressed air as the carrier gas was 5 L min^{-1} . Deposition time was 10 min for all experiments.

After USP deposition, samples were heat treated in dynamic vacuum ($2 \cdot 10^{-1} \text{ Pa}$) at 225°C for 30 min at an average heating and cooling rate of 5°C/min , based on pilot experiments, and previous studies [23,32]. For the sake of convenience, an overview of the conditions used in sample preparation is provided in Table 1.

2.2. Characterization

The phase composition and structure were characterized by X-ray diffraction (Rigaku Ultima IV, Si strip detector D/teX Ultra, θ - 2θ , $\text{Cu K}\alpha_1$ $\lambda = 1.5406 \text{ \AA}$, 40 kV, 40 mA, 5° min^{-1} , step 0.02°). Vibrational properties were measured by Raman spectroscopy (Horiba Labram HR800, backscattering mode, $15 \mu\text{W } \mu\text{m}^{-2}$, 532 nm He-Ne laser) and FTIR spectroscopy (Bruker Alpha, diamond press, absorbance mode, 24 scans, resolution 4 cm^{-1}).

Optical properties were characterized by UV–vis–NIR spectroscopy (Jasco V-670, integrating sphere, air reference). The band gap of Sb_2S_3 was calculated according to the Tauc equation, and the amplitude of interference fringes was reduced by accounting for total reflectance. Morphology and elemental composition were measured on a combined scanning electron microscope (Zeiss HR FESEM Ultra 55, 4 kV) and energy dispersive X-ray spectrometer (Bruker ESPRIT 1.8, 7 kV) system.

The simultaneous TG/DTA/EGA-MS measurement of TA was conducted in a LabSys EVO apparatus (30 – 400°C , 10 K min^{-1} , 20% O_2 in Ar, initial mass 24.5 mg in an open Al_2O_3 crucible). Gases traveled into a ThermoStar GSD320 quadrupole mass spectrometer through a heated (180°C) capillary tube. Data was collected with Calisto software in multiple ion detection mode (MID) monitoring 21 channels between $m/z = 14$ – 76 . The evolved gases were identified based on their MS reference spectra available in the public domain spectral library of NIST [53]. The reaction scheme was drawn with ACD/ChemSketch freeware. The

Table 1

List of conditions used for preparation of Sb_2S_3 layers. Substrate: glass/ITO/ TiO_2 .

Solution composition	SbEX to thioamide molar ratio	Deposition temperature, $^\circ\text{C}$	Post-deposition heat treatment
SbEX	–	105, 135, 165	225°C ,
SbEX & TU	1/1	165	$2 \cdot 10^{-1} \text{ Pa}$,
	1/3	135, 165, 215	30 min
SbEX & TA	1/3	165	
	1/10	135, 165, 215	

proposed mechanism was drawn with Inkscape freeware.

3. Results and discussion

3.1. Layers deposited from SbEX solution

Deposition temperatures of 105°C, 135°C, and 165°C were chosen to reflect the start, the maximum, and the end of the thermal decomposition of SbEX, based on its thermal analysis data [52]. In the span of 10 min at 105°C, powdered SbEX had melted, yet was largely intact [52]. Hence, in the first experiment, layers were deposited from the SbEX solution at 105°C, and were then heat treated in vacuum at 225°C.

The as-deposited layer grown from SbEX solution at 105°C contained intact SbEX, according to XRD (Fig. 1a). The XRD pattern of the as-deposited sample grown at 135°C did not contain peaks attributable to SbEX or Sb₂S₃, although a wide Raman band centered at 300 cm⁻¹ (Fig. 1b), corresponding to amorphous Sb₂S₃ [23], was detected. The sample grown at 165°C contained senarmonite-Sb₂O₃ (ICDD 01-075-0365), as XRD peaks appeared at 2θ of 13.63° and 27.46° (Fig. 1a). As oxidation was contrary to the aim, the samples grown at 165°C were not investigated any further.

After the sample grown at 105°C was heat treated in vacuum at 225°C, signature data of orthorhombic Sb₂S₃, *Pnma* (ICDD 01-075-4015), was detected by XRD (Fig. 1a), and by the Raman bands centered at 127, 156, 190, 238, 283, 300, and 311 cm⁻¹ (Fig. 1b), in line with literature [17,21,23], although vibrational modes at 1025 cm⁻¹ and 1225 cm⁻¹, attributed to SbEX, were still detected by FTIR (Fig. 2). Curiously, the sample grown at 135°C that had been heat treated did not contain any crystalline Sb-related phases (Fig. 1a), nor any vibrational modes attributed to organic species (Fig. 2), whereas Raman bands attributed to crystalline Sb₂S₃ were detected (Fig. 1b). According to EDX, this sample contained a vast amount of carbon compared to sulfur – in terms of atomic ratio, C/Sb 0.57 vs S/Sb 0.36. As long range order was not detected in this heat treated layer by XRD, yet short range order was detected by Raman, it is likely that an impurity phase [55], e.g. Sb₂O₃, or carbonaceous residues, inhibited the crystallization of Sb₂S₃ in this sample.

In summary, based on XRD and Raman, Sb₂S₃ layers were obtained by spraying a layer from a solution of SbEX and heat treating it, although vibrational modes of SbEX were still detected by FTIR, and carbon was detected by EDX. An anti-oxidation agent is clearly needed to produce phase pure Sb₂S₃ layers by USP from a solution of SbEX, as 165°C, and

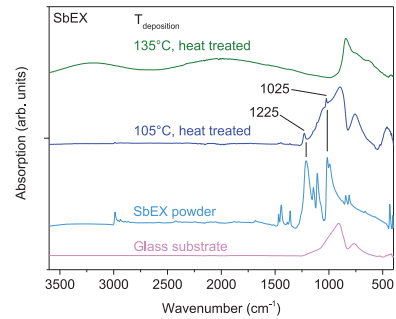


Fig. 2. FTIR spectra of samples grown by USP at a deposition temperature of 105°C, and 135°C from a solution of SbEX after heat treatment. Spectra of glass and SbEX powder are presented for reference. Substrate for heat treated samples: glass/ITO/TiO₂. Heat treatment: dynamic vacuum, 225°C, 2·10⁻¹ Pa, 30 min.

perhaps even 135°C, results in unwanted oxidation. Conveniently, TU [23,32,33,36,37,44], and TA [56], have been applied as additives in solutions of metal halogenide complexes to prevent oxidation of metal sulfide layers during spray pyrolysis. Therefore, it seems prudent to investigate whether adding thioamides to the SbEX spray solution will also suppress oxidation of Sb₂S₃ layers during deposition by USP.

3.2. Layers deposited from SbEX&TU solution

Thiourea (TU) was added to the spray solution to investigate its oxidation suppressing effect on the growing Sb₂S₃ layer, based on previous knowledge, as mentioned at the end of chapter 4.1.

Raman spectra of the as-deposited samples grown from SbEX/TU 1/1 and 1/3 solutions at 165°C contained characteristic bands of amorphous Sb₂S₃ (Fig. 3a). The respective heat treated samples contained crystalline Sb₂S₃, according to Raman (Fig. 3a), and XRD (Fig. S1). The ratio of SbEX/TU of 1/3 was chosen for further experiments to ensure the oxide-free deposition of Sb₂S₃ layers in the deposition temperature series.

According to Raman, the as-grown samples deposited from a solution of SbEX/TU 1/3 at 135°C, 165°C, and 215°C contained amorphous Sb₂S₃ (Fig. S2). The respective heat treated samples contained crystalline Sb₂S₃, according to XRD (Fig. 3b). As vibrational modes attributed

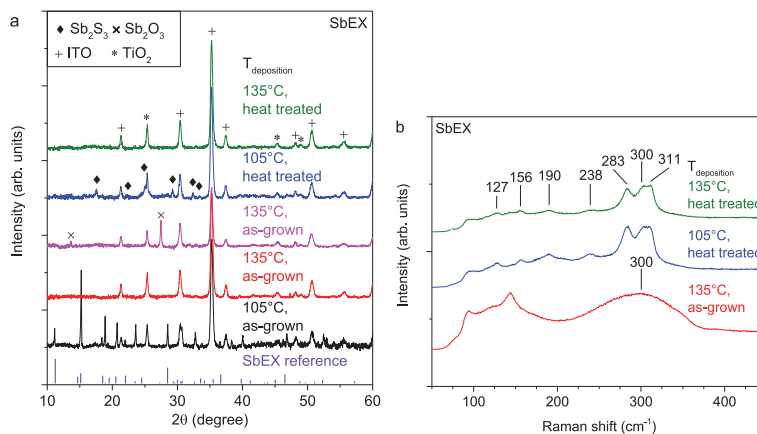


Fig. 1. (a) XRD patterns of layers grown at a deposition temperature of 105°C (as-grown; heat treated), 135°C (as-grown; heat treated), and 165°C (as-grown) from a solution of SbEX by USP. (b) Raman spectra of layers grown at 105°C (heat treated), and 135°C (as-deposited; heat treated) from a solution of SbEX by USP. Substrate: glass/ITO/TiO₂. The SbEX XRD reference was generated from Ref. [54]. Heat treatment: dynamic vacuum, 225°C, 2·10⁻¹ Pa, 30 min.

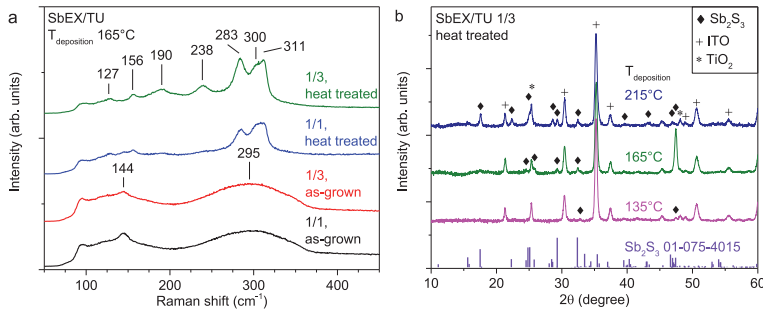


Fig. 3. (a) Raman spectra of samples grown at a deposition temperature of 165°C from a solution of SbEX/TU of 1/1 (as-grown; heat treated), and 1/3 (as-grown; heat treated) by USP. (b) XRD patterns of samples grown at 135°C, 165°C, and 215°C from a solution of SbEX/TU 1/3 by USP after heat treatment. Substrate: glass/ITO/TiO₂. Heat treatment: dynamic vacuum, 225°C, 2.10⁻¹ Pa, 30 min.

to organic species were not detected by FTIR in any of these samples (Fig. S3), the concentration of organic residues in these Sb₂S₃ layers had to be below the detection limit of the setup.

To conclude, as per XRD, Raman, and FTIR, phase pure layers of Sb₂S₃ were obtained by USP at 135°C, 165°C and 215°C from a solution of SbEX/TU 1/3, after heat treatment in vacuum at 225°C.

3.3. Layers deposited from SbEX&TA solution

3.3.1. Thermal analysis of TA

In order to understand how the TA additive influences the USP deposition of SbEX solutions, its thermal behavior in air should be understood. Notably, a thermal analysis coupled with an evolved gas analysis of TA has not yet been conducted. We investigated the thermal decomposition of TA by thermal analysis *via* a combined thermogravimetric and differential thermal analysis system feeding into an online *in situ* evolved gas analysis system connected to a multichannel mass spectrometer. After TA melts at 120°C, it decomposes in one step (Fig. 4a) from 150°C to 210°C, with a DTG peak at 185°C and an endothermic DTA peak at 190°C. 3.2% of the initial mass remained at 210°C. H₂S (*m/z* 34), CH₃CN (*m/z* 15, 41), H₂O (*m/z* 17, 18), and N₂O (*m/z* 14) were the main evolved gases (Fig. 4b). CH₃CN and H₂S are formed by cleavage of the C–S bond in the enol form of TA (Scheme 1), whereas H₂O, N₂O, and SO₂ (minor gas, not shown) are the final oxidation products of H₂S and CH₃CN [57,58].

The thermal analysis data supports the hypothesis that TA could form a protective coating that shields the growing Sb₂S₃ layer from oxidation. Namely, TA liquefies at 120°C, above the melting point of SbEX of 85°C [52], yet below the decomposition temperature of SbEX of 135°C [52], and decomposes into gaseous products at 185°C, by which point the formation of Sb₂S₃ is complete. Therefore, liquid TA is likely to shield the decomposing SbEX, its solid and liquid intermediate products,

and the growing Sb₂S₃ layer from oxidation.

3.3.2. Fabrication of Sb₂S₃ layers

TA was substituted for TU in the SbEX precursor solution to study the effect of the methyl-substituted analogue of TU on the growth of Sb₂S₃ layers. Raman spectra of as-deposited samples, grown at 165°C from a solution of SbEX/TA of 1/3 and 1/10, displayed broad bands related to amorphous Sb₂S₃ (Fig. 5a). The heat treated sample grown with less additive (SbEX/TA 1/3) contained crystalline Sb₂S₃ and Sb₂O₃ (Fig. 5a), yet its counterpart (SbEX/TA 1/10) contained only crystalline Sb₂S₃ (Fig. 5a and b). The solution of SbEX/TA 1/10 was chosen for the deposition temperature series, because, unlike SbEX/TA 1/3, it prevented oxidation of Sb₂S₃ during deposition at 165°C.

After the samples grown at 135°C, 165°C, and 215°C had undergone heat treatment in vacuum, characteristic information of crystalline Sb₂S₃ was detected by XRD (Fig. 5b), and Raman (Fig. S4). Vibrational modes attributable to organic residues were not detected by FTIR in any of these samples (Fig. S5). The facile and thorough decomposition of TA during USP deposition of Sb₂S₃ layers from SbEX/TA solutions at 135–215°C is in agreement with the thermal analysis results (Fig. 4a and b). Therefore, TA decomposing at 150–210°C supports the claim that TA is indeed a prospective additive for SbEX solutions to grow phase pure Sb₂S₃ layers by in-air chemical deposition methods.

In conclusion, according to XRD, Raman, and FTIR, phase pure layers of Sb₂S₃ were obtained by spraying a solution of SbEX/TA 1/10 at 135°C, 165°C, and 215°C after performing heat treatment in vacuum at 225°C, similarly to the results of the TU-based sample series.

3.4. Role of thioamides in USP deposition of Sb₂S₃ thin films from SbEX solutions

Heat treatment of samples grown from SbEX/TU 1/3 solution at a

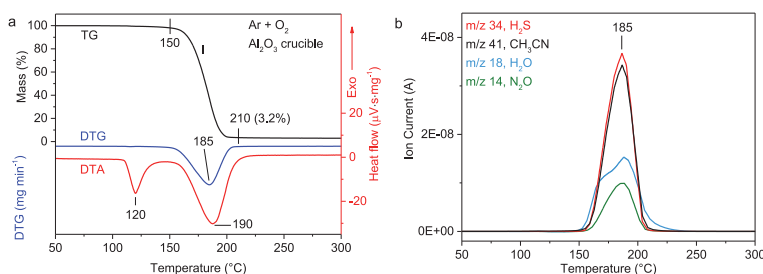
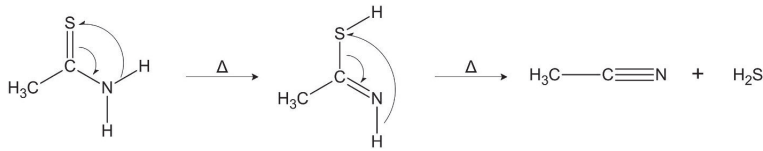


Fig. 4. (a) TG, DTG, and DTA curves of the thermal decomposition of TA, and (b) evolution profiles of main gaseous species as MS fragments. Conditions: synthetic air, flow 60 mL min⁻¹, heating rate 10° min⁻¹, initial mass 24.5 mg.



Scheme 1. Keto-enol tautomerization of TA into its zwitterionic form, followed by cleavage of the C-S bond, yielding acetonitrile and hydrogen sulfide.

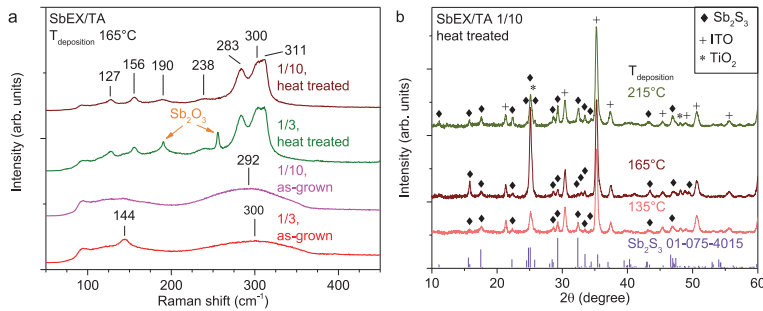


Fig. 5. (a) Raman spectra of samples grown from a solution of SbEX/TA of 1/3 (as-grown; heat treated), and 1/10 (as-grown; heat treated) at a deposition temperature of 165°C by USP. (b) XRD patterns of samples, grown by USP at 135°C, 165°C, and 215°C from a solution of SbEX/TA of 1/10, after heat treatment. Substrate: glass/ITO/TiO₂. Heat treatment: dynamic vacuum, 225°C, 2·10⁻¹ Pa, 30 min.

deposition temperature of 165°C resulted in porous 110 nm thick layers with lateral grain size below 30 nm (Fig. 6a,e). Using the SbEX/TA 1/10 solution instead led to 150 nm thick porous layers with similarly sized agglomerated grains (Fig. 6c,g). Thus, depositing at 165°C with either additive, followed by heat treatment, led to porous layers and minuscule grain size. The porosity probably appeared due to incomplete decomposition of organic residues during the USP deposition step. As growing at 165°C did not produce uniform thin films, samples prepared at temperatures below 165°C were not analyzed further.

In contrast, by growing layers at 215°C from SbEX/TU 1/3 solution, and heat treating them, uniform and flat thin films of Sb₂S₃, 50 nm thick with lateral grain size of 40–280 nm in length and 30–130 nm in width (Fig. 6b,f), were obtained. The morphology of the Sb₂S₃ thin film of the parallel sample, which was grown from SbEX/TA 1/10 solution, was similar: 150 nm thick with lateral grain size of 50–150 nm in length and 25–40 nm in width (Fig. 6d,h). Notably, spraying either the SbEX/TU 1/3 solution, or the SbEX/TA 1/10 solution at 215°C yielded a compact thin film of Sb₂S₃ after heat treatment.

The E_g and S/Sb of the aforementioned heat treated samples, as calculated from UV-vis-NIR and EDX data, is presented in Table 2. In these samples, the band gap of ~1.8 eV of heat treated Sb₂S₃ films (Fig. S6) is in alignment with the literature on chemically and physically deposited crystalline Sb₂S₃ coatings [1,2,4,9,10,12,16,17,23,59]. The slight discrepancy in E_g could be attributed to the error caused by residual interference fringes due to the multi-layered structure of these samples.

The more stoichiometric composition of Sb₂S₃ in the samples grown

Table 2

Band gap and elemental composition data of heat treated samples. Substrate: glass/ITO/TiO₂. Heat treatment: dynamic vacuum, 225°C, 2·10⁻¹ Pa, 30 min.

Deposition temperature, °C	SbEX/TU 1/3		SbEX/TA 1/10	
	E_g , eV	S/Sb, at%/at%	E_g , eV	S/Sb, at%/at%
165	1.77	1.32	1.80	1.39
215	1.79	1.46	1.81	1.41

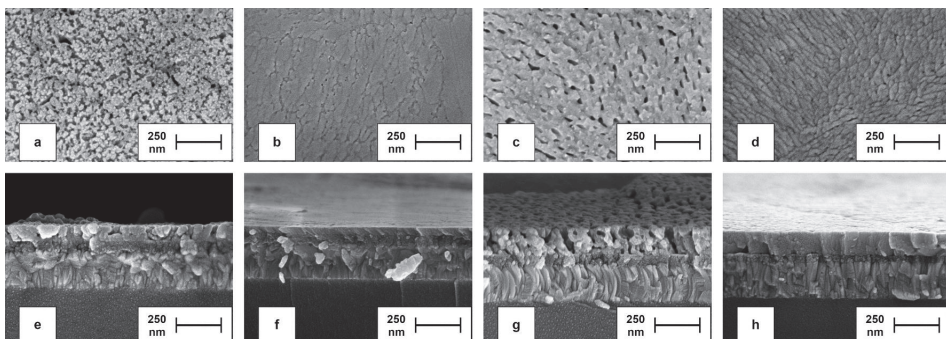


Fig. 6. Top-view and cross-section SEM images of heat treated samples, grown by USP from a solution of SbEX/TU 1/3 at a deposition temperature of 165°C (a, e), and 215°C (b, f), and from a solution of SbEX/TA 1/10 at 165°C (c, g), and 215°C (d, h). Substrate: glass/ITO/TiO₂. Heat treatment: dynamic vacuum, 225°C, 2·10⁻¹ Pa, 30 min.

at 215°C vs 165°C from either solution denotes a more pristine phase composition (Table 2). The amount of oxygen in the Sb_2S_3 layers could not be determined by EDX due to an unavoidable O signal from the underlying glass/ITO/ TiO_2 stack. As heat treatment was made in the same conditions for all samples, the discrepancy in stoichiometry and morphology of Sb_2S_3 layers must be directly related to the deposition temperature.

The decomposition of each portion of TU or TA mixed with SbEX is incomplete at 165°C by the time the substrate is covered again in the next USP cycle. Consequently, carbonaceous residues become trapped inside the as-deposited layers. During heat treatment, the volatilizing residues create porous channels throughout the Sb_2S_3 layer. At 215°C, the decomposition reactions are shifted towards the decomposition products, and are rapid enough to expel the majority of decomposition products during deposition. Thus, fewer residues accumulate inside the as-deposited layers, allowing a continuous thin film to form.

Aggregated data proves that a sufficient quantity of TU or TA at 135–215°C repels oxidation of the growing Sb_2S_3 layer. Spraying the SbEX solution at 135°C–165°C, or the SbEX/TA 1/3 solution at 165°C results in oxidized layers (Fig. 7a). TA decomposes above 150°C (Fig. 4), some 50°C lower, and to a greater extent than TU [60], which could explain the need to use a significantly higher concentration of TA vs TU to avoid oxidation of the growing Sb_2S_3 layer.

In case of spraying the SbEX/TU 1/3, or the SbEX/TA 1/10 solution, a deposition temperature of 165°C or lower is insufficient to burn out the organic residues in time, resulting in a porous layer after heat treatment (Fig. 7b).

In the optimal case (Fig. 7c), spraying the SbEX/TU 1/3 or the SbEX/TA 1/10 solution at 215°C, and heat treating the samples at 225°C in vacuum yields compact and dense thin films of phase pure Sb_2S_3 . As discussed before in this chapter, the thin film morphology is likely achieved due to the more complete combustion of organic residues at 215°C vs 165°C.

4. Conclusions

To conclude, phase pure conformal thin films of Sb_2S_3 were prepared via ultrasonic spray pyrolysis by adding enough TU or TA to a solution of SbEX. The procedure was found to involve, as the first step, the deposition of amorphous Sb_2S_3 layers at a deposition temperature of 215°C from a solution of SbEX/TU 1/3 or SbEX/TA 1/10 by USP in air. Then, as the second step, heat treatment in vacuum at 225°C yielded conformal phase pure crystalline thin films of Sb_2S_3 with $E_g \sim 1.8$ eV, and S/Sb 1.46 (TU-based) or 1.41 (TA-based). According to thermal analysis, TA melts at 120°C, and decomposes at 185°C, meaning that TA, and, by proxy, TU, likely forms a liquid shield that suppresses the oxidation of the growing Sb_2S_3 layer during USP. In comparison, spraying a solution of SbEX without any thioamide at 165°C oxidized the growing layer into Sb_2O_3 . Thus, adding thioamides to a solution containing a halogenide-free coordination complex, e.g. SbEX, provides a facile and effective route to deposit thin films of Sb_2S_3 , and possibly other metal sulfides by ultrasonic spray pyrolysis or plausibly other in-air methods for demanding semiconductor applications. Further studies are foreseen to involve characterization of optoelectronic properties, and fine tuning of fabrication conditions related to SbEX-derived Sb_2S_3 thin films for application as a solar cell absorber.

Funding

This study was funded by: the Estonian Research Council project PRG627, Estonia; the Estonian Centre of Excellence project TK141 (TAR16016EK), Estonia; the European Economic Area and Norway 2014–2021 financial mechanisms project SV3-1624 (BTSC, ETAG21014), Norway, Iceland, Lichtenstein; and the European Commission project Horizon 2020 ERA Chair Emerging next generation photovoltaics, 5GSOLAR (2020–2026) Grant agreement ID: 952509,

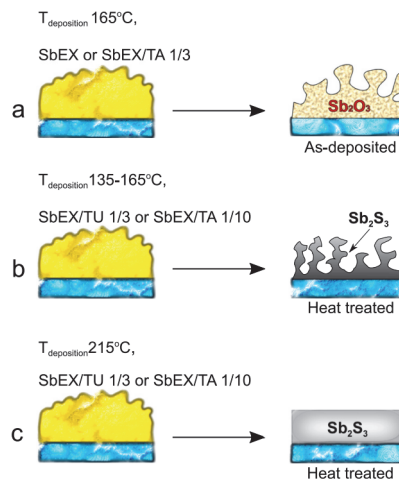


Fig. 7. Formation of Sb-based layers from SbEX by USP. (a) Spraying a solution of SbEX, or SbEX/TA 1/3 at 165°C creates a porous layer containing Sb_2O_3 . (b) Spraying a solution of SbEX/TU 1/3 or SbEX/TA 1/10 at 135–165°C results in porous layers of Sb_2S_3 after heat treatment due to the evolution of organic residues trapped within the layer. (c) Spraying a solution of SbEX/TU 1/3 or SbEX/TA 1/10 at 215°C and performing heat treatment yields uniform phase pure thin films of Sb_2S_3 , as the amount of organic residues is sufficiently low.

European Union.

CRedit authorship contribution statement

Jako S. Eensalu: Conceptualization, Methodology, Validation, Formal analysis, Investigation, Writing – original draft, Visualization. **Kaia Tõnsuaadu:** Investigation, Formal analysis, Resources, Writing – review & editing. **Ilona Oja Acik:** Conceptualization, Resources, Writing – review & editing, Supervision, Project administration, Funding acquisition. **Malle Krunks:** Conceptualization, Resources, Writing – review & editing, Supervision, Project administration, Funding acquisition.

Declaration of competing interest

The authors declare that they have no known competing financial interests or personal relationships that could have appeared to influence the work reported in this paper.

8 Acknowledgements

The authors thank Dr. Valdek Mikli from the Laboratory of Optoelectronic Materials Physics at Tallinn University of Technology (Tal-Tech) for recording SEM and EDX data.

Appendix A. Supplementary data

Supplementary data to this article can be found online at <https://doi.org/10.1016/j.mssp.2021.106209>.

References

- R. Kondrotas, G. Chen, J. Tang, Sb_2S_3 solar cells, *Joule* 2 (2018) 857–878, <https://doi.org/10.1016/j.joule.2018.04.003>.
- O. Savadogo, K.C. Mandal, Studies on new chemically deposited photoconducting antimony trisulphide thin films, *Sol. Energy Mater. Sol. Cells* 26 (1992) 117–136, [https://doi.org/10.1016/0927-0248\(92\)90131-8](https://doi.org/10.1016/0927-0248(92)90131-8).

- [3] Y. Itzhak, O. Niiitsoo, M. Page, G. Hodes, Sb₂S₃-Sensitized nanoporous TiO₂ solar cells, *J. Phys. Chem. C* 113 (2009) 4254–4256, <https://doi.org/10.1021/jp900302b>.
- [4] E. Zimmermann, T. Pfadler, J. Kalb, J.A. Dorman, D. Sommer, G. Hahn, J. Weickert, L. Schmidt-Mende, Toward high-efficiency solution-processed planar heterojunction Sb₂S₃ solar cells, *Adv. Sci.* 2 (2015) 1500059, <https://doi.org/10.1002/adv.201500059>.
- [5] C. Jiang, R. Tang, X. Wang, H. Ju, G. Chen, T. Chen, Alkali metals doping for high-performance planar heterojunction Sb₂S₃ solar cells, *Solar RRL* 3 (2019) 1800272, <https://doi.org/10.1002/solr.201800272>.
- [6] L. Zhang, D. Zhuang, M. Zhao, G. Gong, L. Guo, L. Ouyang, R. Sun, Y. Wei, X. Lyu, X. Peng, Sb₂S₃ thin films prepared by vulcanizing evaporated metallic precursors, *Mater. Lett.* 208 (2017) 58–61, <https://doi.org/10.1016/j.matlet.2017.05.040>.
- [7] F.T.F. O'Mahony, U.B. Cappel, N. Tokmoldin, T. Lutz, R. Lindblad, H. Rensmo, S. A. Haque, Low-temperature solution processing of mesoporous metal-sulfide semiconductors as light-harvesting photoanodes, *Angew. Chem. Int. Ed.* 52 (2013) 12047–12051, <https://doi.org/10.1002/anie.201305270>.
- [8] S.-J. Lee, S.-J. Sung, K.-J. Yang, J.-K. Kang, J.Y. Kim, Y.S. Do, D.-H. Kim, Approach to transparent photovoltaics based on wide band gap Sb₂S₃ absorber layers and optics-based device optimization, *ACS Appl. Energy Mater.* 3 (2020) 12644–12651, <https://doi.org/10.1021/acsaem.0c02552>.
- [9] N.N. Greenwood, A. Earnshaw, in: *Chemistry of the Elements, second ed.*, Butterworth-Heinemann, Oxford, U.K., 1997.
- [10] P. Büttner, F. Scheler, C. Pointer, D. Döhler, M.K.S. Barr, A. Koroleva, D. Pankin, R. Hatada, S. Flege, A. Manshina, E.R. Young, I. Minguez-Bacho, J. Bachmann, Adjusting interfacial chemistry and electronic properties of photovoltaics based on a highly pure Sb₂S₃ absorber by atomic layer deposition, *ACS Appl. Energy Mater.* 2 (2019) 8747–8756, <https://doi.org/10.1021/acsaem.9b01721>.
- [11] H.-H. Kim, S.-J. Lee, M.S. Park, J.-K. Kang, J.H. Heo, S.H. Im, S.-J. Sung, Highly reproducible planar Sb₂S₃-sensitized solar cells based on atomic layer deposition, *Nanoscale* 6 (2014) 14549–14554, <https://doi.org/10.1039/C4NR04148H>.
- [12] P. Kaienburg, B. Klingebiel, T. Kirchartz, Spin-coated planar Sb₂S₃ hybrid solar cells approaching 5% efficiency, *Beilstein J. Nanotechnol.* 9 (2018) 2114–2124, <https://doi.org/10.3762/bjnano.9.200>.
- [13] H. Zhang, S. Yuan, H. Deng, M. Ishaq, X. Yang, T. Hou, U.A. Shah, H. Song, J. Tang, Controllable orientations for Sb₂S₃ solar cells by vertical VTD method, *Prog. Photovoltaics* 28 (2020) 823–832, <https://doi.org/10.1002/ppp.3278>.
- [14] J. Escorcia-García, D. Becerra, M.T.S. Nair, P.K. Nair, Heterojunction CdS/Sb₂S₃ solar cells using antimony sulfide thin films prepared by thermal evaporation, *Thin Solid Films* 569 (2014) 28–34, <https://doi.org/10.1016/j.tsf.2014.08.024>.
- [15] J. Han, S. Wang, J. Yang, S. Guo, Q. Cao, H. Tang, X. Pu, B. Gao, X. Li, Solution-processed Sb₂S₃ planar thin film solar cells with a conversion efficiency of 6.9% at an open circuit voltage of 0.7 V achieved via surface passivation by a SbCl₃ interface layer, *ACS Appl. Mater. Interfaces* 12 (2020) 4970–4979, <https://doi.org/10.1021/acsaami.9b15148>.
- [16] Y.C. Choi, D.U. Lee, J.H. Noh, E.K. Kim, S.I. Seok, Highly improved Sb₂S₃ sensitized-inorganic-organic heterojunction solar cells and quantification of traps by deep-level transient spectroscopy, *Adv. Funct. Mater.* 24 (2014) 3587–3592, <https://doi.org/10.1002/adfm.201304238>.
- [17] R. Parize, T. Cossuet, O. Chaix-Pluchery, H. Roussel, E. Appert, V. Consonni, In situ analysis of the crystallization process of Sb₂S₃ thin films by Raman scattering and X-ray diffraction, *Mater. Des.* 121 (2017) 1–10, <https://doi.org/10.1016/j.matdes.2017.02.034>.
- [18] M.S. You, C.-S. Lim, D.H. Kwon, J.H. Heo, S.H. Im, K.J. Chae, Oxide-free Sb₂S₃ sensitized solar cells fabricated by spin and heat-treatment of Sb(III) (thioacetamide)₂Cl₃, *Org. Electron.* 21 (2015) 155–159, <https://doi.org/10.1016/j.orgel.2015.02.015>.
- [19] H. Lei, T. Lin, X. Wang, S. Zhang, Q. Cheng, X. Chen, Z. Tan, J. Chen, A novel in situ hydrothermal preparation route for Sb₂S₃ and its solar cell application, *Mater. Lett.* 223 (2018) 90–93, <https://doi.org/10.1016/j.matlet.2018.08.058>.
- [20] J. Rodriguez-Castro, P. Dale, M.F. Mahon, K.C. Molloy, L.M. Peter, Deposition of antimony sulfide thin films from single-source antimony thiolate precursors, *Chem. Mater.* 19 (2007) 3219–3226, <https://doi.org/10.1021/cm070405j>.
- [21] M. Medles, N. Benramdane, A. Bouzidi, K. Sahraoui, R. Miloua, R. Desfeux, C. Mathieu, Raman and Optical Studies of spray pyrolysed Sb₂S₃ thin films, *J. Optoelectron. Adv. Mater.* 16 (2014) 726–731.
- [22] R. Parize, A. Katerski, I. Gromyko, L. Rapenne, H. Roussel, E. Kärber, E. Appert, M. Krunks, V. Consonni, ZnO/TiO₂/Sb₂S₃ core-shell nanowire heterostructure for extremely thin absorber solar cells, *J. Phys. Chem. C* 121 (2017) 9672–9680, <https://doi.org/10.1021/acs.jpcc.7b00178>.
- [23] J.S. Eensalu, A. Katerski, E. Kärber, I. Oja Acik, A. Mere, M. Krunks, Uniform Sb₂S₃ optical coatings by chemical spray method, *Beilstein J. Nanotechnol.* 10 (2019) 198–210, <https://doi.org/10.3762/bjnano.10.18>.
- [24] Q. Wang, R. Jin, C. Jia, Z. Gao, C. Yin, M. Wang, J. Wang, S. Gao, Anodic TiO₂ nanotube arrays co-sensitized by uniform Ag₂S and Sb₂S₃ nanoparticles as high-efficiency energy materials for solar cells and photocatalysts, *Ceram. Int.* 43 (2017) 507–512, <https://doi.org/10.1016/j.ceramint.2016.09.186>.
- [25] M.I. Medina-Montes, Z. Montiel-González, N.R. Mathews, X. Mathew, The influence of film deposition temperature on the subsequent post-annealing and crystallization of sputtered Sb₂S₃ thin films, *J. Phys. Chem. Solids* 111 (2017) 182–189, <https://doi.org/10.1016/j.jpcs.2017.07.035>.
- [26] V. Janosevič, M. Mitrić, J. Savič, I.L. Valdižić, Structural, optical, and electrical properties of applied amorphized and polycrystalline Sb₂S₃ thin films, *Metall. Mater. Trans.* 47 (2016) 1460–1468, <https://doi.org/10.1007/s11661-015-3282-9>.
- [27] R.-D. Sun, T. Tsuji, Preparation of antimony sulfide semiconductor nanoparticles by pulsed laser ablation in liquid, *Appl. Surf. Sci.* 348 (2015) 38–44, <https://doi.org/10.1016/j.apsusc.2015.02.041>.
- [28] Q. Han, Y. Yuan, X. Liu, X. Wu, F. Bei, X. Wang, K. Xu, Room-temperature synthesis of self-assembled Sb₂S₃ films and nanorings via a two-phase Approach, *Langmuir* 28 (2012) 6726–6730, <https://doi.org/10.1021/la300244c>.
- [29] F. Alvi, K. Javed, N. Aslam, A. Sattar, L. Sherin, A. Ali, J. Amjad, S.U. Rehman, Structural and optical properties of N-acetyl-L-cysteine capped Sb₂S₃ quantum dots for LED applications, *Opt. Mater.* 111 (2021) 110559, <https://doi.org/10.1016/j.optmat.2020.110559>.
- [30] V. Piacente, P. Scardala, D. Ferro, Study of the vaporization behaviour of Sb₂S₃ and Sb₂Te₃ from their vapour pressure measurements, *J. Alloys Compd.* 178 (1992) 101–115, [https://doi.org/10.1016/0925-8388\(92\)90251-4](https://doi.org/10.1016/0925-8388(92)90251-4).
- [31] P.S. Patil, Versatility of chemical spray pyrolysis technique, *Master. Chem. Phys.* 59 (1999) 185–198, [https://doi.org/10.1016/S0254-0584\(99\)00049-8](https://doi.org/10.1016/S0254-0584(99)00049-8).
- [32] E. Kärber, A. Katerski, I. Oja Acik, A. Mere, V. Mikli, M. Krunks, Sb₂S₃ grown by ultrasonic spray pyrolysis and its application in a hybrid solar cell, *Beilstein J. Nanotechnol.* 7 (2016) 1662–1673, <https://doi.org/10.3762/bjnano.7.158>.
- [33] M. Krunks, V. Mikli, O. Bijakina, H. Rebane, A. Mere, T. Varena, E. Mellikov, Composition and structure of CuInS₂ films prepared by spray pyrolysis, *Thin Solid Films* 361–362 (2000) 61–64, [https://doi.org/10.1016/S0040-6090\(99\)00835-4](https://doi.org/10.1016/S0040-6090(99)00835-4).
- [34] K. Otto, I. Oja Acik, K. Tõnsuaadu, A. Mere, M. Krunks, Thermoanalytical study of precursors for In₂S₃ thin films deposited by spray pyrolysis, *J. Therm. Anal. Calorim.* 105 (2011) 615–623, <https://doi.org/10.1007/s10973-011-1507-8>.
- [35] I. Oja Acik, K. Otto, M. Krunks, K. Tõnsuaadu, A. Mere, Thermal behaviour of precursors for CuInS₂ thin films deposited by spray pyrolysis, *J. Therm. Anal. Calorim.* 113 (2013) 1455–1465, <https://doi.org/10.1007/s10973-013-3155-7>.
- [36] T. Dedova, M. Krunks, I. Gromyko, V. Mikli, I. Sildos, K. Utt, T. Unt, Effect of Zn:S molar ratio in solution on the properties of ZnS thin films and the formation of ZnS nanorods by spray pyrolysis, *Phys. Status Solidi* 211 (2014) 514–521, <https://doi.org/10.1002/pssa.201300215>.
- [37] S. Polivtseva, I.O. Acik, A. Katerski, A. Mere, V. Mikli, M. Krunks, Spray pyrolysis deposition of Sn₂S₃ thin films, *Energy Procedia* 60 (2014) 156–165, <https://doi.org/10.1016/j.egypro.2014.12.358>.
- [38] M. Krunks, T. Leskelä, I. Mutikainen, L. Niinistö, A thermoanalytical study of copper(I) thiocarbamide compounds, *J. Therm. Anal. Calorim.* 56 (1999) 479–484, <https://doi.org/10.1023/A:1010184107901>.
- [39] M. Krunks, T. Leskelä, R. Mannonen, L. Niinistö, Thermal decomposition of copper (I) thiocarbamide chloride hemihydrate, *J. Therm. Anal. Calorim.* 53 (1998) 355–364, <https://doi.org/10.1023/A:1010157528347>.
- [40] K. Otto, P. Bombicz, J. Madarász, I. Oja Acik, M. Krunks, G. Pokol, Structure and evolved gas analyses (TG/DTA-MS and TG-TTR) of *mer*-trichlororotis(thiourea)-indium(III), a precursor for indium sulfide thin films, *J. Therm. Anal. Calorim.* 105 (2011) 83–91, <https://doi.org/10.1007/s10973-011-1524-7>.
- [41] M. Krunks, J. Madarász, L. Hiltunen, R. Mannonen, E. Mellikov, L. Niinistö, Structure and thermal behaviour of dichlorobis(thiourea)cadmium(II), a single-source precursor for CdS thin films, *Acta Chem. Scand.* 51 (1997) 294–301, <https://doi.org/10.3891/acta.chem.scand.51-0294>.
- [42] M. Krunks, J. Madarász, T. Leskelä, A. Mere, L. Niinistö, G. Pokol, Study of zinc thiocarbamide chloride, a single-source precursor for zinc sulfide thin films by spray pyrolysis, *J. Therm. Anal. Calorim.* 72 (2003) 497–506, <https://doi.org/10.1023/A:1024561212883>.
- [43] S. Polivtseva, I. Oja Acik, M. Krunks, K. Tõnsuaadu, A. Mere, Thermoanalytical study of precursors for tin sulfide thin films deposited by chemical spray pyrolysis, *J. Therm. Anal. Calorim.* 121 (2015) 177–185, <https://doi.org/10.1007/s10973-015-4580-6>.
- [44] K. Otto, A. Katerski, A. Mere, O. Volobujeva, M. Krunks, Spray pyrolysis deposition of indium sulphide thin films, *Thin Solid Films* 519 (2011) 3055–3060, <https://doi.org/10.1016/j.tsf.2010.12.027>.
- [45] M. Kriisa, M. Krunks, I. Oja Acik, E. Kärber, V. Mikli, The effect of tartaric acid in the deposition of Sb₂S₃ films by chemical spray pyrolysis, *Mater. Sci. Semicond. Process.* 40 (2015) 867–872, <https://doi.org/10.1016/j.mssp.2015.07.049>.
- [46] J.S. Eensalu, A. Katerski, E. Kärber, L. Weinhardt, M. Blum, C. Heske, W. Yang, I. Oja Acik, M. Krunks, Semitransparent Sb₂S₃ thin film solar cells by ultrasonic spray pyrolysis for use in solar windows, *Beilstein J. Nanotechnol.* 10 (2019) 2396–2409, <https://doi.org/10.3762/bjnano.10.230>.
- [47] N. Maiti, S.H. Im, C.-S. Lim, S.I. Seok, A chemical precursor for depositing Sb₂S₃ onto mesoporous TiO₂ layers in nonaqueous media and its application to solar cells, *Dalton Trans.* 41 (2012) 11569–11572, <https://doi.org/10.1039/C2DT31348K>.
- [48] J. Rodriguez-Castro, K.C. Molloy, Y. Liu, C.S. Lai, Z. Dong, T.J. White, E.R. T. Tiekink, Formation of antimony sulfide powders and thin films from single-source antimony precursors, *J. Mater. Chem.* 18 (2008) 5399–5405, <https://doi.org/10.1039/B810947H>.
- [49] N. Bansal, F.T.F. O'Mahony, T. Lutz, S.A. Haque, Solution processed polymer-inorganic semiconductor solar cells employing Sb₂S₃ as a light harvesting and electron transporting material, *Adv. Energy Mater.* 3 (2013) 986–990, <https://doi.org/10.1002/aem.201300017>.
- [50] J.K. Brown, H.D. Arman, P.V. Poplakhin, E.R.T. Tiekink, Structural systematics in antimony *tris*(xanthates): Sb(S₂COR)₃, *Z. für Kristallogr. - Cryst. Mater.* 224 (2009) 368–374, <https://doi.org/10.1524/zkri.2009.1155>.
- [51] J. Li, X. Liu, J. Yao, The enhanced photovoltaic performance of Sb₂S₃ solar cells by thermal decomposition of antimony ethyl xanthate with thiourea doping, *Energy Technol.* 8 (2020) 1900841, <https://doi.org/10.1002/ente.201900841>.
- [52] J.S. Eensalu, K. Tõnsuaadu, J. Adamson, I. Oja Acik, M. Krunks, Thermal decomposition of *tris*(O-ethylthiocarbonato)-antimony(III)—a single-source

- precursor for antimony sulfide thin films, *J. Therm. Anal. Calorim.* (2021), <https://doi.org/10.1007/s10973-021-10885-1>.
- [53] NIST Chemistry WebBook, (n.d.). <https://webbook.nist.gov/chemistry/>.
- [54] G. Gottardi, The crystal structure of xanthates II. Antimonious xanthate, *Z. für Kristallogr. - Cryst. Mater.* 115 (1961) 451–459, <https://doi.org/10.1524/zkri.1961.115.16.451>.
- [55] P.A. Meenan, S.R. Anderson, D.L. Klug, 3 - the influence of impurities and solvents on crystallization, in: A.S. Myerson (Ed.), *Handbook of Industrial Crystallization*, second ed., Butterworth-Heinemann, Woburn, 2002, pp. 67–100, <https://doi.org/10.1016/B978-075067012-8/50005-7>.
- [56] X. Zeng, S.S. Pramana, S.K. Batabyal, S.G. Mhaisalkar, X. Chen, K.B. Jinesh, Low temperature synthesis of wurtzite zinc sulfide (ZnS) thin films by chemical spray pyrolysis, *Phys. Chem. Phys.* 15 (2013) 6763–6768, <https://doi.org/10.1039/C3CP43470B>.
- [57] P.F. Britt, *Pyrolysis and Combustion of Acetonitrile (CH₃CN)*, Oak Ridge National Laboratory, United States, 2002 (accessed March 3, 2021), <https://www.osti.gov/biblio/814574/>.
- [58] K.P. Shrestha, L. Seidel, T. Zeuch, F. Mauss, Detailed kinetic mechanism for the oxidation of ammonia including the formation and reduction of nitrogen oxides, *Energy Fuels* 32 (2018) 10202–10217, <https://doi.org/10.1021/acs.energyfuels.8b01056>.
- [59] R. Tang, X. Wang, C. Jiang, S. Li, W. Liu, H. Ju, S. Yang, C. Zhu, T. Chen, n-Type doping of Sb₂S₃ light-harvesting films enabling high-efficiency planar heterojunction solar cells, *ACS Appl. Mater. Interfaces* 10 (2018) 30314–30321, <https://doi.org/10.1021/acsami.8b08965>.
- [60] J. Madarász, G. Pokol, Comparative evolved gas analyses on thermal degradation of thiourea by coupled TG-FTIR and TG/DTA-MS instruments, *J. Therm. Anal. Calorim.* 88 (2007) 329–336, <https://doi.org/10.1007/s10973-006-8058-4>.

Curriculum vitae

Personal data

Name	Jako Siim Eensalu
Date of birth	22.04.1993
Place of birth	Estonia
Citizenship	Estonian

Contact data

E-mail	jako.eensalu [at] taltech.ee
--------	------------------------------

Education

2017–2021	Tallinn University of Technology, Chemical and Materials Technology, PhD
2015–2017	Tallinn University of Technology, Chemical and Environmental Engineering, MSC (<i>cum laude</i>)
2012–2015	Tallinn University of Technology, Chemical and Environmental Engineering, BSC
2001–2012	Tallinn French School, secondary education

Language competence

Estonian	Native
English	Proficient
French	Vantage
Russian	Intermediate

Participation in conferences

2021	Online European Materials Research Society 2021 Spring Meeting and Exhibition. Poster presentation.
2017–2021	Graduate School of Functional Materials and Technologies (GSFMT), Tallinn University of Technology and Tartu University, Estonia. Oral and poster presentations.
2020	11 th European Kesterite+ Online Workshop. Poster presentation.
2019	10 th European Kesterite+ Workshop, Uppsala University, Uppsala, Sweden. Poster presentation. European Materials Research Society 2019 Spring Meeting and Exhibition, Nice, France. Oral presentation.
2018	European Materials Research Society 2018 Spring Meeting and Exhibition, Strasbourg, France. Oral presentation.
2017	Baltic Polymer Symposion, Tallinn University of Technology, Tallinn, Estonia. Poster presentation. Conference of Young Scientists on Energy Issues, Kaunas, Lithuania. Oral presentation. 1 st place in Master's and 1 st -2 nd year doctoral students division.

Professional employment

2017–2021	Laboratory of Thin Film Chemical Technologies, Tallinn University of Technology, early stage researcher
2014	Estonian Centre for Environmental Research, analyst (temporary)

Work abroad

2019, September	Short term mobility visit to LMGP, Grenoble-INP, CNRS, Grenoble, France in the frame of project ETAG19009.
2017, February	Short term experimental study at Microelectronics Research and Development Laboratory, Northern Illinois University, IL, USA.

Defended dissertations

2017	Study of ZnO:Al Thin Films Deposited by Chemical Spray. Supervisors: Prof. Malle Krunk, Dr. Inga Gromyko.
------	---

Research projects

- ETAG21014 “Development of Semi-Transparent Bifacial Thin Film Solar Cells for Innovative Applications (BTSC)”.
- PRG627 “Antimony chalcogenide thin films for next generation semi-transparent solar cells applicable in electricity producing windows”.
- TAR16016EK Centre of Excellence “Advanced materials and high-technology devices for energy recuperation systems”.
- IUT19-4 “Thin films and nanomaterials by wet-chemical methods for next-generation photovoltaics”.
- ETAG19009 “Development of the optical layers for improving the design and performances of the extremely thin absorber (ETA) hybrid photovoltaic cells based on ZnO nanowires”.
- VA18048 “Wide band gap oxide semiconductors for photovoltaic applications”.

Supervised dissertations

Siddharth Ashok Kumar, Master’s Degree, 2020, (sup) Jako Siim Eensalu, Sb₂S₃ Thin Films from an Alternative Metal Organic Precursor by Ultrasonic Spray Pyrolysis, Tallinn University of Technology, School of Engineering, Department of Materials and Environmental Technology.

List of publications

1. **J. S. Eensalu**, K. Tõnsuaadu, I. Oja Acik, M. Krunk. “Sb₂S₃ thin films by ultrasonic spray pyrolysis of antimony ethyl xanthate,” *Materials Science in Semiconductor Processing*, vol. 137, p. 106209, Jan. 2022, doi: 10.1016/j.mssp.2021.106209.
2. **J. S. Eensalu**, K. Tõnsuaadu, J. Adamson, I. Oja Acik, M. Krunk. “Thermal decomposition of *tris*(O-ethylthiocarbonato)-antimony(III)—a single-source precursor for antimony sulfide thin films,” *Journal of Thermal Analysis and Calorimetry*, Jun. 2021, doi: 10.1007/s10973-021-10885-1.

3. **J. S. Eensalu**, A. Katerski, E. Kärber, L. Weinhardt, M. Blum, C. Heske, W. Yang, I. Oja Acik, M. Krunks. "Semitransparent Sb₂S₃ thin film solar cells by ultrasonic spray pyrolysis for use in solar windows," *Beilstein Journal of Nanotechnology*, vol. 10, pp. 2396–2409, Dec. 2019, doi: 10.3762/bjnano.10.230.
4. M. Ganchev, A. Katerski, S. Stankova, **J. S. Eensalu**, P. Terziyska, R. Gergova, H. Dikov, G. Popkirov, P. Vitanov. "Tin Dioxide Thin Films Deposited by Sol – Gel Technique," *AIP Conference Proceedings*, vol. 2075, pp. 140001–140008, 2019, doi: 10.1063/1.5091316.
5. M. Ganchev, A. Katerski, S. Stankova, **J. S. Eensalu**, P. Terziyska, R. Gergova, G. Popkirov, P. Vitanov. "Spin – coating of SnO₂ thin films," *Journal of Physics Conference Series*, 1186, 012027, 2019, doi: 10.1088/1742-6596/1186/1/012027.
6. **J. S. Eensalu**, A. Katerski, E. Kärber, I. Oja Acik, A. Mere, M. Krunks. "Uniform Sb₂S₃ optical coatings by chemical spray method," *Beilstein Journal of Nanotechnology*, vol. 10, pp. 198–210, Jan. 2019, doi: 10.3762/bjnano.10.18.
7. **J. S. Eensalu**, A. Katerski, A. Mere, M. Krunks. "Gas sensing capability of spray deposited Al-doped ZnO thin films," *Proceedings of the Estonian Academy of Sciences*, vol. 67, no. 2, pp. 124–130, Mar. 2018, doi: 10.3176/proc.2018.2.02.
8. **J. S. Eensalu**, M. Krunks, I. Gromyko, A. Katerski, A. Mere. "A comparative study on physical properties of Al-doped zinc oxide thin films deposited from zinc acetate and zinc acetylacetonate by spray pyrolysis," *Energetika*, vol. 63, no. 2, 46–55, Sept. 2017, doi: 10.6001/energetika.v63i2.3519.

Popular science publications

2021, April	"Photovoltaic Glass Makes Windows a Source of Electricity", English translation of Novaator, ERR article, Research in Estonia. https://researchinestonia.eu/2021/04/16/photovoltaic-glass-makes-windows-a-source-of-electricity/
2021, March	Laureate video for "Science in 3 minutes" competition organized by the Estonian Academy of Sciences. https://novaator.err.ee/k/teadus3minutiga
2021, February	"Photovoltaic Glass Makes Windows a Source of Electricity", in Estonian, Novaator, ERR. https://novaator.err.ee/1608093676/paikeseptareidest-klasid-muudavad-akna-elektrienergia-allikaks

Elulookirjeldus

Isikuandmed

Nimi	Jako Siim Eensalu
Sünniaeg	22.04.1993
Sünnikoht	Eesti
Kodakondsus	eesti

Kontaktandmed

E-post	jako.eensalu [at] taltech.ee
--------	------------------------------

Hariduskäik

2017–2021	Tallinna Tehnikaülikool, keemia- ja materjalitehnoloogia, PhD
2015–2017	Tallinna Tehnikaülikool, keemia- ja keskkonnakaitsetehnoloogia, MSc (<i>cum laude</i>)
2012–2015	Tallinna Tehnikaülikool, keemia- ja keskkonnakaitsetehnoloogia, BSc
2001–2012	Tallinna Prantsuse Lütseum, keskkharidus

Keelteoskus

Eesti keel	Emakeel
Inglise keel	Kõrgtase
Prantsuse keel	Edasijõudnu
Vene keel	Keskase

Osalemine konverentsidel

2021	Euroopa Materjaliuuringute Seltsi kevadine võrgukonverents ja näitus. Plakatettekanne.
2017–2021	Funktsionaalsete materjalide ja tehnoloogiate doktorikool (FMTDK), Tallinna Tehnikaülikool ja Tartu Ülikool, Eesti. Suulised ja plakatettekanded.
2020	11. Euroopa Kesteriit+ võrgutöötuba. Plakatettekanne.
2019	10. Euroopa Kesteriit+ töötuba, Uppsala Ülikool, Uppsala, Rootsi. Plakatettekanne. Euroopa Materjaliuuringute Seltsi kevadine konverents ja näitus, Nice, Prantsusmaa. Suuline ettekanne.
2018	Euroopa Materjaliuuringute Seltsi kevadine konverents ja näitus, Strasbourg, Prantsusmaa. Suuline ettekanne.
2017	Balti Polümeerisümposium, Tallinna Tehnikaülikool, Tallinn, Eesti. Plakatettekanne. Noorteadlaste energiateemade konverents, Kaunas, Leedu. Suuline ettekanne. 1. koht magistri- ja 1.-2. aasta doktorantide jaotuses.

Teenistuskäik

2017–2021	Keemiliste kiletehnoloogiate teaduslabor, Tallinna Tehnikaülikool, doktorant-nooremteadur
2014	Eesti Keskkonnauuringute Keskus, asenduslaborant

Töö välismaal

- 2019, september Lühiajaline mobiilsusvisiit, LMGP, Grenoble-INP, CNRS, Grenoble, Prantsusmaa, teadusprojekti ETAG19009 raames.
- 2017, veebruar Lühiajaline katseline uurimistöö, Microelectronics Research and Development Laboratory, Northern Illinois University, IL, USA.

Kaitstud väitekirjad

- 2017 "Keemilise pihustamise meetoditel sadestatud ZnO:Al õhukeste kilede uurimine". Juhendajad: Prof. Malle Krunk, Dr. Inga Gromõko.

Teadusprojektid

- ETAG21014 "Poolläbipaistvate kahepoolsete õhukesekeleliste päikeseplatade arendus uuenduslikeks rakendusteks (BTSC)".
- PRG627 "Antimon-kalkogeniid õhukese kiled järgmise põlvkonna poolläbipaistvatele päikeseelementidele kasutamiseks elektrit tootvates akendes".
- TAR16016EK Tippkeskuse projekt "Uudsed materjalid ja kõrgtehnoloogilised seadmed energia salvestamise ja muundamise süsteemidele".
- IUT19-4 "Õhukese kiled ja nanomaterjalid keemilistel vedeliksadestusmeetoditel uue põlvkonna fotovoltseadistele".
- ETAG19009 "ZnO nanovarrastel põhineva üliõhukese hübriid-päikeseelemendi arendamine".
- VA18048 "Laiakeelutsoonilised oksiidpooljuhid fotovoltseadistele".

Juhendatud väitekirjad

- Siddharth Ashok Kumar, magistrikraad, 2020. "Alternatiivsest metallorgaanilisest lähteainest ultrahelipihustussadestuse meetodil sadestatud Sb₂S₃ õhukese kiled", Tallinna Tehnikaülikool, Inseneriteaduskond, Materjali- ja keskkonnatehnoloogia instituut. Juhendaja: Jako Siim Eensalu.

Teaduspublikatsioonid

1. **J. S. Eensalu**, K. Tõnsuaadu, I. Oja Acik, M. Krunk. "Sb₂S₃ thin films by ultrasonic spray pyrolysis of antimony ethyl xanthate," *Materials Science in Semiconductor Processing*, vol. 137, p. 106209, Jan. 2022, doi: 10.1016/j.mssp.2021.106209.
2. **J. S. Eensalu**, K. Tõnsuaadu, J. Adamson, I. Oja Acik, M. Krunk. "Thermal decomposition of tris(O-ethylthiocarbonato)-antimony(III)—a single-source precursor for antimony sulfide thin films," *Journal of Thermal Analysis and Calorimetry*, Jun. 2021, doi: 10.1007/s10973-021-10885-1.
3. **J. S. Eensalu**, A. Katerski, E. Kärber, L. Weinhardt, M. Blum, C. Heske, W. Yang, I. Oja Acik, M. Krunk. "Semitransparent Sb₂S₃ thin film solar cells by ultrasonic spray pyrolysis for use in solar windows," *Beilstein Journal of Nanotechnology*, vol. 10, pp. 2396–2409, Dec. 2019, doi: 10.3762/bjnano.10.230.
4. M. Ganchev, A. Katerski, S. Stankova, **J. S. Eensalu**, P. Terziyska, R. Gergova, H. Dikov, G. Popkirov, P. Vitanov. "Tin Dioxide Thin Films Deposited by Sol – Gel Technique," *AIP Conference Proceedings*, vol. 2075, pp. 140001–140008, 2019, doi: 10.1063/1.5091316.

5. M. Ganchev, A. Katerski, S. Stankova, **J. S. Eensalu**, P. Terziyska, R. Gergova, G. Popkirov, P. Vitanov. "Spin – coating of SnO₂ thin films," *Journal of Physics Conference Series*, 1186, 012027, 2019, doi: 10.1088/1742-6596/1186/1/012027.
6. **J. S. Eensalu**, A. Katerski, E. Kärber, I. Oja Acik, A. Mere, M. Krunks. "Uniform Sb₂S₃ optical coatings by chemical spray method," *Beilstein Journal of Nanotechnology*, vol. 10, pp. 198–210, Jan. 2019, doi: 10.3762/bjnano.10.18.
7. **J. S. Eensalu**, A. Katerski, A. Mere, M. Krunks. "Gas sensing capability of spray deposited Al-doped ZnO thin films," *Proceedings of the Estonian Academy of Sciences*, vol. 67, no. 2, pp. 124–130, Mar. 2018, doi: 10.3176/proc.2018.2.02.
8. **J. S. Eensalu**, M. Krunks, I. Gromyko, A. Katerski, A. Mere. "A comparative study on physical properties of Al-doped zinc oxide thin films deposited from zinc acetate and zinc acetylacetonate by spray pyrolysis," *Energetika*, vol. 63, no. 2, 46–55, Sept. 2017, doi: 10.6001/energetika.v63i2.3519.

Populaarteaduspublikatsioonid

- | | |
|----------------|--|
| 2021, aprill | "Photovoltaic Glass Makes Windows a Source of Electricity", Research in Estonia, Novaator, ERR artikli ingliskeelne tõlge. https://researchinestonia.eu/2021/04/16/photovoltaic-glass-makes-windows-a-source-of-electricity/ |
| 2021, märts | Eesti Teaduste Akadeemia "Teadus 3 minutiga" võistluse võiduvideo. https://novaator.err.ee/k/teadus3minutiga |
| 2021, veebruar | "Päikesepatareidest klaasid muudavad akna elektrienergia allikaks", Novaator, ERR. https://novaator.err.ee/1608093676/paikesepatareidest-klaasid-muudavad-akna-elektrienergia-allikaks |

ISSN 2585-6901 (PDF)
ISBN 978-9949-83-782-3 (PDF)